AD-A272 015

WL-TR-93-2079

ELECTRONICALLY METASTABLE MOLECULES OF HIGH SYMMETRY

HANSPETER HELM

SRI INTERNATIONAL
333 RAVENSWOOD AVENUE
MENLO PARK, CA 94025-3493

MAY 1993

FINAL REPORT FOR PERIOD 3/16/90 - 4/15/93
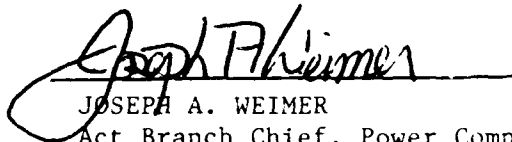
DTIC
SELECTED
NOV 0 8 1993
B

93-27248

NOTICE

When Government drawings, specifications, or other data are used for any purpose other than in connection with a definitely Government-related procurement, the United States Government incurs no responsibility or any obligation whatsoever. The fact that the government may have formulated or in any way supplied the said drawings, specifications, or other data, is not to be regarded by implication, or otherwise in any manner construed, as licensing the holder, or any other person or corporation; or as conveying any rights or permission to manufacture, use, or sell any patented invention that may in any way be related thereto.

This report is releasable to the National Technical Information Service (NTIS). At NTIS, it will be available to the general public, including foreign nations.
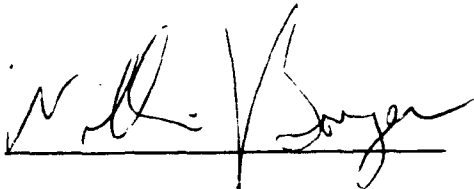
This technical report has been reviewed and is approved for publication.

Research Physicist
Plasma Research Section
Power Component Branch
Aerospace Power Division
Aero Propulsion and Power Directorate

JOSEPH A. WEIMER
Act Branch Chief, Power Components Branch
Aerospace Power Division
Aero Propulsion and Power Directorate

WILLIAM U. BORGER
Chief, Aerospace Power Division
Aero Propulsion & Power Directorate

If your address has changed, if you wish to be removed from our mailing list, or if the addressee is no longer employed by your organization please notify WL/POOC , WPAFB, OH 45433- 7650 to help us maintain a current mailing list.

Copies of this report should not be returned unless return is required by security considerations, contractual obligations, or notice on a specific document.

REPORT DOCUMENTATION PAGE

Public reporting burden for this collection of information is estimated to average 1 hour per response, including the time for reviewing instructions, searching existing data sources, gathering and maintaining the data needed, and completing and reviewing the collection of information. Send comments regarding this burden estimate or any other aspect of this collection of information, including suggestions for reducing this burden, to Washington Headquarters Services, Directorate for Information Operations and Reports, 1215 Jefferson Davis Highway, Suite 1204, Arlington, VA 22202-4302, and to the Office of Management and Budget, Paperwork Reduction Project (0704-0188), Washington, DC 20503.

1. AGENCY USE ONLY (Leave blank)	2. REPORT DATE MAY 1993	3. REPORT TYPE AND DATES COVERED FINAL (3/16/90 – 4/15/93)

4. TITLE AND SUBTITLE ELECTRONICALLY METASTABLE MOLECULES OF HIGH SYMMETRY	5. FUNDING NUMBERS C F33615-90-C-2007 PE 61102 PR 2301
6. AUTHOR(S) HANSPETER HELM	TA S2 WU 11

7. PERFORMING ORGANIZATION NAME(S) AND ADDRESS(ES) SRI INTERNATIONAL 333 RAVENSWOOD AVENUE MENLO PARK CA 94025	8. PERFORMING ORGANIZATION REPORT NUMBER PYU 8878, MP 93-078

9. SPONSORING/MONITORING AGENCY NAME(S) AND ADDRESS(ES) AEROPROPULSION AND POWER DIRECTORATE WRIGHT LABORATORY AIR FORCE MATERIEL COMMAND WRIGHT PATTERSON AFB OH 45433-7650	10. SPONSORING/MONITORING AGENCY REPORT NUMBER WL-TR-93-2079

11. SUPPLEMENTARY NOTES

12a. DISTRIBUTION/AVAILABILITY STATEMENT APPROVED FOR PUBLIC RELEASE; DISTRIBUTION IS UNLIMITED.	12b. DISTRIBUTION CODE

13. ABSTRACT (Maximum 200 words)

This project is part of the search for a novel propellant based on molecules with excess internal energy for use in the combustion process. Spectroscopic properties of neutral molecules of triatomic hydrogen, tetraoxygen, superexcited oxygen, and hydronium were investigated using laser ionization, laser photodissociation, and charge neutralization techniques. The neutrals were prepared in a fast beam by electron transfer from stationary gas targets to mass selected ions. Excited state lifetimes and electronic, vibrational, and rotational structures were examined as well as the dissociation products and the effect that external electric fields have on the stability of the molecules.

14. SUBJECT TERMS Photoionization, photodissociation, electronically excited states, Rydberg states, autoionization, Stark effect, polyatomic oxygen, triatomic hydrogen.	15. NUMBER OF PAGES 119
	16. PRICE CODE

17. SECURITY CLASSIFICATION OF REPORT	18. SECURITY CLASSIFICATION OF THIS PAGE	19. SECURITY CLASSIFICATION OF ABSTRACT	20. LIMITATION OF ABSTRACT
UNCLASSIFIED	UNCLASSIFIED	UNCLASSIFIED	UL

CONTENTS

FIGURES

INTRODUCTION

The research program High Energy Density Matter is based on the quest for a novel propellant based on molecules with excess internal energy for use in the combustion process. Our analysis of the various research goals in the projects of this program finds three schools of thought for accomplishing this goal.

One, the initial impetus for this program, centers on the stability of the H_4 molecule. This molecule has now been demonstrated theoretically[1] to be unstable as an isolated species.

A second class of thought addressed species which can generally be named either "strained" or "hypervalent". The origin of the energy content of these species arises from unsaturated or oversaturated electron configurations, which can confine molecules into geometries that are separated from the lowest dissociation limit of the system by energetic barriers. Some of the molecules that were investigated in this class are more conventional strained ring-structures, while others address the issue of novel bonding situations in unconventional species such as H_3O.

The third category of study in the metastable fuels program centers on the effects of trapping excited and radical species in matrices. This subject encompasses both the possibility of stabilizing excess energy by the cold crystal lattice as well as the general problem of storage, once suitably long-lived metastable species are identified.

As far as we can tell, no single species has yet been identified that satisfies the three requirements for a novel fuel: low weight, high specific impulse, and long lifetime. However, the theoretical part of this program has led to several significant advances in our understanding of energetic species. Two examples are the prediction of stable sulfur-like ring geometries of oxygen and the prediction of a stable species of H_3O and its deuterated counterpart.

The intent of this research program was to explore specifically these and similar systems, partly because our experiments can serve as a test for the theoretical work and partly because the synthesis and spectroscopic characterization of these molecules represent a formidable challenge to the experimentalist.

We first briefly review the experimental tools we used for performing this research. Then we discuss the molecules that our experiments focused on.

EXPERIMENTAL TECHNIQUES

Most of our experiments were conducted in fast molecular beams using near-resonant charge transfer as a selective means to produce the excited, long-lived neutral molecule. These molecules can be characterized in either of three configurations. One is a fast neutral beam-laser photodissociation spectrometer in which direct dissociation, predissociation, and radiative dissociation can be studied and the kinetic energy release of the dissociative system can be measured with meV precision. The second is a fast neutral beam laser photoionization spectrometer in which laser-induced direct ionization, autoionization, and field ionization processes are measured. The third experiment uses the first instrument discussed above but without a laser. It is modified to monitor directly the neutral fragment atoms and molecules that are formed in dissociative charge transfer of mass selected ions.

FAST BEAM SPECTROSCOPIES

The virtues of spectroscopy in fast beams of charged and neutral molecules include the possibility of precise definition of the molecule species under study and the reduction of inhomogenous broadening.[2] The species can be precisely defined because a fast molecule ion beam can be mass selected and, if a neutral beam is required, neutralized in a suitable charge transfer gas. This seemingly complex way of preparing the sample molecule offers the possibility of selectively preparing molecules in states other than the ground electronic state and in nonstatistical vibrational distributions. In the same manner, radicals may be prepared so that they are purified from their chemical precursors or reaction products.

In near resonant charge transfer at keV energies, the nuclear geometry of the ion (vibration and rotation) remains to first order unchanged, and the transferred electron is preferentially attached to the ion core with a binding energy that is similar (near-resonant) to the ionization potential of the neutral target gas. Since little momentum is transferred by the exchanged electron, a neutral beam with qualities comparable to the primary ion beam results, particularly in the case of near resonance. This beam can now be purged of residual ions and apertured to suppress dissociative charge-transfer products. In this manner, we can prepare a fast beam of typically 10^7 to 10^{10} molecules per second traveling at speeds of about 0.1% of the speed of light. Note that the density in this beam is equivalent to pressures ranging from 10^{-5} to 10^{-12} Torr. Nevertheless, laser spectroscopy is readily performed with such beams.

An intrinsic second advantage of spectroscopy in a fast beam lies in the dramatic reduction in the inhomogenous broadening of optical transitions. If the angular spread of the ion beam is kept low by proper ion-optical focusing, the residual spread of relative velocities in the neutral beam is reduced to that of a gas sample at a few degrees kelvin.[3]

A third beneficial property of the fast beam can be used in studying dynamic processes of molecules that are induced by photoexcitation. This advantage derives from the fact that the center of mass of the products of a process such as dissociation, autoionization, or direct ionization retains, except for a negligible photon recoil, the velocity of the parent. Because the parent is fast at keV energies, efficient single-particle detection techniques can be used to monitor the reaction products and to measure their translational energy, thus enabling the monitoring of chemically isolated single-molecule processes.

2

PHOTODISSOCIATION, DISSOCIATIVE CHARGE TRANSFER

A novel approach to the study of dissociative processes in fast neutral beams has become possible with a time- and position-sensitive detector that we have built at SRI and used extensively.[4-7] For the photodissociation studies, the fast beam of excited neutral molecules is crossed with a tunable dye laser in a crossed beam configuration, and the resulting photofragments are detected with a time- and position-sensitive detector; this setup allows us to measure of the momentum distribution of fragment pairs arising from a single dissociation event. A diagram of this experimental arrangement is shown in Figure 1.

The multichannel plate detector consists of two opposing sectors of opening angle 20° that allow separate detection of the two photofragments produced in a single photodissociation event. The detector and its associated electronics permit measurement of the spatial separation, R, of the two fragments at the channel-plate surface with a precision of better than 100 μm; this is accomplished by measuring the center of charge of each electron cloud emitted by the channel plates with a multianode system using the charge division method. The flight-time difference between these two fragments can be measured with a precision of better than 1 ns using the fast current pulses induced in the supply lines to the output face of the channel plates when a particle is detected.

By tuning the laser and monitoring the coincidence count rate at the detector, we obtain absorption spectra of transitions in the neutral beam that lead to photodissociation. Space- and time-resolved spectra of photofragments can then be recorded with the dye laser set to an absorption transition. These time and spatial coordinates of the fragment pair carry all the information required to calculate the center-of-mass angle and energy under which the fragment pair emerges from the dissociation event.

Removing the aperture and the laser beam from the setup shown in Figure 1 transforms the instrument into one that is capable of directly monitoring the neutral particles formed in dissociative charge transfer. From the translational energy release of a molecules formed in a process such as

$$O_4^+ + C_s \rightarrow O_4^* \rightarrow O_2 + O_2 \tag{1}$$

we can infer the energetics and lifetimes of the excited intermediate (O_4^* in case of reaction 1).

PHOTOIONIZATION

Using the experimental setup shown in Figure 2, we obtain photoionization spectra of neutral molecules by detecting the appearance of the parent ion formed in direct ionization, autoionization, and field-ionization.[8-10] In these experiments, the molecules are excited in the 120-cm-long field-free drift region by a collinear dye laser beam. The dye laser operates at 10 to 100 Hz and has an energy of typically 1-50 μJ/pulse.

Ionizing states are detected by separating the product ions from the parent neutral beam into a channeltron, using the electrostatic quadrupole deflector at the end of the beam line in Figure 2. Because energy analysis is used, the mass of the product ion is uniquely determined.
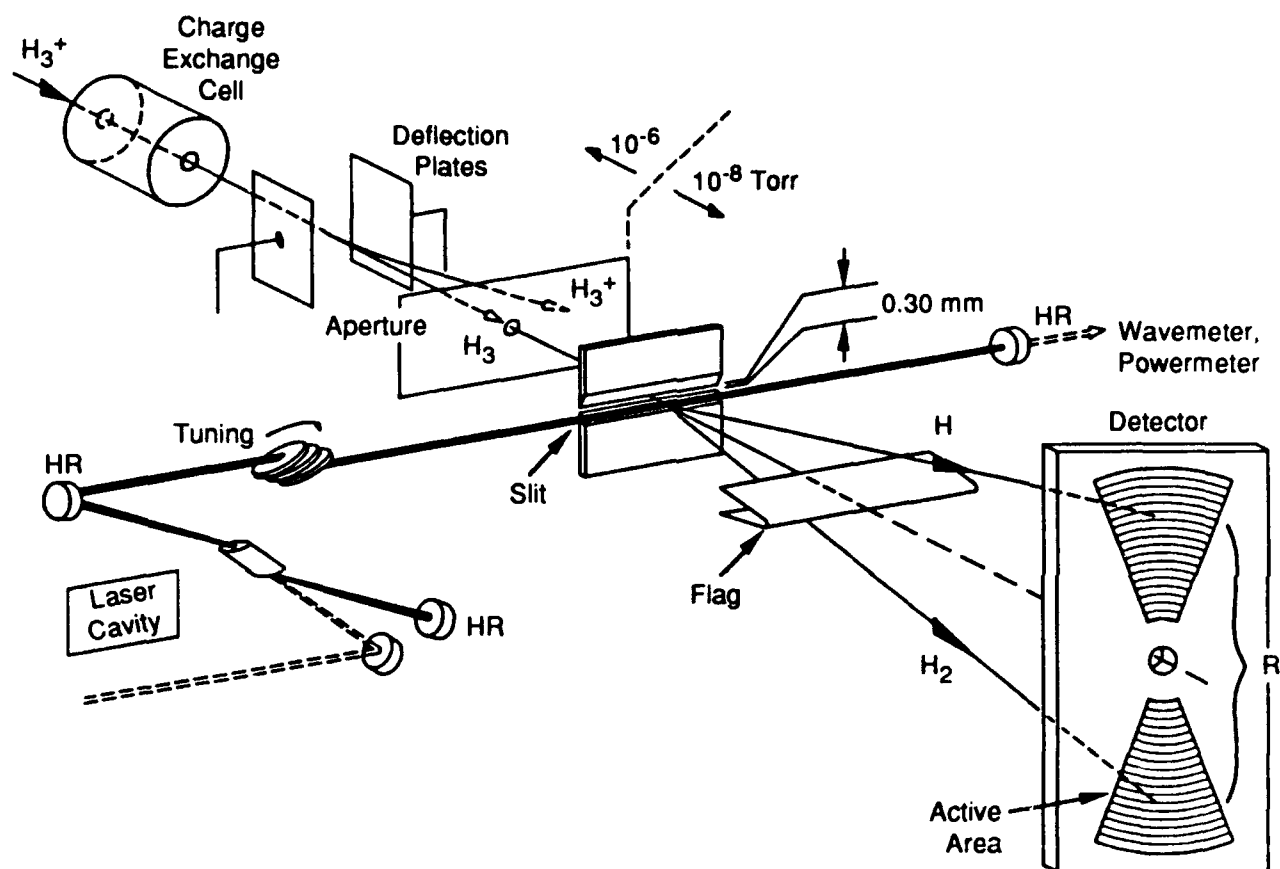
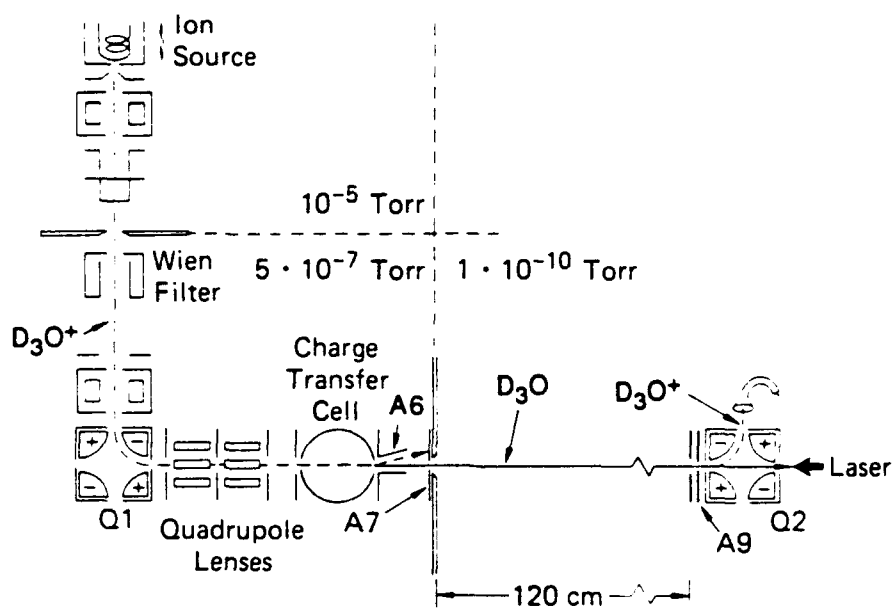Figure 1.   Fast beam photodissociation spectrometer.

Figure 2. Fast neutral beam photoionization spectrometer.

Shown here for the experiment on photoionization of the neutral hydronium molecule.

RESULTS AND DISCUSSION

We have conducted a variety of studies on the spectroscopic properties of triatomic hydrogen, neutral hydronium, tetraoxygen, and superexcited oxygen.

TRIATOMIC HYDROGEN

We used two techniques to determine the lifetime[11] of the long-lived excited state of H_3 in the ground vibrational level and in the symmetric stretch excited state. Both techniques gave similar results that lie about two orders of magnitude shorter than predicted by theory. We attribute the difference to weakly allowed radiative transitions that were not accounted for by theory.

We analyzed the p-electron Rydberg series of triatomic hydrogen using a two-step resonant photoexcitation scheme.[12,13] The excited state structure of triatomic hydrogen characterized by an outer p-electron reveals a complete panorama of all channel interactions that can occur in a poly-atomic molecule: rotational, vibrational coupling, as well as autoionization and competition with predissociation. A multichannel quantum defect theory was developed to identify and explain the dominant spectral features.

The Stark effect of triatomic hydrogen was examined in detail[14] because it was found that the excited states of H_3 showed unprecedented sensitivity to even weak external fields, specifically in inducing dissociation of selected states.[15] This work lead to an examination of the properties of H_3 in electric field ionization.[16] Details of this work are given in Appendices A through F.

NEUTRAL HYDRONIUM

The quantum chemistry calculations by Talbi and Saxon[17] on the potential energy surfaces of H_3O predict a local minimum at 1.0 eV above the lowest dissociation limit. According to their calculations, the molecule in this minimum is barred from dissociation by an electronic barrier height of 150 meV (see Figure 3). Transition states of H_3O, electronically excited states of this molecule, and transition moments were also calculated by these authors, as well as the ionization potential.

Experimental information on the existence of this molecule is available, although with some conflicting, or at least unexplained, observations. Gellene and Porter[18] observed the formation of long-lived D_3O, but not its analog[19] containing O^{18}, and no species where D was replaced by H. However, Beynon and coworkers[20] found both D_3O as well as H_3O formed with lifetimes exceeding 1 μs in charge transfer of the ionic species with alkalis.
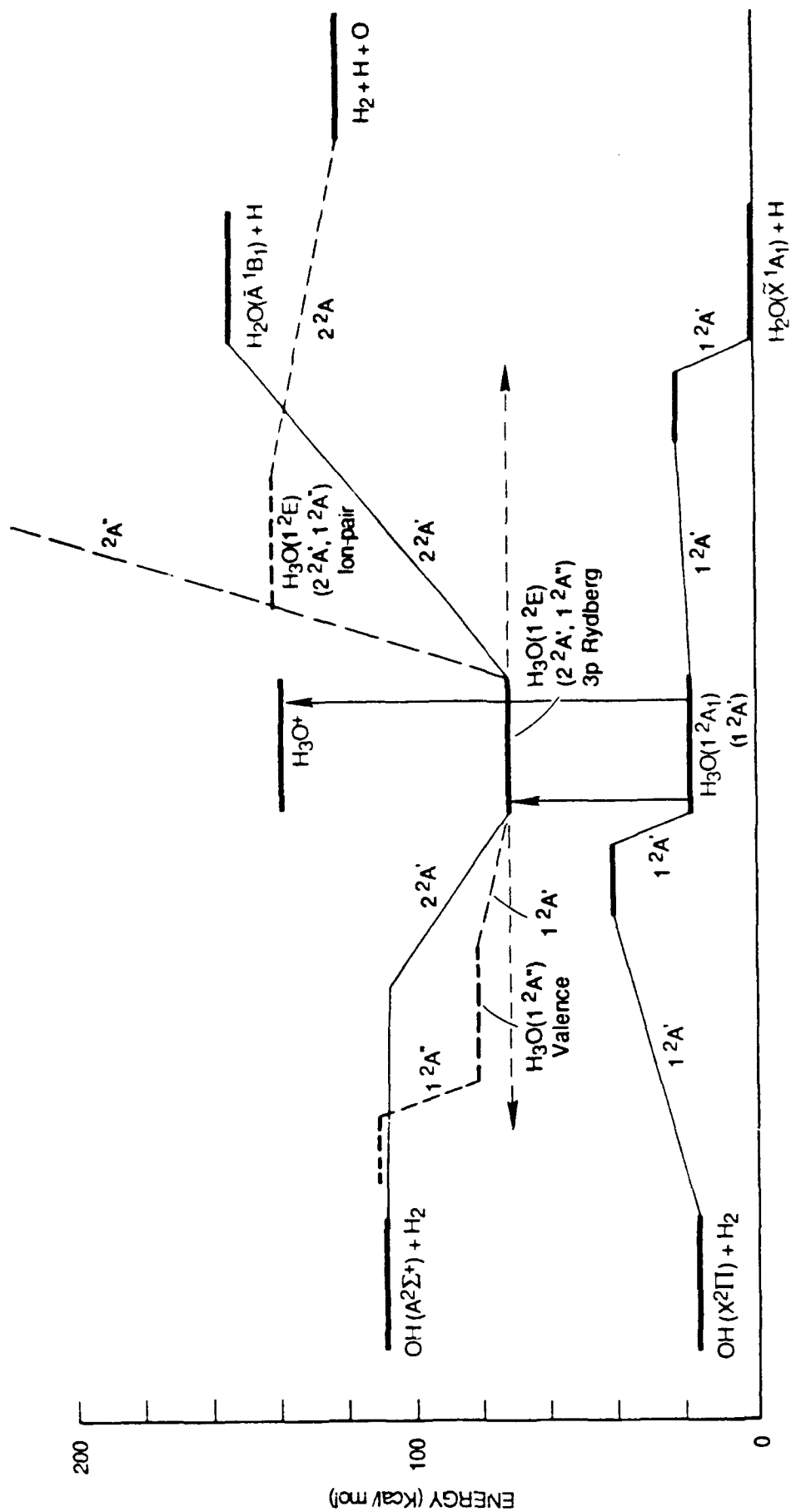
6

Figure 3. Minima and transition states for the H₃O system calculated by Talbi and Saxon. The proposed photodissociation and photoionization reactions are indicated.

We used a variety of excitation schemes to probe the excited state spectrum of long-lived D_3O molecules formed in charge transfer of mass selected D_3O^+ ions in cesium. The energy diagram in Figure 3 indicates that direct ionization should occur at wavelengths shorter than ~235 nm. We found evidence for direct ionization of the neutral D_3O molecule when exciting with tunable radiation from 220 to 237 nm. This ionization signal was extremely weak; typically one D_3O molecule was detected for every 25 laser shots. The theoretical calculations also predict that optically allowed bound excited states should lie at about 2.0 eV (3p 1^2E state) and at about 3.7 eV (4p state) above the ground state of the neutral molecule. In a two-color excitation scheme, we used a tunable laser to excite the predicted 3p state (wavelength range 560 to 630 nm) and the tripled output of a Nd:YAG laser at 353 nm to ionize the 3p level. No wavelength-dependent ionization signal could be detected that would prove the existence of a long-lived resonant intermediate 3p state. In a similar experiment, we used the wavelength range from 331 to 340 nm to probe the predicted 4p state. To photoionize the 4p state, we used the doubled output of the Nd:YAG laser at 532 nm. No photoionization signal was detected in this experiment either. Finally, we used very high pulse energies at 532 nm (>100 mJ) in an attempt to nonresonantly ionize the D_3O molecule in a three-photon process. This experiment also gave no unique ionization signature.

This set of experiments left us with no conclusive evidence for the predicted structure of D_3O. The only positive result is that obtained in the one-photon, direct ionization process. Since this signal is not structured in wavelength and since this signal is also extremely weak, such that no meaningful threshold can be deduced, we are unable to provide either a precise ionization potential or proof of the theoretically predicted structure of D_3O. A unique conclusion on the stability of D_3O cannot be given from our results. The negative results imply either (1) that the intermediate excited states of D_3O are unstable against predissociation on a time scale shorter than the direct photoionization route (this requires predissociation lifetimes less than 10^{-12} s) or (2) that the Frank Condon factors for their excitation from the ground state are too small for an efficient transfer of population. The latter is not supported by the theoretical calculations,[17] which predict rather similar geometry for the neutral and ionic species, in agreement with the finding that the neutral species can be formed by charge transfer in the first place.

RING STRUCTURES OF OXYGEN

The calculations of Seidl and Schaefer[21] predict the existence of stable oxygen ring configurations such as O_4, O_8, and O_{12}. The original impetus to the study of the stability of cyclic oxygen derived from the close electronic analogy between oxygen and sulfur, which had already been explored in previous work.[22] Numerous ring structures are observed for sulfur, the most stable allotrope being the orthorhombic α form of cyclo-S_8.

To our knowledge, no cyclic oxygen species are known experimentally, although several recent discussions of unknown details in the oxygen photochemistry invoke the possible involvement of four-atomic oxygen. Some of the cases, such as the pressure dependence of the intensity[23] of the important Herzberg bands of O_2 and the catalytic formation of ozone at high altitude,[24] are attributed to the presence of van der Waals dimers. Other effects, such as the efficient energy pooling[25] of $O_2 {}^1\Delta_g$, in liquid oxygen,

$$O_2{}^1\Delta_g + O_2{}^1\Delta_g \rightarrow (O_2{}^1\Delta_g)_2 \tag{2}$$

which is followed by photoemission at about twice the $^1\Delta$ ($v = 0$) energy, near 6340 Å, are also attributed to dimerized oxygen.[26]

Note that the ring form of oxygen predicted by Seidl and Schaefer[21] is *not* the weakly bound van der Waals form, but rather a tightly packed ($R_e \approx 1.43$ Å) nearly planar structure, approximately 4 eV above the lowest dissociation threshold, $O_2 + O_2$.

We undertook two experiments to search for the ring structures of oxygen. One involves the fast beam method, and the other is a novel approach based on a plasma reactor, as described below.

Tetraoxygen in Fast Beam Experiments

We investigated electron transfer to O_4^+ in reactions with O_2, NO, and Cs. We observed the formation of O_4 molecules that decay by predissociation and by direct dissociation,[27] and we determined the kinetic energy release in dissociation as well as the nature of the dissociation products. We found signatures of three short-lived electronic states of tetraoxygen at energies near 2 eV above $O_2 + O_2$ in electron transfer from O_2 and NO. In the experiment with cesium, we identified longer-lived electronic states ($10^{-13} < \tau < 10^{-7}$ s) at 9.4 and 10.5 eV. The energy release and symmetry of the dissociation pattern suggest that the high lying states are symmetric molecular configurations at extended bond lengths (~2.5 Å). Details of this work are given in Appendix G.

Synthesis of O_4 from Neutral Oxygen

The calculations[21] place the stable O_4 ring about 4 eV above the ground state products $O_2 + O_2$, at a 1.43-Å internuclear separation of the oxygen atom from its nearest neighbor. Formation of the cyclic species from ground state oxygen thus faces two substantial hurdles: one is to supply the activation energy to get 2 eV above ground, and the second is to change the internuclear separation from the regular equilibrium distance of O_2, 1.19 Å. Both obstacles could be overcome if one succeeds in forming O_4 in collisions between electronically excited O_2 and ground state O_2 or in collisions between ozone and excited oxygen atoms or molecules. The long-lived O_2 species in the electronic states A, A', and c (radiative lifetimes of 0.16, >16, and 10 s, respectively) all have internuclear separations similar to those predicted for O_4, and they lie energetically above the predicted stable form of O_4. The known quenching rates for either species in oxygen are relatively slow;[28] however, they are faster than the natural lifetime. We therefore anticipate that the formation of cyclic O_4 could occur in three-body reactions such as

$$O_2^*(A,A',c) + O_2 + O_2 \rightarrow O_4 + O_2 + 2\,eV \tag{3}$$
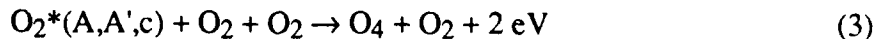
or in the energy pooling processes

$$O_2^* + O_2^* + O_2 \rightarrow O_4 + O_2 \tag{4}$$

and in similar reactions involving ozone and atomic oxygen. To reach Schaefer's stable O_4 in such collisions requires a nonadiabatic transition from an excited state surface of O_4 into the singlet surface predicted to be stable.

Driving these reactions at high efficiency required both high pressure as well as a high level of excitation. Two experiments were attempted, both involving laser-produced oxygen plasmas at high pressure.

We call one experimental concept "oxygen focus" because it describes both the method used and the size of the reaction volume under study. The setup is shown schematically in Figure 4. The idea was to use a tightly focused high power laser pulse to prepare a miniature volume ($\sim 10^{-8}$ cm^3) of highly ionized and excited oxygen at near atmospheric pressure. The next key to the experiment was to freeze three-body chemistry in this plasma environment after approximately 50 to 200 ns by expanding this miniature volume into a high-vacuum region. The product states were then examined by multiphoton photoionization.
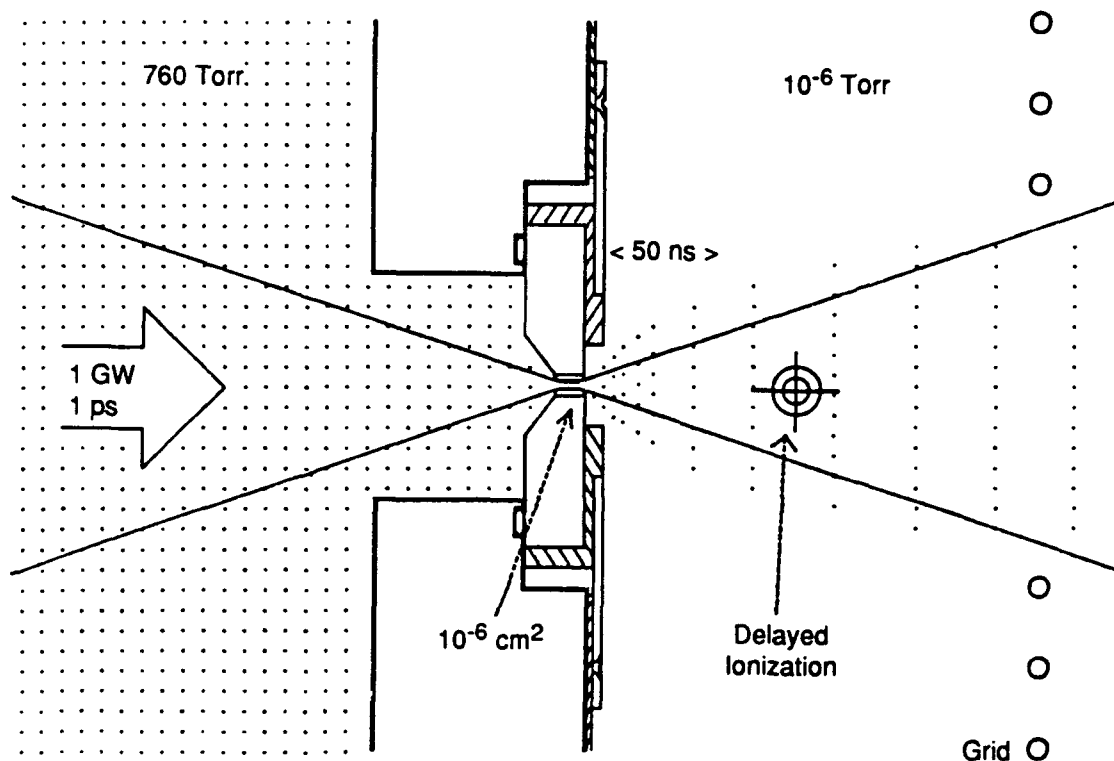

Figure 4. Experimental setup for expanding high-pressure oxygen plasma into a high vacuum environment.

The laser for producing the plasma environment is a home-built tunable dye laser with pulse durations below 1 ps and with pulse energies up to 4 mJ. When this laser is focused to a beam waist of 15-μm diameter, the peak intensities in the focal volume exceed 10^{15} W/cm^2. In the experiment, the focal volume ($\sim 10^{-8}$ cm^3) fills a nozzle that separates a high pressure region (100-1000 Torr) from a high vacuum region (10^{-6} Torr). Hence, the gas present in the focal volume is expanding into the vacuum region as shown schematically in Figure 4. This expansion freezes the three-body chemistry within a few nozzle diameters from the exit and should thus preserve radicals and metastable species that would otherwise be deactivated.

The energy density within the focal region is in principle sufficient to multiply ionize every single molecule. If we assume that only 0.1% of the laser light is absorbed in multiphoton excitation, we are still left with $\sim$ 60 eV per molecule, sufficient to generate O_2^+, O^+, O^{++}, and possibly a small amount of O^{+++}. This is indeed observed when we examine the low pressure (2×10^{-8} Torr) photoionization spectrum of molecular oxygen using this high power laser.

In initial experiments with the setup in Figure 4, we used as the nozzle a diamond pinhole with a diameter of 0.0005 inch. We observed that the pinhole opens in a reasonably short time to about twice this diameter, although the laser beam is 1.5 diffraction-limited[29] and should pass at 1/e^2 intensities through the pinhole. We concluded that intensities outside the focal waist are sufficient to significantly ablate the diamond walls of the pinhole, since C^+, C_2^+, and C_3^+ were always the dominant ions emerging from the focal region, regardless of the gas used in the expansion. Next we began drilling our own pinholes into 0.2-mm tungsten material using the laser itself. Although these pinholes obviously better matched the laser beam waist, we found that tungsten atoms were the main ionization signal generated. Similar results were obtained using molybdenum samples. Owing to this interference from the wall material, the experiment was abandoned and another approach was tried.

This second attempt was based on the supposition that laser energy deposited into a solid substrate containing oxygen could produce a high pressure plasma environment in which reactions (3) and (4) can occur with high frequency. To implement this scheme, we mounted a cooled copper substrate in the source region of a time-of-flight mass spectrometer. The surface was cooled by a liquid nitrogen reservoir that could be evacuated by a forepump to achieve temperatures below 77 K. In initial experiments, we condensed xenon gas that was precooled and directed through a Teflon capillary toward the cold copper surface. In this fashion we were able to build up a solid xenon sample measuring several cubic millimeters in times of $\sim$10 minutes. Using the short pulse laser described above, we generated a laser plasma at the solid xenon surface and monitored the ions emitted using the time-of-flight mass spectrometer. Equivalent experiments using ozone failed to produce solid samples of ozone, most likely because the temperature that could be reached ($\sim$70 K) was too high to permit the stable existence of solid ozone in the high-vacuum environment of the spectrometer.

We have since replaced the liquid-nitrogen-cooled surface with a closed-cycle liquid-helium cold stage. In the first experiments, we were able to form perfectly shaped samples of solid oxygen with volumes up to 15 mm^3 by transferring oxygen gas via a quartz capillary to the cold stage. The experimental setup is shown in Figures 5, and photographs of the sample preparation process are given in Figure 6. When the capillary is retracted from the cold stage, a stable oxygen sample with heights exceeding several millimeters can be sustained in the high vacuum environment.
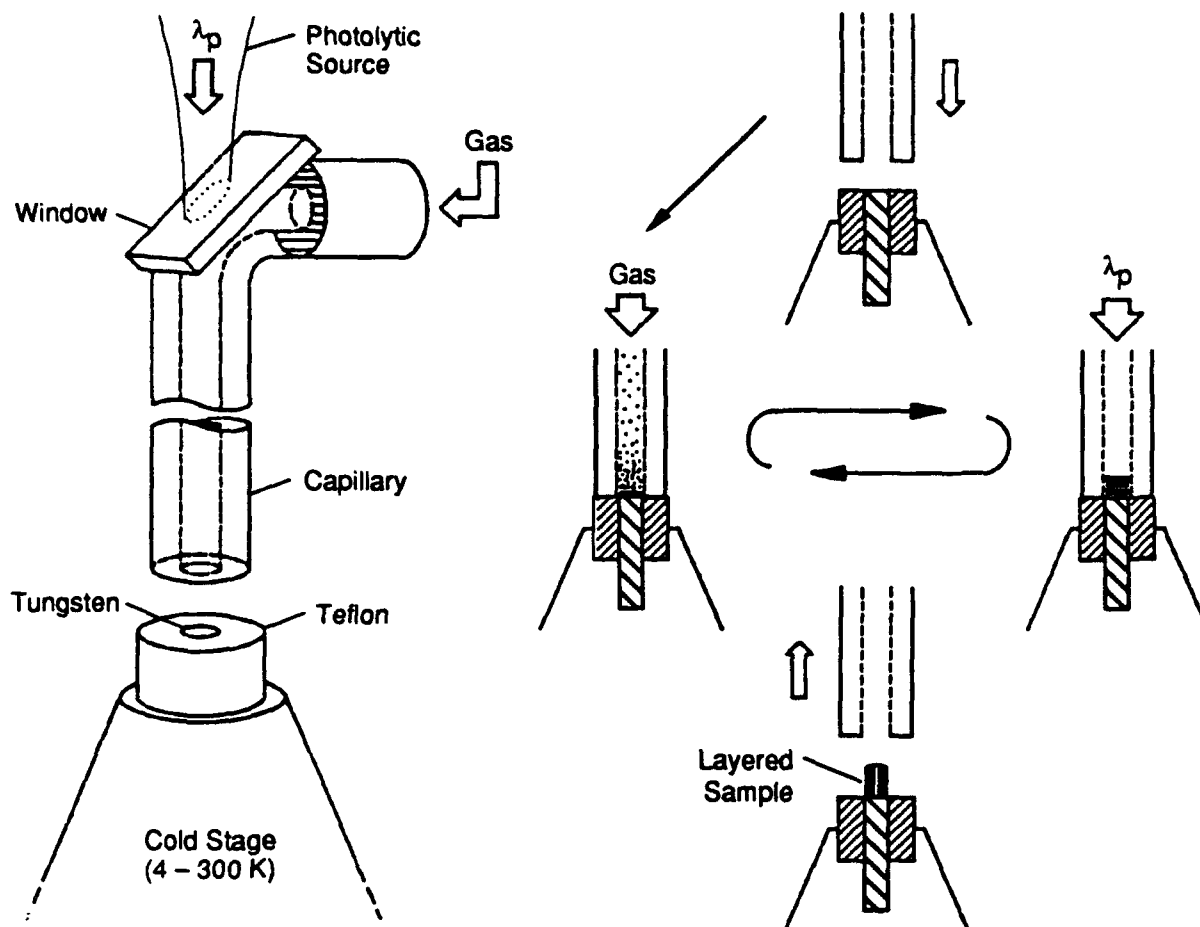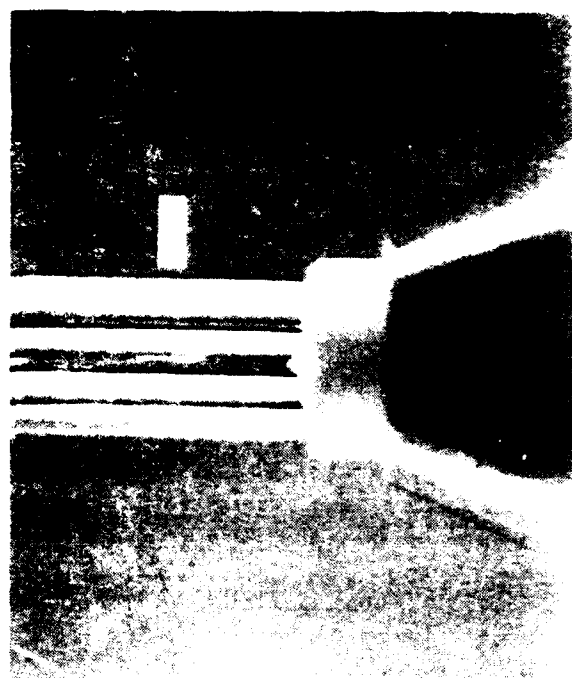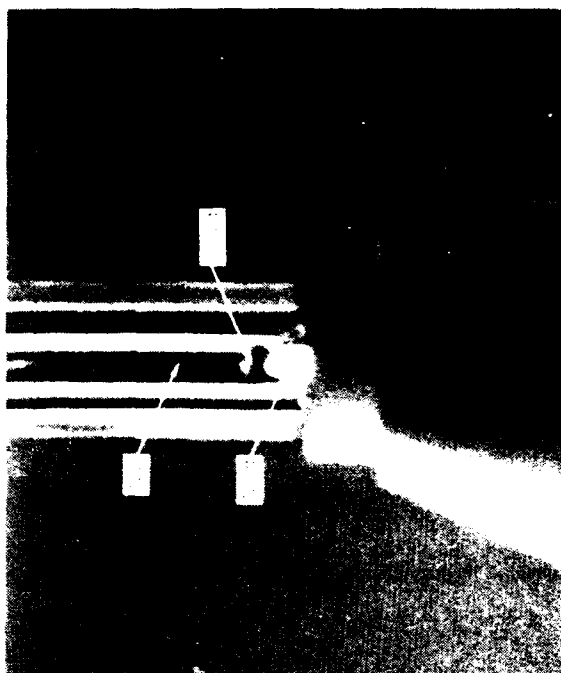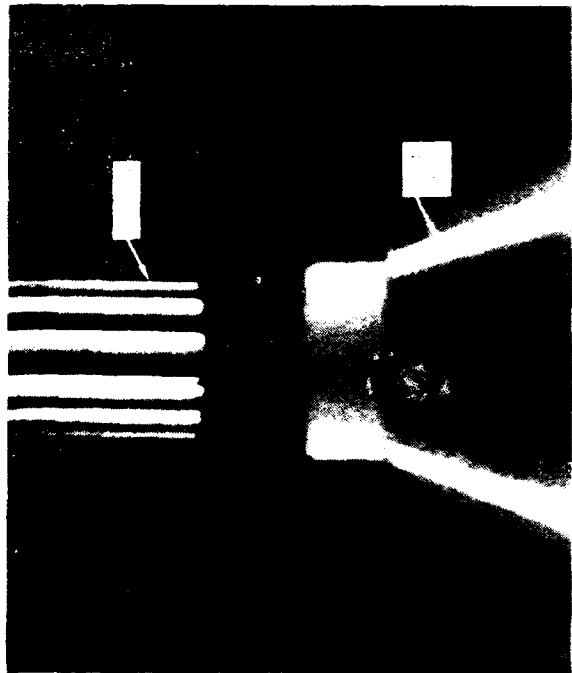
11

Figure 5.   Close-up of cold stage with gas capillary (left). Experimental sequence
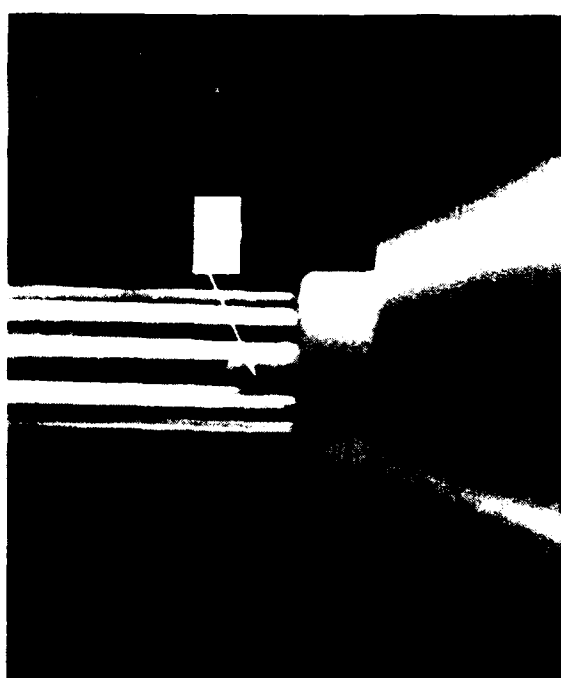for preparing layered solid samples and their photolysis (right).

Figure 6   Photographs showing actual development of solid oxygen sample on cold stage

(a)   (b)   (c)   (d)

In experiments planned for the continuation of this task we will examine the formation of energetic species in solid oxygen following (1) laser excitation of solid oxygen and solid ozone samples and (2) codeposition of photoexcited and ground state oxygen gas/ozone gas onto the cold stage. The diagnostics for characterizing the activated solid samples include stimulated Raman spectroscopy, Fourier transform infrared analysis, solid analysis by stimulated and thermal desorption followed by nonresonant photoionization with mass analysis, as well as resonant photoionization, photodissociation, and photoelectron imaging techniques.

SUPEREXCITED OXYGEN

Rapid predissociation of highly excited states of O_2 was observed to occur as fast (3-5 keV) O_2^* molecules traverse a thin, 300-μm-wide metal slit. Analysis of the correlated dissociation fragments indicated that dissociation occurs when the molecules come close to, but do not touch, the metal surfaces and that the molecules undergoing this process are highly excited Rydberg states of O_2 that lie close to and above the ionization threshold. We explain the cause for the dissociation in terms of the forces exerted on the excited state by the image dipole induced in the metal surface by the Rydberg electron and Rydberg ion core. These forces induce ℓ-mixing in the high Rydberg states (n $\geq$ 24), thereby allowing overlap of the otherwise stable system with valence continuum states.

Rydberg states with core vibrational levels v = 0 to 6 of O_2^+ $X^2\Pi_g$ were identified to undergo this process, and the dissociative branching among the four neutral dissociation limits of O_2 that lie below the ionization limit was measured for each core vibrational level. The molecular dynamics experienced by these Rydberg states is closely related to that involved in dissociative recombination. Therefore, as a corollary to our results, we can provide first experimental answers to the important question of which final atomic states are produced when a specific vibrational level of O_2 undergoes dissociative recombination. A preprint describing this experiment is given in Appendix H.

PRESENTATIONS AND PUBLICATIONS ACKNOWLEDGING THIS CONTRACT

The following papers have been published or written during this contract. Reprints or preprints are given in the Appendices.

"Measurement of the Lifetime of Metastable Triatomic Hydrogen," C. Bordas, P. C. Cosby and H. Helm, J. Chem. Phys. **93**, 6303 (1990).

"Spectroscopy and Multichannel Quantum-Defect Theory Analysis of the np Rydberg series of H_3," C. Bordas, L. Lembo, and H. Helm, Phys.Rev. A **44**, 1817-1827 (1991).

"Metastability and Rydberg States of H_3," C. Bordas and H. Helm, J. de Physique IV **1**, 513-516 (1991).

"Stark Effect in Triatomic Hydrogen Rydberg States," C. Bordas and H. Helm, Phys. Rev. A. **45**, 387-402 (1992).

"Electric-Field Ionization of Rydberg State of H3," C. Bordas and H. Helm, Phys. Rev. A. **47**, 1209 (1993).

"Predissociation of Excited States of H_3," H. Helm, in *Dissociative Recombination, Theory, Experiment, and Applications*, B. Rowe and B. Mitchell, Eds. (Plenum Publishing Corporation, New York, 1993).

"Observation of Electronically Excited States of Tetraoxygen," H. Helm, and C. W. Walter, J. Chem. Phys. **98**, 5444 (1993).

"Dissociation of Rydberg States of O_2 Induced by Image Charges in a Metal Surface," P. C. Cosby, I. Hazell, C. W. Walter, and H. Helm, in preparation, see Appendix H.

The following presentations have been made at conferences during this contract.

"High Symmetry Metastable Molecules," H. Helm, C. Bordas, M. J. Dyer, D. L. Huestis, D. C. Lorents, and H. Bissantz, Proceedings of the High Energy Density Matter Conference, February 1991, Albuquerque, page 249-258.

"Laser Spectroscopy of Vibrationally Excited Rydberg States of H_3," L. J. Lembo, H. Helm, and D. L. Huestis, 46th Int. Symp. on Molec. Spectroscopy, Ohio, June 1991.

"Spectroscopies of Oxygen and Hydrogen Molecules," H. Helm, C. Bordas, C. W. Walter, and M. J. Dyer, Proceedings of the High Energy Density Matter Conference, April 1992, Lancaster.

The following invited papers were presented at conferences.

"Intensity Windows in H_3 Photoexcitation," H. Helm, C. Bordas, L. J. Lembo, and H. Helm, 7th International Laser Science Conference, Monterey, September 1991.

"Atoms and Molecules in Intense Laser Fields," H. Helm, 44th Annual Gaseous Electronics Conference, Albuquerque NM, October 1991.

"Predissociation of Rydberg States of H_3," H. Helm, NATO Workshop on Dissociative Recombination, Theory, Experiment and Applications, St. Jacut France, May 1992.

"Imaging of Photoelectron Wavefunctions," H. Helm, Gordon Conference on Multiphoton Ionization, Colby College NH, June 1992.

The following seminars were presented.

"Stable Configurations of Three Protons and Three Electrons," H. Helm, Joint Institute of Laboratory Astrophysics, Boulder CO, April 1991.

"Photoionization Studies of Triatomic Hydrogen," H. Helm, Brookhaven National Laboratory, Upton, NY, September 1991.

"Photodissociation and Photoionization in Fast Beams," H. Helm, Argonne National Laboratory, January 1992.

"Fast Beam Techniques in Studies of Molecular Structure and Dynamics," H. Helm, University of Freiburg, University of Konstanz, Germany, September 1992.

REFERENCES

1. J. A. Montgomery and H. H. Michels, J. Chem. Phys. **86**, 5882 (1987).

2. H. Helm, in *Electronic and Atomic Collisions,* J. Eichler, I. V. Hertel, and N. Stolterfoht, Eds. (North Holland, 1984), p. 275 and references.

3. N. Bjerre and H. Helm, Chem. Phys. Lett. **134**, 361 (1987).

4. H. Helm, D. P. de Bruijn, and J. Los, Phys. Rev. Lett. **53**, 1642 (1984).

5. H. Helm and P. C. Cosby, J. Chem. Phys. **86**, 6813 (1987).

6. P. C. Cosby and H. Helm, Phys. Rev. Lett. **61**, 298 (1988).

7. H. Helm and P. C. Cosby, J. Chem. Phys. **90**, 4208 (1989).

8. H. Helm, Phys. Rev. Lett. **56**, 42, (1986).

9. L. J. Lembo, N. Bjerre, D. L. Huestis, and H. Helm, J. Chem. Phys. **92**, 2219 (1990).

10. H. Helm, Phys. Rev. A **38**, 3425 (1988).

11. C. Bordas, P. C. Cosby, and H. Helm, J. Chem. Phys. **93**, 6303 (1990).

12. C. Bordas, L Lembo, and H. Helm. Phys. Rev. A **44**, 1817-1827 (1991).

13. C. Bordas and H. Helm, J. de Physique IV **1**, 513-516 (1991).

14. C. Bordas and H. Helm, Phys. Rev. A. **45**, 387-402 (1992).

15. H. Helm, in *Dissociative Recombination, Theory, Experiment, and Applications*, B. Rowe and B. Mitchell, Eds. (Plenum Publishing Corporation, New York, 1993).

16. C. Bordas and H. Helm, Phys. Rev. A. **47**, 1209 (1993).

17. D. Talbi and R. P. Saxon, J. Chem. Phys. **91**, 2376 (1989).

18. G. I. Gellene and R. F. Porter, J. Chem. Phys. **81**, 5570 (1984).

19. A. B. Raksit and R. F. Porter, Int. J. Mass. Spec. Ion. Phys. **76**, 299 (1987).

20. W. J. Griffiths, F. M. Harris, and J. H Beynon, Int. J. Mass Spec. Ion. Phys. **77**, 233 (1987); **77**, R7 (1987).

21. E. T. Seidl and H. F. Schaefer, J. Chem. Phys. **88**, 7043 (1988).

22. V. Amantides, Chem. Phys. **48**, 221 (1980).

23. G. L. Zarur and Y. N. Chin, J. Chem. Phys. **56**, 3278 (1972).

24. T. G. Slanger, L. E. Jusinski, G. Black, and G. E. Gadd, Science **241**, 945 (1988).

25. D. L. Huestis, G. Black, S. A. Edelstein, and R. L. Sharpless, J. Chem. Phys. **60**, 4471 (1974).

26. C. Long and D. R. Kearns, J. Chem. Phys. **59**, 5729 (1973).

27. H. Helm and W. Walter, J. Chem. Phys. **98**, 5444 (1993).

28. M. J. Dyer and H. Helm, J. Opt. Soc. Am. B **10**, 1071 (1993).

29. T. G. Slanger, in *Reactions of Small Transient Species,* A. Fontijn and M.A.A. Clyne, Eds. (Academic Press, New York, 1983), p. 241.

Appendix A

MEASUREMENT OF THE LIFETIME OF METASTABLE TRIATOMIC HYDROGEN

Measurement of the lifetime of metastable triatomic hydrogen

C. Bordas, P. C. Cosby, and H. Helm

Molecular Physics Laboratory, SRI International, Menlo Park, California 94025

We measured the survival probability of the metastable ($N = 0$, $K = 0$) level of the $2p^2A_2''$ of H_3 as a function of time elapsed from formation of the molecule by probing its population with photoionization. We find lifetimes $\tau = 640 \, ^{+300}_{-100}$ ns for the ground vibrational state and $\tau = 740 \, ^{+300}_{-100}$ ns for the symmetric stretch-excited level. Equally short lifetimes are obtained from an analysis of the photoinduced bleaching of the spontaneous dissociation signal of metastable H_3. These lifetimes are about 2 orders of magnitude shorter than those expected on the basis of the allowed radiative transition $2p^2A_2'' \to 2s^2A_1'$. We attribute the faster decay channel to weakly allowed radiative transitions between the metastable state and the degenerate mode-excited repulsive ground state of H_3, as well as to predissociation of the metastable levels by the repulsive ground state of H_3 induced by spin–orbit coupling.

INTRODUCTION

The metastability of the energetically lowest rotational level of A_2'' symmetry of triatomic hydrogen has recently been used to conduct a variety of photoexcitation studies[1-8] on this fundamentally unstable molecule. The lowest long-lived H_3 state is the lowest rotational level in the $2p^2A_2''$ state.[9] It is characterized by the quantum numbers $N = 0$, $K = 0$. Here, N and K represent the total angular momentum, excluding spin, and its projection onto the figure axis of the molecule. As shown in Fig. 1, the $2p^2A_2''$ level lies 8738 cm^{-1} above[10] the three-atom ground state dissociation limit, $H - H - H$, and 44 856 cm^{-1} above the $H_2 - H$ dissociation limit.

A long-lived neutral H_3 molecule had appeared in a variety of experiments dating back as far as 1968,[11] but it was not until 1983 that Gellene and Porter,[9] on the basis of their own experimental findings and the spectroscopic studies by Herzberg *et al.*,[12-15] correctly identified a path to the stability of this molecule. The main arguments for the stability of the state are that (1) there is no vibronic coupling between the $2p^2A_2''$ and $2p^2E'$ states to allow vibrational predissociation. (2) for fixed nuclei there is no electric dipole-allowed transition between the two states, and (3) for the level $N = 0$, $K = 0$ there is no rotational coupling path that connects the $2p^2A_2''$ and $2p^2E''$ states in rotational predissociation.

The lifetime has so far been considered to be controlled by the infrared transition[9] from the $N = 0$ level of $2p^2A_2''$ to the $N = 1$ level of $2s^2A_1'$. On the basis of combination differences of observed[12-15] emission lines in H_3, this transition is expected to occur at a (vacuum) wavelength of 11.136 μm. From the photon energy and the theoretical[6,17] transition moment for the $2p - 2s$ transition, a lifetime of about 88 μs has been predicted for the metastable level.

We recently observed a significant degree of unimolecular (not collision induced) dissociation of long-lived H_3 and suspected that the lifetime could be substantially shorter than that predicted 88 μs value. We report here on two experiments specifically designed to measure the lifetime of long-lived H_3. A surprisingly short value is found in these measurements, which can, however, be reconciled with known interactions.

PHOTOIONIZATION EXPERIMENT

The neutral molecules are produced in near-resonant charge transfer of a mass-selected ion beam in a cesium charge transfer cell using the apparatus[1] shown in Fig. 2. After the cell, the remaining ions are deflected from the beam using the deflection plates (A6) and the neutral beam enters a separate vacuum chamber through the 1 mm aperture (A7). The beam is photoexcited over a distance of 120 cm *in a field-free region in ultrahigh vacuum.* Photoionization events are monitored 150 cm downstream from the charge transfer cell by detecting mass selected H_3^+ ions on a multichannel plate detector. A pulsed dye laser is used, and
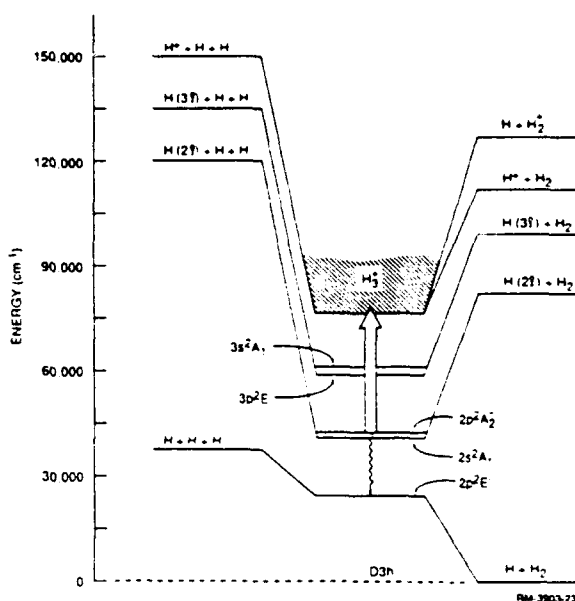

FIG. 1 Schematic energy level diagram showing the long-lived $2p^2A_2''$ state in relation to the ground state and other excited states of H_3.
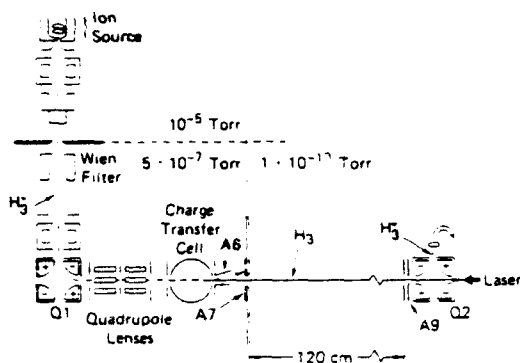
21

FIG. 2. Experimental apparatus used to measure the lifetime: Neutral H_3 molecules are formed by charge exchange of H_3^+ in a cesium cell. A pulsed laser photoionizes the neutral particles along the beam path between A7 and A9. The time of arrival of ions following the laser pulse is recorded on the channel plate detector.

FIG. 3. Arrival time spectrum of H_3^+ ions formed in photoionization of the metastable level $2p^2A\,{}_2''(v_1 = 0, v_2 = 0)$.

the arrival time of ions after the excitation pulse is recorded using a precise (1 ns) time-to-digital converter with 3 ns dead time. The laser pulse width (~ 15 ns) is short compared with the time needed for neutral H_3 molecules to travel along the laser-neutral beam interaction region (3.5 μs at 1.5 keV beam energy). Thus ionization events induced by the laser record a snapshot of the distribution of neutral molecules along the beam line at the time the laser fires. This distribution is displayed in the arrival time spectrum of ions at the detector. If the lifetime of the neutral species is long compared with the passage time through the interaction region, the arrival time spectrum of ions will appear constant with time. On the other hand, species lost by any decay mechanism will show up with an arrival time spectrum that displays the loss of particle density as the neutral species travel farther from their birthplace.

This latter case is clearly evident from Fig. 3, where we show a typical arrival time spectrum of H_3^+ ions formed by photoionizing the H_3 using radiation at 29 575 cm^{-1}. We know from previous experiments[1,7] that at this wavelength > 90% of the ionization signal is comprised of contribution from the lowest nonvibrating metastable level, $2p^2A\,{}_2''(0,0)$. The numbers in parentheses stand for the symmetric stretch and degenerate (bending-asymmetric stretch) mode quantum numbers (v_1, v_2). A rather sharp variation of the H_3^+ signal with arrival time is noted here. The shortest arrival times shown correspond to ionization closest to A9 in Fig. 2. On the other hand, ions arriving at 3560 ns (the spike in the spectrum) correspond to neutrals photoionized near the aperture (A7). The signal decrease at yet longer arrival times (> 3560 ns) reflects the increasing action of the deflection field applied on A6. This field suppresses ions formed too close to the charge transfer cell. The noisy trace represents the raw data from accumulating arrival times of individual ions in 4 ns wide bins over a total of 64 000 laser shots. The full curve represents an exponential of best fit with a decay time of 640 ns and a fitting uncertainty of 4 ns.

Several experimental parameters could, of course, influence the measured arrival time distribution. Significant radiation cascading into the level studied should lead to an in-
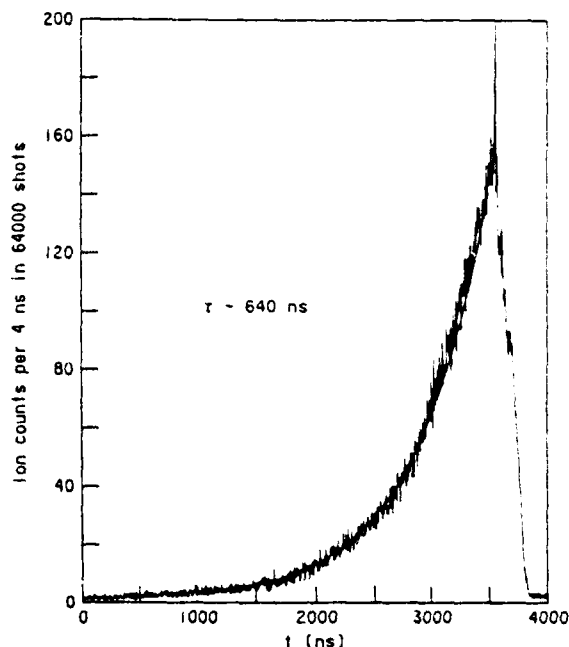
crease in particle density away from the charge transfer cell. This effect must be slight in the spectrum shown in Fig. 3 although we notice a small but distinct deviation from the exponential fit at longer times. On the other hand, varying overlap between the laser and the particle beam along the observation region will be reflected in a varying ionization probability as a function of position.

To check for this effect, we recorded spectra such as that shown in Fig. 3 with collimated laser beams of varying diameter ($1/e^2$ diameters between 3 and 10 mm) and performed cross checks using a metastable atomic hydrogen beam. H(2s) was formed by charge transfer of protons in cesium and was photoionized at 27 427 cm^{-1}. Slight deviations from the expected constant arrival time spectrum were noted according to the misalignment of the laser and the neutral beam. Misalignment in the beam gave rise to a maximum of a factor of 2 difference in the current of H(2s) detected near A7 and near A9. Another correction factor might arise from the slightly different particle trajectories for neutrals and ions in the vacuum chamber owing to residual fields. This effect would also influence the data for H(2s), likely even magnifying them because of the lighter mass. If we apply corrections to the H_3 data, according to the maximum deviations from the constant arrival time spectrum observed for H(2s), the lifetime in Fig. 3 could, at most, be raised by about 300 ns or lowered by 100 ns.

Another cross check was performed by measuring the arrival time spectrum for $n = 38d$ Rydberg states formed in photoexcitation from the metastable $2p^2A\,{}_2''(0,0)$ level. The Rydbergs were field ionized just past A9 and detected as ions on the multichannel plate. These lifetime measurements gave values consistent with those obtained by monitoring

ions directly. Finally, the neutral beam divergence itself does *not* constitute a correction factor so long as the recoil from the outgoing photoelectron does not modify the heavy particle path.

Similar experiments were performed for the symmetric stretch-excited, long-lived H_3 molecule by pumping members of the autoionizing $n = 7$ manifold. In Fig. 4 we show a photoexcitation spectrum of the levels involved. The arrival time spectra recorded by pumping the $2p(1,0)$ level to the autoionizing $7d(1,0)$ and $7s(1,0)$ levels are shown in Fig. 5. They are similar to the spectrum for the $2p(0,0)$ level, but the fits yield lifetimes of 720 ± 8 and 740 ± 20 ns, respectively.

Allowing for the correction factors discussed above, we feel that all measured lifetimes could at worst be 300 ns longer or 100 ns shorter than the best fit values quoted.

PHOTODISSOCIATION EXPERIMENT

We have recently reported[5] a study of photodissociation of H_3, $2p^2A_2''$ via optical excitation to the $3s^2A_1'$ and $3d^2E''$ states. In that report, we noted that a spontaneous dissociation of H_3 to $H + H_2$ products occurred in the absence of laser radiation. We also noted depletion of the spontaneous dissociation channel when the metastable H_3 state was photodissociated. It was therefore concluded that the spontaneous dissociation occurred from the long-lived ($N = K = 0$) levels of the $2p^2A_2''$ state.

An independent estimate of the lifetime of the $2p^2A_2''$ state can be obtained from the detection of fragments that arise from the spontaneous dissociation of H_3. In this experiment, the H_3 beam passes through a narrow (0.3 mm) slit

FIG. 5. Arrival time spectra of H_3^+ ions formed in photoexciting the $2p^2A_2''(1,0)$ and $2p^2A_2''(0,1)$ levels via the autoionizing $7d$ resonances shown in Fig. 4.

positioned 66.5 cm downstream from the Cs charge transfer cell (see Fig. 6). Molecules or atoms passing through this slit are collected by a 2.2 mm high beam flag positioned an additional 10.0 cm downstream from the slit. If a molecule dissociates in the interval between the slit and the beam flag such that its fragments escape collection by the beam flag, the escaping fragments travel a distance of 78.5 cm beyond the beam flag to a position and time sensitive detector. Both correlated fragments from a single dissociated molecule must arrive at the detector, which measures their spatial and temporal separations. Given the initial energy of the H_3 mol-

FIG. 4. Wavelength-dependent photoionization spectrum of H_3. This portion shows the vibrationally autoionizing $7d$ and $7s$ members.

FIG. 6. Experimental arrangement for the dissociation experiment (not to scale). Fragments produced by spontaneous unimolecular dissociation of H_3 in the region between the slit and the beam flag are monitored by the detector. Photodissociation of H_3 near the slit monitors the flux of H_3 entering this region.

J. Chem. Phys   No 9, 1 November 1990

23

ecule and the distance from the point of molecular dissocia-tion to the detector, these fragment separations can be uniquely transformed to yield the center-of-mass transla-tional energy release in the dissociation (W), the angle of ejection of the fragments, and the mass ratio of the frag-ments.[18]

Any decay path of the $2p$ state, whether direct predisso-ciation, radiative decay into the predissociated $2s$ state, or radiative decay into the dissociative ground state is necessar-ily accompanied by the p. oduction of dissociation frag-ments. If we denote the flux of fragments pairs produced by spontaneous dissociation in the region defined by the slit and the b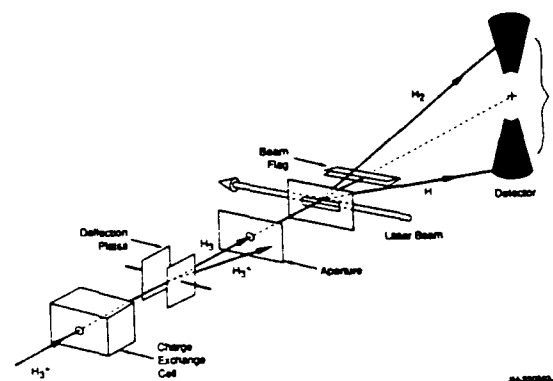eam flag as I, and the flux of H_3 molecules entering the slit as I_0, the lifetime τ of the H_3 molecules is

$$\tau = -\Delta t/\ln(1 - I_s/I_0). \tag{1}$$

where Δt is the effective time required for the H_3 molecules to transverse this region. All three variables on the right-hand side of Eq. (1) are explicit functions of the H_3 beam energy.

The observed flux of the spontaneous dissociation frag-ments produced by a 3000 eV beam of H_3 is shown as a function of W in the top spectrum of Fig. 7. The distribution of these fragments extends from a threshold near $W \sim 0.5$ eV through a broad maximum near $W = 2$ eV to a maximum translational energy release near $W \sim 5.9$ eV. This high W
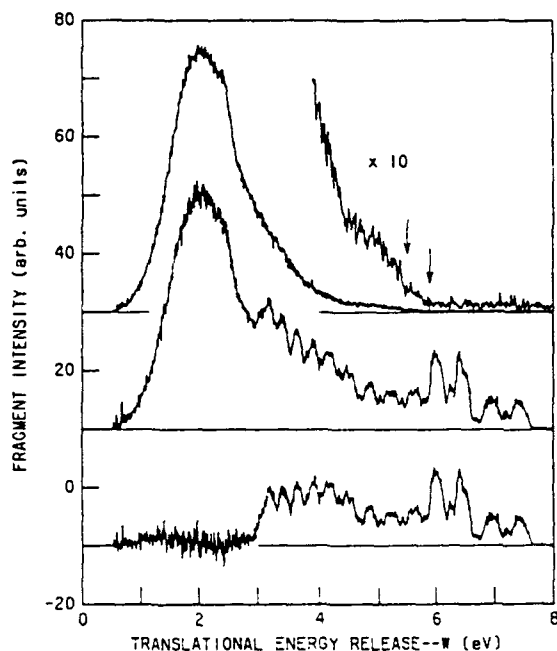

FIG 7 Fragments observed in the dissociation of H₃, given as a function of center-of-mass translational energy release. The top spectrum is observed in the absence of laser radiation. It reflects the fragment energy distribution characteristic of spontaneous unimolecular H₃ dissociation. The center spectrum, observed with the laser tuned to excite the $3s^2A_1''(0,0) - 2p^2A_2''(0,0)$ transition, shows a depletion in the unimolecular dissociation flux in addition to fragments produced by predissociation of the photoexcited 3s state. The bottom spectrum, obtained by scaling the top spectrum by 0.889 and subtracting it from the center spectrum, reflects the photodissociation

region is shown with the fragment intensity magnified by a factor of 10 in the figure. Summation of the fragments over W is a direct measure of I_s in Eq. (1). Determination of Δt is also straightforward. Although the interval between the slit and the beam flag determines the maximum possible interval over which the H_3 molecule can dissociate to produce frag-ments, not all fragments produced in this region can simulta-neously escape collection by the beam flag and hit the active area of the detector. Monte Carlo simulation of the fragment trajectories produced with the experimental W distribution (Fig. 7) allows the effective interval to be determined, and thereby Δt, from the known H_3 beam energy.

A determination of the H_3 flux passing through the slit I_0 requires some consideration because the neutral flux in the region beyond the slit contains contributions not only from H_3, but also from the spontaneous dissociation prod-ucts H and H_2 as well as the neutral dissociative charge transfer products falling within the solid angle subtended by the slit and the charge transfer cell aperture. Our approach to determining I_0 is to photodissociate the H_3 molecules and measure the photofragment flux. The 2 mm diameter inter-activity beam of a tunable cw dye laser, chopped at 1 Hz with a 50% duty cycle, intersects the H_3 beam a distance 0.3 cm downstream from the slit. The fragments produced with the laser tuned to the $3s^2A_1''(0,0) - 2p^2A_2''(0,0)$ transition are shown by the center spectrum in Fig. 7. This spectrum is composed of photofragments from predissociation of the op-tically excited $3s$ state which appear as the structured fea-tures in the spectrum, as well as the spontaneous dissociation fragments produced by H_3 molecules that were not photo-dissociated. Comparison of the fragment intensity in the broad maximum near $W = 2$ eV in the top (laser off) and center (laser on) spectra of Fig. 7 shows that as expected, fewer spontaneous dissociations occur when the H_3 beam is photodissociated. If we make the initial assumption that all contributions in the center spectrum over the interval 0.5 eV $\leqslant W \leqslant 2.7$ eV arise from spontaneous dissociation, we can scale the fragment intensity distribution in the upper spec-trum by a multiplicative factor $(1 - f)$ to reproduce the in-tensity distribution of the center spectrum over this interval. In this particular spectrum, $f = 0.111$. Subtracting the scaled spontaneous dissociation spectrum from the laser on (center) spectrum yields the bottom spectrum in Fig. 7. We wish to equate the bottom spectrum with the fragment flux I_{pf} that is produced solely by photodissociation of H_3:

$$I_{pf}(W) = I_L(W) - (1 - f)I_s(W), \tag{2}$$

where I_L is the fragment flux of the laser on spectrum. Here we have explicitly assumed that excitation of the $3s$ state produces no fragments within the 0.5 eV $\leqslant W \leqslant 2.7$ eV inter-val. Direct predissociation of the $3s$ state meets this criterion, since conservation of energy restricts $W \geqslant 3.155$ eV. Radia-tive transitions from the $3s$ state into the ground state could produce fragments in this energy interval. However the ra-diative decay rate[19] of the $3s$ state ($\Gamma_{rad} \sim 2.10^7$ s^{-1}) is small compared to the predissociation rate[20] (5×10^8 s^{-1} $> \Gamma_{pre} > 10^8$ s^{-1}), allowing a maximum of 20% of the frag-ments below 2.7 eV to arise from the $3s$ state.

A second assumption in Eq. (2) is that photodissocia-

tion and spontaneous dissociation originate in the same initial state $2p^2A\,''_2$. Photodissociation necessarily probes only one vibrational mode of the $2p$ state, in the case considered here the (0,0) level, whereas any long-lived vibrational mode populated in the H₃ beam can contribute to the spontaneous dissociation spectrum. From the peak heights in the previously reported wavelength dependence of the H₃ photodissociation (see Fig. 1 of Ref. 5), we know that (0,0) constitutes only 88% of the H₃ beam population at the point of laser irradiation, with 9% in (1,0) and 3% in (0,1) levels that lie higher in energy than (0,0) by 0.417 and 0.317 eV, respectively.[5] Since only the spontaneous dissociation from the (0,0) level is depleted by photodissociation in the selected transition, the contributions to spontaneous dissociation from the vibrationally excited levels are proportionally enriched in the laser on spectrum. Our neglect of this enrichment likely also contributes to the small, nonzero fragment flux within the $0.5 < W < 2.7$ eV region of the bottom, subtracted spectrum (which constitutes less than 5% of the observed fragments).

Within the approximations noted above, the flux of neutral H₃ at the point of laser intersection can be represented by

$$I = \Sigma I_{pf}(W)/0.88f, \tag{3}$$

where the summation is over all energy releases W for $I_{pf}(W)$ given by Eq. (2) and where 0.88 represents the fractional contribution of the (0,0) level to the total beam flux and f represents the fractional depletion of (0,0) by photodissociation. Using I from Eq. (3) as an approximation to I_0, the flux of H₃ at the slit, Eq. (1) can be iteratively solved for τ. By applying this procedure to a variety of fragment spectra measured at H₃ beam energies of 3000 and 5000 eV, we obtain a value $\tau = 318^{+200}_{-225}$ ns, where the error limits reflect only the range of determined values. Considering the possible errors associated with undercounting the photofragments and with determining the collection efficiency of the spontaneous dissociation fragments as a function of distance from the slit, we consider the accuracy of τ to be within a factor of 2 of the "true" lifetime of the $2p^2A\,''_2$ ($N=0$) level. This result is clearly incompatible with a slow radiative decay into the $2s$ state being the dominant decay path of the $2p^2A\,''_2$ ($N=K=0$) levels, but it is compatible with the results of the direct measurement described in the previous section.

DISCUSSION

The metastable level in H₃ has overall symmetry[9,21] ($\Psi_{el} \times \Psi_{vib} \times \Psi_{rot} \times \Psi_{nucl}$) of $A\,''_2$. This state has a symmetric nuclear spin wave function (ortho-H₃) and is characterized by the quantum numbers $N=0$, $K=0$. This metastable state is almost purely described by a configuration built from a $2p(a''_2)$ electronic orbital on the lowest ortho level of the H₃⁺ core: $N^+=1$, $K^+=0$. This species has been observed to be long lived in the ground vibrational state, as well as in symmetric stretch-excited forms.[1] A long-lived para-H₃ species also exists when the ionic core is degenerate-mode excited.[1]

The "metastability" of the $N=0$ levels is due to the

requirement that the total wave function for H₃ be antisymmetric with respect to exchange of any of two identical fermions of the system. Such a wave function cannot be constructed from three hydrogen atoms in the ground state, H(1s), when we require that the total angular momentum (excluding spin) be zero. Consequently, the bound metastable species, while embedded in the continuum of the repulsive ground state of H₃, finds no vibrational or rotational predissociation path that would limit its lifetime.

The current lifetime estimate[9] of 88 μs is based on the allowed transition from the $2p^2A\,''_2$ to the $2s^2A\,'_1$ level. This estimate involves the theoretical transition moment and the experimental energy separation. It appears inconceivable that the calculated[16,17] transition moment for the $2p$-$2s$ transition in H₃ is wrong by 2 orders of magnitude, and it is also impossible to see how Herzberg's assignment on the energy separation from $2p$-$2s$ is off by a factor of 5.[22] We therefore must search for other decay paths of the metastable species of H₃ to explain the rather short lifetime observed here.

There appear to be at least two possibilities: (1) a weak predissociation path, and (2) a weak radiation path, neither of which has been considered so far. To create the predissociation path, we could invoke spin–orbit coupling. Including the electron spin gives the low-lying electronic states of H₃ a doublet character. Thus, the metastable $N=0$ state appears as a single $J=1/2$ level. If we consider the lowest vibrational level of the metastable state we require for spin–orbit coupling that the predissociating state have $J=1/2$ with ortho core. Such a state indeed exists in the form of the $N=1$, $G=0$ ortho level of the $2p^2E'$ state, which also has overall $A\,''_2$ symmetry, as does the metastable level. Including the electron spin will yield a $J=3/2$ and a $J=1/2$ level, so that coupling the $J=1/2$ components may give predissociation.

Approximating the rate by the Fermi golden rule, we write

$$\Gamma_{so} = 2\pi|\langle 2p^2E'|H_{so}|2p^2A\,''_2\rangle|^2, \tag{4}$$

where H_{so} is the spin–orbit operator

$$H_{so} = A\mathbf{L}\cdot\mathbf{S} = A\left[L_z S_z + 1/2(L_+S_- + L_-S_+)\right] \tag{5}$$

and where the operators L_z and S_z define the orbital and spin-angular momentum quantum numbers Λ and Σ. The $J=\tfrac{1}{2}$ levels of the $2p^2A\,''_2$ state with $\Lambda=0$ and $\Sigma=\pm\tfrac{1}{2}$ and of the $2p^2E'$ state with $\Lambda=\pm1$ and $\Sigma=\mp\tfrac{1}{2}$ are coupled[23] by the off-diagonal spin–orbit matrix element in (5):

$$\langle\Lambda=\pm1,\Sigma=\mp\tfrac{1}{2}|\tfrac{1}{2}A(L_+S_-+L_-S_+)|\Lambda=0,$$
$$\Sigma=\pm\tfrac{1}{2}\rangle. \tag{6}$$

Under the assumption that the molecular orbitals for the two states have the same well defined value of the electronic angular momentum we can evaluate[23] this coupling and factor the rate (4) into an electronic and vibrational part

$$\Gamma_{so} = 2\pi|2^{-1/2}A\langle\chi_b|\chi_f\rangle|^2, \tag{7}$$

where $\langle\chi_b|\chi_f\rangle$ is the bound–free overlap function that describes the matching of the bound state wave function in $2pA\,''_2$ with the continuum wave function in the $2pE'$ state appropriately normalized at the required continuum energy. As we will show momentarily, the latter quantity can be

TABLE I. Lifetimes of H_3. (Number in parenthesis represents powers of ten).

Electronic label	Rotational label	τ (s)	Reference	Dominant decay channel
$2s^2A\,''_1$	*	170(− 15)	12	Vibrational predissociation
$2p^2A\,''_2$	$N = 0, K = 0$	640(− 9)	This work	Radiation and predissociation by s–o coupling
$2p^2A\,''_2$	$N = 1, K = 1$	60(− 12)	12	Rotational predissociation
$3s^2A\,'_1$	$N = 1, K = 0$	2(− 9) < τ < 10(− 9)	20	Vibrational predissociation
$4s^2A\,'_1$	$N = 1, K = 0$	7(− 12)	6	Vibrational predissociation

* All rotational levels appear equally affected (Ref. 12).

derived rather precisely from previous experimental information. This result allows us to estimate the spin–orbit element required to produce the observed lifetime.

Herzberg et al.[12,15] observed the rotational predissociation of the $2p^2A\,''_2$ state for $N > 0$ as a function of a rotational quantum number. The predissociation rates follow the expected variation of the rotational coupling

$$\Gamma_{rot} = 2\pi|\langle 2p^2E\,'|H_{rot}|2p^2A\,''_2\rangle|^2 \qquad (8)$$

where H_{rot} is the l-uncoupling operator[23]

$$H_{rot} = -B(N_+L_- + N_-L_+). \qquad (9)$$

Evaluation of (9) for the two states and factorization of the rate (8) leads to the expression

$$\Gamma_{rot} = 2\pi|V_{rot}\langle\chi_b|\chi_f\rangle|^2 \qquad (10)$$

with

$$V_{rot}(N,K) = \sqrt{2}B\,[N(N + 1) - K^2]^{1/2}. \qquad (11)$$

Here B is the rotational constant[12] describing the tumbling motion of H_3, $B \sim 45$ cm^{-1}. For example, the lifetime for the $N = 1, K = 1$ level is $\sim 6 \times 10^{-11}$ s when corrected for the residual Doppler width in the emission data.[24] Using these parameters, we can estimate the vibrational part in Eq. (10) that is required to produce a lifetime of 60 ps. Rotational coupling will involve nuclear wave functions rather similar to those of the spin–orbit case in Eq. (7), and we can insert the vibrational factor to estimate A. To reproduce the observed lifetime of the $N = 0$ level, 640 ns, we would require that the spin–orbit element have a value of about 0.86 cm^{-1}. If a single atom (in our case H $2p^2P^0$) is responsible for the molecular spin–orbit effects then the molecular spin–orbit factor in Eq. (5), A, can be approximately related to the fine-structure splitting of the isolated atom. For a $^2P^0$ atom[25] the splitting is equal to 3/2 A. The fine-structure splitting of the free hydrogen atom,[26] 0.36 cm^{-1}, predicts a value of $A = 0.24$ cm^{-1}. Thus this one-center picture suggests that spin–orbit coupling may account for only about 10% of the observed decay rate. We conclude that spin–orbit-coupling induced predissociation may indeed be one decay path that could shorten the lifetime of metastable H_3.

As a second decay path we invoke a direct radiative transition from the $2p^2A\,''_2$ to the repulsive ground state of

H_3: $2p^3E\,'$. The purely electronic transition moment for an electric dipole transition is zero between the two states. However, transitions between states with electronic symmetry $A\,''_2$ and $E\,'$ become possible when a degenerate vibration is excited concurrent with the electronic transition. In a recent study we found quite strong absorption transitions from the metastable state to various $3p^2E\,'$ degenerate mode excited states.[3,6] We see no reason for this transition not to happen in a bound–free emission process.

We therefore postulate that both predissociation and photoemission to the ground state can be active in raising the decay rate of long-lived H_3. Additional support for this conclusion comes from the observed fragment energies. Both mechanisms will give rise to different kinetic energy distributions for the fragments $H_2 + H$ formed in the spontaneous dissociation of long-lived H_3 (Fig. 7). In the case of predissociation we expect a maximum translational energy[5] in the $H_2 + H$ fragments of 5.56 eV, corresponding to formation of H_2 in $v = 0$, $N = 0$. By contrast, photoemission[16,17] into the ground state in the vicinity of the equilibrium D_{3h} geometry should produce $H_2 + H$ fragments with a maximum energy release of about 3.2 eV, again corresponding to formation of H_2 ($v = 0$, $N = 0$). The actual translational energy distributions will extend from the limits quoted here to values up to 4.48 eV lower in energy, corresponding to formation of H_2 at the highest bound-vibrational levels.

The observed spontaneous dissociation spectrum of metastable H_3 (see top spectrum of Fig. 7) indeed has a cutoff around 5.5 eV, close to the highest energy component expected from the predissociation path.[27] A second onset may lie around 5.9 eV indicative for the decay of the symmetric stretch excited state. Finally, the dominant contribution to the spontaneous fragmentation spectrum peaks below 3 eV, a value consistent with the radiative process. Thus the observed fragment energy distribution from unimolecular decay of $2p^2A\,''_2$ ($N = 0, K = 0$) provides direct evidence for decay channels other than radiation into the $2s^2A\,'_1$ state.

The finding of this rather short lifetime of the ($N = 0$, $K = 0$) level of the H_3 $2p^2A\,''_2$ state suggests that naming the level metastable may not really be justified. Nevertheless, its extended lifetime still clearly distinguishes this level from

the levels in the other $n = 2$ and $n = 3$ states of H$_3$. The collection of currently known lifetimes of various low-lying states in Table I illustrates this fact.

ACKNOWLEDGMENTS

[1] H. Helm, Phys. Rev. Lett. 56, 42 (1986); Phys. Rev. A 38, 3425 (1988).

[2] A. Dohdy, W. Ketterle, H. P. Messmer, and H. Waltner, Chem. Phys. Lett. 151, 133 (1988).

[3] L. Lembo, H. Helm, and D. L. Huestis, J. Chem. Phys. 90, 5299 (1989).

[4] S. F. Selgren and G. I. Gellene, Chem. Phys. Lett. 146, 485 (1988).

[5] P. C. Cosby and H. Helm, Phys. Rev. Lett. 61, 298 (1988).

[6] L. J. Lembo and H. Helm, Chem. Phys. Lett. 163, 425 (1989).

[7] L. J. Lembo, A. Petit, and H. Helm, Phys. Rev. A 39, 3721 (1989).

[8] W. Ketterle, H. P. Messmer, and H. Walther, Europhys. Lett. 8, 333 (1989).

[9] G. I. Gellene and R. F. Porter, J. Chem. Phys. 79, 5975 (1983).

[10] P. C. Cosby and H. Helm, Chem. Phys. Lett. 152, 71 (1988).

[11] F. M. Devienne, C. R. Acad. Sci. (Paris) B 267, 1219 (1968).

[12] I. Dabrowski and G. Herzberg, Can. J. Phys. 58, 1238 (1980).

[13] G. Herzberg and J. K. G. Watson, Can. J. Phys. 58, 1250 (1980).

[14] G. Herzberg, H. Lew, J. J. Sloan, and J. K. G. Watson, Can. J. Phys. 59, 428 (1981).

[15] G. Herzberg, J. T. Hougen, and J. K. G. Watson, Can. J. Phys. 60, 1261 (1982).

[16] H. F. King and K. Morokuma, J. Chem. Phys. 71, 3213 (1979).

[17] I. D. Petsalakis, G. Theodorakopoulos, and J. S. Wright, J. Chem. Phys. 89, 6850 (1988).

[18] D. P. deBruijn and J. Los, Rev. Sci. Instrum. 53, 1020 (1982).

[19] Ab initio calculations (Refs. 16 and 17) of the transition moments among the states of H$_3$ predict a radiative lifetime of the 3s state around 50 ns.

[20] The width of discrete features in the energy release spectrum is a function of the range of distances from the detector at which the dissociation occurred, viz $\Delta W \sim 2\Delta L / L$, where L is the distance of the dissociation point from the detector assumed in the center-of-mass transformation, i.e., the distance from the mean point of laser intersection to the detector (88.2 cm), and ΔL is the difference between the actual point of molecular dissociation and this assumed value. Analysis of the energy release widths in the 3s predissociation features requires that the lifetime of this state be less than 10 ns. In addition, recent measurements of the natural width of the 3s state by N. Bierre (private communication) suggest the 3s state lifetime to be longer than 2 ns.

[21] H. Helm, L. J. Lembo, P. C. Cosby, and D. L. Huestis, in Fundamentals of Laser Interactions II, Lecture Notes in Physics, edited by F. Ehlotzki (Springer Verlag, Berlin, 1989), Vol. 339, pp. 264–281.

[22] The reason for the factor of 5 is that the energy separation enters into the lifetime estimate via the third power of the transition frequency.

[23] H. Lefebvre-Brion and R. W. Field, Perturbations in the Spectra of Diatomic Molecules (Academic, Orlando, 1986), p. 95.

[24] C. A. Miderski and G. I. Gellene, J. Chem. Phys. 88, 5331 (1988).

[25] D. L. Huestis and N. E. Schlotter, J. Chem. Phys. 69, 3100 (1978).

[26] C. E. Moore, Atomic Energy Levels, Natl. Bur. Stand. (U.S.), Circ. 1, 467 (1949).

[27] This finding cannot by itself be taken as definitive proof that the spin–orbit mechanism is indeed active. The reason is that the radiative cascading into the 2s level will also produce fragments near this energy threshold because the 2s state predissociates rapidly (170 fs, see Ref. 13) to the $2p^2E'$ state. Given our measured lifetime of the $2p^2A_2''$ state, cascading from 2p into 2s can however contribute only ~1% to the spontaneous fragmentation signal. Cascading from levels higher than $2p^2A_2''$ cannot be estimated at this point.

Appendix B

SPECTROSCOPY AND MULTICHANNEL QUANTUM-DEFECT THEORY ANALYSIS OF THE np RYDBERG SERIES OF H_3

Spectroscopy and multichannel quantum-defect theory analysis of the np Rydberg series of H_3

M. C. Bordas,* L. J. Lembo,† and H. Helm

Molecular Physics Department, SRI International, Menlo Park, California 94025

(Received 2 April 1991)

The lowest np Rydberg series of triatomic hydrogen has been studied using optical-optical double-resonance excitation from the metastable $2p^2A_2''$ level. Bound states, detected by field ionization as well as autoionizing states of the p series are characterized using rotational multichannel quantum-defect theory. Deviations from the calculations appear when vibrational interactions give rise to predissociation below threshold or autoionizing interlopers above threshold. The np Rydberg manifold of H_3 provides an almost complete panorama of channel interactions in a polyatomic molecule: rotational and vibrational interactions and autoionization with rich Fano profile structure as well as predissociation.

I. INTRODUCTION

The Rydberg states of triatomic hydrogen resemble in many respects quasihydrogenic atomic Rydberg states. The small size of the core molecular ion H_3^- and its associated small multipole moments allow for only weak rotational interactions in the nonpenetrating Rydberg series with angular momentum $l \geq 2$. The energy levels of the nd and nf Rydberg series appear [1–3] in excitation as very regular quasihydrogenic channels, converging to a single state of the core ion. We show here that the p-electron Rydberg series are quite different, in that the electron approaches the core close enough that short-range electron-core interactions play an important role [4]. The richness of the observed features in the bound spectrum as well as in the continuum makes the H_3 np series a very general example of channel interactions in a polyatomic molecule.

Photoionization [1–3,5,6] and photodissociation [7–10] studies of the fundamentally unstable H_3 molecule have been an active field of research since the first analysis of the emission bands of H_3 by Herzberg and co-workers [11–15] in the early 1980s. Photoexcitation studies of H_3 conducted thus far have relied largely upon the metastability [16] of the lowest rotational level of the $\bar{B}$ $2p^2A_2''$ state. This level has a lifetime of 640 ns [17]. The dominant $2p$ character of the outer electron in the metastable state gives rise to R-branch type transitions into s-type and d-type Rydberg states, which have been detected by means of electric-field ionization [1,2], photoionization [5,6], and predissociation [8,9]. Using double-resonance techniques and a low-lying s or d state as intermediate, one can also study odd-l states, as for example the nf series [3] or the np series presented in this paper. Here, in a two-color stepwise excitation scheme, we first access the nonvibrating $3s^2A_1'$ state and then probe with a second tunable laser, the p-electron series in the bound-state region, and in the region above the lowest ionization threshold.

Rotational interactions among the p-electron Rydberg states have been already discussed from a theoretical point of view [18] and we will show in the following the

relevance of the frame transformation theory of the l-uncoupling effect in H_3. What renders the study of the np Rydberg states of H_3 particularly enlightening is that their spectrum displays examples of noninteracting Rydberg series ($N=0$ or 1), and of two series interacting in the discrete region and in the Beutler-Fano continuum ($N=2$). In addition, vibrational interactions appear in the discrete spectrum, where they cause predissociation, as well as in the continuum, where the presence of vibrational interlopers is evidenced by strong resonances and windows in the excitation spectrum.

The np Rydberg series contain states that match the symmetry of the electronic ground state of H_3, the sole dissociative continuum below the ionization threshold. An understanding of the np Rydberg states therefore appears as key towards an explanation of the occurrence of the very localized predissociations that have been observed in the H_3 molecule [19] and that are attributed to accidental vibrational perturbations that establish coupling paths [20] from high-n Rydberg states into the repulsive ground state of H_3.

We begin with a short description of the energy levels and symmetries of H_3 relevant to the present experiment, followed by the presentation of the experimental technique used. Before discussing the experimental results, we give a brief review of the equations of the multichannel quantum-defect theory (MQDT) that we use in our analysis of line positions and excitation intensities. Following this we present the experimental spectra of the np series in three fundamentally disting regions: (1) the discrete spectrum below the first ortho level of the ground state of the H_3^- ion ($N^+=1$, $K^+=0$); (2) the Beutler-Fano region between the two lowest ortho levels of H_3^+ ($N^+=1$ and 3, $K^+=0$), where we see a classic example of rotational autoionization; and (3) the continuum region above the $N^+=3$ level of the ion. The experimental results are then analyzed in the framework of MQDT and we finally discuss the possibility of including vibrational interactions to account for the presence of intense interloper lines and competition between dissociation and autoionization.

II. EXPERIMENT

A. Experimental principle

An energy-level diagram of triatomic hydrogen in D_{3h} geometry is shown in Fig. 1 together with the excitation scheme used in the present experiments. The figure gives the location of the lowest states involved in our optical scheme and the unstable ground state of H_3 in relation to the two- and three-body neutral and ionic dissociation limits.

The lowest long-lived H_3 state is the lowest rotational level of the $2p^2 A_2''$ state. This level has a symmetric nuclear spin wave function (ortho-H_3), and it is characterized by the quantum numbers $N=0$, $K=0$. Here and in the following, N and K (respectively N^- and K^-) represent the total angular momentum, excluding spin, and its projection onto the top axis for the neutral molecule (respectively the ion). This metastable state is nearly purely described by a configuration built from a $2p(a_2'')$ electronic orbital on the lowest ortholevel of the H_3^- ion: $N^- = 1$, $K^- = 0$.

The excitation of the np Rydberg series is achieved in a two-step process (see Fig. 1). A first photon $h v_1$ (16 694.97 cm^{-1}) [12] induces transition from the vibrationless metastable level of the $\bar{B}$ state $(N=0)$ to the $3s^2 A_1' (N=1, v_1=v_2=0)$ intermediate state (v_1 and v_2 denote, respectively, the symmetric stretch and the degenerate mode vibrational quantum numbers of the molecule):
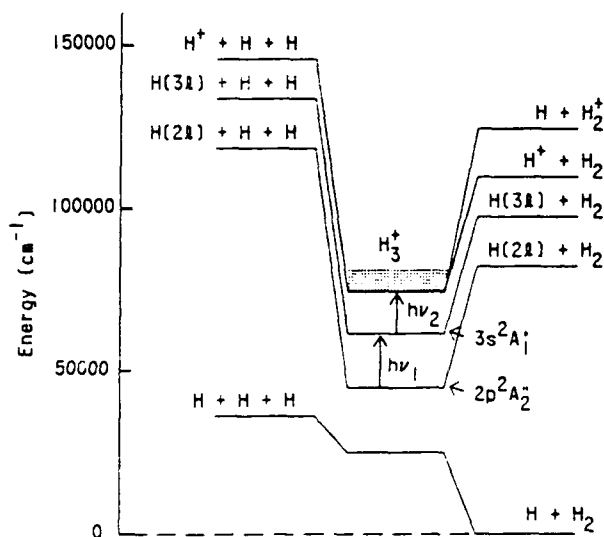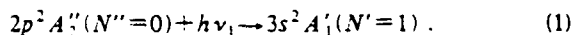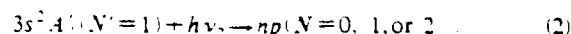
$$2p^2 A_2'' (N''=0) + h v_1 \rightarrow 3s^2 A_1' (N'=1) . \qquad (1)$$

Following the selective excitation of the vibrationless $3s$ state, a second laser is tuned through the ionization threshold regions to excite the p-electron Rydberg series:

$$3s^2 A_1' (N'=1) + h v_2 \rightarrow np (N=0, 1, \text{or } 2) \qquad (2)$$

For the second excitation step, transitions to levels with $N=0$, 1, and 2 are allowed by electric dipole selection rules. We show in Fig. 2 how states with these N values can be generated by combining a p-type electron with the core ion $N^- = 3$, giving a series with $N=2$, and with the core ion $N^- = 1$, giving series with $N=0$, 1, and 2. Depending on the relative orientation of the polarization axes of the two photons $h v_1$ and $h v_2$, one can excite only the $M_N = 0$ (parallel polarizations) or only the $M_N = 1$ levels (perpendicular polarizations). In the first case, only $N=0$ or 2 states can be excited, while in the latter case, transitions to $N=0$ states are forbidden and only $N=1$ or 2 states are excited. This second excitation step is detected by ionization of the Rydberg states. Levels below the threshold appear due to field ionization; levels above threshold generally autoionize or they are induced to ionize by an external electric field. The first laser, which excited the $3s$ state, is kept at an intensity low enough to avoid a background photoionization signal from $1+1$ photon ionization. The second laser operates at moderate intensity to avoid saturation broadening in the np series members.

During the second excitation step, diagonal transitions (i.e., without change in the vibrational excitation of the core) are expected to dominate over nondiagonal transitions (Δv_1 or $\Delta v_2 \neq 0$). The potential-energy surface of the $3s^2 A_1'$ state is very similar to the surface of the ion, and therefore to those of the p Rydberg states with high values of n. Hence, upward transitions from the $3s$ state, accompanied by a change of vibrational excitation, are not expected, with the exception of transitions to vibrational interlopers with low principal quantum number for which the poor Franck-Condon factor is offset by the greater electronic transition moment.

FIG. 1. Energy diagram for H_3 states relevant for the excitation scheme to high-lying p Rydberg states. The first laser $(h v_1)$ is fixed to the $2p^2 A_2'' \rightarrow 3s^2 A_1'$ transition. The second laser $(h v_2)$ is scanned in the vicinity of the two lowest ionization limits of ortho-H_3.
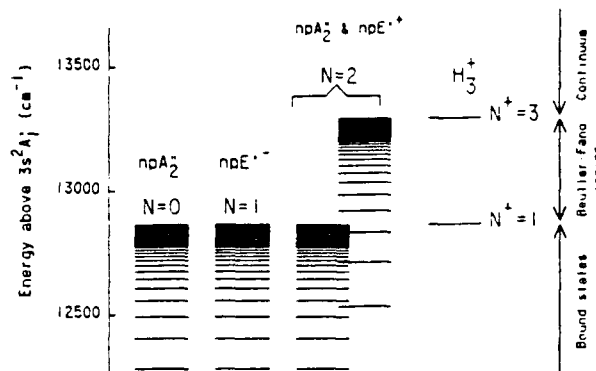

FIG. 2. Schematic representation of the core states of the lowest p Rydberg series.

In the framework of Hund's case (b), the np Rydberg series involved in our experiments are either np^2A_2'' or np^2E', which are analogous to $np\sigma$ and $np\pi$ states of a diatomic molecule. The $N=0$ and 1 series are pure np^2A_2'' and np^2E', respectively, while members of the $N=2$ series are a mixture of the two symmetries. Selection rules and line intensities as well as symmetry classification and the related passage from Hund's case (b) to Hund's case (d) will be discussed in the theoretical section of this paper.

B. Experimental setup

The experimental setup has been described previously [1,3]. H_3^- ions are extracted from a hollow-cathode hydrogen discharge at an energy of 1.5 keV. The H_3 molecules are produced by charge exchange of H_3^+ in a cesium vapor cell. The resulting neutral beam, purged of residual ions by a small electric deflection field, contains only molecules in the rotationaless level of the long-lived $\tilde{B}\, 2p^2A_2''$ state [17]. In an ultrahigh-vacuum chamber, the neutral beam interacts with two superimposed coaxial dye laser beams along a 120-cm-long interaction region. Care is taken to avoid residual electric fields in the excitation region [19]. Both lasers have a pulse duration of about 15 ns, a bandwidth of 0.15 cm^{-1}, and a spot size of about 5 mm^2. The first laser $h\nu_1$ is tuned to the $3s\leftarrow2p$ transition (16 694.97 cm^{-1}) which is easily saturated with pulse energies as low as 50 μJ. The second laser (1 mJ/pulse) excites the molecules from the $3s$ state to the np series. Due to the short lifetime [17,21] of the $3s$ intermediate state (10 ns > $\tau \geq 0.8$ ns), the second laser is not delayed with respect to the first. It is scanned from ~100 cm^{-1} below the first orthoionization limit ($N^+=1$) to ~1300 cm^{-1} above the limit, corresponding to a wavelength scan from 700 and 790 nm. A fixed ionizing field of about 1.7 kV/cm at the entrance of an energy and mass analyzer is used for field ionization of the bound states lying below the threshold or for deflection of the ions created in the autoionization processes. The resulting ions of mass 3 are detected on a microchannel plate and counted. The mass selection ensures that we do not detect H^+ or H_2^- ions produced in dissociative processes.

III. THEORY

The appearance of the excitation spectra of the np Rydberg states is strongly influenced by rotational channel interactions. The theory suitable for the description of these interactions, MQDT, is well developed [21-25] and we outline below how it is applied in the case of H_3. This framework will be used in the following section to identify position, intensity, and line shape of the transitions to the np states. Numerous instances of vibrational channel interactions also appear in our spectra. While these could formally be incorporated in the theory, the current information on the participating core states and their vibrational interaction via the Rydberg electron is too limited for the theory to be predictive.

The basis of the theory is that a Rydberg electron moves essentially outside the core, in a region where it experiences a pure Coulombic potential. The effects of short-range interactions are described by a limited number of parameters that are basically independent of the energy: the quantum defects, which are empirically determined from the experimental spectra, and a molecular frame transformation matrix that we can calculate exactly.

A. MQDT wave function

A key point is to introduce two different basis sets describing the electron-core interaction at infinity (collision channels) or near the origin (close-coupling channels) and to match the expansion of the molecular wave function in these two bases in the intermediate space. These sets must satisfy boundary conditions respectively at infinity and near the core.

The collision-channel wave functions Ψ_i are defined by

$$\Psi_i = \chi_i(f_i\cos\pi\nu_i + g_i\sin\pi\nu_i) ,\qquad (3)$$

where χ_i contains the core wave function and the angular and/or spin part of the electronic wave function. The radial wave function is expressed as a linear combination of regular $[f_i(\nu_i,l,r)]$ and irregular $[g_i(\nu_i,l,r)]$ Coulomb wave functions (defined to be energy normalized for positive energies) and matches the boundary conditions as the electron coordinate r tends to infinity. The coefficients $\cos(\pi\nu_i)$ and $\sin(\pi\nu_i)$ ensure that the wave function ψ_i behaves correctly at large separation of the electron from the core.

The close-coupling channel wave functions Ψ_α take into account the non-Coulombic short-range interactions via the introduction of the quantum defects μ_α ($\pi\mu_\alpha$ represents the phase shift due to the short-range interactions) and the unitary transformation matrix U which relates collision channels i to close-coupling channels α:

$$\Psi_\alpha = \sum_i \chi_i U_{i\alpha}(f_i\cos\pi\mu_\alpha - g_i\sin\pi\mu_\alpha) .\qquad (4)$$

The total wave function Ψ of the system is written as a linear combination of the Ψ_i or of the Ψ_α functions, respectively:

$$\Psi = \sum_i B_i\Psi_i = \sum_\alpha A_\alpha\Psi_\alpha .\qquad (5)$$

The total energy of the system is defined by

$$E = \varepsilon_i + I_i ,\qquad (6)$$

where e_i, the electron energy is connected to the quantum number n_i via

$$\varepsilon_i = -\mathcal{R}/\nu_i^2 .\qquad (7)$$

B. The U matrix

The transformation matrix U is the unitary matrix connecting close-coupling and ionization (or collision) channels. The ionization channels are described by the quantum numbers of the ionic core N^-, K^-, and Γ^- (electronic species), the angular momentum of the Rydberg

electron l, the total angular momentum of the molecule (neglecting spin) N and its projection onto the symmetry axis M_N. In the close-coupled channels, Γ^+, K^+, l, N, and M_N are still good quantum numbers, with the addition of the electronic species of the neutral molecule, Γ. Therefore the U matrix reduces to a transformation from the basis where N^- is defined [Hund's case (d) basis] to the basis where Γ is well defined [Hund's case (a) or (b) basis]. In contrast to atomic physics, where the $LS-jj$ coupling transformation only gives an approximation for the U matrix, the molecular U matrix is strictly the transformation from Hund's case (d) to Hund's case (b) because at short distance Γ is an exact quantum number and at large distance N^- is an exact quantum number. As noted before, only the odd-N^- levels of H_3^+ are present in the ionization channel basis because we start from a $K^+=0$, ortho level of H_3^-. The general expression for the U matrix in the case of a polyatomic molecule in D_{3h} geometry may be derived from the general expression for a diatomic molecule given by Chang and Fano.[23] Exchanging their electronic lable $\bar{\Lambda}$ for our quantum number K^- adapts their formula (Eq. (A9) of Ref. [23]) to triatomic hydrogen. For the different N values that we can access, we have the following U matrices (see Fig. 2)

(i) For $N=0$, only one channel exists ($U=1$). This channel is termed np^2A_2'' in the close-coupled basis and $np(N^+=1)$ in the collision basis.

(ii) For $N=1$, also only one channel exists ($U=1$). This channel is termed np^2E' in the close-coupling basis and $np(N^+=1)$ in the collision basis.

(iii) For $N=2$, two channels appear. They are np^2A_2'' and np^2E' in the close-coupling basis and $np(N^+=1)$ or $np(N^+=3)$ in the collision basis. The transformation matrix in this case is

$$U = \begin{array}{cc} & \begin{array}{cc} |^2A_2'') & |^2E') \end{array} \\ \begin{array}{c} (N^+=1| \\ \\ (N^+=3| \end{array} & \left[\begin{array}{cc} \sqrt{2/5} & \sqrt{3/5} \\ \\ -\sqrt{3/5} & \sqrt{2/5} \end{array} \right] \end{array} . \qquad (8)$$

C. Boundary conditions

Boundary conditions and compatibility of Eqs. (3), (6), and (7) impose, for each ionization channel i,

$$\sum_\alpha U_{i\alpha}\sin[\pi(v_i+\mu_\alpha)]A_\alpha=0 , \qquad (9a)$$

$$\sum_\alpha U_{i\alpha}\cos[\pi(v_i+\mu_\alpha)]A_\alpha=B_i , \qquad (9b)$$

or the equivalent formulation for each close-coupling channel α:

$$\sum_i U_{i\alpha}\sin[\pi(v_i+\mu_\alpha)]B_i=0 , \qquad (10a)$$

$$\sum_i U_{i\alpha}\cos[\pi(v_i+\mu_\alpha)]B_i=A_\alpha . \qquad (10b)$$

A nontrivial solution of (9a) or (10a) requires that

$$\det\{U_{i\alpha}\sin[\pi(v_i+\mu_\alpha)]\}=0 , \qquad (11)$$

while Eqs. (9b) and (10b) allow us to change the representation from Hund's case (b) to Hund's case (d) and reciprocally. These equations hold regardless of whether or not some channels are open to ionization, with the condition that when a channel i is open ($\epsilon_i>0$), the effective quantum number v_i must be replaced by a scattering phase shift τ.

1. Discrete spectrum

In the discrete spectrum the effective quantum number vi_i is real and the electron energies are negative. Equation (11), together with relations (6) and (7), give the level energies, determining the entire discrete spectrum. For bound states, the normalization factor $\mathcal{N}$ for the wave function Ψ is such that [22]

$$\mathcal{N}^2=\sum_i v_i^3(\sum_\alpha A_{i\alpha}\cos[\pi(v_i+\mu_\alpha)])^2 . \qquad (12)$$

To calculate the intensity of the transition between the initial state and the Rydberg state Ψ we need the transition matrix elements in the close-coupling basis, T_α, or in the ionization basis, T_i, connected by

$$T_i=\sum_\alpha \frac{1}{\cos(\pi\mu\alpha)}U_{i\alpha}T_\alpha . \qquad (13)$$

The intensity of the transition is simply

$$I=\frac{(\sum_\alpha T_\alpha A_\alpha)^2}{\mathcal{N}^2}=\frac{(\sum_i T_iB_i)^2}{\mathcal{N}^2} . \qquad (14)$$

The transition matrix elements are functions of the total angular momentum N and of the relative polarization of the two lasers which determines M_N. We now calculate the elements T_α where we chose the polarization axis of $h\nu_1$ as the quantization axis. The general form of the transition matrix elements between an initial state well described in the Hund's case (d) $\{\rho_i,N^+,N_i,l_i,M_i\}$ and a final state described in the Hund's case (b) basis by $\{\rho_f,N_f,\Gamma_fl_f,M_f\}$ can be calculated using standard angular momentum algebra[26] (ρ represents the other quantum number: n, spin, etc.). In the case where both lasers are polarized along the same axis ($M_N=0$) we have

$$T_i^i=U_{N^+\Gamma}\begin{Bmatrix} N_f & 1 & N_i \\ 0 & 0 & 0 \end{Bmatrix}\sqrt{(2N_i-1)(2N_f+1)}\delta_{N_i^+N_f}\begin{Bmatrix} l_f & N_f & N_f \\ N_i & l_i & 1 \end{Bmatrix}\langle\rho_fl_f\|Q_{el}\|\rho_il_i\rangle . \qquad (15a)$$

If the two lasers are polarized along two perpendicular axes ($M_N=1$)

$$T_{\Gamma}^{\perp} = U_{N^+\Gamma} \begin{Bmatrix} N_f & 1 & N_i \\ 1 & -1 & 0 \end{Bmatrix} \sqrt{(2N_i+1)(2N_f+1)} \delta_{N^+ N_f} \begin{Bmatrix} l_f & N_{f^+} & N_i \\ N_i & l_i & 1 \end{Bmatrix} \langle \rho_f l_f \| Q_{el} \| \rho_i l_i \rangle . \qquad (15b)$$

where $U_{N^+\Gamma}$ is the transformation matrix between Hund's case (d) ($i \equiv N^+$) and Hund's case (b) ($\alpha \equiv \Gamma$).

In the particular case of a transition between the $3s^2A_1'$ state ($l_i = 0$, $N^+ = 1$, $N = 1$) and an np Rydberg state we have for parallel linear polarizations, the following. For $P(1)$,

$$T_{A_2''}^{\|} = \tfrac{1}{3} T_{el}, \quad T_{E'}^{\|} = 0 .$$

For $Q(1)$,

$$T_{A_2''}^{\|} = 0, \quad T_{E'}^{\|} = 0 .$$

For $R(1)$,

$$T_{A_2''} = \sqrt{4/45} T_{el}, \quad T_{E'}^{\|} = \sqrt{2/15} T_{el} .$$

And for perpendicular polarizations, for $P(1)$,

$$T_{A_2''}^{\perp} = 0, \quad T_{E'}^{\|} = 0 .$$

For $Q(1)$,

$$T_{A_2''}^{\perp} = 0, \quad T_{E'}^{\perp} = \tfrac{1}{6} T_{el} .$$

For $R(1)$,

$$T_{A_2''}^{\perp} = \sqrt{1/15} T_{el}, \quad T_{E'}^{\perp} = \sqrt{1/10} T_{el} , \qquad (16)$$

where T_{el} is the electronic part of the transition moment:

$$T_{el} = \langle np \| Q_{el} \| 3s^2 A_1' \rangle . \qquad (17)$$

2. Beutler-Fano region

Above the first ionization limit, the $N=0$ and 1 series are in the ionization continuum while the $N=2$ series between the $N^+ = 1$ and 3 levels of the ion is subject to rotational autoionization. In this case, the effective quantum number $v_{N^+=3}$ is real while $v_{N^+=1}$ is purely imaginary. Then $v_{N^+=1}$ must be replaced by a phase shift $-\tau$ related to $v_{N^+=3}$ by Eq. (11), while Eq. (4) has no meaning for v_1 in this region. With a single channel open, as is the case here, the problem is trivial and Eq. (11) has only one solution for a given energy:

$$\Psi = \frac{\sum_i B_i \Psi_i}{\mathcal{N}} . \qquad (18)$$

The summation over i extends over the channels $i = (N^+ = 1)$ and $i = (N^+ = 3)$, with Ψ_i defined by Eq. (3) and the normalization factor $\mathcal{N}$ given by the very simple expression

$$\mathcal{N}^2 = \sum_{i^*} B_i^2 = B_{(N^+=1)}^2 , \qquad (19)$$

where i^* means that channel i is open.

The photoionization intensity in the Beutler-Fano region is then calculated using Eqs. (14), (16), and (17).

3. Continuum

The density of oscillator strength evolves smoothly from the bound-state region to the Beutler-Fano region and to the true continuum. For the $N=0$ and 1 series the continuum is located above the $N^+ = 1$ level of the ion while, for the $N=2$ series, it is located above the $N^+ = 3$ level of the ion. In the continuum, there exist as many independent solutions as there are open channels. These solutions may be arbitrarily chosen to be the close-coupled wave functions Ψ_α defined by Eq. (4). No structure appears in the continuum unless vibrational or electronic interactions with excited core states occur.

IV. EXPERIMENTAL RESULTS

Figure 3 shows a spectrum for a photon energy $h\nu_2$ scanned between about 12770 and 14200 cm^{-1}. This spectrum is recorded with parallel laser polarization (i.e., $M_N = 0$) and is normalized to the laser intensity. We note here that the lower energy limit of detecting the excitation spectrum is imposed by the field-ionization efficiency. For the experimental setup used here, the efficiency decreases rapidly when the principal quantum number n is lower than 30. Here and in the following, the photon energy is relative to the $3s^2 A_1'$ state. The "absolute" energy relative to the lowest metastable state of H_3 may be obtained by adding [12] 16694.97 cm^{-1} to this value.

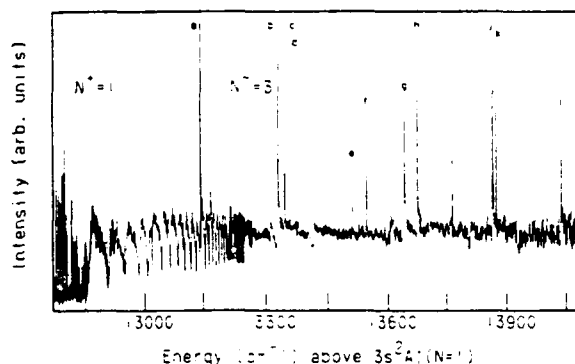Excitation of the Rydberg states occurs from a single level of the $3s$ state, with $N=1$ ($K=0$) and no vibration.

FIG. 3. Excitation spectrum of H_3 $3s^2 A_1'$ from 12700 to 14200 cm^{-1} ($M_N = 0$) showing the three distincts regions: the discrete spectrum below $N^+ = 1$, the Beutler-Fano region between the limits $N^+ = 1$ and 3, and the continuum beyond $N^+ = 3$.

Since vibrationally diagonal transitions (i.e., $\Delta v_1 = \Delta v_2 = 0$ are by far stronger than nondiagonal, the dominant observed series are the vibrationless $N=0$ 1, and 2 np series converging to the $N^+=1$ or 3 ($K^+=0$) levels of the ion. These two ionization limits separate the spectrum into three different regions. These regions are indicated schematically in Fig. 2 and 3 and they correspond to the three cases described in the preceding section. Below the lowest ortho level of H_3^- $N^-=1$, $K^+=0$ (photon energy lower than 12 867.6 cm^{-1}), the Rydberg states are strictly stable relative to autoionization because no accessible ionization continuum exists. An ensemble of discrete narrow peaks is observed in this region. This portion of the spectrum is shown on an expanded scale in Fig. 4. Between the $N^-=1$ and $N^+=3$ levels of the ion (12 867.6 $< h v_2 <$ 13 297.5 cm^{-1}), the $N^+=1$ continuum is open and the np Rydberg states can autoionize. This region, referred to as the Beutler-Fano region, exhibits a structured continuum where the $N^+=3$ series members appear as dips in the ion signal. The reason for the window formation is that we start from a 3s state that has a pure $N^-=1$ core. Note that the window formation only applies to the $N=2$ np Rydberg series. The $N=0$ and 1 Rydberg states are built from an np electron surrounding an $N^+=1$ core. Their excitation spectrum in the region above threshold is a pure continuum. These continua underly the $N=2$ features and they are the reason why the intensity minima do not reach zero value. An expanded view of the Beutler-Fano region is given in Fig. 5. Finally, above the $N^+=3$ level ($h v_2 >$ 13 297.5 cm^{-1}) we are in the true continuum of all vibrationless series with $N=0$, 1, and 2.

FIG. 5. Beutler-Fano spectrum with $M_v=0$ (bottom) and MQDT simulation (top). General agreement between theory and experiment is observed except for the presence of localized perturbations such as the extra window resonance near $v_1=20$ and a strong interloper near $v_3=27$.

This region should in principle be a flat continuum with the exception of strong autoionizing lines pertaining to vibrationally excited series. We now discuss in more detail each of these three regions.

A. The discrete spectrum: $h v_2 <$ 12 867.6 cm^{-1}

A close-up of the bound-state region is displayed in Fig. 4 together with a two-channel quantum-defect calculation. As mentioned previously, with our excitation scheme, one can selectively excite the $N=0$ and 2 ($M_N=0$) series if the two lasers are linearly polarized along the same axis or the $N=1$ and 2 ($M_N=\pm1$) series if they are polarized along the perpendicular axis. An immediate advantage of this characteristic is the possibility of studying directly the unperturbed $npA''(N=0)$ and $npE'(N=1)$ series. We can derive their quantum defects using a simple Rydberg formula:

$$E_a = E(H_3^+ N^+=1, K^+=0) - \frac{\mathcal{R}}{(n-\mu_a)^2}, \quad (20)$$

where a designates the symmetry of the series (pA'' or pE') and μ_a its quantum defect. The Rydberg constant $\mathcal{R}$ is 109 717.40 cm^{-1} for H_3. The knowledge of these two quantum defects is then sufficient to analyze the $N=2$ series where A'' and E' symmetry are mixed by rotational interaction (l uncoupling). The spectrum of Fig. 4 has been recorded with $M_N=0$ and hence only $N=0$ and 2 lines are visible. The energy position of each line is very precisely calculated with a two-channel MQDT treatment as shown by the good agreement between experiment and calculated line position in Fig. 4. The values of the quantum defect fitted to the experimental
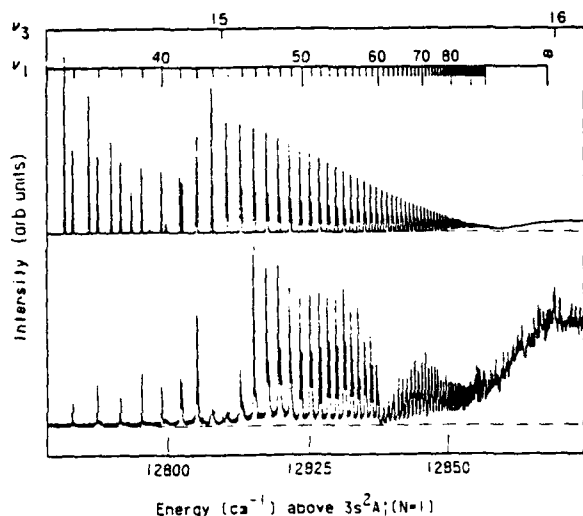

FIG. 4. Experimental spectrum ($M_N=0$, bottom) and MQDT simulation (top) below the first ionization limit (discrete-state region). The numbers at the top are the effective quantum numbers v_1 relative to the first ionization limit $N^+=1$ and the integer quantum numbers v_3, relative to the limit $N^+=3$. The calculated line positions are in good agreement with the experiment while the line intensities are obviously perturbed.
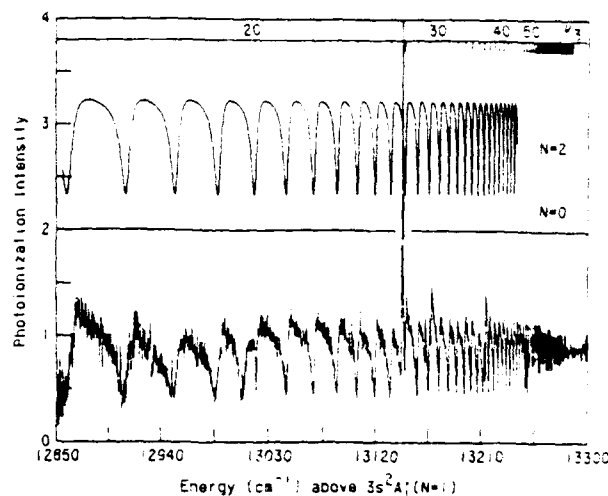
line positions are

$$\mu_{pA_2''} = 0.05 \pm 0.01 , \tag{21a}$$

$$\mu_{pE} = 0.39 \pm 0.01 . \tag{21b}$$

The agreement between experimental and calculated values is generally better than our experimental resolution (0.15 cm^{-1}) with a standard error of about 0.03 cm^{-1} for the unperturbed $N=0$ lines and 0.10 cm^{-1} for the $N=2$ lines. Note that the calculated spectrum has been broadened to a width of 0.15 cm^{-1} comparable to our experimental resolution. However, noticeable disagreements are observed as far as the line intensities are concerned. Three points are worthy of mention here.

(1) The calculation predicts that the intensity of the $N=2$ series converging to the $N^+=1$ limit should vanish near $n=40$. This is due to the presence of the $n=15$ interloper state of the $N^+=3$ series near this energy. The theory also predicts that lines corresponding to $N=2$ states with $n<38$ should be more intense than the companion $N=0$ lines. In fact, no $N=2$ states are observed below $n \approx 41$ while the $N=0$ lines are present in the experimental spectrum.

(2) Additional intensity windows appear in the experimental spectrum around $n=43$ and 61. Near $n=61$ only the $N=2$ series is diminished in intensity but for $n=43$ both series are affected.

(3) Finally, the experimental intensities of the low-n lines are weaker than expected in comparison to the intensity of the high-n lines. The overall scaling rule of $1/n^3$ is not observed in the experimental spectrum. A hydrogenic simulation shows that with the ionizing-field value and with the geometry (time of flight of the neutrals in the detection field) we use, field ionization must be 100% efficient above $n=35$; therefore the field-ionization efficiency should not be responsible for this deviation.

In the present experiment, the H$_3$ molecules excited to a discrete state below the ionization limit have a time of flight between 1 and 4 μs in a field-free space before reaching the field-ionization detector. Thus, if any decay process is fast enough to occur during that time frame, no ions will be detected and the observed line intensity may be low even for strong transitions. Low-lying states of H$_3$ are known to be rapidly predissociated [17,21] on picosecond to nanosecond time scales due to interactions with the vibrational continuum of the dissociative ground state. It is therefore not really surprising to observe such decay processes, occurring on a longer time scale, for the higher Rydberg states. However, the localization of this process to very confined regions and at even very high n values (the n^3 scaling factor holds also for predissociative lifetimes in Rydberg states) remains to be clarified.

The region around $n=61$ is of particular interest and we have already discussed this region in a previous paper [19] where we show that predissociation of the nd states near $n=61$ is induced by extremely weak fields by coupling of nd states with the np series. Figure 6 is an enlargement of the p-series spectrum in this region. This portion of the spectrum shows that the intensity of the $N=2$, np Rydberg series displays a broad window extending from about $n=60$ to 64, centered at $n=61$ where the
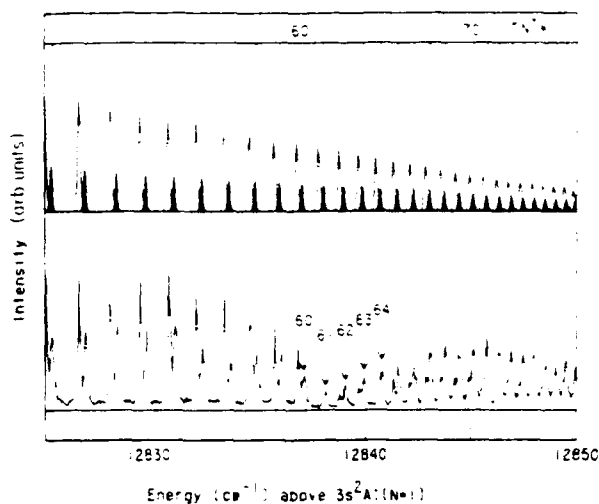

FIG. 6. Close-up of the discrete spectrum in the vicinity of $n=61$ (bottom) and MQDT simulation (top). In the calculated spectrum the $N=0$ lines are filled in black. The numbers 60 to 64 indicate the $np(N=0)$ Rydberg states. The $n=61$ and 64 ($N=2$) lines are clearly missing. Below $v_1=60$, calculated and experimental intensity match, while at higher energy the experimental intensity of the $N=2$ lines is smaller than predicted.

intensity of the $N=2$ transition is zero. By contrast, the $N=0$, np series is not visibly affected. In the calculated spectrum of Fig. 6, the $N=0$ lines are marked in black for clarity. The calculated intensity ratio between $N=0$ and 2 lines is in agreement with our observations for levels lying below the window resonance but it appears inverted for the higher Rydberg members. The wide energy range over which the intensity perturbation occurs points to the existence of a giant resonance, the origin of which is considered to be a homogeneous (electrostatic) interaction [27] of the Rydberg states with an interloper state $|A\rangle$.

$$61p(N=2) \leftrightarrow |A\rangle(N=2) . \tag{22a}$$

The interloper state in turn is predissociated to the ground state of H$_3$:

$$|A\rangle(N=2) \rightarrow 2p^2E'(N=2) . \tag{22b}$$

From the electric-field-induced predissociation of the nd Rydberg states near $n=61$, we have deduced [19] that the state $A\rangle$ is a low-n pE' state ($n=2$ or 3) with sufficient vibrational excitation to be quasidegenerate with the $61p$ vibrationless state. The predissociation rate of the interloper $A\rangle$ is found [19] to fall into the range $4\times10^8 < \Gamma_A < 4\times10^{10}$ s^{-1}. A more precise characterization of the core state responsible for the $n=61$ window is not possible at this point. A similar coupling mechanism to a predissociated state with lower principal quantum number and excited core vibration is likely responsible for the window formation near $n=43$ (see Fig. 4). But also its assignment and the origin for the absence of $N=2$ states below $n=38$ remain open at this point.

The knowledge of the two quantum defects $\mu_{pA_2''}$ and

μ_{pE} obtained by fitting the discrete spectrum is sufficient, together with the knowledge of the energy levels of the ion, to analyze precisely the Beutler-Fano region, which we discuss next.

B. The Beutler-Fano region: $12\,867.6 < h\,\nu_2 < 13\,297.5$ cm^{-1}

This region, located between the $N^+=1$ and 3 ortho levels of H_3^+, is displayed in Fig. 5. It is the region where rotational autoionization occurs. According to the excitation scheme used, this spectrum is a superposition of the $N=2$ series, the structured continuum, where $N^+=3$ members appear as dips in the $N^+=1$ continuum with the flat continuum of the $N=0$ or 1 series. The theory predicts that the appearance of the $M_N=0$ or 1 Beutler-Fano region is qualitatively similar except for the larger relative intensity of the flat continuum of $N=1$ when perpendicular polarizations are chosen. The upper spectrum in Fig. 5 gives the prediction of the two-channel MQDT calculation for $M_N=0$. The quantum defects derived from the analysis of the discrete spectrum are used in this simulation without adjustment. The agreement between experiment and theory is satisfactory, especially for the energy dependence of the photoionization intensity. This is opposite to the situation for discrete spectrum (see Fig. 4). The very regular series of typically asymmetric Fano profiles in the calculated spectrum matches almost perfectly the experimental spectrum. However, localized shifts of the position of the dips appear as well as several interloper resonances and windows.

The better agreement between calculated and experimental intensities in the Beutler-Fano region in comparison with the discrete spectrum is easy to understand. Most of the disagreement in the discrete spectrum comes from the fact that, during the few microseconds the Rydberg molecules exist before being field ionized, relatively slow decay processes (of the order of 1 μs) such as radiative decay or predissociation have time to occur. On the contrary, in the Beutler-Fano region, rotational autoionization is very fast, as seen from the broad width of the dips, and radiative processes are not able to compete with autoionization. Thus, unless rapid predissociation is induced by an interloper state, all the excited molecules may be detected. More quantitatively, we can estimate the lifetime of the Beutler-Fano resonances using the classic formula [28]

$$\tau \approx \frac{\nu_{N^-=3}^3}{2\pi^2 \mathcal{R} c\,(\mu_{pE}-\mu_{pA})^2} \approx 1.33 \times 10^{-16} \nu_{N^+=3}^3 \text{ s}. \quad (23)$$

According to this expression, the lifetime of the first resonance $(\nu_{N^-=3}=17)$ above the $N^-=1$ threshold is as short as 0.7 ps, while for $\nu_{N^-=3}=50$ the lifetime is still less than 20 ps. It is clear that rotational autoionization is the largely dominant process.

We now address the discrepancies that appear between calculation and experiment in the Beutler-Fano region. The spectrum in Fig. 7 exhibits several additional dips in the autoionization signal that are not expected from the MQDT treatment. A substantial shift in the position of the $N^+=3$ series members occurs near $\nu_{N^-=3}=20$, and
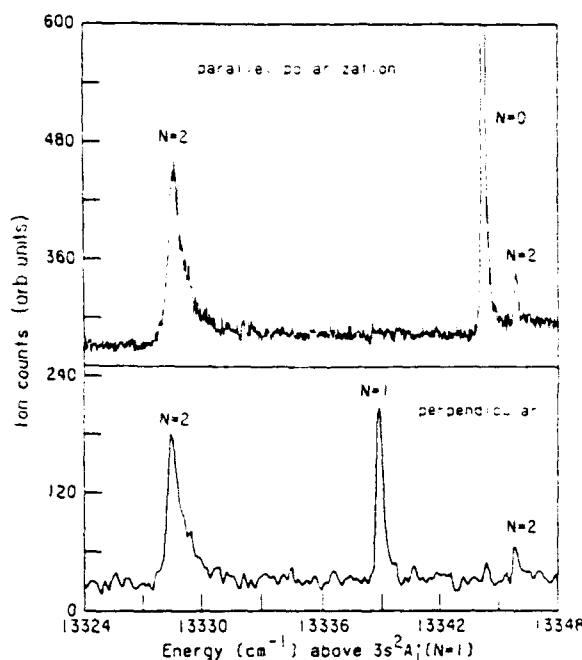
FIG. 7. Close-up of some vibrational interlopers appearing in the continuum of the vibrationless series: $M_N=0$ (top) and $M_N=1$ (bottom). These spectra demonstrate the assignment of the angular momentum quantum number N.

at least one very strong line appears near $\nu_{N^+=3}=27$. The only possible origin of these lines and dips, rather narrow as compared to the rotationally autoionizing lines, is that they correspond to Rydberg states built on a vibrationally excited core. Electronically excited core states [29] of H_3^+ lie too high in energy to be involved in the perturbations observed here. The large number of such features above the second ionization limit may eventually help us to specify the nature of these interlopers. In the case of the dip near $\nu_{N^+=3}=20$, the interaction between the vibrationless np series and the interloper must be very strong because the $n=20$ member of the $N^+=3$ series is shifted, about 10 cm^{-1} to the red while the levels below are shifted to a smaller degree. The interloper itself appears as a dip in the $N=2$ continuum. We therefore require that the interloper itself is characterized by the quantum number $N=2$. The dip occurs either due to a destructive interference that lowers the excitation probability, or else because this interloper has a predissociation lifetime shorter than its rovibrational autoionization lifetime. On the other hand, the extremely strong transition at 13 143 cm^{-1} $(\nu_{N^+=3}\approx27)$ does not seem to induce any noticeable shift in the vibrationless lines in its vicinity. This is an indication that the coupling between this interloper and the $N^-=3(0,0)$ series is relatively small and its angular momentum could be either $N=0$ or 2.

C. The true continuum: $h\nu_2 > 13\ 297.5\ \mathrm{cm}^{-1}$

If vibrational interactions and off-diagonal transitions were negligible, the continuum above $N^+ = 3$ should appear with a constant photoionization intensity proportional to T_1^2. In fact, the examination of the broad $M_N = 0$ spectrum (Fig. 3) shows that even this region displays significant structure. The dozen intense lines observed in this spectrum, together with the line lying in the Beutler-Fano region and a few measured for $M_N = 1$ are reported in Table I together with a tentative assignment for some of these transitions. The assignment of the angular momentum quantum number N is possible when spectra were recorded with perpendicular and parallel orientation of the laser polarization. If a line appears in both spectra it is likely to be an $N = 2$ line and if a line appears only when parallel (perpendicular) polarizations are used it is a transition to $N = 0$ ($N = 1$). An example is given in Fig. 7. The assignment of a principal quantum number or of vibrational quantum numbers is more difficult and, so far, all assignments must be taken as tentative.

The difficulty in assigning the interloper states is related to the large number of core states that may participate in resonance formation. We show in Fig. 8 the lowest vibrational levels [30] of the ion core. The vibrational levels are separated into states with electronic symmetry A and E. The most intense transitions to interlopers with core states of A symmetry will be to npE' and npA_2'' states as is the case for excitation to Rydberg states with the vibrationless core. On the other hand, core states with E symmetry require degenerate mode excitation in the electronic transition and therefore the Rydberg electron must either remain $l = 0$ or possibly change into $l = 2$. The assignments suggested in Table I use the core energies calculated by Tennyson and Henderson [30] and they are chosen on the basis of consistency of the effective quantum defects with those known from the vibrationless states at low principal quantum number. Significant vibrational excitation is observed for several intense resonances. In view of our recent observations of vibrational excitation in transitions from the vibrationless $2p^2 A_2''$ level to $3s$, $3p$, and $3d$ states [5,9] this is not surprising if we keep in mind that the electronic transition moment to the interloper states is weighted relative to the high-n Rydberg states by the cubed ratio of principal quantum numbers involved. We note (footnote a in Table I) that many resonances remain unassigned. We suspect that some of these will involve electronic states with principal quantum numbers $n = 3$ and 2 with very high core excitation.

A surprising feature in the excitation spectrum are four fairly strong members of the $nf3$ Rydberg series (see Table I). The assignment of these transitions,

$$3s^2 A_1'(N' = 1) + h\nu \to nf3 , \qquad (24)$$

is based on the observation of an effective quantum defect of zero ($\delta < 0.01$) for the final states involved. The members observed belong to the nf series that converges to the core level $N^+ = 3$, $K^+ = 0$ of the vibrationless ground state. We may think of two ways how intensity can be generated for the transitions (24). These transitions require an effective change in core rotation from $N^+ = 1$ to 3. For one the $3s^2 A_1'(N' = 1)$ lower state lies 1036 cm^{-1} below the $3d^2 A_1'(N' = 1)$ level which has a core wave function that is greater than 99% of $N^+ = 3$ character [3]. Hence, through s-d mixing the $3s$ state may pick up a minute attribute of the $N^+ = 3$ core that is required to drive a transition to the $nf3$ series. Alternatively, the transition strength derives from p-f mixing in the final states between the $(N = 2)nf3$ members and the $(N = 2)np3$ series which is accessed in the "allowed" transition (2).
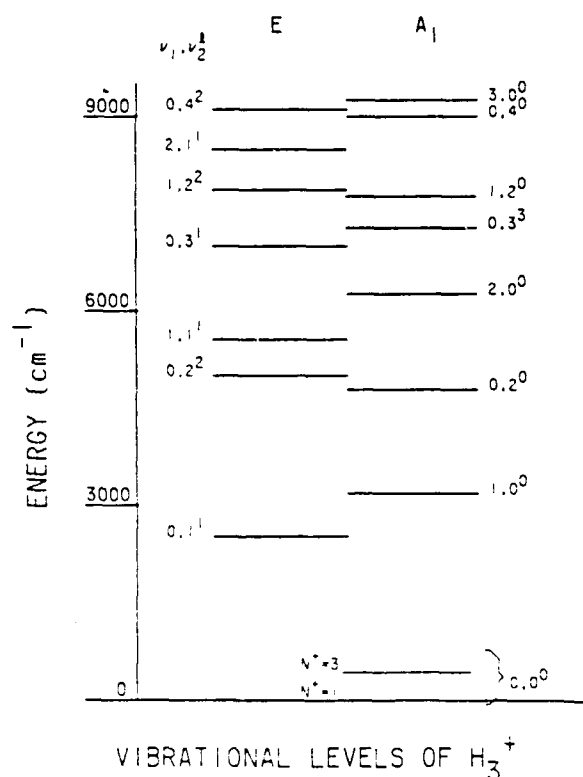

FIG. 8. Low-lying vibrational core states of H_3^+ of A_1 and E symmetry as calculated by Tennyson and Henderson [30]. The single level with A_2 symmetry in this energy range $(\nu_1 = 0, \nu_2 = 3, l = 3)$ at 7493 cm^{-1}, is omitted. The rotational spacing of the lowest ortholevels of H_3^+ with quantum number $K^+ = 0$ is shown for comparison with the vibrational gaps.

V. CONCLUSION

Given the well-established success of MQDT in analyzing molecular spectra, it is hardly surprising that the very simple rotational theory used in the present work reproduces fairly well many of the observed features. Exceptions occur due to vibrational interactions, which are not included in the theoretical model. It is in principle possi-

TABLE I. Vibrational and rotational interlopers[a] appearing in the photoexcitation spectrum of the vibrationless $3s^2A_1'(N=1)$ state. Excitation linewidths δ are given where measured. Tentative assignments for the Rydberg states and the core states of H_3^- are also given. The effective quantum numbers of the Rydberg states are calculated using the core energies of Tennyson and Henderson [30].

Label	$h\nu_1$ (cm^{-1})	δ (cm^{-1})	N	$nl\Gamma$	$(N^-,G^-\nu_1\nu_2^l)$	ν_{eff}
	12 809.6			$15fE'$	$(3,0,0,0^0)$	15.00
	12 868.8			$16fE'$	$(3,0,0,0^0)$	16.00
	12 875.9	W^b		$5pE'$	$(3,0,0,2^0)$	4.59
	12 918.0			$17fE'$	$(3,0,0,0^0)$	17.00
	12 958.9			$18fE'$	$(3,0,0,0^0)$	18.00
	13 125.5	1.0	1	$4pA_2''$	$(1,0,0,3^3)$	3.92
(a)	13 143.0	0.8	2	$5pA_2''$	$(1,0,0,2^0)$	4.94
(b)	13 328.7	1.0	2	$4pE'$	$(1,0,0,4^0)$	3.59
	13 338.9	0.4	1	$5sA_1'$	$(1,0,0,2^2)$	4.92
(c)	13 344.3	0.2	0	$7dA_1'$	$(2,0,0,1^1)$	6.98
(d)	13 345.9	0.2	2	$7dA_1'$	$(2,0,0,1^1)$	6.99
(e)	13 510.1	0.4		$7pE'$	$(1,0,1,0^0)$	6.58
(f)	13 545.8	0.3		$4pE'$	$(1,0,0,4^0)$	3.63
(g)	13 641.7	1.8		$4pA_2''$	$(1,0,0,2^0)$	3.96
(h)	13 674.7	0.6		$4pE'$	$(1,0,3,0^0)$	3.61
(i)	13 764.1	0.3		$7pA_2''$	$(1,0,1,0^0)$	6.94
(j)	13 864.8	0.8		$4pE'$	$(3,0,0,4^0)$	3.61
(k)	13 873.7	0.3		$4pE'$	$(1,0,3,0^0)$	3.65
(l)	14 037.0	0.4		$7dA_1'$	$(1,0,0,1^1)$	8.98

[a]Additional, weaker resonances appear at the following photon energies: 12 905.0, 12 930.9, 12 949.2, 12 966.4, 13 107.0, 13 162.6, 13 380.5, 13 506.6, 13 547.0, 14 029.7 cm^{-1}. Additional window resonances appear at 13 019.5, 13 057.8, 13 099.4, 13 312.5, and at 13 418.0 cm^{-1}.
[b]Window in excitation intensity.

ble to extent the MQDT to include the vibrational channels [28,31] and to treat the competition between predissociation and autoionization [32]. On the basis of the very precise calculations of the H_3^+ levels by Tennyson and co-workers [30,33] and the predictions on the variation of the quantum defect with nuclear geometry by Nader and Jungen [20] such an analysis may soon be tractable.

[*]Permanent address: Laboratoire de Spectrométrie Ionique et Moléculaire, Université Claude-Bernard Lyon I, Bâtiment 205, 43 Boulevard-du 11 Novembre, 69622 Villeurbanne CEDEX, France.
[†]Permanent address: TRW, Space & Technology Group, MS R1/1176, One Space Park Drive, Redondo Beach, CA 90278.

[1] H. Helm, Phys. Rev. Lett. **56**, 42 (1986); Phys. Rev. A **38**, 3425 (1988).

[2] A. Dohdy, W. Ketterle, H. P. Messmer, and H. Walther, Chem. Phys. Lett. **151**, 133 (1988).

[3] L. J. Lembo, C. Bordas, and H. Helm, Phys. Rev. A **42**, 6660 (1990).

[4] H. F. King and K. Morokuma, J. Chem. Phys. **71**, 3213 (1979).

[5] L. J. Lembo, H. Helm, and D. L. Huestis, J. Chem. Phys. **90**, 5299 (1989).

[6] L. J. Lembo, A. Petit, and H. Helm, Phys. Rev. A **39**, 3721 (1989).

[7] S. F. Selgren and G. I. Gellene, Chem. Phys. Lett. **146**, 485

(1988).

[8] P. C. Cosby and H. Helm, Phys. Rev. Lett. **61**, 298 (1988).

[9] L. J. Lembo and H. Helm, Chem. Phys. Lett. **163**, 425 (1989).

[10] P. C. Cosby and H. Helm, Chem. Phys. Lett. **152**, 71 (1988).

[11] I. Dabrowski and G. Herzberg, Can. J. Phys. **58**, 1238 (1980).

[12] G. Herzberg and J. K. G. Watson, Can. J. Phys. **58**, 1250 (1980).

[13] G. Herzberg, H. Lew, J. J. Sloan, and J. K. G. Watson, Can. J. Phys. **59**, 428 (1981).

[14] G. Herzberg, J. T. Hougen, and J. K. G. Watson, Can. J. Phys. **60**, 1261 (1982).

[15] J. K. G. Watson, S. C. Foster, A. R. W. McKellar, P. Bernath, T. Amano, F. S. Pan, W. M. Crofton, R. S. Altman, and T. Oka, Can J. Phys. **62**, 1875 (1984).

[16] G. I. Gellene and R. F. Porter, J. Chem. Phys. **79**, 5975 (1983).

[17] C. Bordas, P. C. Cosby, and H. Helm, J. Chem. Phys. **93**,

6303 (1990).

[18] Shao-hua Pan and K. T. Lu, Phys. Rev. A 37, 299 (1988).

[19] C. Bordas and H. Helm, Phys. Rev. A 43, 3645 (1991).

[20] Ch. Nader and M. Jungen, Chem. Phys. 70, 189 (1982).

[21] N. Bjerre, I. Hazell, and D. C. Lorents (unpublished).

[22] U. Fano, Phys. Rev. A 2, 353 (1970).

[23] E. S. Chang and U. Fano, Phys. Rev. A 6, 173 (1972).

[24] C. H. Greene and Ch. Jungen, Adv. At. Mol. Phys. 21, 51 (1985).

[25] C. H. Greene, U. Fano, and G. Strinati, Phys. Rev. A 19, 1485 (1979).

[26] A. R. Edmonds, *Angular Momentum in Quantum Mechanics* (Princeton University Press, Princeton, NJ, 1960).

[27] H. Lefebvre-Brion and R. Field, *Perturbations in the Spectra of Diatomic Molecules* (Academic, New York, 1986).

[28] Ch. Jungen and D. Dill, J. Chem. Phys. 73, 3338 (1980); Ch. Jungen and M. Raoult, *ibid.* 74, 3388 (1981).

[29] D. Talbi and R. P. Saxon, J. Chem. Phys. 89, 2235 (1988).

[30] J. Tennyson and J. R. Henderson, J. Chem. Phys. 91, 3815 (1989).

[31] C. Bordas, P. Labastie, J. Chevaleyre, and M. Broyer, Chem. Phys. 129, 21 (1989).

[32] A. Giusti-Suzor and Ch. Jungen, J. Chem. Phys. 80, 986 (1984).

[33] J. Tennyson, O. Brass, and E. Pollak, J. Chem. Phys. 92, 3005 (1990).

Appendix C

METASTABILITY AND RYDBERG STATES OF H_3

Metastability and Rydberg states of triatomic hydrogen.

Christian Bordas* and Hanspeter Helm.
Molecular Physics Laboratory, SRI International
333 Ravenswood Avenue, Menlo Park Ca 94025 USA
and * LASIM, Université Lyon I, 43 Bd du 11 Novembre
69622 Villeurbanne Cedex, France

Abstract : The np,nd and nf Rydberg series of H_3 have been studied by one- or two-photon excitation from the lowest metastable state of H_3 : B 2p $^2A_2^-$. The lifetime of the metastable state has been measured and the influence of an external electric field on the Rydberg states has been studied under both aspects of dynamics (field-ionization and field-induced predissociation) and structure (Stark effect).

1 - Introduction.

Although the H_3^+ ion, one of the most compact and stable molecular ion, has been among the first species known to mass spectroscopists, it was not until 1968 that the first observation of the neutral triatomic hydrogen species was reported [1]. The repulsive character of the ground state of H_3 was the major impediment to the observation of this unstable molecule. Since then, long-lived H_3 molecules have been observed in a variety of experiments but the metastability of the B 2p $^2A_2^-$ state [2] in its rotationless level has been understood only during the past decade [3]. Taking advantage of the metastability of this state in a single rotationnal level (N=0) while all other low-lying states are strongly predissociate, very simple excitation spectra of H_3 Rydberg series may be obtained. Owing to the very high stability of the H_3^+ ion, Rydberg states of H_3 are tightly bound while embedded in the continuum of the repulsive ground state X $(1sa_1)^2$ 2p $^2E'$ of H_3. No repulsive state cross the Rydberg states and thus they do not suffer direct predissociation. On the other hand, penetration effects are weak and electron-core couplings are limited due to the small size of the H_3^+ core.

In our experiments, a 1.5 keV beam of H_3^+ ions is mass selected and neutralized in a Cs charge exchange cell to produce a neutral H_3 beam consisting almost completely of molecules in the B state (more than 80 % in the vibrationless level). The molecular beam interacts with a counterpropagating pulsed laser beam over a region about 120 cm long. In the central portion of this interaction region, a well defined electric field is applied and the production of excited states is monitored by electric field ionization of the resulting H_3^+ ions. An appropriate gating allows us to record only the ions corresponding to neutral molecules excited in the region where the electric field is well defined. This experimental set-up enables us to characterize the B state which is largely dominant in the beam, and to study Rydberg series by one- or two-photon resonance excitation.

45

2 - Metastability of the B $2p\,^2A_2''$ state.

Using direct photoionization [4] of the neutral molecules (with a UV photon, $\lambda < 338$ nm) in the absence of any external field and recording the ion signal as a function of the time of flight of the H_3 molecules, we can deduce the amount of neutral molecules in the beam as a function of the time elapsed since their formation and then determine directly the lifetime of the metastable state. We find the value of $640\,^{+300}_{-100}$ ns, in complete disagreement with the expected value of 88 µs calculated [5] on the assumption of a purely radiative decay towards the dissociative $2s\,^2A_2'$ state. We attribute the faster decay channel to weakly allowed radiative transitions between the metastable state and the degenerate mode excited repulsive ground state H_3, as well as to predissociation induced by spin-orbit coupling. Numerical estimations are not available for the radiative process while one can estimate that the spin-orbit coupling may account only for 10% of the fast observed decay rate.

3 - Field free Rydberg states spectroscopy.

Using the B state which has a strong 2p character as initial state, ns and nd Rydberg series may be excited by one photon transitions while the excitation of np or nf series requires a two photon excitation via a ns or nd state respectively. Figure 1 shows the np, nd and nf series converging to the first ortho-level of the H_3^+ ion ($N^+=1$). The ns series has not been observed for high n values because it is about 40 times less intense than the nd series and it is probably predissociate.
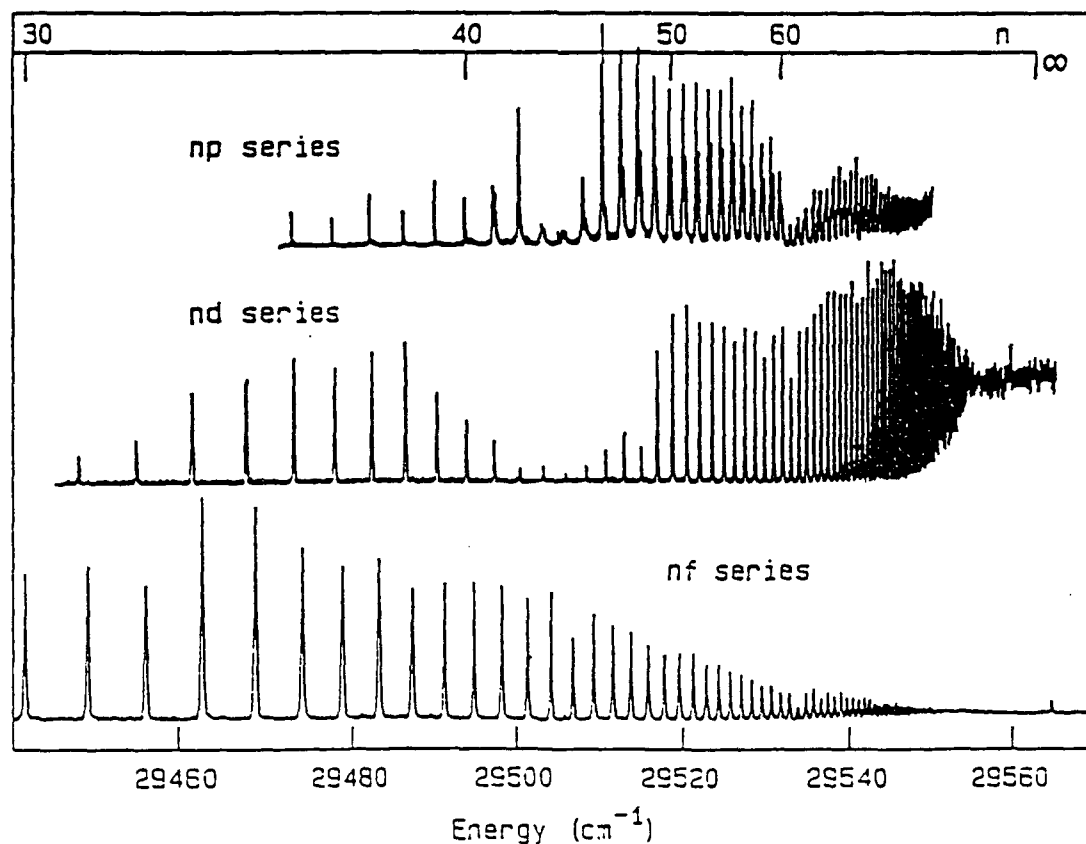

Figure 1. from top to bottom, np, nd, and nf Rydberg series of H₃ converging toward the lowest ortho-level (N+=1) of the ion.

46

np series : these series have been excited [6] using optical-optical double resonance via the $3s\ ^2A_1'$ (N=1, v_1=0, v_2=0) intermediate level. Bound states below the N^+=1 level of the ion detected by field-ionization as well as autoionizing states between the N^+=1 and N^+=3 levels of the ion have been characterized using a two-channel rotationnal quantum defect theory. MQDT allows us to analyse simply the mixing of the np $^2A_2''$ and np $^2E'$ series in Hund's case (b) that correspond to npN$^+$=1 and npN$^+$=3 series in Hund's case (d). Deviations from the calculation appear when vibrational interactions give rise to accidental predissociation below threshold or autoionizing interlopers above threshold. As opposed to the other Rydberg series of H_3 which show almost now electron-core interactions, the np series of H_3 provide a complete panorama of channel interactions in a simple polyatomic molecule: rotationnal and vibrationnal interactions and autoionizations with rich Fano-profiles structure above threshold as well as indirect predissociation induced by high v - low n interlopers.

nd series : very simple nd series converging toward the N^+=1 level of the H_3^+ ion has been observed [7] for n values ranging from n=25 to n=125. A precise value of the ionization potential of H_3 has been extrapolated from this series: 29562.58 cm^{-1} above the metastable level. The nd series is almost free of core interactions (very small quantum defect of 0.02) and it has a quasi atomic aspect except the very strong intensity window observed in the region n=40 to 48 (Fig. 1) and related to predissociation induced by a highly vibrationnaly excited interloper.

nf series : from the initial B state, two 3d levels are accessible by one photon ation. The 3d $^2E''$ and the 3d $^2A_1'$ states (N=1) which are used as initial levels to excite the nf series. The observed spectra [8] show that: (i) the nf series is even less perturbed than the nd series by electron-core interactions (quantum defect $\approx$ 0.01 and almost no observed predissociation) (ii) the 3d $^2E''$ and the 3d $^2A_1'$ states are in fact almost pure case (d) states and the notation 3dN$^+$=1 and 3dN$^+$=3 respectively should be preferred instead. This is emphasized by the nf spectrum of figure 1 recorded with the intermediate state " 3d $^2E''$ " where only N$^+$=1 states are seen

4 - Electric field effects :

At moderate field strength, predissociation affects selected p and d Rydberg states of high n values. Predissociation causes a decrease in the observed intensities (no H_3^+ ions are produced), this is clearly visible for instance in the region around n=44 of the nd spectrum (Fig. 1). The field-induced predissociation is strikingly demonstrated in the nd series at n=61 (see Fig. 2): an electric field as low as 0.4 V/cm is responsible for the complete disappearance of the n=61 line, which, according to our experimental conditions, corresponds to a lifetime relative to predissociation of about 300 ns. We have shown [9] that a relatively weak coupling with a vibrationnaly excited state of low principal quantum number that exhibits significant coupling to the repulsive ground state may be responsible for this effect. Quantitative interpretation of the field-induced predissociation processes that are crucial for dissociative recombination of H_3^+ is presently under way. At higher field strength, partly resolved Stark spectra have been obtained in the intermediate and strong (n-mixing) field regime [10]. We have developed a perturbative model of the Stark effect of H_3 which takes into account the n-mixing and the coupling of the different angular momenta. This treatment represents the first complete calculation of the Stark effect in molecular
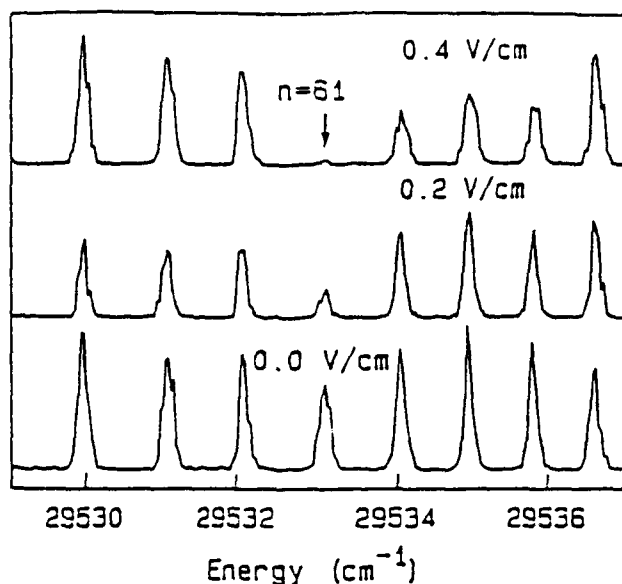
Fig 2 : nd Rydberg series in the vicinity of n = 61 for low field values.
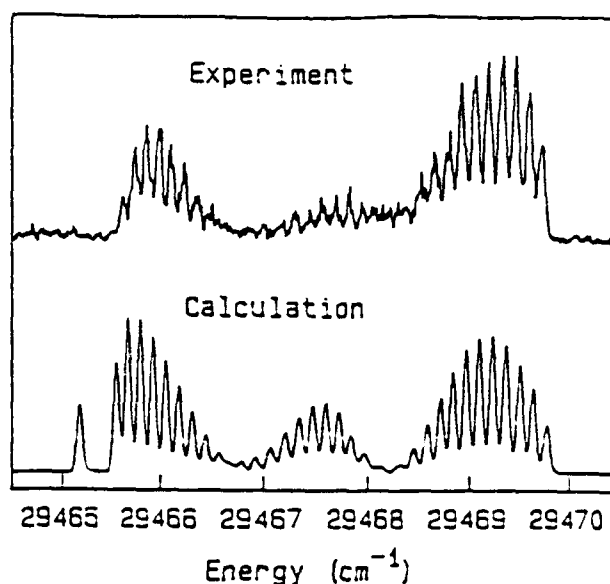
Fig. 3 : experimental and calculated Stark manifold for $n=34$, $M_N=0$ and $F=30$ V/cm.

Rydberg states. The good knowledge of all the quantum defects combined with the single $N^+=1$ level of the ionic core involved in the problem has allowed this very succesful treatment. Fig. 3 shows the excellent agreement between experiment and calculation for the $n=34$, $M_N=0$ manifold in a field $F=30$ V/cm. This perturbative model accounts very well for the observed spectra except for the intensity windows attributed to accidental predissociation.

Conclusion :

Though relatively recent, the study of the Rydberg series of H_3 is nowadays one of the most complete in the area of molecular Rydberg states. The very good agreement between ab-initio calculations and experimental results usually observed will probably allow in the future the complete understanding of the complex interactions leading to the numerous predissociations observed below the ionization threshold.

[1] / F. M. Devienne, C. R. Acad. Sci., Ser. B 267, 1279 (1968)

[2] / G. Herzberg, J. Chem. Phys. 70, 4806 (1979)

[3] / G. I. Gellene and R. F. Porter, J. Chem. Phys. 79, 5975 (1983)

[4] / C. Bordas, P. C. Cosby and H. Helm, J. Chem. Phys. 93, 6303 (1990)

[5] / H. F. King and K. Morokuma, J. Chem. Phys. 71, 3213 (1979)

[6] / C. Bordas, L. J. Lembo and H. Helm, Phys. Rev. A 44 (1991)

[7] / H. Helm, Phys. Rev. A 38, 3425 (1988)

[8] / L. J. Lembo, M. C. Bordas and H. Helm, Phys. Rev. A 42, 6660 (1990)

[9] / C. Bordas and H. Helm, Phys. Rev. A 43, 3645 (1991)

[10] / C. Bordas and H. Helm, submitted to Phys. Rev. A

Appendix D

STARK EFFECT IN TRIATOMIC HYDROGEN RYDBERG STATES

Stark effect in triatomic hydrogen Rydberg states

Christian Bordas[*] and Hanspeter Helm

Molecular Physics Laboratory, SRI International, 333 Ravenswood Avenue, Menlo Park, California 94025
(Received 25 June 1991)

The influence of an external electric field on the Rydberg states of triatomic hydrogen has been studied from the viewpoint of the structure of the spectra and the dynamics of the excited states. Rydberg states with principal quantum numbers ranging from 30 to 125 were observed, and low-field as well as very-strong-field regimes investigated. A perturbative treatment taking into account the coupling between the core rotation and the Rydberg-electron motion was developed. The good knowledge of the low-*l* Rydberg series in H_3 (*ns, np, nd,* and *nf*) allowed us to achieve this treatment without adjustable parameters. The agreement between calculation and experimental results is excellent and reveals features resulting from predissociation of selected members of the Stark manifold. Accidental predissociations due to vibrationally excited interlopers are clearly distinguished from the systematic predissociation induced by the mixing with the *ns* Rydberg series. This is a complete perturbative treatment of the Stark effect in molecular Rydberg states.

PACS number(s): 33.80.Rv, 33.55.Be

I. INTRODUCTION

The influence of an external electric field on atomic and molecular spectra is one of the oldest problems of spectroscopy. The Stark effect was discovered in 1913, and the theory of its effect in atomic hydrogen was the first application of perturbation theory in quantum mechanics [1]. Nowadays, the hydrogenic Stark effect is a textbook application of quantum mechanics [2,3].

Despite this early interest in the Stark effect and its historical importance, the Stark effect in excited states of nonhydrogenic systems has long been rather poorly known owing to several experimental and theoretical difficulties. With the advent of tunable dye lasers in the 1970's, most of the experimental problems have been overcome and interest in this phenomenon has been renewed: Recent investigations of the Stark effect of Rydberg states in alkali metal [4–9] and, more recently, in alkaline-earth atoms [10,11] and rare-gas atoms [12–16] show that it is still a dynamic field of investigation.

The theoretical difficulties are more serious and are still a subject of development. The large number of theoretical papers concerned with the Stark effect during the past 15 years is a good indication of these difficulties. Most of the theoretical works are concerned with the purely hydrogenic Stark effect. For example, Silverstone has derived perturbative calculations to an arbitrarily high order [17], and Luc-Koenig and Bachelier [18] and Damburg and Kolosov [19] have developed exact quantum calculations, including ionization effects. Nonhydrogenic systems have been studied by perturbative methods [4,14] and, more recently, by a multichannel quantum-defect theory (MQDT) [20–25] that takes advantage of the hydrogenic properties of the Stark Hamiltonian.

The Schrödinger equation of a hydrogen atom in an electric field is separable in parabolic coordinates [2,3]. Although the equation is not analytically solvable, this particular symmetry is fundamental and leads to the existence of exact quantum numbers. However, exact quantum numbers cannot be defined in any nonhydrogenic system where the parabolic symmetry is broken.

An essential problem related to the treatment of the Stark effect is the following: As soon as an external electric field is present, the potential experienced by the outer electron decreases monotonically in the direction opposite to the field, with the consequence that the electronic motion is (strictly speaking) unbounded and leads to resonances of finite width. This causes divergence of the perturbation series. At sufficiently high fields, quasidiscrete structures disappear. Another problem, although less fundamental, is also very serious in the practical analysis of the Stark effect in nonhydrogenic systems: Calculation of the Stark spectra of any species requires, in principle, knowing all of the zero-field states (that is, all the quantum defects), and in a multielectron system, the electric field induces additional couplings between the Rydberg electron and ionic core that must be taken into account. This last factor is generally dramatic in a molecule where the electric field couples all the *l* and *J* values, and the perturbation basis becomes prohibitively large. Combined with the usually fragmented information about the various *l* series, this aspect often precludes a standard perturbative treatment of the molecular Stark effect. Extension of the MQDT [20–25] to include an electric field could, in principle, avoid or at least reduce these obstacles. However, the MQDT treatment of the Stark effect in simple molecules such as diatomic hydrogen [23] or sodium dimer [25] is presently not complete.

These difficulties together with the relative lack of information about molecular Rydberg series as compared with atoms explain why, almost 80 years after the discovery of the Stark effect, the molecular Stark effect is still an open field of investigation. The effects of an external electric field on highly excited molecules have mainly been studied from the point of view of the dynamics in-

volved. Glab and Hessler, for example, have studied field-induced predissoci ion [26] in H_2, and electric-field ionization has been analyzed in various molecules such as H_2 [26], Na_2 [27], and Li_2 [28]. Electric-field ionization of H_3 is planned to be discussed in a forthcoming paper [29] on the basis of the model described here. However, these studies did not include analysis of the Stark effect. With the exception of the fragmentary results of Seaver *et al.* [30] on NO and Cooper *et al.* [31] on H_2, the only comparable study performed so far on a molecular system was done on Na_2. Partly resolved Stark spectra of the Rydberg series of the sodium dimer have been recorded [32], and these spectra in the weak-field regime have been analyzed in the framework of MQDT [25]. However, the limited knowledge of the quantum defects in Na_2 allowed only a qualitative approach. In contrast, the limited character of electron-core interactions and detailed knowledge of the various quantum defects in triatomic hydrogen make a complete analysis of that molecule more easily feasible.

The Stark effect in the molecular Rydberg series is of general interest, but three specific aspects of its relationship to the Rydberg states of H_3 motivated this study.

First of all, if one wishes to investigate in detail the influence of an electric field on molecular Rydberg states, H_3 is one of the best choices because it provides a unique opportunity for studying a complex molecular system having many quasihydrogenic properties. An extensive description of the general aspects of the Rydberg states of H_3 (symmetries, classification, calculated energies, and oscillator strengths) is given by King and Morokuma [33]. Because of the small size of the ionic core (the equilibrium internuclear distance in the ground state of H_3^+ is 0.86 Å; in comparison, that of H_2^+ is 1.06 Å), penetration effects are weak and most of the quantum defects are small. For the same reasons, the core energies are extremely high even in the lowest rotational level and rarely is more than one core level involved in our spectra ($N^+=1$). The gap [34] between the first two ortho levels of H_3^+ ($N^+=1$ and 3, $K^+=0$) is 429.9 cm^{-1}, far larger than the separation between the Rydberg states considered here (less than 8 cm^{-1} for $n=30$). Thus electron-core interactions and couplings are weak compared to those of any other molecule. From this point of view, a comparison of the Rydberg spectra of diatomic [35] and triatomic hydrogen reveals stronger rovibrational interactions in H_2.

A second interesting aspect of the Stark effect in a molecule is the possible onset of chaos. A fairly large amount of work is now being performed with Rydberg atoms in electric or magnetic fields, or both, to understand the correspondence between the quantum mechanics of the atom (and a hypothetical quantum chaos) and classical chaotic motion. In molecular Rydberg states, classical chaos may occur even without an external field, as described by Lombardi *et al.* [36]. However, the presence of an external perturbation which introduces a coupling of adjustable strength may considerably enrich this possibility. Before studying "quantum chaos" in a molecule-plus-field system, it is crucial to understand

qualitatively the Stark effect in a relatively simple system such as H_3.

Finally, this work is the logical continuation of the general study of the Rydberg series of H_3 started a few years ago by Helm and co-workers. The np [37], nd [38,39], and nf [40] series of H_3 as well as other aspects [41] of the dynamics of this fundamental molecule have been investigated recently in our group or elsewhere [42,43]. The nd series, the most extensively studied, has been investigated by one-photon excitation from the metastable $\tilde{B}(2p)^2 A_2''$ state in a fast neutral beam. While the energy levels of this series are well described by the simple Rydberg formula, the line intensities are strongly perturbed. Very intriguing window features appear in the photoionization spectrum. In a previous paper [44], the presence of interlopers belonging to vibrationally excited series that are coupled to the dissociative ground state has been invoked to explain this phenomenon. To understand the extreme sensitivity of some of these windows to the external field and the appearance of similar features in the np Rydberg series, we have systematically studied the evolution of the Rydberg spectrum as a function of the field strength. We can observe not only the Stark effect itself, but also the evolution of the interactions between the Rydberg states and dissociative interloper states.

In the next section, we present a short overview of the Stark effect in atomic hydrogen. From this simple model, we discuss the order of magnitude of the field effects and the difference between hydrogenic and nonhydrogenic Stark effects.

After a short description of our experimental techniques, we present low-resolution Stark spectra for principal quantum numbers ranging from 30 to about 125 and higher-resolution spectra for $n=34$. In both cases, there are strong differences according to whether the experiments were performed with the laser polarization parallel or perpendicular to the Stark field. These results are first analyzed with the help of the simple hydrogenic model. We then introduce a perturbative theory that takes into account all the interactions, but has the restriction that the H_3^+ core itself is not affected by the field. The agreement between experimental and theoretical spectra is satisfactory in view of the complexity of the molecular system and the fact that the model includes no adjustable parameters. Differences between predicted and observed spectra appear when the electric field induces decay channels that remove Rydberg population prior to their detection.

We finally compare the respective abilities of the perturbative model used in the present case and a more sophisticated multichannel quantum-defect theory presented elsewhere [20–25].

II. SUMMARY OF THE HYDROGENIC STARK EFFECT

The hydrogenic Stark effect and separation of the Schrödinger equation in parabolic coordinates is presented in quantum-mechanics textbooks [2,3] and described in detail in many papers [17–21]. This summary merely

reviews the basic results of the theory to indicate the order of magnitude of the field effects and to outline qualitatively the Stark effect in a nonhydrogenic system.

The nonrelativistic Coulomb-plus-Stark Hamiltonian of a hydrogen atom in an electric field F directed along the z axis is

$$H = -\frac{\hbar^2}{2m}\Delta - \frac{e^2}{r} + eFz .$$

(1)

The total wave function ψ, the solution of the Schrödinger equation for a particular energy E,

$$H\Psi = E\Psi ,$$

(2)

is exactly separable in parabolic coordinates,

$$\xi = r+z, \quad \eta = r-z, \quad \phi = \arctan(y/x) ,$$

(3)

and may be written as

$$\Psi(\xi,\eta,\phi) = \Xi(n_1,\xi)\Upsilon(n_2,\eta)e^{im\phi} ,$$

(4)

where the parabolic quantum numbers $\{n_1, n_2, m\}$, which are related to the principal quantum number n via the relation

$$n_1 + n_2 + |m| + 1 = n ,$$

(5)

replace the spherical quantum numbers $\{n, l, m\}$.

Note that in a nonhydrogenic atom, m is still a good quantum number, while n_1 and n_2 are not defined because the separability in parabolic coordinates does not hold. The principal quantum number n is strictly conserved in the nonrelativistic approximation in hydrogen, but it is a good quantum number in the other systems at only low-field strength.

At the first order of the perturbation theory, the energy of a (n_1, n_2, m) level is [2,3]

$$E(n_1, n_2, m) = -\frac{1}{2n^2} + \frac{3}{2}nF(n_1 - n_2)$$

(in atomic units [45]) ,   (6a)

$$E(n_1, n_2, m) = -\frac{\mathcal{R}}{n^2} + \alpha nF(n_1 - n_2)$$

(in customary units) ,   (6b)

where $\mathcal{R}$ is the Rydberg constant for hydrogen, F is the electric field, and the constant α is 0.640×10^{-4} V^{-1}.

At large values of η, the effective potential along the η axis is proportional to $-F\eta$ and no real bound states exist. However, below the classical saddle-point energy $(-2\sqrt{F})$, the states are quasidiscrete, while above this energy the states are field ionized and broaden rapidly as the field increases. In fact, in atomic hydrogen, the ionization threshold corresponds to the classical saddle-point energy only for $n_1 = 0$ and $m = 1$. The actual ionization threshold is strongly dependent on the value of the parabolic quantum number via the separation constant β [21] [$\beta \approx (2n_1 + m + 1)/2n$ at low field] and is approximately equal to $[(1-\beta)F]^{1/2}$ (see Ref. [29]). There are two direct consequences of Eq. (6) taken together with relation (5).

(i) For a given m value, a given n state is split into $(n - |m| - 1)$ sublevels (the sublevels being separated by $3nF$), which constitute a manifold having a width $\simeq 3n^2F$.

(ii) As the electric field increases, the successive manifolds overlap. This happens when the width of the n manifold ($3n^2F$) equals the energy separation between two Rydberg states (n^{-3}). The field strength F_c corresponding to this effect is called the Inglis-Teller limit. In atomic units [45],

$$F_c = \frac{1}{3n^5} .$$

(7)

For a given value of the principal quantum number, the Inglis-Teller limit defined by Eq. (7) determines the relative strength of the applied electric field.

In a nonhydrogenic system, a Rydberg electron with low angular momentum penetrates the core and the departure of the short-range interaction from a pure Coulomb potential is the source of the major part of the quantum defects and the reason that the symmetry of the effective potential is broken. The consequence is a coupling between the different n manifolds. As long as the n and $n\pm 1$ manifolds do not overlap, the intramanifold coupling (n mixing) is negligible and n is almost a good quantum number. However, as soon as the electric field is larger than F_c, the n mixing begins and the quantum number n loses its significance; this is called the strong-field regime, as opposed to the low-field regime where $F \ll F_c$. It is important to keep in mind the n^{-5} scaling law of Eq. (7) because F_c varies extremely strongly with n. The Inglis-Teller limit is on the order of 70 V/cm for $n = 30$, but only 0.17 V/cm for $n = 100$. Another consequence of the presence of the quantum defects (in other words, of the nondegeneracy of the various l states) is the quadratic Stark effect. If F is low enough, the Stark shift of the nondegenerate states (low-l values) is quadratic. States that have a nonzero quantum defect μ keep their zero-field l character as long as they are outside the hydrogenic manifold, which holds true approximately as long as F is smaller than μF_c. In this regime, nondegenerate states exhibit a quadratic Stark effect. Such behavior occurs for the ns and np series of H_3 (see Sec. V B, below). Then, as F increases, the Stark interaction becomes comparable to the core interaction responsible for the quantum defects and the Stark effect becomes linear. At this point begins the intermediate-field regime, where the behavior of most of the atoms is quasihydrogenic, while typically nonhydrogenic behavior is pronounced at low field.

The position of the classical saddle-point energy determines another important scaling factor. The significance of this point in atomic hydrogen is rather limited because the field-ionization rate [19] and the above-mentioned ionization threshold depend very strongly on $\{n_1, n_2\}$. However, the classical saddle-point energy determines a sharp limit between stable and field-ionized states in nonhydrogenic systems such as H_3 because n_1 and n_2 are no longer exact quantum numbers. This consequence of the breaking of parabolic symmetry is discussed in detail

in a related paper [29] we are preparing that describes the electric-field ionization of H_3. In atomic units, the value of the electric field F_s which corresponds to an effective quantum number n at the saddle point $E_s = -2\sqrt{F}$ is

$$F_s = \frac{1}{16n^4} . \tag{8}$$

Note that for any n value larger than 5, F_s is always larger than F_c, and that the ratio F_s/F_c is proportional to n. This means that the relative importance of the strong-field regime increases linearly with n.

We can summarize the four regimes of the Stark effect in a nonhydrogenic system as follows.

(i) Low-field regime: $F < \mu_{max} F_c$ (where μ_{max} is the largest quantum defect). Quadratic effect for the nondegenerate states; l is still a good quantum number if μ_l is large enough (note that in a molecule l is only an approximate quantum number).

(ii) Intermediate-field regime: $\mu_{max} F_c < F < F_c$. Linear effect; n is conserved but not l (l-mixing region).

(iii) Strong-field regime: $F_c < F < F_s$. Neither n nor l is conserved (n-mixing region), and only m_l is a good quantum number (in a molecule, m_l has no meaning; only M_N, the projection of the total angular momentum N onto the field axis, is conserved).

(iv) Field ionization: $F > F_s$. No stable states.

The influence of the ionic core is not limited to penetration effects. If the Stark interaction is comparable to the energy gap between different core levels, then the structure of the core may influence the Stark spectrum. The coupling scheme between the various angular momenta of the system also plays an important role. In H_3 the energy gap between the ionic levels is large compared to the magnitude of the Stark interaction in the present experiments, but the total angular momentum N of H_3 is not conserved and the coupling between the electronic angular momentum and core rotation is crucial.

Finally, the relative intensities of the transitions to the individual Stark components may also be estimated using the hydrogenic model. For a transition originating from the ground state ($1s$) of hydrogen, the intensity of a $\Delta m = 0$ transition is proportional to $(n_1 - n_2)^2$ and for $\Delta m = 1$ it is proportional to $(n_1 + 1)(n_2 + 1)$ (see the general formula in Sec. 65 of Ref. [2]). Thus, in the hydrogenic case, the intensity distribution is parabolic over the Stark manifold for $m = 0$ (peaks on the red and blue sides of the manifold, where, respectively, $n_1 = 0$ and $n_1 = n - |m| - 1$), while it peaks at the center of the manifold ($n_1 \sim n/2$) for $m = 1$. Intensities for transitions originating from the $2p$ state, for which no simple analytic formulas are available in the literature, are qualitatively similar except a small local maximum in the middle of the $\Delta m = 0$ manifold.

III. EXPERIMENTAL SETUP

The experimental fast-beam apparatus has been described in detail previously [38–41] and is shown schematically in Fig. 1. A fast neutral beam of H_3 molecules is generated by charge transfer of a 1.5-keV H_3^+
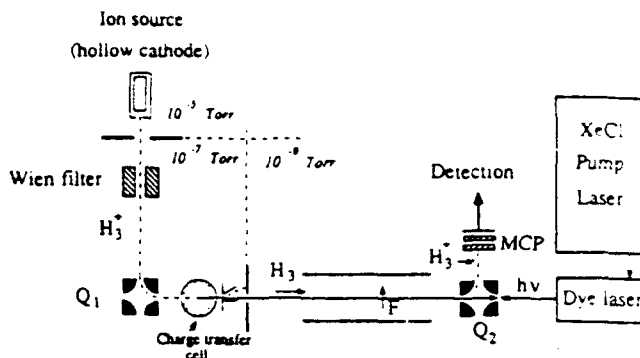

FIG. 1. Experimental setup. The H_3^+ ions produced in a hollow-cathode discharge are mass selected in a Wien filter, deflected in the electrostatic quadrupole Q_1, and then neutralized in the cesium charge-transfer cell. The resulting fast H_3 beam is collinearly excited by the pulsed laser beam. The neutral molecules that are excited but not ionized in the Stark field are field ionized in Q_2, and the H_3^+ ions are detected on a tandem microchannel plate (MCP) and counted during an appropriate time gate.

beam in cesium vapor. Residual ions are deflected by a small field at the exit of the charge-exchange cell. The charge-transfer process initially produces a wide spectrum of neutral states, but only the rotationless $N = 0$ levels (N being the total angular momentum of the molecule, excluding spin) of the $\tilde{B}(2p)^2 A_2''$ state are long lived [46], with a lifetime [47] on the order of 700 ns. In this paper, we are only concerned with molecules in the lowest vibrational level of this metastable state; these amount to more than 80% of the total number of neutral in the beam. These molecules are characterized by the quantum numbers $N = K = 0$, with symmetric nuclear wave function (ortho-H_3), while the ionic core is characterized by the quantum numbers $N^+ = 1$ and $K^+ = 0$.

The fast molecular beam is photoexcited coaxially by an excimer-pumped pulsed dye laser (dye PTP, 338–340 nm) in a region where a well-defined electric field is applied. An electrostatic potential is applied on two parallel metal plates 60 cm long, 5 cm wide, and 24.4 mm apart to produce the Stark field. Along the beam axis between the two plates and over a length of about 45 cm, the homogeneity of the electric field is better than 1%. About 30 cm downstream from the Stark plates, a high value of the electric field is applied in the quadrupole Q_2 (detection field). It ensures that all Rydberg states passing through it with a principal quantum number larger than 30 are field ionized. The resulting H_3^+ ions are energy and mass analyzed in the electrostatic quadrupole (H^+ or H_2^+ fragments are eliminated) and detected on a microchannel plate. The Stark and detection fields are both perpendicular to the propagation of the molecular beam. The neutral beam traverses the interaction region with a velocity of about 3×10^7 cm/s, while the laser-pulse duration is about 10 ns. This arrangement allows us to use the time of arrival of each ion on the detector, measured relative to the laser pulse, to record only the ions produced from a neutral H_3 molecule that was pho-

toexcited in the region where the Stark field is well defined.

A typical "zero-field" excitation spectrum is shown in Fig. 2. In the absence of an external field, owing to the strong p character of the initial state, the excited states are purely nd [38]. This nd series converges toward the first ionization limit [39], 29 562.58 cm^{-1} above the initial state. The ns series is not visible in our spectra because the hydrogenic value of the ratio between $2p \rightarrow ns$ transitions intensity and $2p \rightarrow nd$ transition intensities is almost $\frac{1}{40}$ (see Ref. [2]), and moreover, the ns states are suspected to be affected by rapid predissociation over the entire spectrum.

As described in the preceding section, the relative strength of a given electric field increases as n^5. A field as low as 0.2 V/cm may be considered a very high field for a Rydberg state with a principal quantum number $n = 100$. Moreover, as described in Ref. [44], the relative intensities of certain transitions (for example, toward $61d$) are strongly dependent on the field strength at the 0.1-V/cm scale. The question of the definition of the "zero field" is thus of particular importance. Great care was taken to avoid parasite electric fields or external magnetic fields, which, owing to the high velocity of the neutral beam, can generate an appreciable motional electric field. For example, the Earth's magnetic field (about 0.35 G) gives rise to a motional electric field of 0.1 V/cm in the

molecular frame. The orientation of the field plates allows us to compensate for this motional field, but other stray fields may still be present. The high-resolution spectrum of Fig. 2 (recorded with a laser equipped with an intracavity Fabry-Perot etalon), where Rydberg states around $n = 125$ are resolved, allows us to assume that the residual field is not larger than the Inglis-Teller limit corresponding to $n = 125$, that is, ~ 0.05 V/cm. The limited resolution of our spectrum (about 0.07 cm^{-1}) prevents a more refined estimate of the residual field.

IV. EXPERIMENTAL RESULTS

A. Low-resolution spectra

Owing to the field-ionization technique used for detecting the vibrationless Rydberg states, we are not able to monitor the excitation of states with n values lower than 30. The ionizing field is applied perpendicularly to the beam in an electrostatic quadrupole that is simultaneously used as an energy selector. Hence the exposure time to this field is determined by the velocity of the beam and the geometry of the quadrupole. According to our experimental design, the maximum field experienced by the molecules is about 1.8 kV/cm during a few nanoseconds after they enter the quadrupole through a 3-mm aperture. Under these conditions, field ionization is energetically possible for $n > 21$, but is efficient only for $n > 30$. On the other hand, the molecules excited in the Stark field F between the classical saddle-point energy $E_s = -2\sqrt{F}$ (a.u.) and the zero-field-ionization limit are rapidly ionized and hence deflected in the Stark field, and they are not detected on the microchannel plate. These two characteristics [29] cause the spectra to present a gradual onset on the low-n side around $n \approx 30$ and a sharp drop on the blue side of the saddle-point energy.

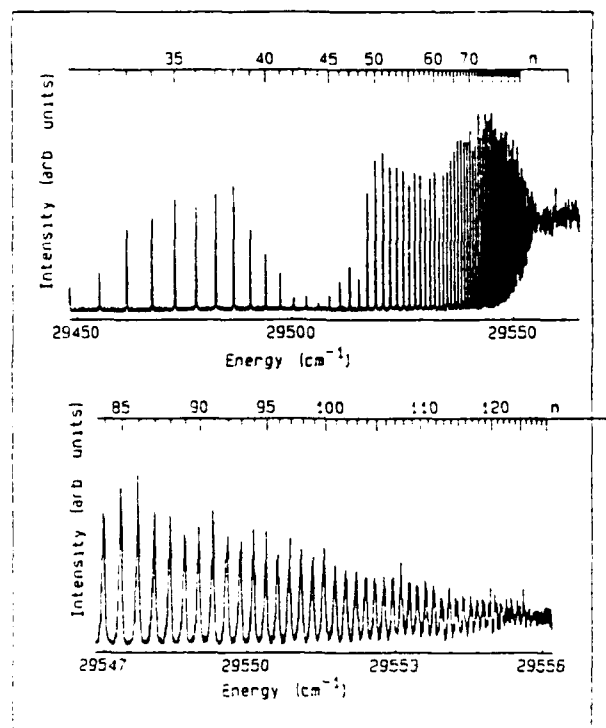Figures 3 and 4 show entire Stark spectra, from $n = 30$

FIG. 2. Zero-field nd-series spectrum. Entire spectrum at low resolution (0.2 cm^{-1}, top) and detail of the high-n region ($n = 84$ to ~ 125) at high resolution (0.07 cm^{-1}, bottom). Here and in all our spectra, the energy is measured from the metastable $\tilde{B}(2p)^2 A_1''$ ($N = 0$) state and n is the principal quantum number relative to the $N^+ = 1$ ($K^+ = 0$) ionization limit (29 562.58 cm^{-1}).
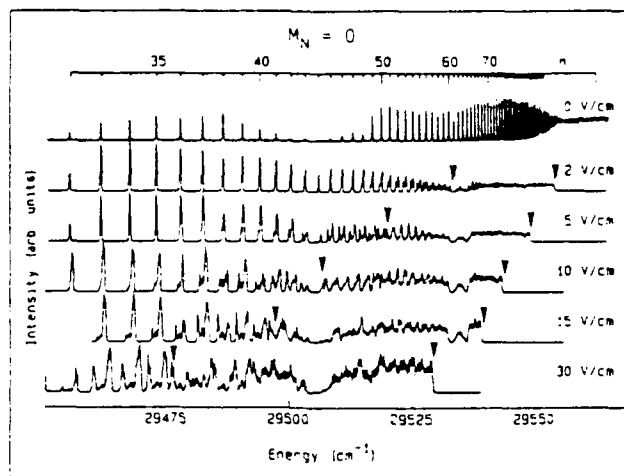

FIG. 3. Entire Stark spectra for $F = 0$, 2, 5, 10, 15, and 30 V/cm with $M_N = 0$. The arrows indicate the position of the classical saddle-point energy E_s and, at lower energy, the energy E_c (where $F = F_c$) above which n mixing occurs. The windows around $n = 40-48$ and at $n = 61$ are clearly visible. Note that the $n = 40-48$ window almost disappears at $F = 2$ V/cm.
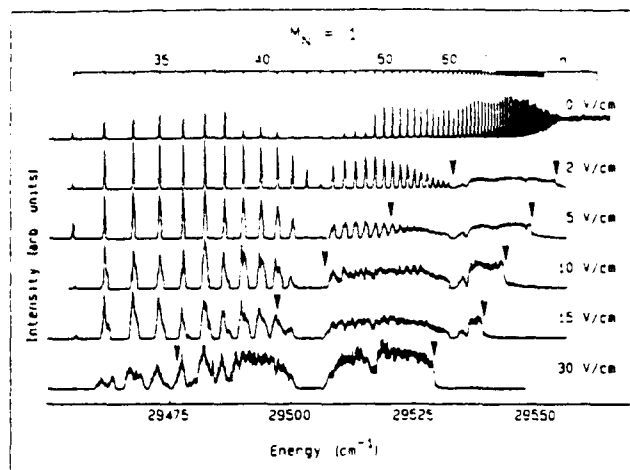
FIG. 4. Stark spectra same as in Fig. 3 except $M_N = 1$. Note the different behavior of the windows, especially the wider window around $n = 44$.

FIG. 5. Expanded view of the $F = 5$ V/cm spectra from $n = 41$ to 60 with $M_N = 0$ (top) and $M_N = 1$ (bottom), showing the characteristic shape of the manifold; the minimum is in the center for $M_N = 0$, and the maximum is in the center for $M_N = 1$. The $n = 43$ hydrogenic manifolds for a transition starting from an s initial state are represented in black: top, $m_l = 0$; bottom, $m_l = 1$.

to the continuum, with, respectively, the laser polarization parallel and perpendicular to the Stark field. The metastable level of the $\tilde{B}(2p)^2 A_2''$ state is characterized by $M_N = N = 0$. As usual, the field axis is chosen as the quantization axis. If the laser polarization is directed along the field axis, the projection of the total angular momentum remains unchanged and $M_N = 0$ in the excited states. Similarly, if the laser polarization is perpendicular to the Stark field, only $M_N = \pm 1$ states are excited. Figure 5 shows enlargements of a typical portion of both spectra recorded with a field $F = 5$ V/cm, revealing the different aspects of the $M_N = 0$ and ± 1 spectra.

The spectra in Figs. 3–5 are recorded at a resolution of about 0.2 cm^{-1}. For a typical low-n value (~ 30) and a field of 30 V/cm, the interval between two adjacent hydrogenic levels (Stark splitting $= 3nF$) is on the order of 0.1 cm^{-1}. The field strength at which n mixing begins for $n = 30$ is about 70 V/cm. With a resolution of 0.2 cm^{-1}, we could partly resolve the spectra only in the most favorable case of a field $F \approx F_c$ and for the lowest n values. Practically, this limited resolution allows only observation of the envelope of the Stark manifolds. However, much information can be drawn from these unresolved spectra. The position of the saddle-point energy with respect to the zero-field-ionization limit [$E_s = -2\sqrt{F}$ (a.u.) ($-6.11\sqrt{F}$ in cm^{-1}, with F in V/cm)] as well as the position of the critical energy E_c at which the Stark field equals the Inglis-Teller limit F_c [given by Eq. (7)] are indicated in each case. The sharp drop in the spectra at E_s clearly indicates that almost all of the molecules excited above this energy are field ionized during passage through the Stark field. Regarding the critical energy E_c, it is also clear that below E_c each manifold can be distinguished from its neighbor (n is meaningful in this region), while they are merged above E_c (n mixing). As discussed previously, this observation is closely connected to the total width of the Stark manifold, which is measured to have roughly the hydrogenic value ($3n^2F$) at low- and intermediate-field strengths.
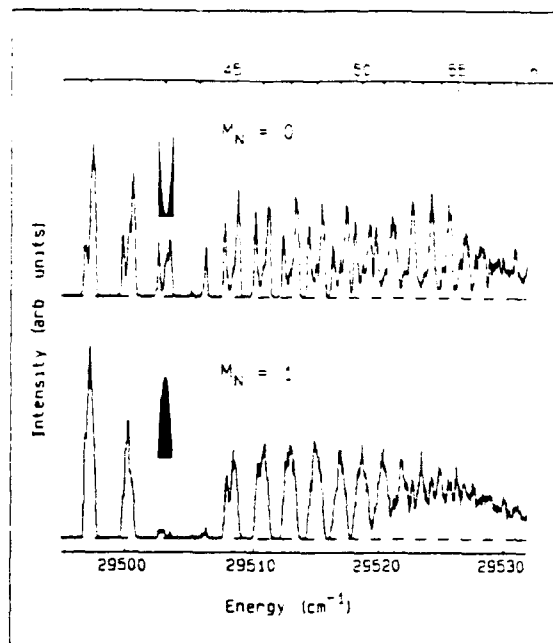
This last observation, although not surprising, is of some interest, however: It means that no large quantum defect exists which precludes the mixing of all l components in the low-field regime. Even at moderate field, the Stark effect of H_3 is almost hydrogenic. This characteristic is completely different from the case of Na$_2$, where large quantum defects were responsible for a smaller observed width of the Stark manifold at moderate field [25,32] and a more pronounced nonhydrogenic behavior.

The shape of each manifold, i.e., the distribution of the transition strength as a function of (n_1, n_2), is of particular interest. Note that, although the quantum numbers n_1 and n_2 are not strictly defined in H_3, one can assign such numbers to the various Stark sublevels by correlation with the hydrogenic model. From this point of view, the two spectra in Fig. 5 represent a good example of the intensity variation among members of each n manifold. In the case where $M_N = 0$, each manifold presents a maximum intensity on each side, the blue side (high-n_1 values) being more prominent than the red side (low-n_1 values), and a minimum in the middle. In the other case, $M_N = \pm 1$, the intensity is greatest in the center and vanishes at the outer wings. The expected shape of the hydrogenic manifold in the case of a $1s \rightarrow (n_1, n_2, m_l = 0$ or 1) transition is also represented in Fig. 5 at the position of $n = 43$. The similarity between the observed intensity distribution and hydrogenic pattern is striking.

The most important departure from the atomic Stark effect, and the most obviously molecular aspect of our spectra, is observed in the region $n = 40$–48 and near

$n = 61$, where intensity windows (i.e., regions of the spectra where the ion signal is notably lower than expected) appear. The window formation is strongly field dependent. No trivial channel interactions such as coupling with the rotationally excited series may be invoked to explain any of these windows. This point will be discussed in more detail in Sec. IV C.

B. Partly resolved spectra

We now look for finer details in the H_3 Stark spectra in a region where no obvious perturbations affect the observed intensities. For this purpose, we chose to record high-resolution spectra, using an intracavity Fabry-Pérot étalon to reduce the laser bandwidth to about 0.07 cm^{-1}, in a region where this resolution is finer than the $3nF$ Stark splitting. Such spectra recorded in the vicinity of $n = 34$ with $M_N = 0$ and $=1$ are presented in Figs. 6 and 7, respectively. The Stark field is scanned from 0 to 50 V/cm in increments of 10 V/cm. The Inglis-Teller limit at $n = 34$ is about 38 V/cm. Accordingly, the spectra at $F = 40$ V/cm show the onset of n mixing: The $n = 34$ and 35 manifolds merge, while $n = 33$ and 34 are still separated. Below this critical value, the $n = 34$ complex is isolated, its simple structure being dominated by the $3nF$ splitting for all field values larger than 20 V/cm, at which value the hydrogenic splitting is resolved. Actually, we will show in Sec. V that, because of the coupling of the electronic angular momentum with the core rotation, each observed line should contain three components. This substructure is not resolved here.
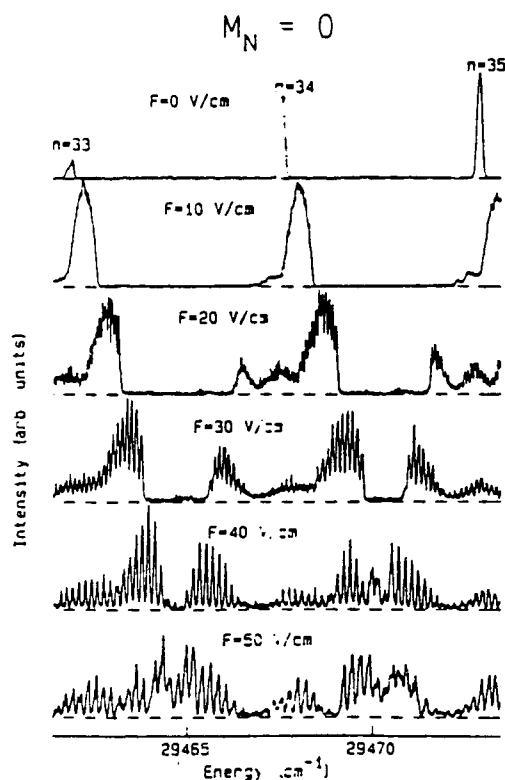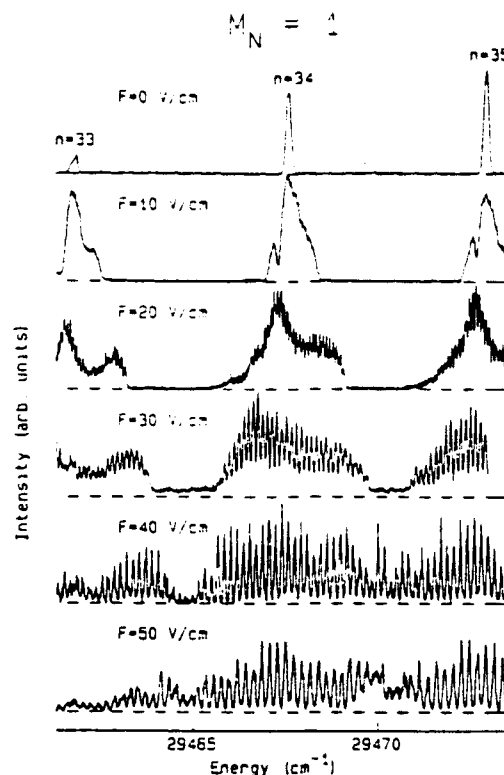

FIG. 7. Stark spectra same as in Fig. 6 except $M_N = 1$.

As far as the relative intensities of each individual transition are concerned, the comments made previously apply, with some minor additions. The intensity of the $M_N = 0$ states is still maximal at either side of the manifold, although we note that the intensity does not peak at the extreme components. A weak local maximum near the center of the manifold (i.e., near the zero-field energy) is clearly visible in the spectra for $F = 20$ and 30 V/cm, in accordance with the expected $2p \rightarrow$ high Rydberg intensities in atomic hydrogen. The transitions to the blue states ($n_1 > n_2$) are noticeably more intense than those to the red states. This difference is particularly pronounced for $F = 10$ V/cm, where the red side is almost entirely missing. When the Stark field is larger than the Inglis-Teller limit (40- and 50-V/cm spectra), this aspect persists except that adjacent manifolds overlap. Similar comments apply to the case where $M_N = \pm 1$, except that here the intensity peaks near the center of each manifold. Note that the low-field spectrum (10 V/cm) shows an aberration on the red side of the multiplet in the form of a small hole in the unresolved contour. This extremely localized window has been observed for every manifold in the case of $M_N = \pm 1$, and it will be qualitatively explained in the following section.

The relative simplicity and regularity of the spectra displayed in Figs. 3-7 is reminiscent of the Stark spectra of alkali-metal atoms rather than the Stark spectra of alkali-metal molecules [32] such as Na_2 in the sense that rotational structure is absent. The small values of the quantum defects are also responsible for this simplicity. A peculiarity of the H_3 spectra is, however, the appearance of intensity windows, which we discuss below.

FIG. 6. Stark spectra for $n = 33-35$, $M_N = 0$, at $F = 0$, 10, 20, 30, 40, and 50 V/cm at high resolution (about 0.07 cm^{-1}).

C. Windows

The frequent occurrence of window resonances in the bound-state region is probably the most unique aspect of the Rydberg series in triatomic hydrogen. This phenomenon is pronounced in the zero-field spectrum of the nd series, as displayed in Fig. 2. The intensities of the transitions in the region from $40d$ to $48d$ is low compared to the neighboring transitions. Transitions toward $n = 42$, 43, and 44 are almost absent from the spectrum. In fact, the observed intensities of all transitions below $n = 80$ are lower than expected from the $1/n^3$ law, which is obeyed for the high-n members ($n \geq 80$). The window in the region from $n = 40$ to 48 is about 25 cm^{-1} wide. At zero-field, this giant window is the most prominent irregularity in the nd series in our spectrum, although Ketterle and co-workers [42] observed another giant window in the nd series, spanning from $n = 12$ to 24. A smaller window [44] is observed in the vicinity of $n = 61$, but we attribute its presence in the zero-field spectrum to the stray field, which has been estimated at about 0.05 V/cm. Other windows are also visible near $n = 32$, 64, 86, 128,... . We have carried out double-resonance depletion experiments, such as described in Ref. [44], in order to measure the absolute absorption intensity of the transitions to ns and nd states from $n = 9$ to 80. These experiments have shown that no local minimum exists in the excitation probability which obeys the $1/n^3$ law. The lack of field-ionizable H_3 molecules at the window positions is therefore only attributable to a dissociative or radiative loss. The time of flight of a H_3 molecule between the optical excitation in the Stark-field region and the field ionization in the detection quadrupole is about 1–2.5 μs. Therefore, if a molecule is excited in a Rydberg state which does not survive this time of flight (either because of predissociation or radiative decay), no H_3^+ signal is detected.

In a previous study [44], we have shown that the $n = 61$ window is due to a localized predissociation induced by a vibrational interloper state, the electric field being responsible for mediating the coupling path. Observations of a similar nature have been reported in H_2 where field-induced predissociation is known as being a dominant decay mechanism for many Rydberg states below the ionization threshold [26]. The Rydberg spectra in the vicinity of $n = 61$ at low field (0–0.4 V/cm) are displayed in Fig. 8. The intensity of the transition toward $n = 61$ is drastically lowered by extremely low fields. The coupling of the $n = 61$ state with the dissociative interloper occurs via the np series (the window is observed at zero field in the np spectrum [37,44]). It is induced by the Stark field through the l mixing. The interloper identified to induce this window is an npE' ($N = 0$) state of high vibrational excitation.

The evolution of the broad window near $n = 44$ as the field is increased is different from the one at $n = 61$ (see Figs. 3 and 4). The window is widely open at zero field, but progressively closes up as the Stark field grows. At $F = 2$ V/cm, the window has almost disappeared from the $M_N = 0$ spectrum and is limited to the vicinity of $n = 44$ in the $M_N = 1$ spectrum. At higher-field strengths,
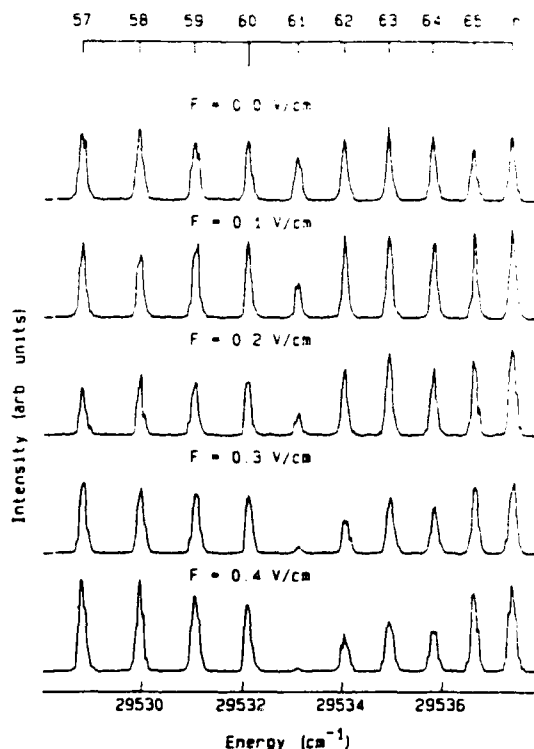

FIG. 8. Low-field (0–0.4 V/cm) nd Rydberg spectra around $n = 61$, with $M_N = 0$ (the appearance of the $M_N = 1$ spectra is similar). The disappearance of the $n = 61$ line at $F \approx 0.4$ V/cm is caused by field-induced predissociation (see Ref. [44]).

the window reappears and its shape is stable, but still depends on the value of M_N. The high-field limit of the total width of the giant window is about 5 cm^{-1} for $M_N = 0$ and 8 cm^{-1} for $M_N = \pm 1$.

We propose the following qualitative explanation for this behavior: In the region $n = 40$–48, the nd states are coupled to a dissociative interloper, likely a high vibrational level of a low-n Rydberg state in energy near the vibrationless $n = 44$ states. Interaction with this interloper at zero field causes accidental predissociation of the neighboring nd series members, with a typical lifetime on the order of 1 μs. The coupling required to produce this effect can in fact be exceedingly small. For example, if the lifetime of the interloper state is on the order of 1 ps (corresponding to a width of 5 cm^{-1}), then a contribution by the interloper of only 10^{-6} in the Rydberg wave function is sufficient to induce predissociation on the observed time scale. The coupling has to be weak, because no shift of the nd states is observable in the window region. The coupling is almost certainly homogeneous ($\Delta N = 0$), and a likely candidate among low excited states of H_3 is the $2s\,^2A_1'$ state, which, for low vibration, has a width of 30 cm^{-1} (lifetime $\tau = 170$ fs) [48]. The coupling may, even at zero field, be due to a weak degree of s-d mixing induced by the quadrupole moment of the core ion.

In this picture, the coupling between the Rydberg states and interloper state in the window region is controlled by the magnitude of d character in each sublevel. This magnitude decreases as the Stark field increases (at least in the sublevels corresponding to the strongest tran-

sitions), thus reducing the coupling strength and width of the window. We will return to this discussion later in this paper after introducing the appropriate Stark map.

The electric field is also responsible for the appearance of other windows around $n = 32, 64, 86, 128, \ldots$. Complete discussion and quantitative interpretation of the processes leading to these windows are beyond the scope of this paper and will require a better knowledge of the low-n Rydberg states with high vibrational excitation. In particular, the nature of the dissociative interlopers and of the coupling itself have yet to be investigated.

Nevertheless, the observation of predissociation near the ionization threshold of H_3 may be of great importance for dissociative recombination of H_3^- with low-energy electrons [49–51] where the stability of highly excited states with respect to dissociative channels is crucial.

V. PERTURBATIVE TREATMENT OF THE MOLECULAR STARK EFFECT

A. Model

The total Hamiltonian of the triatomic hydrogen molecule in a uniform electric field F directed along the z axis is

$$H = H_0 - eFz , \tag{9}$$

where H_0 is the zero-field total Hamiltonian.

Since the total Hamiltonian of a hydrogen atom in an electric field is separable in parabolic coordinates, the energy matrix of a system having small quantum defects (such as H_3) is almost diagonal in the parabolic basis $\{n_1, n_2, m\}$. However, because of the small non-Coulombic terms in the Hamiltonian H_0 and the presence of the core angular momentum, it is not convenient to derive the expressions for the diagonal and small off-diagonal terms of the energy matrix in the parabolic basis. The formal derivation of these matrix elements is straightforward in the usual spherical basis $\{n, l, m\}$, which has been systematically used in similar calculations in atomic physics [4,14,16]. The ease of calculating the matrix elements compensates for the lack of the symmetry of the hydrogenic Stark effect and the separability in parabolic coordinates.

In the spherical basis that diagonalizes H_0, the diagonal elements of the energy matrix are obviously the eigenvalues of the Hamiltonian H_0 (zero-field energies), while the off-diagonal terms contain only the contribution of eFz. A simplification arises from the fact that, in H_3 and zero field, all the high Rydberg states except the np series are well described using a pure Hund's case d basis. That is, the rotational quantum number of the ionic core (N^+) is a good quantum number. Of course, N^+ is not affected by the optical (electronic) excitation and has the same value as in the initial $\bar{B}(2p)^2 A_2''$ state: $N^+ = 1 (K^+ = 0)$. The l uncoupling in the np [37], nd [38,39], and nf [40] series has already been studied in detail. The mixing in N^+ introduced by the l uncoupling is completely negligible for $l \geq 2$ where all quantum defects are smaller than 0.02, and it is not relevant to the case where $l = 0$. In ad-

dition, the separation ΔE_{rot} between the $N^- = 1 (K^- = 0)$ and $N^- = 3 (K^- = 0)$ levels (because of proton-spin statistics, there is no even N^- level with $K^- = 0$) is far larger than the highest Stark matrix element corresponding to our experimental conditions. In atomic units, the magnitude of this matrix element is $3n^2 F$, while the maximum field to be considered is the ionizing field $F_i = 1/16n^4$, above which no stable states are observed. That is, the maximum matrix element is $3/16n^2 \leq 45$ cm^{-1} for $n > 30$. Even in the worst case, this term is one order of magnitude smaller than $\Delta E_{rot} = 429.9$ cm^{-1}. The effect of the Stark field on the electronic orbitals of H_3^- is therefore negligible at the fields considered here. These considerations allow us to set $N^- = 1 (K^- = 0)$ in our perturbation basis.

However, the l uncoupling in the np series is not negligible and is responsible for appreciable mixing of the $np(N = 2, N^- = 1)$ series with the core-excited $np(N = 2, N^- = 3)$ Rydberg series. The rotational mixing is particularly strong in the vicinity of the $n = 15$ member of the $N^+ = 3$ series, which quite coincidentally lies in the region of the giant window resonance $n \approx 40–48$. Since this mixing is limited to the $np(N = 2)$ series and the $n = 15(N^+ = 3)$ state is almost unaffected by the fields considered here $(3n^2 F \approx 1.4$ cm^{-1} at $F = 50$ V/cm for $n = 15$, compared with a 14–15 splitting of about 70 cm^{-1}), we introduce N^+ mixing in the energy matrix phenomenologically and neglect the marginal contribution of the $N^+ = 3$ component in the off-diagonal elements. The energy and amplitude of the $N^- = 1$ component of the wave function are both calculated using a two-channel quantum-defect theory described in Ref. [37]. The $N = 0$ and 1 np series are not perturbed by any rotational interaction and are purely $N^+ = 1$.

Because the electric field breaks the spherical symmetry, all the l values $(l \leq n - 1)$, and consequently all the N values, must be included in the perturbation basis, with the restriction

$$N^+ + l = N . \tag{10}$$

Owing to the unique value of $N^+ = 1$, the perturbation basis is limited to the values $N = l$ or $l \pm 1$ if $l \neq 0$ and $N = 1$ if $l = 0$.

The diagonal elements of the energy matrix are calculated with the Rydberg formula using the quantum defects μ_l (see Tables I and II). For $l \neq 1$,

$$H_0^{nl} = E_{ion} - \frac{\mathcal{R}}{(n - \mu_l)^2} , \tag{11a}$$

and for $l = 1$,

$$H_0^{np\sigma_2''} = E_{ion} - \frac{\mathcal{R}}{(n - \mu_{p\sigma_2''})^2} \quad (N = 0) , \tag{11b}$$

$$H_0^{np e'} = E_{ion} - \frac{\mathcal{R}}{(n - \mu_{pe'})^2} \quad (N = 1) , \tag{11c}$$

and $H_0^{n^*(N = 2)}$ is calculated using a two-channel quantum-defect theory [37]. E_{ion} is the first ionization limit [39] of H_3 $(N^+ = 1, K^+ = 0$ vibrationless level of the

CHRISTIAN BORDAS AND HANSPETER HELM

TABLE I. Effective quantum defects of the low-ns A'_1 states.

| | Effective quantum defect | | | | |
	a	b	c	d	e
2s a'_1	0.0836	0.08	0.08		
3s a'_1	0.0706	0.07	0.07	0.080	
4s a'_1	0.0663	0.05	0.05		
High n's					0.075

[a]King and Morokuma [33].
[b]Jungen [52].
[c]Martin [53].
[d]Lembo, Helm, and Huestis [41].
[e]Ketterle and co-workers [42].

ground state of the H_3^+ ion) and equals $29\,562.58$ cm^{-1} when measured from the initial metastable state. $\mathcal{R}$ is the Rydberg constant for H_3 and equals $109\,717.40$ cm^{-1}. The values of the quantum defects used in our calculation are reported in Tables I and II. Table I lists calculated [33,52,53] and measured [41,42] values of the ns-series quantum defects of low Rydberg states. High Rydberg states of the ns series ($n > 30$) are not known and are not visible in our spectra, partly because of the low intensity of the $2p \rightarrow ns$ transition as compared to $2p \rightarrow nd$ (hydrogenic value of the intensity ratio $\approx \frac{1}{40}$) and partly because of the strong predissociation that is suspected to affect this series [42].

The np-, nd-, and nf-series quantum defects have been measured [37–40] in our group for $n > 30$ and are reported in Table II. Comparisons with low-n calculated effective quantum defects show a remarkable agreement between experiment and theory. Such an agreement must be emphasized because it is not very frequent in molecular physics and it is encouraging for further use of results of ab $initio$ calculations. Finally, the quantum defects of the high-l series are assumed to be zero ($\mu_{l>3}=0$).

By using the Wigner-Eckart theorem and the general expression for the reduced matrix element of the product of two operators [54], the off-diagonal matrix elements of the total Hamiltonian may be expressed in the spherical basis as

$$H^{n'l',N'M_{N'}N^{+'}}_{nl,NM_N N^+} = -eF\langle nl,NM_N N^+|z|n'l',N'M_{N'}N^{+'}\rangle$$

$$= -eF(-1)^{N-M_N+l+N^++N'}\begin{bmatrix} N & 1 & N' \\ -M_N & 0 & M_N \end{bmatrix}\begin{Bmatrix} l & N & N^+ \\ N' & l' & 1 \end{Bmatrix}\sqrt{(2N+1)(2N'+1)}$$

$$\times \sqrt{l_{max}}R^{n'l'}_{nl}\delta(N^+,N^{+'})\delta(M_N,M_{N'})\delta(l',l\pm1) ,$$ (12)

where l_{max} is the larger of l and l'.

The selection rules for the matrix element (12) are $l'=l-1$ or $l+1$, $M_{N'}=M_N$, $N'=N$ or $N\pm1$, $N^{+'}=N^+=1$, and $K^{+'}=K^+=0$ (the last two selection rules are a consequence of the negligible effect of the Stark field on the core ion).

The radial integral $R^{n'l'}_{nl}$ is

$$R^{n'l'}_{nl} = \int_0^\infty R_{n'l'}(r)rR_{nl}(r)r^2dr ,$$ (13)

where $R_{nl}(r)$ represents the hydrogenic radial function and where n can take noninteger values. The generalized Coulombic integral is calculated with the help of the numerical method proposed by Edmonds et $al.$ [55]. In this integral, the principal quantum number is replaced by the effective zero-field quantum number $n^*=n-\mu_l$. The magnitude of the radial integral oscillates and decreases rapidly as $n^*-n'^*$ increases. No strict selection rule or simple approximate formula for $R^{n'l'}_{nl}$ exists when the difference $n^*-n'^*$ is not an integer and numerical evaluation of Eq. (12) is required. This term is directly respon-

TABLE II. Calculated and measured quantum defects of the np, nd, and nf Rydberg series of H_3. The quantum defect of the nd series quoted in column d is the effective quantum defect of the nd $N^+=1$ series (same comment applies to the nf series), which is an admixture of a'_1 and e' symmetries. Considering the uncertainties in the experimental values of the quantum defects (≈ 0.02), the agreement between calculated and experimental values is excellent.

| | Quantum defects | | | |
Orbital symmetry	a	b	c	d
np e'	0.3380	0.35	0.34	0.39
np a''_2	0.0244	0.02	0.00	0.05
nd e'	0.0236	0.02	0.02	
nd e''	−0.0047	−0.04	−0.01	0.019
nd a'_1	−0.0134	−0.02	−0.02	
nf				0.012

[a]King and Morokuma [33].
[b]Jungen [52].
[c]Martin [53].
[d]Our results: np series [37], nd series [38,39], and nf series [40].

sible for the coupling between the different n manifolds. This fundamental difference from atomic hydrogen is especially sensible when the energy gap between levels arising from different n manifolds is small, as, for example, in the n-mixing region, where one has to include several n values in the perturbation basis. Comparing Eqs. (12) and (13) with similar formulas for the case of atomic helium [14] shows the striking similarity between the molecular and atomic coupling schemes. The expression of the off-diagonal Stark matrix element in atomic helium is similar to the one given by Eq. (12) if one replaces the core-electron, Rydberg-electron, and total electronic angular momenta in helium (l_1, l_2, and L) with the core angular momentum N^-, the Rydberg-electron angular momentum l, and the total angular momentum (excluding spin) N of H_3, respectively.

To compare our calculation with our experimental results, it is necessary to calculate the intensity of excitation—or absorption intensity—of the Stark state from the initial low-lying metastable state. The oscillator strength for a transition from the initial state $|\bar{B}(2p), N=0\rangle$ to a Stark state $|E, M_N\rangle$ is

$$f_{B,E} = \left| \sum_{E', l', N'} C^E_{E'l'N'M_N}(F) \right.$$

$$\left. \times \langle \bar{B}2p, N=0 | \varepsilon r | E'l'N'M_N \rangle \right|^2, \quad (14)$$

where the term $C^E_{E'l'N'M_N}(F)$ represents the components of the $|E, M_N\rangle$ state in the perturbation basis. The matrix element involved in Eq. (14) is easily separated into an angular and a radial part. Obviously, the sum over l' is limited to $l'=0$ or 2, the former being almost negligible compared to the latter. The angular part is trivial. Starting from an initial state with $N=0$, only $N=1$ terms have a nonzero contribution. The radial part is more delicate to estimate. The Coulombic approximation, even generalized to noninteger values, is not well suited for accurate calculation of matrix elements involving a low-lying state, especially in the case of a molecular core, because the integral is sensitive to the small-r part of the wave function. However, it can give accurate relative values for the various Rydberg states [4].

The number of terms in a given n manifold of our perturbation basis is $3n-2$ when $M_N=0$ or $3n-3$ when $M_N=1$ (there is no $N=0$ state in that case). Combining these terms with the large-n values of the observed Rydberg states leads rapidly to a large size for the matrix that has to be diagonalized. To avoid excessive size, we must truncate our perturbation basis to a limited range of n values. We chose to limit ourselves to field values not too much larger than the Inglis-Teller limit where n mixing begins. Without making a large error in calculating the n manifold (probably less than 0.1 cm^{-1}), we can rely on a calculation that includes the $n-1$, n, and $n+1$ terms to calculate the n manifold. The $n-1$ and $n+1$ levels are not necessarily correctly computed, and only the central manifold is correct. This is valid as long as the $n-2$ and $n+2$ manifolds are not too close to the n manifold, i.e., for field values not larger than about $1.5F_c$. With this re-

striction, the size of the Hamiltonian matrix is $9n_0-6$ for $M_N=0$ and $9n_0-9$ for $M_N=1$. A typical matrix dimension is about 350 for $n \sim 40$. Of course, there is no fundamental obstacle (other than the computer capabilities) to including more n components in the basis if a higher accuracy is needed or if the field strength greatly exceeds the Inglis-Teller limit.

Figure 9 shows an example of such a model calculation using the quantum defects listed in Tables I and II for the $n=10$ manifold and an electric field $F=8$ kV/cm (about one-half of F_c). We chose this low-n value for clarity, because then the number of Stark states is small. We recognize the splitting of the $n=10$ manifold into groups of lines. The hydrogenic levels which are separated by $3nF$ are indicated at the top of each model spectrum, and it is possible to establish a correlation between these hydrogenic levels and each group of lines of the H_3 calculated Stark manifold. Each group corresponds to a particular value of the parabolic quantum numbers (n_1, n_2) in the hydrogenic limit and is composed of three transitions corresponding to three different dominant values of the total angular momentum N. Only the $N=1$ amplitude contributes to the intensity of the transition, and generally only one of these three sublevels bears the dominant oscillator strength.

Several differences between the $M_N=0$ and 1 spectra are visible in this model calculation. First, as stated before, the line intensity is maximal for $n_1 \approx 0$ or n when $M_N=0$, while the $n_1 \approx n/2$ lines are the most intense when $M_N=1$. Second, the shift with respect to the hydrogenic position is important, especially at the field strength used in Fig. 9, where one sublevel (np, $N=1$) is still outside the hydrogenic multiplet. Finally, the splitting between individual lines within each group of lines labeled as having the same value of n_1 is strongly dependent on n_1 and M_N, and it evolves irregularly with the
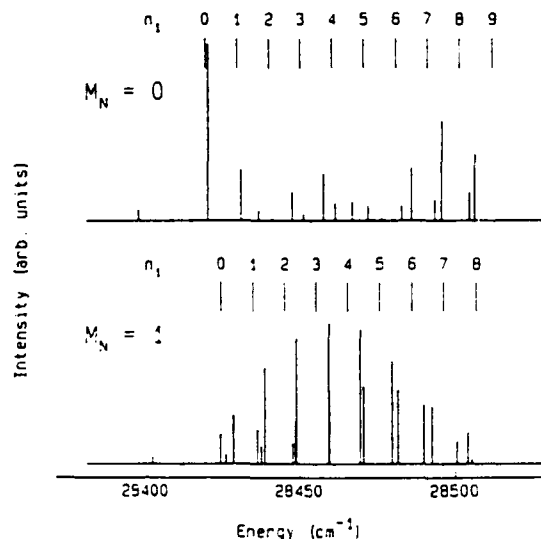

FIG. 9. Model calculation for $n=10$, $F=8000$ V/cm, and $M_N=0$ (top) and 1 (bottom). The markers labeled $n_1=0,1,2,\cdots$ represent the hydrogenic Stark states. Note the splitting of each n_1 line into three lines (only one may be visible in some cases).

61

field strength (see also the Stark maps in Sec. IV B). Unfortunately, this typical molecular "fine structure" due to the l-N^+ coupling is too narrow in the case of Rydberg states $n > 30$ to be resolved in our spectra, and we will not investigate this aspect further.

B. Comparison with experiment

In comparing the theoretical predictions with the experimental spectra, one must keep in mind that the model we use does not account for any decay process of the Rydberg states following their excitation. As we shall see, the predissociative decay of selected window regions of the spectrum discussed above also inflicts a selective loss of those Stark states that contain a substantial amplitude of low-l character.

Calculated spectra convoluted with an experimental width of 0.07 cm^{-1} are displayed in Figs. 10 and 11. These calculations correspond to the experimental conditions of Figs. 6 and 7, i.e., $n = 34$, $F = 0$–50 V/cm, and $M_N = 0$ and 1, respectively. Comparison of Figs. 6 and 10 and Figs. 7 and 11 shows a satisfactory agreement between calculation and experiment, especially in the case of high-field values where the n mixing is well accounted for by our model. A more direct comparison of experimental and theoretical spectra for the $n = 34$, $M_N = 0$ manifold is presented in Fig. 12 for $F = 10, 20, 30$, and 40 V/cm. The quantum defects used in these calculations were chosen according to the zero-field experimental re-
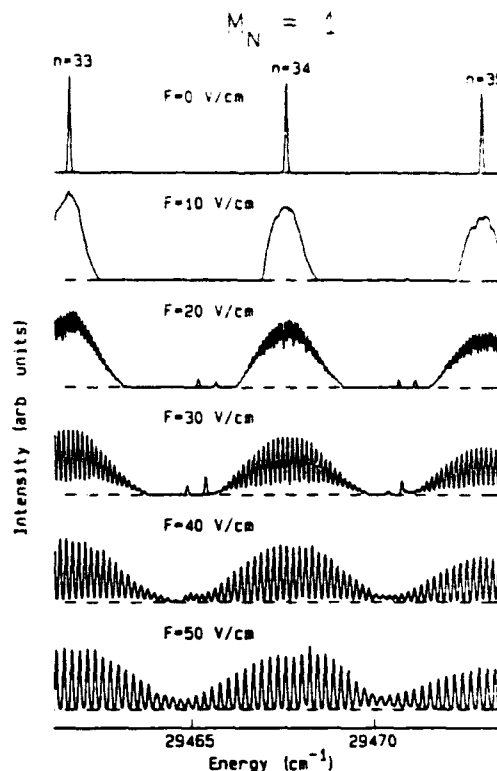
FIG. 11. Calculated Stark spectra in the vicinity of $n = 34$, $M_N = 1$, at $F = 0, 10, 20, 30, 40$, and 50 V/cm. Compare with experimental data in Fig. 7.
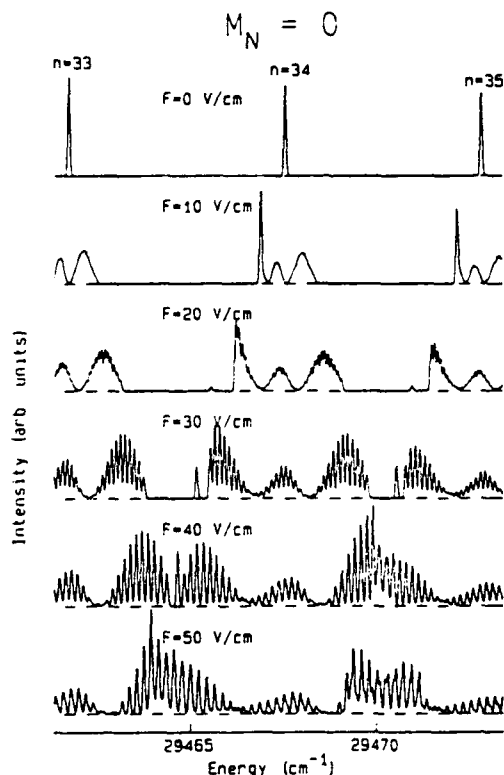
FIG. 10. Calculated Stark spectra for $n = 33$–35, $M_N = 0$, at $F = 0, 10, 20, 30, 40$, and 50 V/cm. Compare with experimental data in Fig. 6. Calculated lines are broadened to an experimental width of 0.07 cm^{-1}.

FIG. 12. Direct comparison of experimental and calculated spectra for $n = 34$, $M_N = 0$, and $F = 10, 20, 30$, and 40 V/cm. In each case, the calculated spectrum (bottom trace) is superimposed on the experimental one (top trace; all intensities are in arbitrary units). Low-n_1 lines (red "wings" of the manifolds) are clearly missing from the experimental spectra, especially at moderate fields.

sults (Tables I and II). The following parameters were used:

$$\mu_s = 0.07, \quad \mu_{pa_2''} = 0.05 ,$$

$$\mu_{pe'} = 0.39, \quad \mu_d = 0.02 ,$$

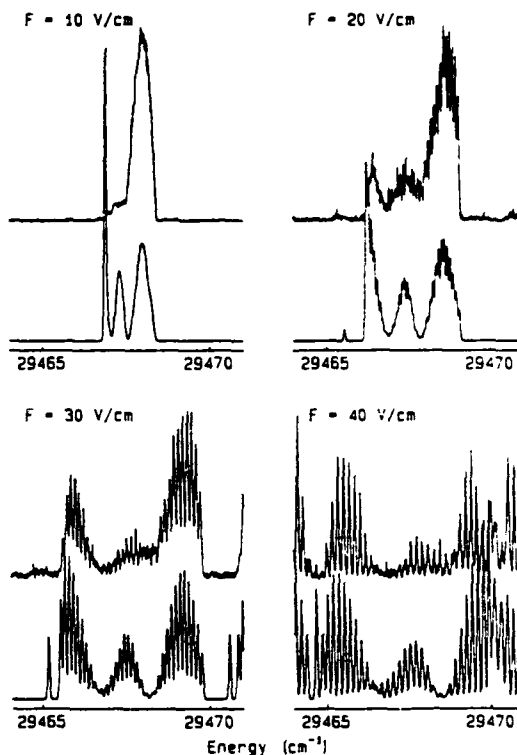$$\mu_f = 0.01, \quad \mu_{l>3} = 0.00 .$$

Let us first discuss the $M_N = 0$ spectra (Figs. 6, 10, and 12). The agreement between calculated and experimental line positions is excellent and is generally better than the experimental precision. This agreement is particularly evident in Fig. 12. Note, however, that since only the $n = 33, 34$, and 35 terms are included in the calculation, only the $n = 34$ manifold is predicted correctly. Small discrepancies in the $n = 33$ and 35 manifolds occur owing to the absence of the $n = 32$ and 36 manifolds in the perturbation basis.

Nevertheless, especially at low fields (10 and 20 V/cm), the intensities of the low-n_1 components (red side of the manifold)—or the low-l components since the ns and np states are located on the red side of the multiplet—are predicted to be much stronger than those observed in our spectra. This discrepancy diminishes as the field increases and as the particular l character of these low-n_1 components is diluted throughout the manifold. It is important to note that, at low and moderate fields, states on the red side of the manifold have still one (or two) relatively dominant l components. Indeed, of all the l states, only the s and p states have quantum defects larger than 0.05. Hence, as long as the field is not too strong, the low-n_1 states possess strong s and p components and thus acquire to an appreciable degree the character of these low-l states. This is manifest on the $M_N = 0$ Stark map displayed in Fig. 13. The nondegenerate states are, starting from the lowest-term value, $34p(N = 1)$,
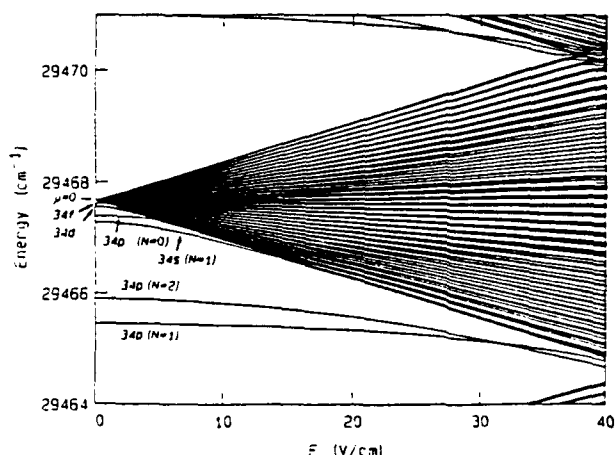

FIG. 13. Calculated Stark map for $n = 34$, $M_N = 0$, and field values (F) ranging from 0 to 40 V/cm. The $34p(N=0)$, $34s(N=1)$, $34p(N=2)$, and $34p(N=1)$ states are merged with the rest of the manifold at field strengths of about 5, 10, and 40 V/cm, respectively. Below these values, they exhibit the characteristic quadratic Stark effect. Note the avoided crossings between the $N = 1$ and 2 $34p$ levels and between the $n = 34$ and 35 manifolds.

$34p(N=2), 34s(N=1), 34p(N=0), \ldots$ These states are initially isolated from the hydrogenic multiplet and thus retain approximately their l character until field values of about 40 V/cm are reached for the $34p$, $N = 1$ and 2 states, and about 10 and 5 V/cm for the $34s(N=1)$ and $34p(N=0)$ states, respectively. Note that $34p(N=1)$ and $34p(N=2)$ states show an avoided crossing near $F = 32$ V/cm, indicating the stronger coupling of the $p(N=2)$ states to the other l states.

Assuming the unstable character of the low-l states (and especially the s states) with respect to predissociation, this picture explains qualitatively the lack of field-ionization signal, which appears on the red side of the manifold in terms of a loss of population via predissociation and possibly radiation. We expect that if the Stark spectra were recorded in absorption, no such loss would occur. The selective loss of states with appreciable s or p character is attributed to the fact that s and p states are the more penetrating (origin of their fairly large quantum defects); thus they are the most sensitive to interaction with the core and particularly to predissociation. On the other hand, if the electric field is strong enough (on the order of F_c), no particular l component dominates in any level and the coupling to the decay channels is diluted, afflicting equally all Stark levels.

If we now compare the $M_N = 1$ spectra (Figs. 7 and 11), we find that similar conclusions can be drawn: The line positions are well reproduced, but the calculated intensities of the low-n_1 components are too strong. Although the experimental manifolds are less regular than the calculated ones with respect to the distribution of the observed intensity, the agreement is better than in the $M_N = 0$ case. This is obviously a consequence of the low-n_1 components, which are the most affected by predissociation, corresponding to the weakest transitions when $M_N = 1$.

However, a particular departure of the experimental spectrum from the theoretical predictions is seen in the $M_N = 1$, $F = 10$ V/cm spectra (see Fig. 7). At an energy of $29\,467.30$ cm^{-1}, the intensity of the $n = 34$ manifold shows a significant drop in the unresolved experimental contour. Such extremely localized windows may be seen for many n values at comparable relative positions and field strengths. Examination of the detail of the $M_N = 1$, $n = 34$ Stark map in Fig. 14 suggests the following explanation. Starting from the lowest-term value, the $M_N = 1$ states are $34p(N=1)$, $34p(N=2)$, $34s(N=1)$, and $34d(N=1, 2,$ and $3)$. The $np(N=0)$ state is absent from the $M_N = 1$ Stark map. A consequence of its absence is that the $ns(N=1)$ state couples in first order only to states that are located lower in energy. Thus the ns state is repelled toward higher energy by the np states and it crosses a large part of the $n = 34$ manifold [indicated by a dashed line in Fig. 14(b)]. Indirect couplings via the p states result in the crossings being avoided, but the computed wave function shows that the s component largely dominates near the crossing, revealing that the s state preserves its character while embedded in the high-l states as long as the np states are isolated from the rest of the manifold. This holds true until a field value of about 30 V/cm for $n = 34$. Note that $34p(N=1)$ and

$34p, N = 2$ do not cross when $M_N = 1$. At $F = 10$ V/cm, the predicted position of the quasi-s-state that crosses half of the manifold is 29 467.34 cm^{-1} (its s component is 0.75, i.e., this state has more than 50% s symmetry), which corresponds with good accuracy to the energy where we observe the small hole in the ionization signal. This example suggests that the embedded s state inflicts selective predissociation to the neighboring Stark states in accordance with the arguments invoked previously. It may also explain the different width of the window around $n = 44$ depending on M_N, at least at intermediate-field strengths, because the quasi-s-state is closer from the state having the largest excitation amplitude when $M_N = 1$.

Taking into account the calculated amplitude of the s component and estimating empirically the lifetime of the zero-field ns state, we could, in principle, reproduce this effect phenomenologically. However, most of the states that have a strong s component also have a small nd component and thus should not dominate the observed intensity. For this reason, simulation of the s-coupling-

induced predissociation based on this simple model is precluded. Previous results for the np series [37], coupled in first order to the nd series that bears all the oscillator strength, have shown that predissociation of np states is localized and is not the general case, as opposed to what we believe about the ns series. Thus, in addition to the mechanism caused by the field-induced mixing with the s states, one has to assume that the d states possess a small amount of s character even in zero field. Therefore, it appears that s-d mixing would also have to be accounted for if one wishes to understand the dynamics of these Rydberg states. A non-negligible s-d mixing rate supports the observation of the giant window caused by a low-ns interloper around $n = 40-48$ and the relatively low intensity of nd states below $n = 40$. Indeed, even if the s-d mixing is constant over the entire Rydberg region, we expect the lifetime to evolve as $1/n^3$, which could explain why the evolution of the observed line intensities in the nd series is not in agreement with the $1/n^3$ law, the high-n lines being relatively stronger than the low-n lines.

Perturbation theory has proved here to be a very powerful tool for predicting the energy levels and redistribution of oscillator strength among the Stark states. Comparing the observed field-ionization intensity and calculated absorption intensity gives a qualitative idea of the magnitude of the coupling of the Rydberg states to the dissociative states. Moreover, this comparison has allowed us to distinguish between two fundamentally different decay processes: (1) rovibrational interactions with low-n interlopers with several quanta of vibration, leading to accidental predissociation and apparently randomly distributed window resonances, and (2) preferential decay of states that acquire s character.

A further step in reconciling theory and experiment could be to resolve the internal structure of each n_1 component. More precise information about electron-core couplings could be extracted from such spectra, and there is no doubt that direct observation of this yet unobserved molecular Stark structure would reveal interesting features about the dynamics of molecular Rydberg states in an electric field.

C. Perturbative treatment versus MQDT

The above results demonstrate that the classical perturbative treatment gives correct results for calculating the energy positions and intensities of Stark spectra of H_3 Rydberg states. Deviations appear when l-selective decay channels remove the population in specific Stark states before they are detected. The single important approximation, that the core remains in its ($N^- = 1$, $K^- = 0$) vibrationless level and is not affected by the external field, is easy to accept in H_3 and does not falsify the calculated energy levels. Owing to its simple formalism, perturbation theory is clearly well suited for this purpose in cases where the perturbation basis does not become immoderately large.

We could have used a multichannel quantum-defect theory such as those described by Sakimoto [23] for H_2 or by Brevet et al. [25] for Na_2. The MQDT formalism has the advantages that it benefits from the separability of the
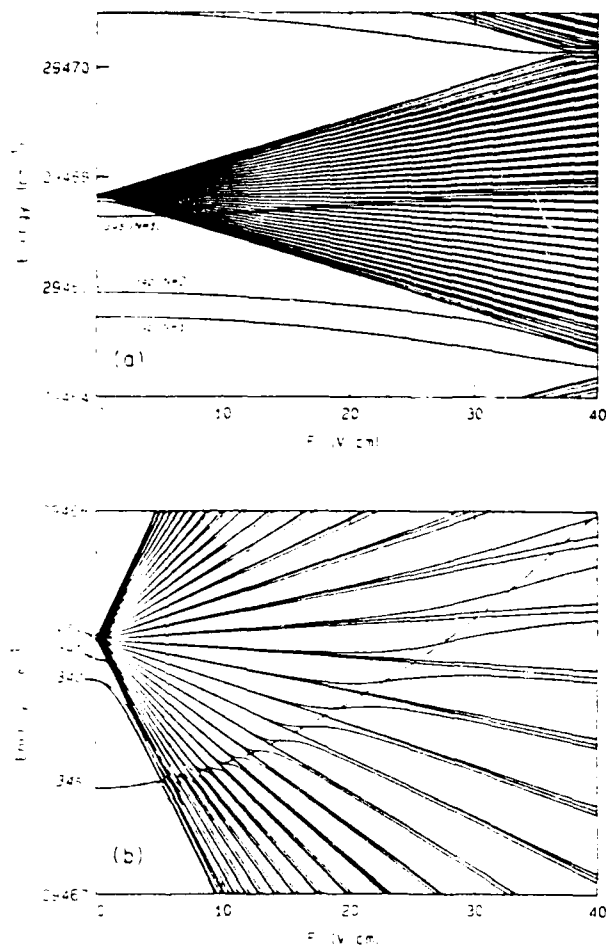

FIG. 14. (a) Calculated Stark map for $n = 34$, $M_N = 1$, and field values (F) ranging from 0 to 40 V/cm. (b) Detail showing the evolution of the s state as it is repelled through the manifold (dashed line) by the lower-lying np states. Note that only one "fine-structure" component of each n_1 Stark state follows and avoided crossing with the $34s(N = 1)$ state.

hydrogenic problem in parabolic coordinates and reduces the size of the calculation basis, which renders MQDT extremely powerful in situations where angular couplings are complex and where a prohibitive number of channels (or basis vectors) would have to be included in a perturbative method. The MQDT formalism allows also in principle the calculation of the spectra above the ionization threshold in the region where no discrete states exist. However, in the high-field regime, application of MQDT requires calculation of several elliptic integrals at each step of energy; the simple and elegant analytic hydrogenic formulas can only be used in the low-field regime.

In the particular case of H_3, where the limited number of core states (only $N^- = 1$, $K^- = 0$) leads to a relatively modest perturbation basis, the perturbative method presented here is clearly a good choice and the results obtained here substantiate our claim. Nevertheless, for a heavier molecule, where many rotational channels participate, the size of the perturbation problem may become problematic. Thus far, however, MQDT treatment of the molecular Stark effect in H_2 or Na_2 is only fragmentary, while the present perturbative treatment is carried through completely and requires no adjustable parameters.

Considering these arguments, the perturbative treatment is clearly useful in understanding the coupling schemes and relative orders of magnitude of the interactions involved in the molecular Stark effect. It has also proved to be very powerful in substantiating the very selective predissociations that affect the s and p states at such high electronic energies.

VI. CONCLUSION

Stark spectra of high Rydberg states ($n = 30-125$) of triatomic hydrogen have been obtained at low- and high-field strengths, and the observed Stark structures have been analyzed using perturbation theory where only minor approximations have to be made. Experimental zero-field data (quantum defects) have been used, and despite the absence of fitting parameters, the agreement between theory and experiment is highly satisfactory. This result is remarkable in the sense that it is the first complete quantitative perturbative treatment of molecular Rydberg states in an external field.

Comparison of the experimental spectra with the predictions of the perturbative treatment also revealed field-induced predissociation. A more complete analysis of this effect will require a more thorough understanding of the highly excited vibrational states of H_3, their coupling to the vibrationless states presented in this paper and their coupling to the repulsive ground state of H_3. From this point of view, recent findings about the vibrationally excited levels of the ground state of the H_3^- ion [56] and detailed calculation of the potential surfaces of some Rydberg states [57] are encouraging. The process leading to the apparent systematic predissociation of the ns states as well as the magnitude of the s-d mixing will also have to be examined in more detail.

We expect that a quantitative understanding of the Stark effect in highly excited molecules can teach us about the influence of the electric field on the molecular dynamics and about the hypothetical quantum chaos, for which a molecule in a field is a privileged system.

*Permanent address: Laboratoire de Spectrométrie Ionique et Moléculaire, Université Claude Bernard Lyon I, 43 Bd. du 11 Novembre 1918, 69622 Villeurbanne CEDEX, France.

[1] E. Schrödinger, Ann. Phys. (Leipzig) 80, 437 (1926).

[2] H. A. Bethe and E. E. Salpeter, *Quantum Mechanics of One- and Two-electron Atoms* (Plenum, New York, 1977).

[3] L. D. Landau and E. M. Lifshitz, *Quantum Mechanics, Non-Relativistic Theory*, 3rd ed. (Pergamon, New York, 1976).

[4] M. L. Zimmerman, M. G. Littman, M. M. Kash, and D. Kleppner, Phys. Rev. A 20, 2251 (1979).

[5] C. Fabre, P. Goy, and S. Haroche, J. Phys. B 10, L183 (1977); C. Fabre, Y. Kaluzny, R. Calabrese, Liang Jun, P. Goy, and S. Haroche, *ibid.* 17, 3217 (1984).

[6] C. Chardonnet, F. Penent, D. Delande, F. Biraben, and J. C. Gay, J. Phys. (Paris) 44, L-517 (1983).

[7] D. Tuan, S. Liberman, and J. Pinard, Opt. Commun. 18, 533 (1976).

[8] R. R. Freeman and N. P. Economou, Phys. Rev. A 20,

2356 (1979).

[9] J. M. Lecomte, S. Liberman, E. Luc-Koenig, J. Pinard, and A. Taleb, Phys. Rev. A 29, 1929 (1984).

[10] H. Rinneberg, J. Neukammer, G. Jönsson. H. Hieronymus, A. König, and K. Vietzke, Phys. Rev. Lett. 55, 382 (1985).

[11] D. E. Kelleher and E. B. Saloman, Phys. Rev. A 35, 3327 (1987).

[12] A. Nussenzweig, E. E. Eyler, T. Bergeman, and E. Pollack, Phys. Rev. A 41, 4944 (1990).

[13] J. W. Cooper and E. B. Saloman, Phys. Rev. A 26, 1452 (1982).

[14] C. T. W. Lahaye and W. Hogervorst, Phys. Rev. A 39, 5658 (1989).

[15] R. D. Knight and L.-G. Wang, Phys. Rev. A 32, 896 (1985).

[16] P. F. Brevet, M. Pellarin, and J. L. Vialle, Phys. Rev. A 42, 1460 (1990).

[17] H. J. Silverstone, Phys. Rev. A 18, 1853 (1978); H. J. Silverstone, B. G. Adams, J. Cizek, and P. Otto, Phys.

Rev. Lett. **43**, 1498 (1979).

[18] E. Luc-Koenig and L. Bachelier, J. Phys. B **13**, 1743 (1980); **13**, 1769 (1980).

[19] R. J. Damburg and V. V. Kolosov, J. Phys. B **9**, 3149 (1976); Phys. Lett. **61A**, 233 (1977); J. Phys. B **11**, 1921 (1978); **12**, 2637 (1979); R. J. Damburg and V. V. Kolosov, in *Rydberg States of Atoms and Molecules*, edited by R. F. Stebbings and F. B. Dunning (Cambridge University Press, Cambridge, England, 1983).

[20] U. Fano, Phys. Rev. A **24**, 619 (1981).

[21] D. A. Harmin, Phys. Rev. A **24**, 2491 (1981); **26**, 2656 (1982); **30**, 2413 (1984).

[22] D. A. Harmin, Comments At. Mol. Phys. **15**, 281 (1985).

[23] K. Sakimoto, J. Phys. B **19**, 3011 (1986); **22**, 2727 (1989).

[24] G. Jalbert, P. Labastie, P. F. Brevet, C. Bordas, and M. Broyer, Phys. Rev. A **40**, 784 (1989).

[25] P. F. Brevet, C. Bordas, M. Broyer, G. Jalbert, and P. Labastie, J. Phys. (Paris) II **1**, 875 (1991).

[26] W. L. Glab and J. P. Hessler, Phys. Rev. Lett. **62**, 1472 (1989); Phys. Rev. A **42**, 5486 (1990).

[27] C. Bordas, P. F. Brevet, M. Broyer, J. Chevaleyre, and P. Labastie, Europhys. Lett. **3**, 789 (1987).

[28] C. R. Mahon, G. R. Janik, and T. F. Gallagher, Phys. Rev. A **41**, 3746 (1990).

[29] C. Bordas and H. Helm (unpublished).

[30] M. Seaver, W. A. Chupka, S. D. Colson, and D. Gauyacq, J. Phys. Chem. **87**, 2226 (1983).

[31] J. W. Cooper, E. B. Saloman, B. E. Cole, and Shardanand, Phys. Rev. A **28**, 1832 (1983).

[32] J. Chevaleyre, C. Bordas, M. Broyer, and P. Labastie, Phys. Rev. Lett. **57**, 3027 (1986); C. Bordas, M. Broyer, J. Chevaleyre, and P. Labastie, J. Phys. (Paris) C7-647 (1987).

[33] H. F. King and K. Morokuma, J. Chem. Phys. **71**, 3213 (1979).

[34] J. K. G. Watson, S. C. Foster, A. R. W. McKellar, P. Bernath, T. Amano, F. S. Pan, M. W. Crofton, R. S. Altman, and T. Oka, Can. J. Phys. **62**, 1875 (1984).

[35] G. Herzberg and Ch. Jungen, J. Mol. Spectrosc. **41**, 425 (1972).

[36] M. Lombardi, P. Labastie, C. Bordas, and M. Broyer, J. Chem. Phys. **89**, 3479 (1988).

[37] C. Bordas, L. J. Lembo, and H. Helm, Phys. Rev. A **44**, 1817 (1991).

[38] H. Helm, Phys. Rev. Lett. **56**, 42 (1986).

[39] H. Helm, Phys. Rev. A **38**, 3425 (1988).

[40] L. J. Lembo, C. Bordas, and H. Helm, Phys. Rev. A **42**, 6660 (1990).

[41] L. J. Lembo, H. Helm, and D. L. Huestis, J. Chem. Phys. **90**, 5299 (1989).

[42] A. Dohdy, W. Ketterle, H.-P. Messmer, and H. Walther, Chem. Phys. Lett. **151**, 133 (1988); W. Ketterle, H.-P. Messmer, and H. Walther, Europhys. Lett. **8**, 333 (1989).

[43] N. Bjerre, I. Hazell, and D. C. Lorents (unpublished).

[44] C. Bordas and H. Helm, Phys. Rev. A **43**, 3645 (1991).

[45] One atomic unit of electric field is 5.14228×10^9 V/cm; one atomic unit of energy is $219\,474.63$ cm^{-1}.

[46] G. I. Gellene and R. F. Porter, J. Chem. Phys. **79**, 5975 (1983).

[47] C. Bordas, P. C. Cosby, and H. Helm, J. Chem. Phys. **93**, 6303 (1990).

[48] I. Dabrowski and G. Herzberg, Can. J. Phys. **58**, 1238 (1980).

[49] T. Amano, J. Chem. Phys. **92**, 6492 (1990).

[50] N. G. Adams, D. Smith, and E. Alge, J. Chem. Phys. **81**, 1778 (1984).

[51] H. Hus, F. Youssif, A. Sen, and J. B. A. Mitchell, Phys. Rev. A **38**, 658 (1988).

[52] M. Jungen, J. Chem. Phys. **71**, 3540 (1979).

[53] R. L. Martin, J. Chem. Phys. **71**, 3541 (1979).

[54] A. R. Edmonds, *Angular Momentum in Quantum Mechanics* (Princeton University Press, Princeton, 1957).

[55] A. R. Edmonds, J. Picart, N. Tran. Minh, and R. Pullen, J. Phys. B **12**, 2781 (1979).

[56] J. Tennyson, O. Brass, and E. Pollak, J. Chem. Phys. **92**, 3005 (1990).

[57] Ch. Nager and M. Jungen, Chem. Phys. **70**, 189 (1982).

Appendix E

ELECTRIC-FIELD IONIZATION OF RYDBERG STATES OF H_3

Electric-field ionization of Rydberg states of H_3

C. Bordas* and H. Helm

Molecular Physics Laboratory, SRI International, 333 Ravenswood Avenue, Menlo Park, California 94025

(Received 10 August 1992)

The stability of Rydberg states of triatomic hydrogen in an external electric field is investigated for principal quantum numbers ranging from $n = 50$ to 110. When excited in the presence of an electric field, the states with an electric-field projection of the total angular momentum $M_N = 0$ are found to be rapidly field ionized above the classical saddle-point energy. However, a significant proportion of the states for $M_N = 1$ is observed to be stable above this threshold, with lifetimes exceeding 10^{-8} s. A perturbative treatment of the molecular Stark effect indicates that different behavior of $M_N = 0$ and 1 Stark states is a consequence of the stronger coupling among the states of the $M_N = 0$ manifold. Following excitation under near-zero field conditions, a predominantly diabatic evolution of the Stark manifold of H_3 is observed, for slew rates of a few times 10^7 (V/cm)/s. This behavior results from the nondefinition of the projection of the total angular momentum of the molecule excited at near-zero field, where a broad manifold of l states is prepared within the bandwidth of the laser. For a comparison, similar experiments are carried out in atomic hydrogen and helium.

PACS number(s): 33.90.+h, 32.60.+i

I. INTRODUCTION

Electric-field ionization (EFI) of Rydberg states has been widely investigated in atoms as well as in molecules. Experiments with atomic hydrogen [1,2], the prototype for all processes involving Rydberg states, confirm precisely the theoretical predictions [3–11]. Alkali-metal atoms, which in many aspects resemble atomic hydrogen, have been more widely studied [12–26], and the nonhydrogenic effects of alkali-metal atoms in EFI have been analyzed in detail. Investigations of the rare gases helium [27] and xenon [28] have also confirmed that many-electron systems behave similarly to alkali-metal atoms. Electric-field ionization of molecules has been mainly confined to the molecules H_2 [29–32], Li_2 [33–35], and Na_2 [36–38]. Some work on the polyatomic molecules naphthalene and benzene has also been reported [39].

Beyond its intrinsic interest, a motivation for studying field ionization is that it is a most sensitive and frequently used method for detection of Rydberg states of atoms and molecules. The method can also be selective, because the field-ionization threshold as well as the field-ionization dynamics depend on the binding energy of the electron [17] and vary with the m_l quantum number for a given state [16,18,23].

On the basis of the many theoretical treatments of the Stark effect in atomic hydrogen, field ionization in atoms is well understood. However, many aspects of field ionization of molecular states are still incompletely resolved. Obviously core structure adds to the complexity of the phenomenon, giving rise to processes such as forced ionization [26] or field-induced rotational autoionization [32–37].

In the present study on H_3, complications related to autoionization are avoided because we concern ourselves with the Rydberg series that converge to the lowest rovibrational level of the electronic ground state of ortho-

H_3^+. In addition, owing to the very large energy separations between the rotational and vibrational levels of H_3^+, the mixing with core excited series is generally negligible except for specific interlopers [40].

Field ionization of Rydberg states of H_3 has been a primary tool to investigate photoabsorption to excited states of H_3. In these studies, many unexpected intensity windows in the ionization efficiency have appeared and anomalous electric-field-dependent variations in the intensity of low- and high-Rydberg states have been noted [40–45]. The goal of the present study was to investigate in more detail the EFI properties of H_3 and their possible influence on the appearance of the absorption spectra of H_3. This article discusses two observations that we consider of general interest (1) the dependence of the field-ionization process on the projection of the total angular momentum ($M_N = 0$ or 1) onto the field axis, and (2) the apparent difference between the behavior of states produced in a near-zero field and subsequently exposed to an electric field and that of Stark states excited in a field of the same magnitude. The latter phenomenon, which has previously been described for atomic hydrogen [1,2,27], is related to the loss of the quantization axis in the absence of a well-defined external field and is largely independent of the properties of the H_3 molecule.

II. DESCRIPTION OF THE EXPERIMENT

A schematic diagram of the experimental setup [45] is given in Fig. 1. The H_3 molecules are produced as a fast neutral beam by charge exchange of mass-selected H_3^+ molecules of 1.5-keV energy in a cesium vapor. The resulting neutral beam is purged of residual ions by a small electric deflection field and contains only molecules in the long-lived rotationless level of the $\bar{B}2p\,^2A_2''$ state [41,46]. Nearly all of these molecules are also in the lowest vibrational level, and all spectra discussed here involve excita-
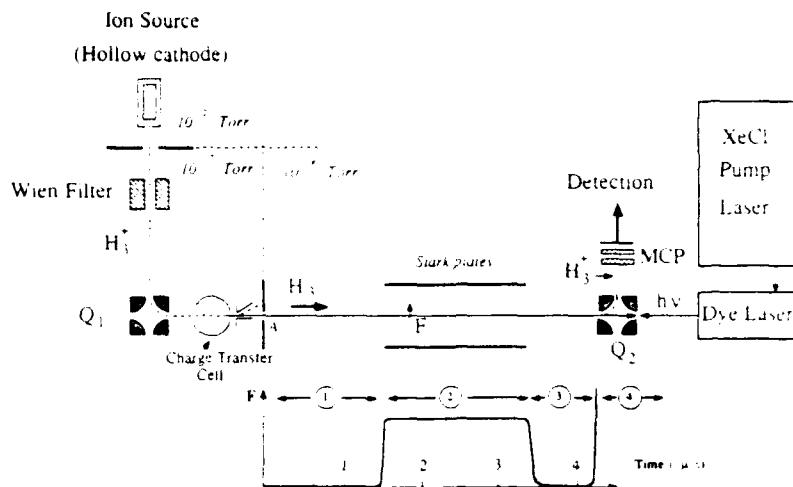
Ion Source

(Hollow cathode)

FIG. 1. Schematic of experimental setup. The fast H_3 neutral beam is collinearly excited by a tunable, pulsed laser beam. The neutral molecules that survive passage through the Stark-field region are field ionized at the entrance of the quadrupole deflector Q_2 and the resulting ions are detected during appropriate time gates corresponding to photoexcitation in region 1 or 2.

tion from the $N=0$, $K=0$, $v_1=v_2=0$ level. This state results from the addition of a $2p$ electron to the lowest rotational level of ortho-H_3^+ ($N^+=1$, $K^+=0$). The neutral beam molecules are photoexcited in an ultrahigh vacuum chamber by a counterpropagating, pulsed dye laser beam [excimer pumped, unfocused 0.05–1 mJ/pulse, 0.15 cm^{-1} (FWHM), P-terphenyl dye] along a 120-cm-long interaction region. A fixed ionizating field at the entrance of the energy analyzer, Q_2, is used for detecting those excited molecules that survive passage through the interaction region as neutral species. The magnitude of this detection field (2.3 kV/cm) is the same in all the experiments described here. Ions resulting from EFI in the detection field are separated by mass in the electrostatic quadrupole Q_2 and monitored by a microchannel plate detector.

During their path along the interaction region, the H_3 molecules successively traverse four regions of different electric fields. These regions are separated by transition zones where the field is not precisely defined but varies over a few centimeters, corresponding to transit times of about 100 ns. These four different regions (labeled 1 through 4 at the bottom of Fig. 1) can be described as follows.

Region 1 is a near-zero field region between aperture A and the Stark plates. Here the electric field is small (about 0.1 V/cm) and is mainly due to the motion of the neutral molecules in residual magnetic fields. At a beam energy of 1.5 keV, the motional electric field induced by the uncompensated magnetic field of the earth has a magnitude of 0.09 V/cm and is directed nearly parallel to the Stark field applied in region 2. Other small residual fields that are not precisely characterized exist in this region.

Region 2 has a well-defined transverse electric field (hereafter called the Stark field) that is defined by two parallel plates 45 cm long, 10 cm wide, and 2.44 cm apart. At a beam energy of 1.5 keV, H_3 molecules spend about 1.5 μs in this region. In region 2, one component of the motional electric field due to the earth's magnetic field can be compensated by the applied field. In a previ-

ous publication [45], we estimated that the lowest achievable value of the residual field in our experiment is on the order of 0.05 V/cm in region 2 and ~0.1 V/cm in region 1.

Region 3 is another field-free (near-zero field) region with the same properties as region 1.

Region 4 is a region of strong electric field at the entrance of Q_2 (the detection field) where the Rydberg molecules are ionized before being mass selected.

Since a pulsed laser is used to prepare the Rydberg states and since the molecules propagate through the interaction region with a velocity of 3×10^7 cm/s, we use the time of arrival of each ion to determine where along the interaction region the neutral precursor to the ion was photoexcited. Thus, with proper electronic gating (see time scale in Fig. 1), we can simultaneously record two distinct processes: (a) photoexcitation of states under near-zero-field conditions in region 1 followed by passage of the molecules through the Stark-field region, and (b) excitation of states in the Stark field.

In both cases, the Rydberg states that survive passage through the Stark field without being ionized reach the detection field (region 4), where they are field ionized for principal quantum numbers larger than $n \gtrsim 30$. Ions falling into the arrival time "windows" set by gates 1 and 2 are recorded to give a near-zero-field spectrum and a Stark spectrum, respectively. Ions formed in the Stark-field region are bent away from the neutral beam direction by the perpendicular field and thus are lost for the detection process. Consequently, EFI in the Stark-field region appears as a decrease in the detected ion signal.

We perform the identical experiment with atomic hydrogen or helium by simply changing the mass selection of the ion beam in the Wien filter from H_3^+ to H^+ or He^+ and adjusting the electronic gating times for the detection. Charge exchange in cesium vapor produces neutral atoms in the H(2s) and the He(2s $^1S^o$) states, and we use one-photon photoexcitation to produce either the Balmer series or the np $^1P^o$ series members from these states.

III. SUMMARY OF THE THEORY OF ELECTRIC-FIELD IONIZATION

A. Classical thresholds

In discussing our experimental spectra, it is useful to refer to three model thresholds that are often defined in EFI work: the saddle-point energy, the "red-state" diabatic threshold, and the "blue-state" diabatic threshold (see Fig. 2).

The saddle-point energy E_{SP} corresponds to the local maximum of the sum of the Coulomb and Stark potentials along the field axis. From a classical point of view, the states above this energy are in the continuum and therefore ionize. This classical threshold has a hydrogenic value of [12,47]

$$E_{SP} = -2\sqrt{F} + |m|F^{3/4} + \tfrac{1}{16}m^2F \approx -2\sqrt{F} , \qquad (1)$$

where m is the projection of the electronic angular momentum along the field axis, F is the Stark field, and all quantities are given in atomic units (1 a.u. of electric-field strength is $5.142\,208\,2\times10^9$ V/cm). A zero-field state with effective principal quantum number n^* reaches the saddle-point energy at the threshold field:

$$F_{sp} = \frac{1}{16n^{*4}} . \qquad (2)$$

The separation of the Schrödinger equation for atomic hydrogen in parabolic coordinates [3] leads to the introduction of the parabolic quantum numbers n_1 and n_2,
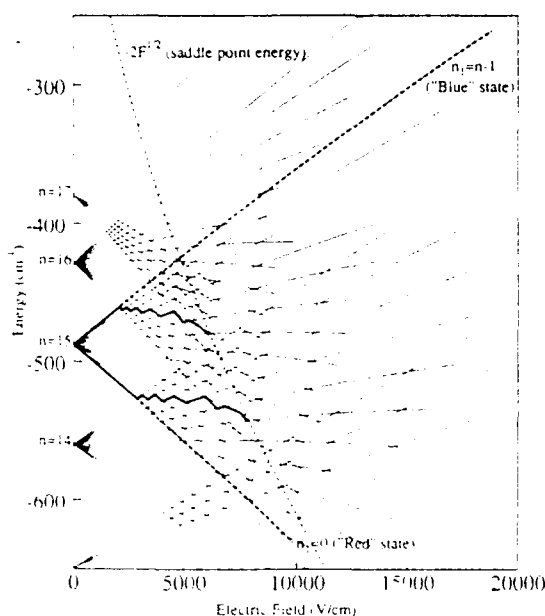

FIG. 2. Hydrogenic Stark map in the vicinity of $n=15$ $(m=0)$. For each parabolic state $(n,n_1,m_i=0)$, the curve representing the energy as a function of the electric field ends when the ionization rate becomes larger than 10^6 s^{-1}. The dashed line labeled $-2F^{1/2}$ represents the position of the saddle-point energy. Bold solid lines show examples of adiabatic passage to ionization, while bold dashed lines give the limits of the diabatic passage from zero field to high field for the $(n=15, n_1=0)$ and $(n=15, n_1=14)$ states.

where $n_1 + n_2 + m - 1 = n$. In this framework it is possible to calculate the lifetime of each Stark sublevel (n_1, n_2) against field ionization. This lifetime decreases when n or F increases, whereas, for a given n manifold and a given field, lifetime and energy increase with n_1.

In parabolic coordinates $(\xi = r + z, \eta = r - z, r$ being the distance from the ion core to the electron position and z being the coordinate along the external electric-field axis) the effective potential along the ξ coordinate is always attractive while it passes over a local maximum before decreasing toward $-\infty$ along the η coordinate. The magnitude of this local maximum depends on the parabolic quantum numbers n_1 and n_2 and has been termed "critical energy" by Herrick [6]. It varies between the two limits defined below.

In first-order, the energy of the reddest member of the n manifold $(n_1=0, m=0)$ in a field F is [3]

$$E_{(n_1=0,\, m=0)} = -\frac{1}{2n^2} - \tfrac{3}{2}n^2F . \qquad (3)$$

The wave function of the red Stark state is mainly localized on the side of the saddle point, and therefore the red state should ionize when $E_{(n_1=0)} \approx -2\sqrt{F}$ and the approximate ionization field for the $n_1=0$ state is given by

$$F_r \approx \frac{1}{9n^4} . \qquad (4)$$

This gives, for the zero-field energy of a state whose reddest Stark component ionizes at a given field value F,

$$E_r \approx -\tfrac{1}{3}\sqrt{F} . \qquad (5)$$

This value is referred to as the "red-state" diabatic threshold.

At very large principal quantum numbers, a variational calculation developed by Herrick [6] gives the field value for ionization of the bluest Stark component $(n_1 = n - |m| - 1)$ as

$$F_b \approx \frac{32}{81n^4} . \qquad (6)$$

Equation (6) predicts the zero-field energy of a state whose bluest Stark component ionizes at a specific electric-field value F as

$$E_b \approx -\tfrac{9}{8}\sqrt{F/2} . \qquad (7)$$

This value is referred to as the "blue-state" diabatic threshold.

These various thresholds do not correspond to specific ionization rates. Rather, the onset of EFI near threshold is so rapid that the system can be considered stable below and unstable above these thresholds.

B. Results of quantum calculations

The quantum calculations do not predict an EFI threshold but instead a field-ionization rate. An effective threshold field can be defined once the observation time scale for the field-ionization process is specified. Damburg and Kolosov [7] developed a semiempirical formula for the ionization rates. Their treatment is based on the energy expression at the fourth order of the perturbation theory.

71

$$E(n,n_1,n_2,m,F) = -\frac{1}{2n^2} + \tfrac{1}{2}n(n_1-n_2)F - \frac{n^4}{16}[17n^2 - 3(n_1-n_2)^2 - 9m^2 + 19]F^2$$

$$+ \tfrac{3}{32}n^7(n_1-n_2)[23n^2 - (n_1-n_2)^2 + 11m^2 + 39]F^3$$

$$- \left|\frac{n^{10}}{1024}\right|[5487n^4 + 35\,182n^2 - 1134m^2(n_1-n_2)^2$$

$$+ 1806n^2(n_1-n_2)^2 - 3402n^2m^2 + 147(n_1-n_2)^4 - 549m^4$$

$$+ 5754(n_1-n_2)^2 - 8622m^2 + 16\,211]F^4 . \tag{8}$$

In an experiment, the effective "threshold" field is defined by the average time a molecule spends in the Stark-field region (in our case $\sim 10^{-6}$ s). In the vicinity of the critical field values [for the extreme Stark components these are defined by Eqs. (4) and (6)], the ionization rate varies by several orders of magnitude when the field is varied by only a few percent. As a consequence, near the critical field, effective thresholds and critical energies are similar within a few percent.

For hydrogenic ionization rates Damburg and Kosolov [7] have given the semiempirical formula given by

$$\Gamma = \frac{(4R)^{2n_2+m+1}e^{-2R/3}}{n^3 n_2!(n_2+m)!}$$

$$\times \exp\left[-n^3\frac{F}{4}(34n_2^2 + 34n_2m + 46n_2 + 7m^2\right.$$

$$\left. +23m + \tfrac{53}{3})\right], \tag{9}$$

where $R = (-2E)^{3/2}/F$ and E is the energy calculated from Eq. (8).

The relation between the energy and the field strength at the ionization threshold for a given n manifold depends primarily on the value of n_1 and to a lesser extent on m_l. The red state ($n_1 = 0$) has the lowest energy and the highest ionization rate, because its wave function has a high probability density near the saddle point. For an ionization rate of 10^6 s^{-1}, the approximate values of the critical field [Eq. (4)] and the critical energy [Eq. (5)] of the reddest state differ by only a few percent from the threshold values calculated using Eqs. (8) and (9). On the other hand, the bluest state ($n_1 = n - |m| - 1$) has the highest energy, but its wave function shows only a very small electron density near the saddle point and consequently its ionization rate is small. Numerical calculations show that, in the region of interest here ($50 < n < 100$), F_{blue} is two or three times larger than F_{red} for a given n manifold, consistent with the variational results [6] (4) and (6).

The hydrogenic Stark manifolds displayed in Fig. 2 have been computed from Eqs. (8) and (9). For each n and n_1, the energy of the $m = 0$ Stark level is plotted as a function of the electric field. Curves end at a field value where the ionization rate reaches 10^6 s^{-1}.

IV. EXPERIMENTAL RESULTS

Two types of spectra were examined using the apparatus shown in Fig. 1. One type is obtained by scanning the wavelength of the exciting laser; this spectrum is recorded for a fixed setting of the Stark field, the detection field, and the laser polarization. A second kind of spectrum is obtained by scanning the magnitude of the Stark field; it is recorded for a fixed setting of the excitation wavelength, the detection field, and the laser polarization. EFI thresholds appear in both spectra. An important point concerning the observed EFI thresholds is that, if a molecule is ionized in the Stark field, the ion is also deflected by the Stark field and thus never reaches our detector. Thus, in our spectra, contrary to the usual experiments, the ionization thresholds correspond to a decrease in the ion signal.

A. Threshold spectra of H_3

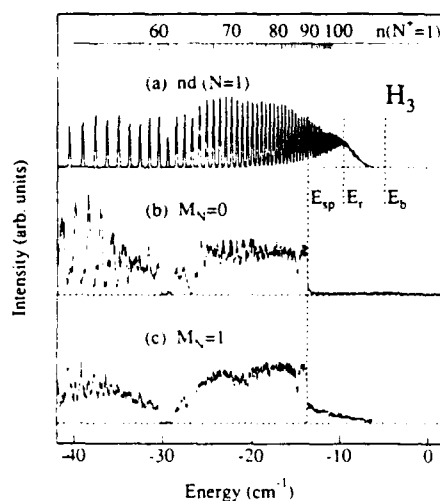A typical set of wavelength-dependent spectra for H_3 is given in Fig. 3. These spectra are recorded with a field of

FIG. 3. Excitation spectra of H_3 with a Stark field of 5 V/cm for states excited in zero field (a), in the Stark field with $M_N = 0$ (b), and in the field with $M_V = 1$ (c). E_{SP}, E_r, and E_b indicate the positions of the saddle-point energy, the red-state ($n_1 = 0$) threshold, and the blue-state ($n_1 = n - 1$) threshold, respectively. Here and in the following figures, the energy scale origin is the lowest ionization limit of H_3: 29562.58 cm^{-1} above the metastable state.

5 V/cm applied in the Stark region. In the top spectrum (a), the molecules are excited in region 1 (near-zero field) and then enter the Stark-field region. This spectrum shows the excitation of the nd ($N = 1$) Rydberg series that converges to the lowest ortho level of H_3^+ ($N^+ = 1$, $K^+ = 0$). This limit lies 29 562.58 cm^{-1} above the initial metastable state and is used as the origin of the energy scale given. A significant decrease in the ion signal is observed for n values greater than 106, and no Rydberg molecules with quantum numbers exceeding 140 are found to reach the detector. The conclusion is that the higher n members are field ionized in the Stark field and hence prevented from reaching the detection field. No sharply defined ionization threshold exists in this case where the states are excited prior to the ionizing field. The model thresholds calculated for 5 V/cm are indicated in the figure. We see that the states lying between E_r and E_b, well above the saddle-point energy E_{SP}, are stable on the time scale required to traverse the Stark field (~ 1 μs).

A generally different picture emerges when excitation occurs in the Stark-field region (region 2), as is evident in traces (b) and (c) in Fig. 3. Rather well-defined thresholds appear in these two spectra near $n = 90$, the predicted saddle-point energy for a field of 5 V/cm. The projection of the total angular momentum of the molecule (neglecting spins) onto the field axis, M_N, is the only quantum number conserved in the field. In the metastable state, $M_N = N = 0$. Thus, depending on the orientation of the laser polarization with respect to the Stark field, we can excite states with $M_N = 0$ ($E_{laser} \| E_{Stark}$, center spectrum in Fig. 3) or $M_N = \pm 1$ ($E_{laser} \perp E_{Stark}$, bottom spectrum in Fig. 3). In the following, we use the notation $M_N = 1$ instead of $M_N = \pm 1$.

We see that the $M_N = 0$ spectrum exhibits a distinct threshold at the zero-field energy of the 90d state, with practically all $M_N = 0$ states being ionized above the classical threshold E_{SP}. In the $M_N = 1$ spectrum, we again observe a sharp decrease in the ion signal at the saddle-point energy; however, a significant proportion of the states are observed to be stable above this threshold.

These differences are also apparent from Figs. 4 and 5, which show the results for Stark-field values ranging from 0 to 10 V/cm. Figure 4 gives spectra obtained by exciting in the near-zero field and then subjecting the Rydberg states to the Stark field indicated. The model thresholds are shown by arrows, and we see that EFI becomes gradually complete between E_r and E_b when the states are prepared at near-zero-field conditions. Spectra recorded with atomic helium under identical conditions give results basically identical to those in Fig. 4. Figures 5(a) and 5(b) correspond to excitation in the Stark field for $M_N = 0$ and 1, respectively. The arrows represent the position of the saddle-point energy. For each field value, it is clear that ionization is nearly 100% efficient above the saddle-point energy when $M_N = 0$ but less complete (varying from 60% for $F = 2$ V/cm to 80% for $F = 10$ V/cm when $M_N = 1$.

We can look at EFI in finer detail by using the second technique described above, namely, exciting a Rydberg state at a given photon energy and then measuring the
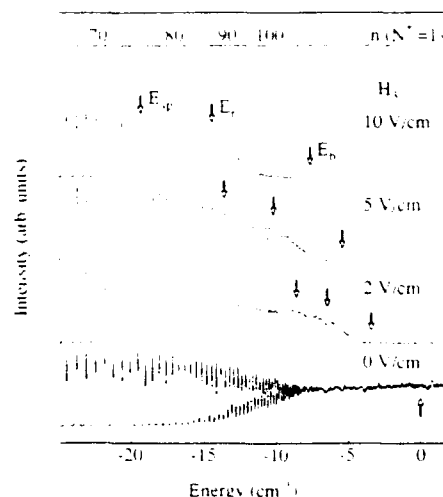

FIG. 4. H_3 Rydberg spectra when the molecules are excited in a near-zero field and then exposed to a Stark field. Arrows indicate the saddle-point energy and the red-state and blue-state diabatic thresholds. Field ionization occurs between E_r and E_b, well above E_{SP}.

remaining ion signal as a function of the magnitude of the Stark field. Figure 6 shows such spectra at a wavelength corresponding to excitation of the field-free 70d ($N = 1$) state. The upper spectrum refers to excitation at zero field, prior to the interaction with the Stark field. The bold dashed line is a hydrogenic simulation based on Eqs. (8) and (9). A small portion (about a quarter) of the molecules are found to be field ionized just above F_{SP}, but ionization only gradually reaches completion above the red-state threshold. The blue-state threshold field for $n = 70$ lies at ~ 85 V/cm, outside the field scale shown in Fig. 6. The lower spectrum in Fig. 6 corresponds to states excited in the field for $M_N = 0$. Obviously ionization is complete above F_{SP} for $M_N = 0$ states excited in the field.

B. Threshold spectra of atomic hydrogen

Several aspects of the ionization phenomena described so far become clearer in the context of atomic hydrogen, for which exact calculations are available. We show in Figs. 7 and 8 spectra for atomic hydrogen recorded under conditions identical to those used for H_3 in Figs. 3 and 6, respectively. In the top spectrum in Fig. 7, the Balmer series $np \leftarrow 2s$ is excited in the near-zero field and subsequently the atoms traverse the Stark-field region, where a field of 5 V/cm is applied. We see that the ion signal decreases only gradually between the thresholds E_r and E_b, quite analogous to the results for H_3 in the uppermost spectrum of Fig. 3. The lower spectrum in Fig. 7 corresponds to atomic hydrogen being excited in a field of 5 V/cm with the laser polarization perpendicular to the Stark field ($m_l = 1$). This spectrum is quite different from the analagous spectrum for triatomic hydrogen in Fig. 3. In atomic hydrogen, the threshold region spreads from the saddle-point energy E_{SP} (where $n_1 = 0$ states are ionized) all the way to the ionization limit (where states with $n_1 \approx n$ are ionized). In Fig. 7 (bottom), the thin trace gives the experimental spectrum and the bold trace the

result of a hydrogenic calculation which shows the high degree of reliability of the hydrogenic theory [Eqs. (8) and (9)].

A similar difference is apparent in Fig. 8, which gives fixed-wavelength spectra for excitation of H $(n = 70)$ that can be compared with those shown in Fig. 6 for H_3. The dashed line in Fig. 8 (top) gives the result of a hydrogenic simulation which fits almost perfectly the experimental spectrum.

V. DISCUSSION

The field-ionization properties of the Stark states of nonhydrogenic systems depend on the strength of the mixing between pure parabolic states of different n value and the dynamics at the avoided crossings between these states. However, this mixing alone is not sufficient to explain the hydrogenic behavior of H_3 states excited in the region of near-zero field, as will be detailed in Sec. V B. Section V C gives a qualitative explanation of the
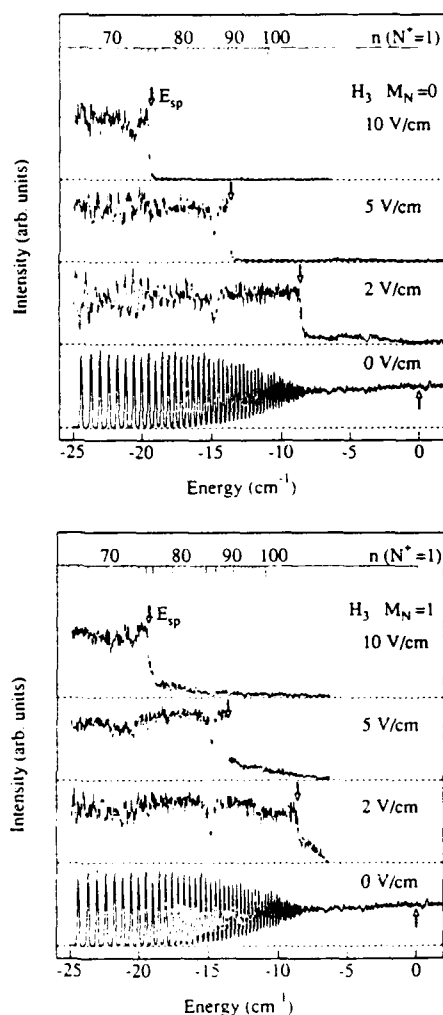

FIG. 6. H_3^+ signal as a function of field strength after excitation of H_3 molecules at the energy of the $70d$ $(N = 1)$ state with excitation in the near-zero field (top) or in the Stark field (bottom). The bold dashed line (top spectrum) is a hydrogenic simulation (see text). The top spectrum shows that about 25% of the molecules are ionized just above the saddle-point energy, i.e., at the field strength F_{SP}, where the energy of the $70d$ state equals the saddle-point energy.

FIG. 5. Stark spectra of H_3 for different field values (0–10 V/cm) and $M_N = 0$ (a) or $M_N = 1$ (b). The arrows indicate the saddle-point energy. The spectra clearly show a sharp decrease in the signal at E_{SP} as well as the stability of part of the $M_N = 1$ states above this threshold.
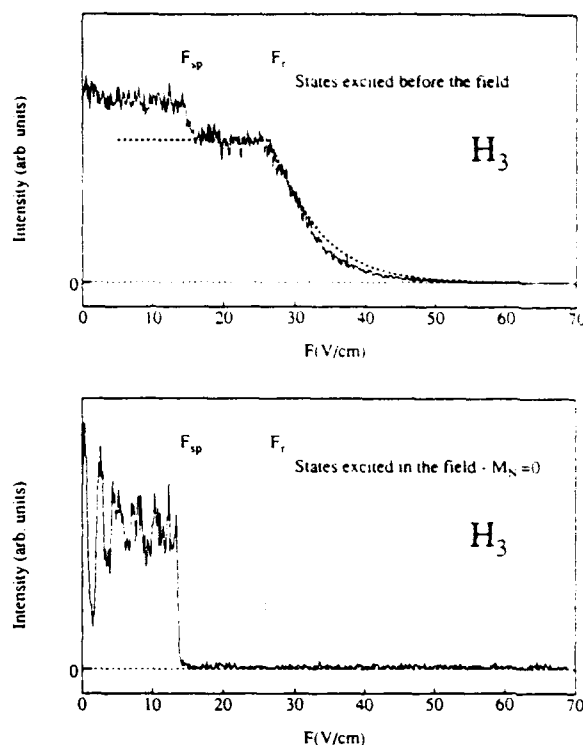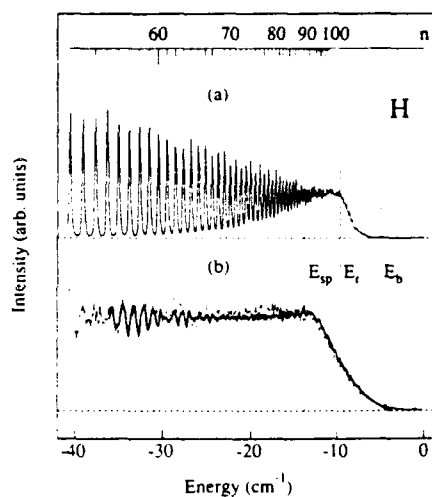

FIG. 7. Excitation spectra of atomic hydrogen with a Stark field of 5 V/cm for states excited in near-zero field (a) and in the Stark field with $m_l = 1$ (b) (thin line: experiment, bold line: calculation). Compare with the spectra of Fig. 3 to see the nonhydrogenic behavior of H_3 when excited in the Stark field and its hydrogenic behavior when excited in the zero field.
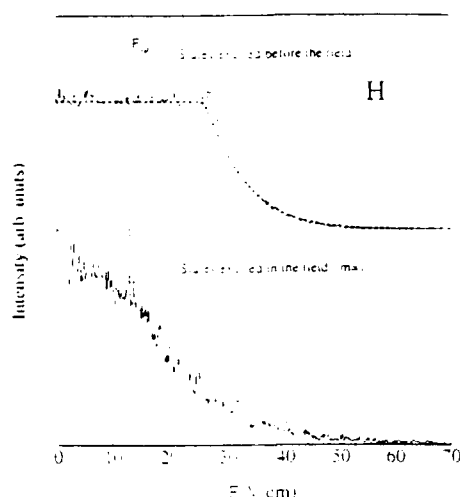
FIG. 8. Same as Fig. 6 but for atomic hydrogen. The excitation takes place at the energy of the $70p$ state in the zero field (top) and in the Stark field (bottom), with $m_l = 1$. The bold dashed line (top spectrum) is a hydrogenic simulation assuming $m_l = 1$ and an ionization rate of $10^6 s^{-1}$.

different EFI processes observed for $M_N = 0$ and $M_N = 1$ series. Unlike the previous point, this one is a consequence of particular characteristics of H_3. Finally, we analyze the dynamic evolution of states that are excited in the near-zero field and then subjected to the Stark field.

A. Adiabaticity and diabaticity

In the nonrelativistic approximation, the Stark levels from different n manifolds of atomic hydrogen are strictly uncoupled. In the nonhydrogenic case, however, the Stark states cannot be described by purely parabolic $|n_1, n_2, m\rangle$ wave functions and the crossings between the Stark states are avoided. The coupling among different $|n_1, n_2, m\rangle$ states of different n value determines the dynamic path along which the Stark states evolve in a time-varying electric field, and two extreme cases can be distinguished.

If the electric field is increased gradually, such that the mixing between the various n_1, n_2 components has time to be established, then a specific state will evolve along the adiabatic path. For example, if the zero-field excited state was an nlm state, then the path followed toward ionization is such that the energy of the system is forced to stay between the zero-field energy of the $n-1$ and $n+1$ states because all crossings are avoided. In this case, the experimental ionization threshold follows rather closely the classical formula $1/16n^{*4}$, where n^*, the effective principal quantum number at ionization, differs at most by about 0.5 from the original n value [32]. This is why the saddle-point threshold is sometimes referred to as the adiabatic threshold. Ionization can occur in the vicinity of the saddle-point energy because there is always mixing with a rapidly ionized "red" component from a higher n manifold.

On the other hand, if the field is increased very rapidly, the avoided crossings may be traversed diabatically and a zero-field state could follow along any of the paths be-

tween the "red" $(n_1 = 0)$ state and the "blue" $(n_1 = n - m - 1)$ state from zero field to ionization. As a consequence, we would expect to observe a gradual ionization of the different Stark sublevels at field values between F_{red} and F_{blue}. This difference is indicated in Fig. 2, where the bold tracks give examples of adiabatic passage to ionization whereas the thin lines are examples of diabatic passage.

Direct evidence for both adiabatic and diabatic behavior is apparent in the upper trace in Fig. 6. Some H_3 molecules about 25% are observed to ionize near the saddle-point energy, while the remainder show a field dependence similar to that seen for atomic hydrogen (compare with top curve in Fig. 8). To explain this observation we first have to characterize the nature of states excited in region 1.

B. Properties of the "zero-field" states

States that are photoexcited in region 1 are not prepared under truly zero-field conditions, but they are formed in a region of ill-determined residual fields whose direction and magnitude is not constant along the beam path. A main component of this field comes from the motional electric field that results from the earth's magnetic field $(\leq 100 \text{ mV/cm})$. When optical excitation occurs under such conditions, then at time $t = 0$ an $M_N = 0$ or 1 state will be excited because the initial state has $N = M_N = 0$. At the time of excitation, the quantization axis is defined by the local field. However, this quantization axis will be lost during the passage from the point of excitation to the region of the Stark field, and the total angular momentum N of the molecule will precess around the random directions of the residual field. This would be true even if the field was as close as possible to zero [1,2,27]. However, if the electric field was really negligible, the accessible values of M_N would fall into the range from 0 to ± 3, owing to the low values of the core kinetic momentum $(N^+ = 1)$ and the electronic angular momentum $(l = 0$ or 2) that can be prepared from our initial state of H_3.

To explain the EFI behavior in the upper curve in Fig. 6, we first consider the result of a perturbative calculation [45] for the oscillator strength of the Stark states belonging to the $n = 70$ manifold. The calculation used the quantum defects listed in Table I. Figure 9 gives these results for $M_N = 0$ and 1 at $F = 0.1$ V/cm. Calculated intensities have been normalized so that the sum of the line intensities for a given n manifold is 1. Two results from

TABLE I. Quantum defects used in our calculations.

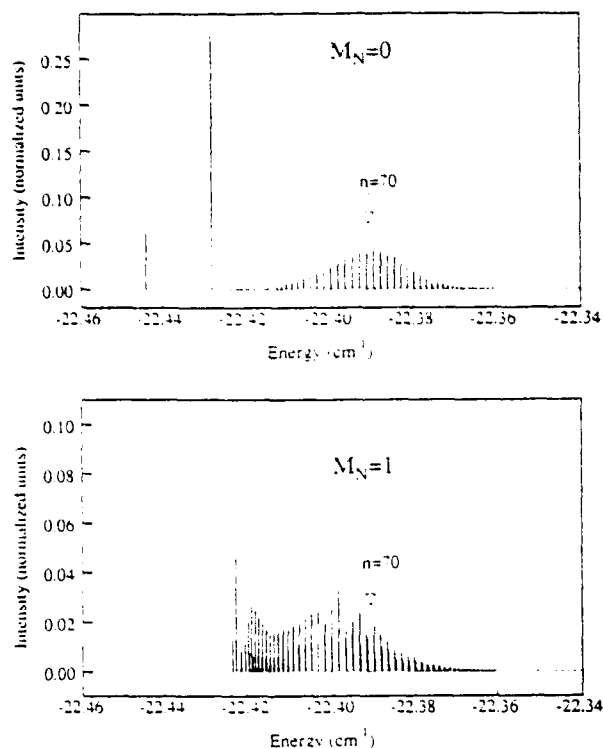| Orbital symmetry	Quantum defects	Reference
s	0.07	[45]
pa''	0.05	[43]
pe'	0.39	[43]
d	0.02	[41]
f	0.01	[42]
$l > 3$	0.00	

FIG. 9. Perturbative calculation of the oscillator strength for the $n=70$ manifold of H_3 in a field $F=0.1$ V/cm. The top spectrum shows results for $M_N=0$ and the bottom spectrum for $M_N=1$.

Fig. 9 are important for the discussion of the ionization behavior seen in Fig. 6.

(1) The energy spread of the $n=70$ Stark manifold at an electric-field strength of 0.1 V/cm is $\lesssim 0.08$ cm^{-1}. Our experimental resolution is given by the laser bandwidth ($\lesssim 0.15$ cm^{-1}). Thus the laser will excite all the components of the manifold under the conditions that apply to the top spectrum of Fig. 6.

(2) The intensity of each unresolved Stark component is approximately proportional to the square of its d ($l=2$) character. The oscillator strengths show that the intensity is distributed over the entire manifold. The strongest line bears 27% of the total oscillator strength for $M_N=0$ and 5% for $M_N=1$. The intense transitions on the red side of the manifolds correspond to the states that correlate to the nd states at the zero-field limit. More generally, all the lines on the red side of $n=70$ correlate to states with a positive quantum defect in zero field, that is, with low-l states ($l<3$), while the lines between -22.42 and -22.36 cm^{-1} correspond to the hydrogenic complex ($\mu \sim 0$) of high-l states.

In our calculation, the quantum defects are nonzero for $l\leq 3$, which corresponds to the ten lowest states of the manifold for $M_N=0$ (the nine lowest for $M_N=1$). The sum of the line intensities of these Stark states is 0.341 for $M_N=0$ and 0.078 for $M_N=1$. When these data are combined with a 1:2 statistical branching ratio for $M_N=0$ and $M_N=1$, this leads to a total of $(0.341\times\frac{1}{3}+0.078\times\frac{2}{3})\sim 17\%$ of the intensity going into

low-l components when broadband excitation occurs at 0.1 V/cm. This information can now be used to estimate the composition of states that enter the Stark-field region under the conditions of Fig. 6. For a given l value, the total angular momentum N with $N^+=1$ may take any value from 0 to l, and so does M_N. If we assume an equal partitioning of all the M_N values for each N subset (this is strictly true only if no quantization axis exists), the probability that an excited molecule is in a low-M_N state (say, $M_N<3$) is 0.17 (the 17% corresponding to the low-l components) plus ~ 0.05 (the proportion of low M_N for high-l: high-N states $\sim 3:70$). In other words, only about 22% of the molecules excited in region 1 enter the Stark region with $M_N<3$.

The experimental results in Figs. 5(a) and 5(b) suggest that, for $n=70$, about 100% of the $M_N=0$ states and about 80% of the $M_N=1$ states will be field ionized above E_{SP} when a field of ~ 13 V/cm (value of F_{SP} from $n=70$) is applied. Similarly, we can assume that a significant proportion of $M_N=2$ states are also ionized, but states with high M_N should behave purely hydrogenically, since no states with significant quantum defects participate in the $M_N>2$ manifolds.

The above considerations suggest that about 22% of the excited molecules should ionize at the saddle-point energy or in its vicinity (depending on which adiabatic path they follow, E_{SP} may correspond to an effective $n^*=n\pm\frac{1}{2}$), while the remaining 78% of the molecules should ionize hydrogenically. This result fits almost perfectly the top spectrum in Fig. 6, where we see that about 25% of the molecules excited in the $n=70$ manifold in region 1 are field ionized just above F_{SP} while the remaining signal follows rather precisely the hydrogenic simulation shown by the dashed line (see also the experimental results for atomic hydrogen in Fig. 8). We observed rather similar behavior in experiments in atomic helium, and it is obvious from the above discussion that such behavior should be observed whenever the laser bandwidth encompasses the entire Stark manifold.

C. Influence of M_N on the electric-field ionization process

In Figs. 3 and 5, we note a difference in the behavior of the $M_N=0$ and $M_N=1$ Stark states. A significant proportion of $M_N=1$ states are stable, on the time scale of about 1 μs, above the saddle-point energy while nearly all $M_N=0$ states ionize within this time frame. The fraction of M_N states that are "stable" decreases as the field strength increases. For $M_N=1$, almost 40% of the molecules are stable above E_{SP} when $F=2$ V/cm. This fraction decreases to 30 at $F=5$ V/cm, and to 20% at $F=10$ V/cm. For $M_N=0$, the fraction is 15% at $F=2$ V/cm, less than 5% at $F=5$ V/cm, and not measurable at $F=10$ V/cm. According to Eq. (2), these field values for E_{SP} correspond n^*_{SP} (values of the effective quantum number at the saddle point) of 113, 90, and 75, respectively. Below, we attempt to explain the difference in the $M_N=0$ and 1 spectra by using the results from a perturbative description of the Stark manifold of H_3.

While a calculation for such large values of n is quite straightforward, we considered such an exercise out of proportion to our purpose and unnecessarily complicating owing to the very large number of Stark states involved at high n values. For reasons of clarity, we chose to examine the Stark manifolds for $n = 19$ and 20. The results for these states should contain the essence of what is important for the higher n values, and they can be scaled to the case for the higher values. Figures 10 and 11 exhibit the Stark states predicted by the perturbative theory in the region of the crossing between the $n = 19$ and 20 manifolds for $M_N = 0$ (Fig. 10) and $M_N = 1$ (Fig. 11). The Stark maps appear to be similar, but they reveal significant differences between the two cases.

For $M_N = 0$, some avoided crossings are large (> 0.1 cm^{-1}) and some nearly negligible (< 0.01 cm^{-1}). Examination of a particular state from low field strength into the crossing region shows that it is always part of an ensemble of three states which never get closer than ~ 0.1 cm^{-1} to any another triplet. This feature is particularly apparent in the close-up view shown in the lower part of Fig. 10. Sets of three sublevels exist because the $N^+ = 1$ value of the core kinetic momentum gives rise to three components for each (n_1, n_2) state that correspond [45] to the three orientations of N^- in the relation $N = I + N^+$, despite the fact that N and l are not well-defined quantum numbers in the presence of the field. We note from the

manifold shown in the top part of Fig. 10 that this triplet character persists up into the high-field region.

For $M_N = 1$ (Fig. 11), particular levels cannot be uniquely grouped into triplets once they reach the region of n mixing. One member of each triplet develops along a diabatic path as F increases. Such paths are indicated by a dashed arrow in the detail of Fig. 11. The calculation shows that these diabatic states have negligible s and p character ($\sim 10^{-4}$ for $n \simeq 20$) while they possess a significant d component ($0.1-0.2$ for $n \simeq 20$). We also conclude from the examination of the results of the perturbative calculation that these diabatic states bear about one-third of the total oscillator strength. We attribute the appearance of stable states above the saddle point in Fig. 5(b) to the existence of these diabatic components of the Stark manifold.

As a further difference to the $M_N = 0$ case in Fig. 10, the adiabatic components of the $M_N = 1$ manifold show generally smaller avoided crossings than those for $M_N = 0$ (by about one order of magnitude). For atomic species, it is well known that the hydrogenic character becomes more pronounced as m_l increases, because of the diminution of the quantum defect with l. In the atomic case, a given m_l manifold includes only those states that have $l > m_l$. It is not clear a priori that the same situation exists in a molecular system, where the good quantum number M_N (m_l is not defined) does not formally impose a restriction on the value of l. Hence, the origin of the weak-

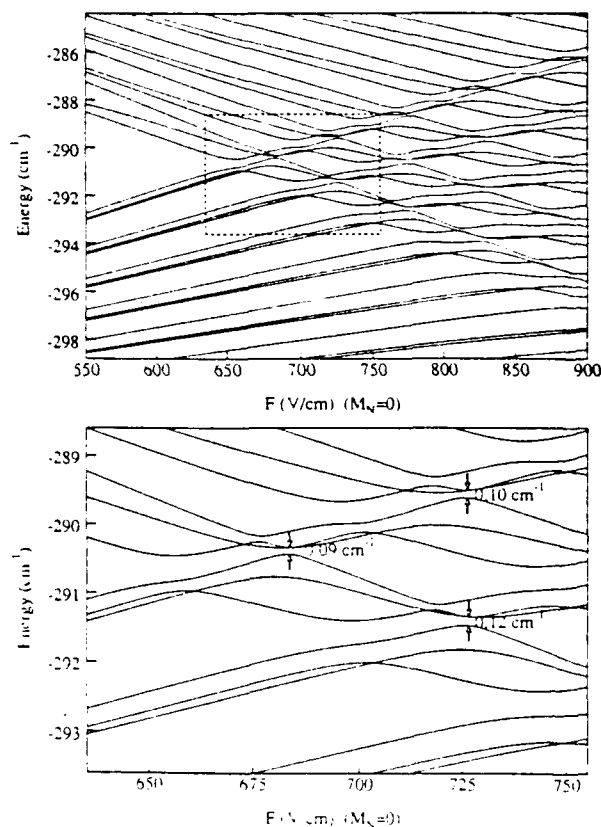FIG. 10. Stark map of H_3, $M_N = 0$, showing the region of the crossing between the $n = 19$ and $n = 20$ manifolds (top) and details of the area within the dashed rectangle (bottom). Arrows in the bottom figure indicate the largest avoided crossings (see text).
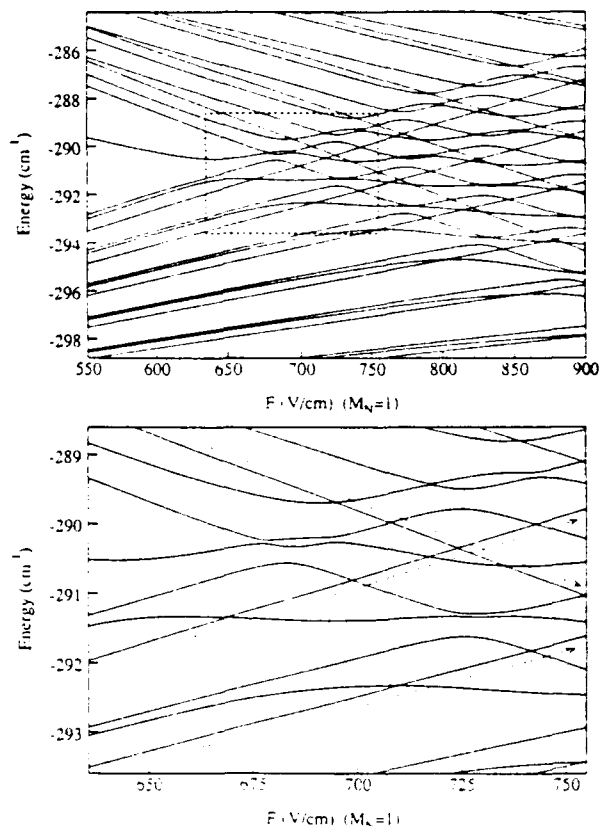

FIG. 11. Same as Fig. 10 but for the case $M_N = 1$. Long dashed arrows underline the paths followed by the "diabatic" component of the Stark manifold.

er couplings occurring among the $M_N = 1$ states is not obvious *a priori*. Inspection of the perturbation basis for $M_N = 0$ and 1 shows that their only difference is the absence of the $(np, N = 0)$ element in the $|M_N = 1\rangle$ basis. Experiments described in Ref. [40] show that the $(np, N = 0)$ state is a strong mediator between the s and d states.

The lack of the $(np, N = 0)$ element in the $M_N = 1$ case therefore appears to lead to a diminution of the coupling, and we consider this lack to be the origin of the different behavior of states above the saddle-point energy. The width of the avoided crossings is a measure of the strength of the couplings between states from neighboring n manifolds and hence also of the importance of the mixing between these states. A comparison of Figs. 10 and 11 therefore suggests that the $M_N = 0$ manifolds are more strongly coupled and mixed than the $M_N = 1$ states. The magnitude of the avoided crossings suggests that this difference is about one order of magnitude. This difference is a particular characteristic of H_3.

D. Dynamic evolution of Stark states

The results of the perturbative calculation presented in Figs. 10 and 11 can be used to analyze the dynamic evolution of states that are excited in a near-zero field and then subjected to a Stark field. We choose the example of Fig. 6 (top spectrum), where molecules are first excited to $n = 70$ in a near-zero field and then enter (in about 100 ns) the Stark-field region. We examine the dynamic path followed by the $M_N = 0$ and $M_N = 1$ components. To apply the results in Figs. 10 and 11, we extrapolate these calculations to $n \sim 70$. The matrix elements of the Stark Hamiltonian between two neighboring states are proportional [45] to $n^2 F$. The field strength corresponding to the onset of n mixing is $F_c = (3n^5)^{-1}$ (in a.u.). Hence, in the region of the avoided crossings, Stark Hamiltonian matrix elements between adjacent states are proportional to n^{-3}. The width of the avoided crossings is directly proportional to these matrix elements. Therefore the width of the avoided crossings for $n = 70$ should be about $(\frac{70}{20})^3$ times smaller than that for $n = 20$. In the $n = 70$ manifold, the width of the large avoided crossings between each triplet will be of the order of 2×10^{-3} cm^{-1} for $M_N = 0$ and 2×10^{-4} cm^{-1} for $M_N = 1$. Using the Landau-Zener formula [48], we next calculate the probability for the system to jump from a diabatic state 0 to a diabatic state 1 at the crossing

$$P_{01} \approx \exp - \left| \frac{\eta_{01}}{v} \right| , \tag{10}$$

where

$$\eta_{01} = \frac{\frac{2\pi}{\hbar} V_{01}^2}{\left| \frac{\partial E_1}{\partial F} - \frac{\partial E_0}{\partial F} \right|}$$

and

$$v = \frac{\partial F}{\partial t} .$$

E_0 and E_1 are the Stark energies of states 0 and 1, and V_{01} is the matrix element between the two states (one-half of the width of the avoided crossing). For the extreme members of two neighboring manifolds $[(n, n_1 \sim n)$ and $(n+1, n_1 \sim 0)]$ and for the values $n = 70$, $F = 10$ V/cm, $\Delta t = 100$ ns, Eq. (10) leads to

$$1 - P_{01} = \begin{cases} 2 \times 10^{-2} & (\text{for } M_N = 0) \\ 2 \times 10^{-4} & (\text{for } M_N = 1) . \end{cases}$$

The number of large avoided crossings that a given state encounters is on the order of (nF_{SP}/F_c), which is about $(3n^2/16)$. Under the (very crude) assumption that P_{01} is of similar magnitude at each crossing, the total probability that the system remains in the same diabatic state when F is increased from 0 to F_{SP} is about

$$P_{01}^{tot} = (P_{01})^{3n^2/16} . \tag{11}$$

In the present case this gives

$$P_{01}^{tot} \approx \begin{cases} 0 & (\text{for } M_N = 0) \\ 0.83 & (\text{for } M_N = 1) . \end{cases}$$

We conclude that under our experimental conditions the evolution of the $M_N = 0$ components is globally adiabatic while the evolution of the $M_N = 1$ components is mainly diabatic. This discussion also shows that diabaticity and hydrogenic behavior are far from synonymous.

VI. CONCLUSIONS

Ionization of high-Rydberg states of triatomic hydrogen in an external electric field has been investigated. The experimental results have demonstrated a fundamentally different behavior between states prepared in the electric field and those prepared prior to application of the electric field. A significant difference in character between the $M_N = 1$ states and the $M_N = 0$ states has been found. Both results have been discussed in the framework of a perturbative treatment of the Stark effect. The first aspect has been shown to be a rather general consequence of the lack of a durable quantization axis in a near-zero-field region. The second point is related to the weaker couplings that exist between the $M_N = 1$ series members and it results mainly from the absence of the np ($N = 0$) component in the $M_N = 1$ manifold.

*Permanent address: Laboratoire de Spectrometrie Ionique et Moleculaire, Universite Lyon I, Bâtiment 205, 43 Boulevard du 11 Novembre 1918, 69622 Villeurbanne CEDEX, France.

[1] J. E. Bayfield and P. M. Koch, Phys. Rev. Lett. **33**, 258 (1974).

[2] P. M. Koch and D. R. Mariani, Phys. Rev. Lett. **46**, 1275 (1981).

[3] H. A. Bethe and E. E. Salpeter, *Quantum Mechanics of One- and Two-Electron Atoms* (Plenum, New York, 1977).

[4] D. S. Bailey, J. R. Hiskes, and A. C. Riviere, Nucl. Fusion **5**, 41 (1965).

[5] M. H. Rice and R. H. Good, Jr., J. Opt. Soc. Am. **52**, 239 (1962).

[6] D. R. Herrick, J. Chem. Phys. **65**, 3529 (1976).

[7] R. J. Damburg and V. V. Kolosov, J. Phys. B **9**, 3149 (1976); **11**, 1921 (1978); **12**, 2637 (1979).

[8] D. Banks and J. G. Leopold, J. Phys. B **11**, 37 (1978).

[9] H. J. Silverstone, Phys. Rev. A **18**, 1853 (1978).

[10] H. J. Silverstone, B. G. Adams, J. Cizek, and P. Otto, Phys. Rev. Lett. **43**, 1498 (1979).

[11] E. Luc-Koenig and A. Bachelier, J. Phys. B **13**, 1743 (1980); **13**, 1769 (1980).

[12] M. L. Zimmerman, M. G. Littman, M. M. Kash, and D. Kleppner, Phys. Rev. A **20**, 2251 (1979).

[13] D. Kleppner, M. G. Littman, and M. L. Zimmerman, in *Rydberg States of Atoms and Molecules*, edited by R. F. Stebbings and F. B. Dunning (Cambridge University Press, Cambridge, England, 1983); M. G. Littman, M. M. Kash, and D. Kleppner, Phys. Rev. Lett. **41**, 103 (1978).

[14] T. W. Ducas, M. G. Littman, R. R. Freeman, and D. Kleppner, Phys. Rev. Lett. **35**, 366 (1975).

[15] D. Tuan, S. Liberman, and J. Pinard, Opt. Commun. **18**, 533 (1976).

[16] T. F. Gallagher, L. M. Humphrey, R. M. Hill, and S. M. Edelstein, Phys. Rev. Lett. **37**, 1465 (1976).

[17] C. Fabre, P. Goy, and S. Haroche, J. Phys. B **10**, L183 (1977).

[18] T. F. Gallagher, L. M. Humphrey, W. E. Cooke, R. M. Hill, and S. A. Edelstein, Phys. Rev. A **16**, 1098 (1977).

[19] J. L. Vialle and H. T. Duong, J. Phys. B **12**, 1407 (1979).

[20] T. H. Jeys, G. W. Foltz, K. A. Smith, E. J. Beiting, F. G. Kellert, F. B. Dunning, and R. F. Stebbings, Phys. Rev. Lett. **44**, 390 (1980).

[21] F. G. Kellert, T. H. Jeys, G. B. McMillian, K. A. Smith, F. B. Dunning, and R. F. Stebbings, Phys. Rev. A **23**, 1127 (1981).

[22] T. H. Jeys, G. B. McMillian, K. A. Smith, F. B. Dunning, and R. F. Stebbings, Phys. Rev. A **26**, 335 (1982).

[23] F. B. Dunning and R. F. Stebbings, in *Rydberg States of Atoms and Molecules* Ref. [13].

[24] S. Feneuille, S. Liberman, J. Pinard, and A. Taieb, Phys. Rev. Lett. **42**, 1406 (1979).

[25] S. Liberman and J. Pinard, Phys. Rev. A **20**, 507 (1979).

[26] W. Sandner, K. A. Safinya, and T. F. Gallagher, Phys. Rev. A **33**, 1008 (1986).

[27] W. Van der Water, D. R. Mariani, and P. M. Koch, Phys. Rev. A **30**, 2399 (1984).

[28] R. F. Stebbings, C. J. Lattimer, W. P. West, F. P. Dunning, and T. B. Cooke, Phys. Rev. A **20**, 2251 (1979).

[29] C. F. Barnett, J. A. Ray, and A. Russek, Phys. Rev. A **5**, 2110 (1972).

[30] T. J. Morgan, C. F. Barnett, J. A. Ray, and A. Russek, Phys. Rev. A **20**, 1062 (1979).

[31] R. Kachru and H. Helm, Phys. Rev. Lett. **55**, 1575 (1985).

[32] E. Y. Xu, H. Helm, and R. Kachru, Phys. Rev. Lett. **59**, 1096 (1987).

[33] C. R. Mahon, G. R. Janik, and T. F. Gallagher, Phys. Rev. A **41**, 3746 (1990).

[34] D. Eisel and W. Demtröder, Chem. Phys. Lett. **88**, 481 (1982).

[35] G. R. Janik, O. C. Mullins, C. R. Mahon, and T. F. Gallagher, Phys. Rev. A **35**, 2345 (1987).

[36] C. Bordas, M. Broyer, P. Labastie, and B. Tribollet, in *Photophysics and Photochemistry Above 6 eV*, edited by F. Lahmani (Elsevier, Amsterdam, 1985).

[37] C. Bordas, P. Brevet, M. Broyer, J. Chevaleyre, and P. Labastie, Europhys. Lett. **3**, 789 (1987).

[38] E. D. Poliakoff, J. L. Dehmer, A. C. Parr, and G. E. Leroi, Chem. Phys. Lett. **111**, 128 (1984).

[39] M. A. Duncan, T. G. Dietz, and H. E. Smalley, J. Chem. Phys. **75**, 2118 (1981).

[40] C. Bordas and H. Helm, Phys. Rev. A **43**, 3645 (1991).

[41] H. Helm, Phys. Rev. Lett. **56**, 42 (1986); Phys. Rev. A **38**, 3425 (1988).

[42] L. J. Lembo, C. Bordas, and H. Helm, Phys. Rev. A **42**, 6660 (1990).

[43] C. Bordas, L. J. Lembo, and H. Helm, Phys. Rev. A **44**, 1817 (1991).

[44] A. Dodhy, W. Ketterle, H.-P. Messmer, and H. Walther, Chem. Phys. Lett. **151**, 133 (1988).

[45] C. Bordas and H. Helm, Phys. Rev. A **45**, 387 (1992).

[46] G. I. Gellene and R. F. Porter, J. Chem. Phys. **93**, 6303 (1990).

[47] W. E. Cooke and T. F. Gallagher, Phys. Rev. A **17**, 1226 (1978).

[48] *Atomic and Molecular Processes*, edited by D. R. Bates (Academic, New York, 1962).

Appendix F

PREDISSOCIATION OF EXCITED STATES OF H_3

PREDISSOCIATION OF EXCITED STATES OF H₃

Hanspeter Helm

Molecular Physics Laboratory
SRI International
Menlo Park, Ca 94025.

A review of experimental observations on predissociation of excited states of the triatomic hydrogen molecule is presented. The possible significance of the various predissociation channels observed for bound states of H$_3$ as decay paths in dissociative recombination of H$_3^+$ with low energy electrons is discussed.

INTRODUCTION

Evidence for predissociation of triatomic hydrogen comes from line broadening observed in emission[1,2] and in absorption,[3] from observation of the neutral fragments that are formed in photodissociation[4] and dissociative electron capture[5] and from observations of rapid loss of excited state density in specific rovibrational levels in high Rydberg states.[6-8]

The coupling of excited states of H$_3$ to the continuum has also been of theoretical interest,[9-11] specifically in view of the importance of dissociative states of H$_3$ for the dissociative recombination reaction of H$_3^+$. The magnitude of the recombination rate has a rich history of controversy[12-15] with several recent experiments pointing to the existence of a fast recombination channel for 'cold' H$_3^+$ with low energy electrons,[15-17] confirming the earliest report on this reaction.[12] Theory has found it impossible to explain a high rate for dissociative recombination by low energy electrons,[9,10] and one set of experiments[13] has reported consistently small recombination rates for 'cold' H$_3^+$. The reason that theory finds no significant reactions for the lowest vibrational level of H$_3^+$ and thermal electrons is the apparent absence of suitable dissociative continua through which the reaction

$$H_3^+ + e \rightarrow H_3^{**} \rightarrow H_2 + H \tag{1}$$

could proceed. In the D$_{3h}$ geometry of ground state H$_3^+$ the repulsive ground state of H$_3$ is the sole continuum state below the ionization threshold. This surface lies 7 eV below H$_3^+$ at the equilibrium geometry of the ion.

Here we discuss the various experimental observations of predissociation of excited states of H$_3$ and the roles that bound excited states of H$_3$ could play in the dissociative recombination process.

POTENTIAL ENERGY CURVES

In Figure 1 we show the results of molecular structure calculations of Petsalakis et al.[11] for three special geometries of neutral triatomic hydrogen. The curves in the center of the figure correspond to the equilibrium geometry of the ionic ground state, D_{3h}. All spectroscopic observations of Rydberg states of H_3 refer to excited states with geometries close to this one. In D_{3h} representation the lowest energy potential curve, $1^2E'$, depicts the Jahn-Teller seam of the degenerate ground state surface along the diagonal coordinate of the lower surface shown in Figure 2. That is, the minimum along the curve, $1^2E'$, in Figure 1 represents the saddle point energy in the continuum of the ground state. The upper sheet of the Jahn-Teller surface (not shown in Figure 2) grows from this seam.[18] A similar description applies to all other potential energy curves with E symmetry. However for the higher-lying degenerate states the lower and uppers sheets remain bound up to energies above the ionization threshold. Energy surfaces of these states have been calculated by Nader and Jungen[19] for n=2,3,4 and 5.

The nondegenerate states of A''_1 and A''_2 symmetry can be described (in D_{3h}) by surfaces that lie nearly parallel to the ionic ground state surface, as long as the energy lies below the ionization threshold. A representation of the ionic ground state surface is given in the upper part of Figure 2.

As a consequence of the strong binding energy[20] of H_3^+ (4.373 eV) and the low ionization potential of H(n=2), 3.402 eV, the sole dissociation limits that fall below the ionization threshold are the limits formed from ground state atomic hydrogen, H(1s) + H(1s) + H(1s) and $H_2(X^1\Sigma_g^+)$ + H(1s). Any dissociation process of H_3 states with energies in the vicinity of, or below the ionization threshold must connect to the ground state surface of H_3. As long as neutral H_3 is restricted to D_{3h} geometry (or one such as chosen in Figure 2) the excited state surfaces are embedded in the ground state surface, but they do not intersect at energies below the ionization threshold.
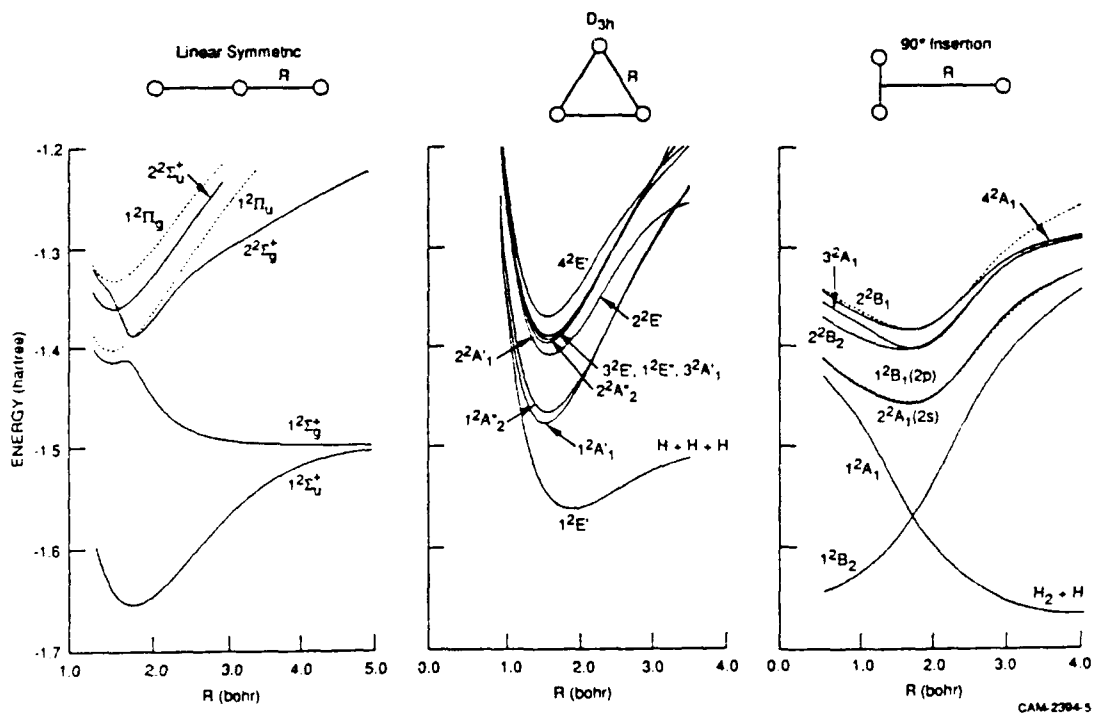

Figure 1. Potential energy curves of H_3 for the linear symmetric, D_{3h}, and 90° insertion configurations. (Petsalakis et al., Ref 11).
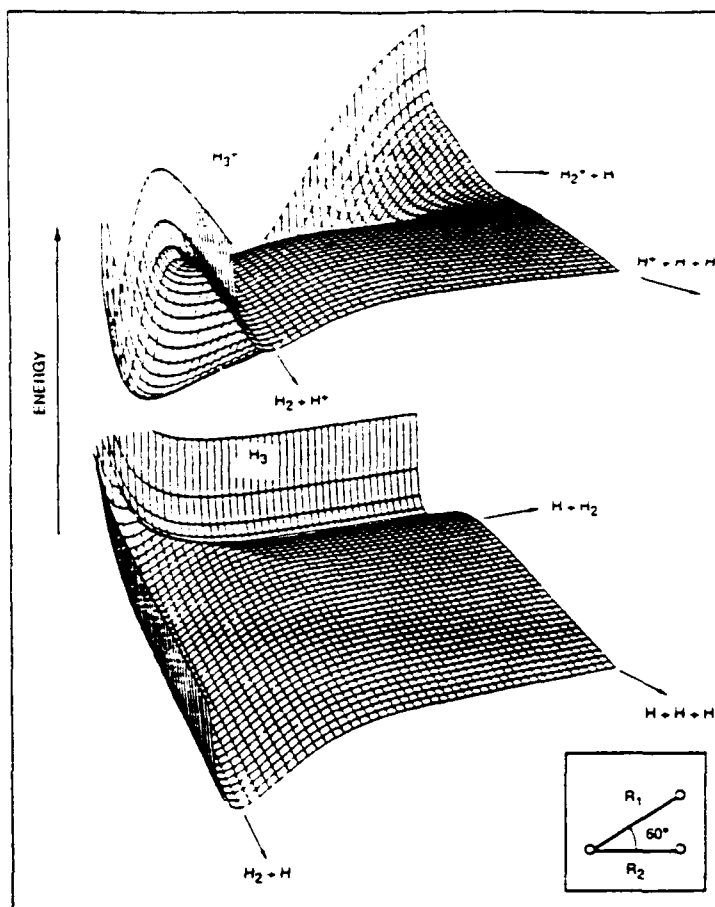
Figure 2. Potential energy surfaces for ground state H_3 and ground state H_3^+ (Murrell et al., Ref. 18).

By contrast, when the triangular configuration is opened to a linear one, the resultant Σ_g^+ states follow a sequence of avoided crossings (Figure 1, left diagram) indicating that gerade states are subject to rapid dissociation to ground state atomic hydrogen. In an adiabatic path the A_1' and E' states connect to Σ_g^+ states.[21] The energy difference between the lowest vibrational level of H_3^+ (D_{3h} geometry) and the lowest linear symmetric configuration is ~ 2.5 eV. Therefore an electronic state of H_3 in low vibrational excitation needs to tunnel through a significant barrier in order to find the efficient dissociation paths that exist near the linear geometry. For the $1^2A_1'$ state (2s) an energy of 1.5 eV is required to reach the barrier in the $1^2\Sigma_g^+$ curve (see Figure 1 center and left).

Additional dissociation limits are open only above the ionization threshold. The first of these, $H_2(X^2\Sigma_g^+) + H(n=2)$ lies 973 meV above the lowest level of H_3^+. In Figure 3 we show the energy of this limit together with the lowest vibrational levels of H_3^+.

In the framework of the theoretical potential energy surfaces known to date, predissociation of triatomic hydrogen in low vibrational levels can be efficient only for states that exhibit good Frank-Condon factors with the electronic ground state of H_3. This is certainly the case for states belonging to the n=2 manifold, the states labeled $1^2A_1'$ and $1^2A_2''$ in Figure 1. Experimental observations confirm this case as will be discussed in the next section. We then review observations that indicate significant predissociation in Rydberg states of higher principal quantum numbers. In order to explain the existence of these predissociation channels we need to invoke a fairly efficient mechanism for coupling among the Rydberg states. This coupling refers to the transfer between electronic and vibrational energy in the high Rydberg states. The origin for an efficient transfer is not obvious when considering the potential energy curves in D_{3h} geometry. This coupling is likely to play a role in dissociative channels for recombination, a topic we discuss in the final section.
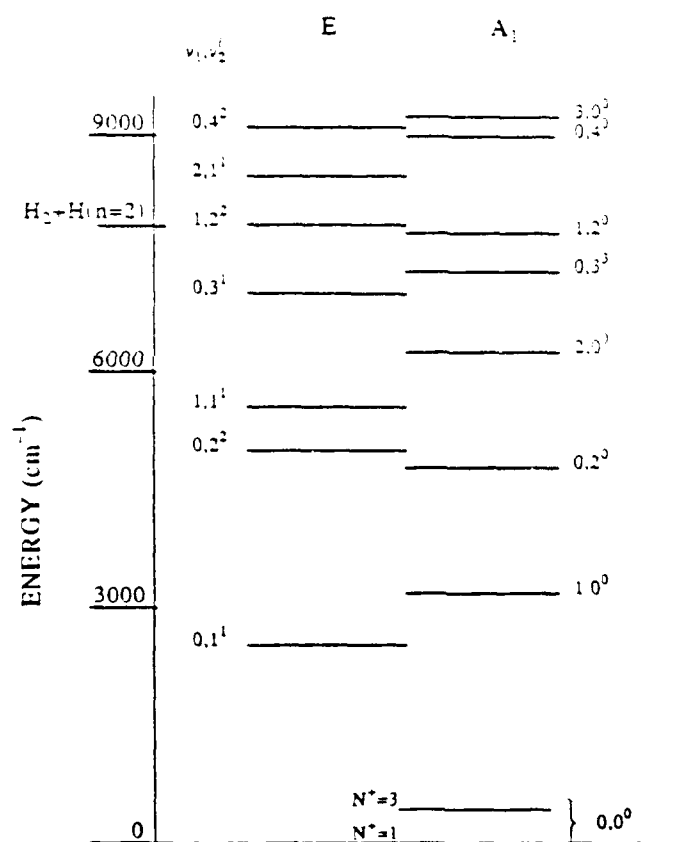
Figure 3. Energy of the lowest vibrational levels of H_3^+ and the lowest excited state dissociation limit of H_3 (Tennyson and Henderson, Ref. 29).

PREDISSOCIATION CHANNELS IN D_{3h} GEOMETRY

Table 1 gives a list of states for which explicit predissociation lifetimes have been determined.

Table 1. Predissociation rates of neutral states of triatomic hydrogen, H_3. Energies (cm^{-1}) are given relative to the lowest ionization threshold of H_3^+.

State	v_1,v_2,N,K	Energy	Rate		Coupling	Ref.
$2s^2A_1'$	0,0,1,0	30460	6.2	(12)	vibrational	(1)
$3s^2A_1'$	0,0,1,0	12868	<1.0	(9)	vibrational	(22)
$4s^2A_1'$	0,0,1,0	7140	1.4	(11)	vibrational	(3)
$4s^2A_1'$	1,0,1,0	3931	4.1	(10)	vibrational	(3)
$5s^2A_1'$	0,0,1,0	4530	2.5	(11)	vibrational	(3)
$2p^2A_2''$	0,0,1,1	29480	1.4	(10)	rotational	(2)
$3d^2E''$	0,0,1,0	12265	<1.0	(9)	rotational	(22)
I(61p)	?,?,2,0	29	2.5	(9)	vibrational	(6)
$2p^2A_2''$	0,0,0,0	29562	1.5	(5)	spin-orbit	(24)

86

Electronic states of A_1'' symmetry are coupled to the dissociative ground state, $1^2E'$, by the bending vibration (which is of symmetry E'). The lowest A_1' state, $2s^2A_1'$, (labeled $1^2A_1'$ in Figure 1) is observed[1] to be rapidly predissociated in its ground vibrational level. The lifetime is 160 fs for H_3 and about 300 fs for D_3. The strength of this dissociation channel is due to the good Franck-Condon factor. This can be envisioned from the proximity of the respective potential energy curves in Figure 1 (center). However, the latter give the energies along the symmetric stretch coordinate, which is not what couples the two states. The apparent mass effect is attributed to changes in the Franck-Condon factor,[1] the vibrational coupling element itself being mass independent.

Similar considerations should apply to the higher lying excited states of A_1' symmetry, however the increasing separation from the ground state surface leads us to expect that the wavefunction overlap diminishes, thereby decreasing the probability of predissociation. Indeed a very low rate of predissociation[20,22] is observed for the lowest vibrational level of the $3s^2A_1'$ state (labeled $2^2A_1'$ in Figure 1). The predissociation rate for this state is at least 3 orders of magnitude smaller than that of the $2s^2A_1'$ state, and radiation is a dominant decay channel for $3s^2A_1'$. Unexpectedly, the predissociation rates for the 4s and 5s states are observed to be large again,[3] a feature that does not square with the picture of an interaction between an isolated Rydberg state and the ground state surface. Before addressing this anomaly further we discuss other experimental observations of predissociation.

Electronic states of A_2'' symmetry are coupled to the ground state surface primarily by rotational coupling. The most direct evidence for this mechanism comes from the observations by Herzberg, Hougen, and Watson[2] who show that the widths of the rotational levels in the $2p^2A_2''$ state increase proportional to the quantity $B[N \cdot (N+1)-K^2]$. Here B is the rotational constant, N the total angular momentum and K the projection of N along the figure axis. This quantity represents the energy of tumbling motion around an axis in the plane containing the three hydrogen atoms. This motion turns the configuration of $2pA_2''$ (p orbital perpendicular to the plane of H_3^+) into the ground state configuration, $1^2E'$ (p-type orbital in the plane of the nuclei). This predissociation channel is quite strong for the $2pA_2''$ state but it is significantly slower for the corresponding 3p state (labeled $2^2A_2''$ in Figure 1) for which radiation is the dominant decay path.[1,23] For the deuterated species, D_3, the rotational coupling effect is expected to be smaller by about factor of two. However the experimental linewidths[1] observed for the $2pA_2''$ state of D_3 suggest a reduction in linewidth larger than this.

No experimental information is available for predissociation of the higher lying p-states except for 43p and 61p.[7] We will discuss these states later.

Predissociation has also been observed for d-type Rydberg states.[3,4] The dominant coupling path for the d^2E'' states is rotational coupling. The predissociation is observed to be slow for the n=3 d-states.

In addition to vibrational and rotational coupling, other weaker terms will contribute to predissociation for all states. The likely strongest among these is spin-orbit coupling. Its contribution to the decay rate of the N=0,K=0 level of $2p^2A_2''$ has been estimated[24] at $1.5 \cdot 10^5$ s^{-1}.


PREDISSOCIATION OF HIGH LYING RYDBERG STATES

Predissociation of selected high-lying Rydberg states of H_3 is suggested by the observations of windows in the excitation spectra of the Rydberg series. In these experiments[6-8,25,26] Rydberg states are photoexcited from the long-lived N=0,K=0 level of the $2p^2A_2''$ state and the resultant excited state population is interrogated a few 10 ns to several 100 ns later by electric field ionization. Dodhy et al.[6] attributed the absence of high lying s-states in their experimental spectrum to predissociation. Intensity windows in the

d-Rydberg series between n=17 and n=25 and around n=43 were also observed[6,7,25] and attributed to selective predissociation of these states.

In order to proof that the absence of exited state population in these experiments is indeed a result of rapid loss of the Rydberg levels, rather than a result of diminuation of excitation probability (due to channel interactions), various depletion experiments were carried out. The depletion experiments probe the loss of lower state population, rather than the existence of long lived Rydberg states.[7,27] These experiments showed that those s- and d-type Rydberg levels that are missing in the spectra detected by field-ionization are photoexcited as efficiently as those Rydberg states that do appear in the field-ionization spectra.

In the field ionization experiments, the time between detection of the Rydbergs and their creation is fairly long (10 to several 100 ns). The loss of Rydberg population may therefore in principle either be due to enhanced radiative loss or due to predissociation. Considering typical radiative lifetimes[28] of H_3 (they fall into the 10 ns range) we conclude that extremely strong mixing with radiative states would have to occur to achieve the removal of these selected Rydberg states on the time scale of observation. This suggests that moderate to weak mixing with rapidly predissociated states is more likely responsible for the absence of selected high lying Rydberg states. Only this latter mechanism is consistent with the appearance of windows that cover many neighboring Rydberg levels (for example 18s to 24s).

The lifetime of one of the high lying states has been measured explicitly.[7] This state lies close in energy to the 61 p state. In Table 1 this state is identified as I(61p), where I should indicate an interloper state (dark state).
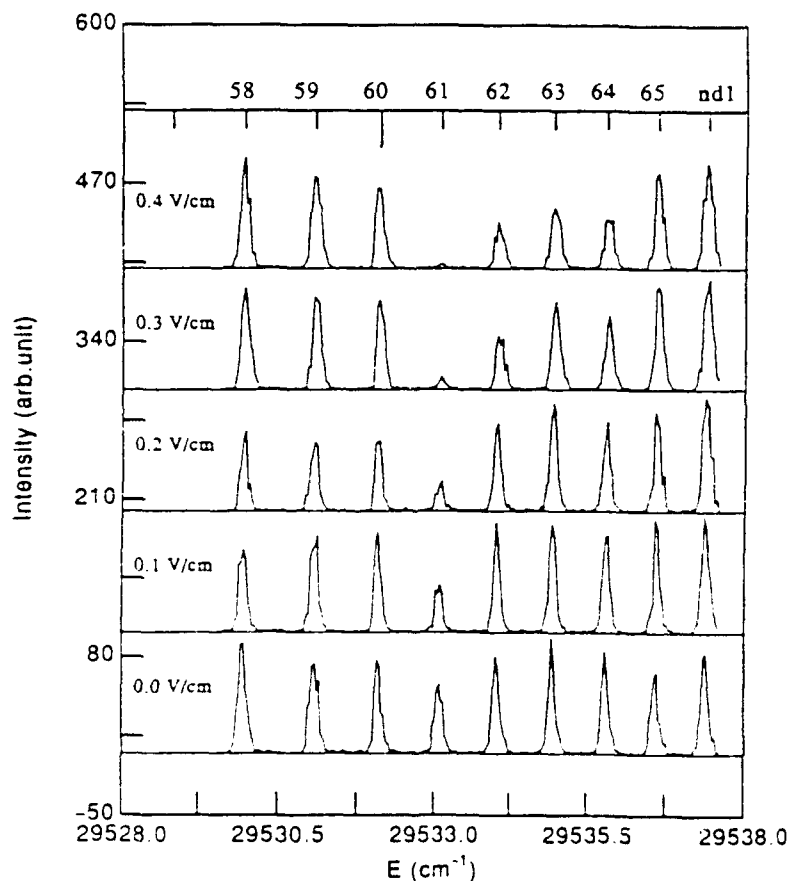
Figure 4. Low field Rydberg spectra in excitation from N=0, K=0 of the $2p^2A_2$ state. The window at the position of the 61 d state level is due to field induced predissociation (Bordas and Helm, Ref. 7).

The experimental observation is that this interloper state is responsible for the accidental predissociation of the (N=2) 61p Rydberg. This particular interloper is fairly narrow and lies within 0.2 cm⁻¹ of the 61p state. In this way it can selectively influence the 61p state, but its effect is much weaker on the n=60 and n=62 Rydbergs. Further evidence for its presence is the observation that when only very weak electric fields are applied, the ensuing Stark mixing gradually affects also the lifetime of the 61d Rydberg state which also lies close in energy. An example is shown in Figure 4. The gradual loss of 61d state population due to electric-field-induced coupling to an interloper state is clearly apparent from these results.

Several isolated window resonances such as shown in Figure 4 have been observed (43p, 61p, 64d, 86d, 129d), in addition to the wider windows that affect broad ranges of n-values in the s and d-type series. The windows are distributed in a seemingly irregular way across the entire energy spectrum, and they appear predominantly for low values of ℓ.

In the framework of the potential energy curves of Figure 1 (center) the question arises as to the mechanism that can induce predissociation at such energies, where the bound state wavefunction of the Rydberg states is spatially well removed from the dissociation continuum.

In the following we discuss possible mechanisms for these effects and their implications for dissociative recombination of H_3^+.

RYDBERG-RYDBERG COUPLING

The proximity of the energy surfaces of the n=2 Rydberg states ($2s^2A_2'$ and $2p^2A_2''$) with the ground state continuum is the origin for the high predissociation rates observed for the 2s and 2p levels. We should expect similarly high predissociation rates for the vibrationally exited levels in the n=2 states. Even higher rates appear possible at vibrational energies where the bound state wavefunction can explore the surface in the vicinity of the barrier in the $2\Sigma_g^+$ states that exist near the linear geometry (Figure 1 left). We can estimate the number of such rapidly predissociated levels per energy interval by considering the density of states of the ionic core, H_3^+. For a single rotational value, the density of vibrational levels[29,30] in H_3^+ is of the order of 50 per eV at 2 eV of vibrational excitation, increasing to > 300 per eV at 3 eV of vibrational excitation. Comparable densities of levels will exist in the $2s^2A_2'$ and $2p^2A_2'$ states. The width of the individual vibrational levels in these states will be of the order of 1 - 10 cm⁻¹, and likely higher for levels with vibrational energies that exceed the barrier between the D_{3h} and linear configuration.

This leads us to a situation where excited bound states of the higher Rydberg manifolds find themselves embedded in a dense manifold of highly vibrationally excited levels of the n=2 manifold. The high vibrational states are rapidly predissociated and therefore Rydberg states of higher principal quantum number will in many occasions lie degenerate with highly vibrationally excited Rydberg levels of the n=2 manifold, leading to accidental predissociation.

The predissociation properties of the n=2 states can be transmitted to the high Rydberg provided a good coupling mechanism exists between the two. In the absence of actual crossings of potential energy curves and in the absence of mediating electronic states (such as the repulsive doubly excited states of H_2) an efficient coupling between a low-n interloper and a high-n Rydberg state is however difficult to reconcile to be strong. The magnitude of the coupling depends on the variation of the quantum defects of the two states with internuclear distance. In a first approximation we might analyze the coupling strength analogous to that for vibrational autoionization.[31] Introducing a generalized distance coordinate, R, the coupling matrix element between an interloper characterized by quantum number n_I and a Rydberg state with quantum number n_R can be written as

$$W = [2Ryd/(n_I n_R)^{3/2}]\frac{\delta \Delta\mu}{\delta R} \langle \chi_I | R | \chi_R \rangle \tag{2}$$

Here Ryd is the Rydberg constant, χ_I and χ_R are the vibrational wavefunctions of the ion cores of the interloper and the Rydberg, respectively, and $\Delta\mu$ is the difference of R-dependent quantum defects between the two electronic states. According to the calculations of Nader and Jungen[19] the largest variation of the quantum defect with R occurs for the E' states. Nevertheless the coupling will be small if greatly disparate vibrational levels are involved because of the importance of the vibrational overlap integral in (2).

This picture has not yet been tested in a quantitative calculation but it provides for an irregular distribution of interloper levels through which accidental predissociations can occur. The interlopers spread over the entire region where the n=2 Rydberg states are bound.

DISSOCIATIVE RECOMBINATION

Dissociative recombination of diatomic molecules such as $H_2^+ + e$ has been analyzed in terms of two mechanisms, the so-called direct and indirect processes.[32] The direct process refers to a transition from the incoming continuum electron scattering state to a dissociative neutral state. The indirect process is one where the incoming electron vibrationally excites the core and is captured into a bound Rydberg orbital. The Rydberg state subsequently predissociates.

In the case of H_3^+ both processes will play an important role for vibrationally excited ions. However, for ground state H_3^+ the absence of a continuum state at the appropriate nuclear geometry suggests that the direct mechanism can only weakly contribute to recombination. The indirect process on the other hand, merely relies on the existence of Rydberg states that undergo predissociation. Experiments reviewed in this paper have shown the existence of many such states below the ionization threshold. The nature of these states suggest that similar states will exist above threshold as well, in the form of Rydberg states that converge to excited core states of the ion.

The mechanism that leads to predissociation of the Rydberg states is direct coupling and accidental coupling to the repulsive ground state of H_3. The direct coupling is be most important for the levels belonging to the n=2 Rydberg states. The accidental mechanism is appropriate for the high Rydberg states. It relies on degeneracies between high Rydberg states in low vibrational excitation and low Rydberg states (presumably n=2) in high vibrational states. The predissociation properties of the latter being shared with the former. The key event for this mechanism to be efficient is significant vibrational excitation in the electron capture process. For highly vibrationally excited states the wavefunction can extend into the dissociative region that characterizes the linear geometry, and in this way even a system such as cold H_3^+ could find dissociative recombination paths.

The author is unable to estimate even the magnitude of the indirect process but hopes that the observations of predissociation of states of H_3 near the ionization threshold and of high rates for dissociative recombination will trigger a thorough theoretical analysis of this subject.

ACKNOWLEDGMENTS

REFERENCES

1. I. Dabrowski and G. Herzberg, *Can. J. Phys.* 58:1239 (1980).
2. G. Herzberg, J. T. Hougen, and J. K. G. Watson, *Can. J. Phys.* 60:1261 (1982).
3. L. J. Lembo and H. Helm, *Chem. Phys. Lett.* 163:425 (1989).
4. P. C. Cosby and H. Helm, *Phys. Rev. Lett.* 61:298 (1988).
5. J. R. Peterson, P. Devynck, Ch. Hertzler, and W. G. Graham, *J. Chem. Phys.* 96:8128 (1992).
6. A. Dohdy, W. Ketterle, H.-P. Messmer and H. Walther, *Chem. Phys. Lett.* 151:133 (1988).
7. C. Bordas and H. Helm, *Phys. Rev. A* 43:3645 (1991).
8. C. Bordas, L. J. Lembo and H. Helm, *Phys. Rev. A* 44:1817 (1991).
9. K. C. Kulander and M. F. Guest, *J. Phys. B* 12:L501 (1979).
10. H. Michels and R. H.Hobbs, *Astrophys. J.* 286:L27 (1984).
11. I. D. Petsalakis, G. Theodorakopoulos, and J. S. Wright, *J. Chem. Phys.* 89:6850 (1988).
12. M. T. Leu, M. A. Biondi, and R. Johnson, *Phys. Rev. A* 8:413 (1973).
13. N. G. Adams, D. Smith, and E. Alge, *J. Chem. Phys.* 81:1778 (1984).
14. H. Hus, F. Youssif, A. Sen, and J.B.A. Mitchell, *Phys.Rev. A* 38:658 (1988).
15. T. Amano, J. Chem. Phys. 92:6492 (1990).
16. A. Canosa, J. C. Gomet, B. R. Rowe, J.B.A. Mitchell and J. L. Queffelec, *J. Chem. Phys.* 97:1028 (1992).
17. M. Larsson, H. Danared, J. R. Mowat, P. Sigray, G. Sundström, L. Broström, A. Filevich, A. Källberg, S. Mannervik, K. G. Rensfelt, and S. Datz , *Phys. Rev. Lett.* (1993)
18. J. N. Murrell, S. Carter, S. C. Farantos, P. Huxley, and A. J. C. Varandas, *Molecular Potential Energy Functions*, John Wiley (Chichester) 1984.
19. Ch. Nader and M. Jungen, *Chem. Phys.* 70:189 (1982).
20. P. C. Cosby and H. Helm, *Chem. Phys. Lett.* 152:71 (1988).
21. D. L. Huestis, private communication.
22. I. Hazell, N. Bjerre and D. C. Lorents,
23. G. Herzberg, H. Lew, J. J. Sloan, and J. K. G. Watson, *Can. J. Phys.* 59:428 (1981).
24. C. Bordas, P. C. Cosby, and H. Helm, *J. Chem. Phys.* 93:6303 (1990).
25. H. Helm, Phys. Rev. A 38:3425 (1988).
26. C. Bordas and H. Helm, *Phys. Rev. A* 45:387 (1992).
27. H. Helm, unpublished.
28. H. Figger, Y. Fukuda, H. Ketterle and H. Walther, *Can. J. Phys.* 62:1274 (1984).
29. J. Tennyson and J. R. Henderson, *J. Chem. Phys.* 91:3815 (1989).
30. M. Berblinger, C. Schlier, J. Tennyson and S. Miller, *J. Chem. Phys.* 96:6842 (1992).
31. G. Herzberg and Ch. Jungen, *J. Mol. Spectrosc.* 41:425 (1972).
32. J. N. Bardsley, *J. Phys. B. At. Mol. Phys.* 1:349 (1968).

Appendix G

OBSERVATION OF ELECTRONICALLY EXCITED STATES OF TETRA OXYGEN

Observation of electronically excited states of tetraoxygen

H. Helm and C. W. Walter

Molecular Physics Laboratory, SRI International, Menlo Park, California 94025

We have investigated electron transfer to O_4^- in reactions with O_2, NO, and Cs. We observe formation of O_4 molecules that decay by predissociation and by direct dissociation. The kinetic energy release in dissociation as well as the nature of the dissociation products are determined. Evidence for three short-lived electronic states of tetraoxygen at energies near 2 eV above $O_2 + O_2$ is obtained in electron transfer from O_2 and NO. In the experiment with cesium we find evidence for longer-lived electronic states ($10^{-13} < \tau < 10^{-7}$ s) at 9.4 and 10.5 eV. The energy release and symmetry of the dissociation pattern suggests that the high lying states are symmetric molecular configurations at extended bond lengths (~ 2.4 Å).

BACKGROUND

Ab initio theoretical studies of the O_4 molecule point to the existence of a metastable, covalent O_4 molecule that has a geometry quite different from the van der Waals structure, $(O_2)_2$, detected experimentally.[1] The weakly bound van der Waals molecule is characterized by a large O_2–O_2 equilibrium distance, ~ 3.3 Å.[2] On the other hand, the metastable molecule is predicted[3-5] to be quasisquare (side length of 1.433 Å), and slightly twisted out of plane, belonging to the symmetry group D_{2d} [see Fig. 1(e)]. The initial investigation of this structure by Adamantides *et al.*[3] has recently been confirmed at a higher level of theory in the work of Seidl and Schaefer[4] and by Dunn *et al.*[5] This metastable O_4 state represents a true minimum of the ground state surface of $O_2 + O_2$ and it is calculated to lie ~ 3.60 eV above the limit for two separated ground state O_2 molecules. Theory[4] further predicts the existence of larger ring forms of oxygen, analogous to those well known for sulfur.

Røeggen and Wisløff-Nilssen[6] explored the stability of a D_{3h} structure of O_4, characterized by a central oxygen atom and three equivalent ligand atoms [see Fig. 1(f)]. This form is analogous to the stable, isoelectronic molecule NO_3^-. At an equilibrium bond length of 1.330 Å this state is predicted to lie 100 meV above the energy of ground state ozone and oxygen in the ^1D state, and it is stable with respect to dissociation into $O_3 - O(^1D)$. It lies 6.18 eV above two separated O_2 molecules in their ground state. The equilibrium bond lengths in both predicted O_4 states are longer than in the diatomic species [see Figs. 1(a) and 1(b)].

Experimental work on the structure of O_4 has been restricted to studies of the van der Waals molecule and to the molecular ion. The ground state molecule, $[O_2(^3\Sigma_g^-)]_2$, and the excited dimer state $[O_2(^1\Delta_g)]_2$ are weakly bound (87 and 50 cm^{-1}, respectively).[7] By contrast the molecular ion shows substantial bonding (~ 400 meV).[8] The very detailed spectroscopic study of O_4^- isolated in a neon matrix by Thompson and Jacox[9] identifies the geometry of the ion as the *trans*-planar configuration (C_{2h}) [see Fig. 1(g)]. Recent theoretical work[10] suggests a rectangular form (D_{2h})

at slightly lower energy [Fig. 1(h)] but this structure is inconsistent with the species isolated in the matrix. The ESR matrix study of O_4^- by Knight *et al.*[11] shows that the ground state of O_4^- is nonlinear with quartet symmetry ($S = 3/2$), a finding consistent with either form of O_4^-.

To our knowledge the only experimental work on electronically excited states of O_4 is on cooperative fluorescence and absorption of $[O_2]_2$ in the liquid phase.[1,12,13] The work described here was undertaken with the goal of locating excited states of the O_4 molecule under conditions where geometries other than the van der Waals geometry are accessible. The interest in searching for the predicted metastable species is that it represents a high energy density material[14] potentially present in energized forms of liquid oxygen and ozone. While we cannot confirm the predicted structures[3-6] we have found first evidence for dissociative and predissociated bound excited states of O_4.

EXPERIMENTAL APPROACH

To explore excited electronic states of O_4 at geometries other than the van der Waals structure we have chosen charge transfer neutralization of fast (3–5 keV) O_4^+ ions. This technique has been applied successfully to study electronically excited states in a variety of molecules[15-20] (O_2, O_3, H_2, H_3, N_2, N_2^+, He_2, and HeH) and has also been used to prepare long-lived neutral excited states for photoionization[21] and photodissociation[22] experiments. The crux of this approach is that electron transfer from a neutral donor molecule to a molecular ion occurs with sizable cross section at elevated collision energies. The charge transfer is most efficient if the energy defect in the reaction is low, if the geometry of the parent ion and the newly formed neutral overlap, and if merely one electron has to be moved. However, these rules represent general trends and they are by no means strict.[23]

The power of the charge transfer technique in fast beams is that excited molecular states prepared in this way can be monitored with high sensitivity. For the present experiments we use a time and position sensitive detector[24] to monitor neutral fragments that are formed when these
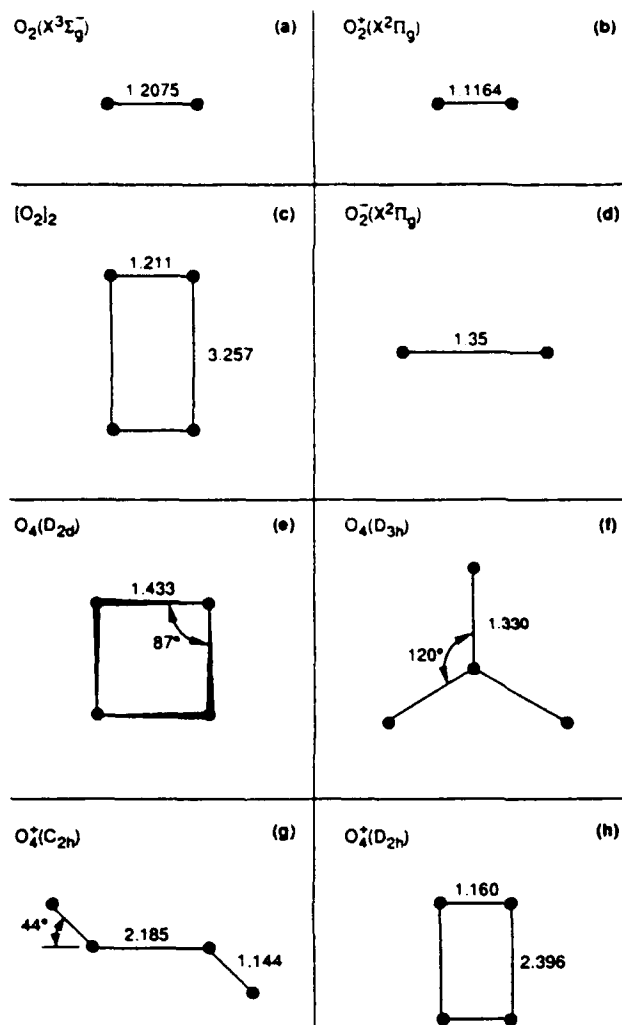
95

FIG. 1. Geometries of O_2, O_2^+, O_2^-, O_4, and O_4^+ from various experimental and theoretical sources [(a) Ref. 7, (b) Ref. 7, (c) Ref. 2, (d) Ref. 7, (e) Ref. 4, (f) Ref. 6, (g) Refs. 9, 10,(h) Ref. 10].
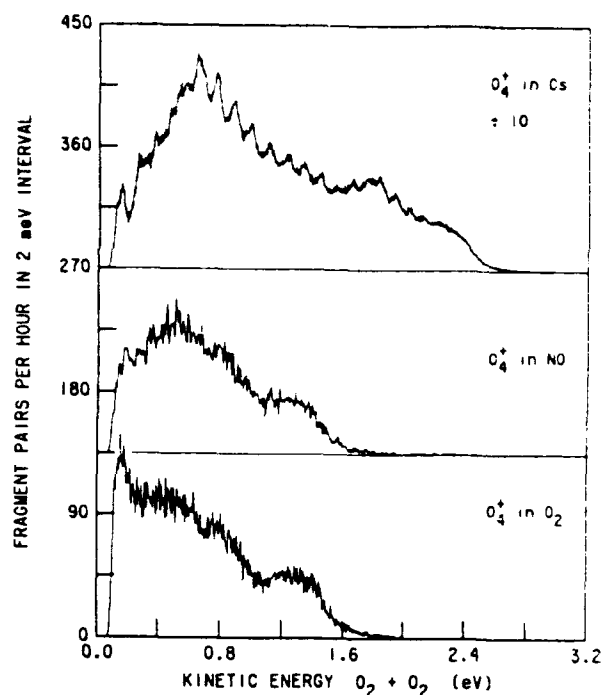

FIG. 2. Distribution of O_4 center-of-mass fragment kinetic energy obtained in charge transfer of O_4^+ with O_2, NO, and Cs. In all three cases only the fragments $O_2 + O_2$ were observed. Typical accumulation time for each spectrum is 8 h. The signal from Cs transfer has been divided by a factor of 10.

excited states decay by unimolecular dissociation and we determine the kinetic energy release to these fragments.

Our experiment is carried out using a beam of mass selected O_4^+ ions at a typical current of 10^{-11} A. Oxygen ions are first produced by electron impact ionization of a low pressure oxygen gas target and subsequent ion–molecule reactions lead to the formation of O_4^+. The ions are extracted from the source, accelerated to typically 4 keV energy and mass selected. The O_4^+ beam then passes through a short gas cell (5 mm length, 2000 mm from the ion source) containing the electron-donor molecules at a gas pressure of $\sim 10^{-4}$ Torr. O_2, NO, and Cs were used as electron donors in the present studies. Neutral molecules and atoms emerging from the gas cell are monitored after deflection of residual ions, using two methods.

One is the measurement of the total neutral beam that emerges from the cell in the original ion beam direction, using a picoammeter and relying on the electron emission induced by impact of fast neutrals on a stainless steel tar-

get. To enable detection as a neutral beam in the forward direction, the neutral molecules need to have a lifetime exceeding a few hundred nanoseconds. A detectable neutral beam in the forward direction is observed only with Cs as electron donor. It amounts to $\leq 0.5\%$ of the parent ion beam.[25] The absence of a neutral beam with O_2 or NO as electron donor implies that no long-lived O_4 molecules are formed in these cases.

The second measurement is the coincident detection and measurement of the kinetic energy of neutral fragments formed when O_4 dissociates following neutralization of O_4^+ in the electron transfer process. This measurement is carried out, one molecule at a time, using a position and time sensitive detector located ~ 1640 mm from the exit of the charge transfer cell.[24] O_4 molecules that dissociate within a short time after their formation ($< 10^{-7}$ s) are observed with all three electron donors, Cs, NO, and O_2. The characterization of these O_4 molecules forms the topic of this paper.

RESULTS AND DISCUSSION

A substantial signal from O_4 molecules that dissociate subsequent to formation by electron transfer is obtained with all three donors (Cs, O_2, and NO). At similar values of the pressure of the donor gas the fragment count rate with cesium exceeded that observed with O_2 and NO by about an order of magnitude. The fragment energy distributions are different in each case. The results are summa-
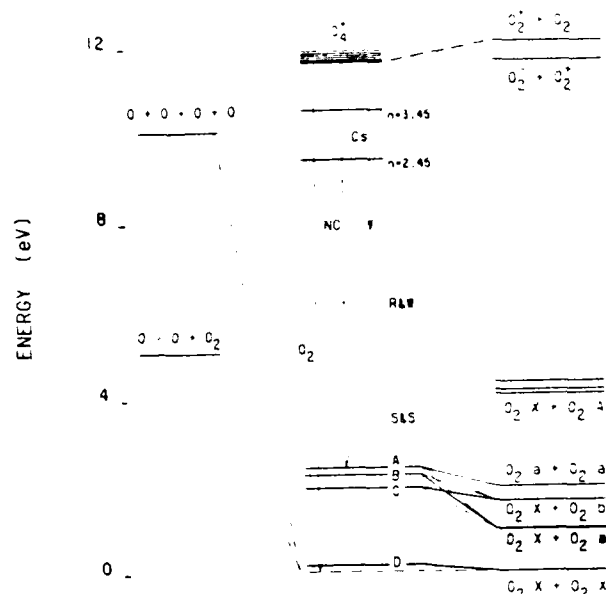
FIG. 3. Energy diagram pertaining to the three charge transfer processes. The length of the arrows indicates the cases of electron transfer with zero energy defect. In the center of the figure we indicate by the full lines the energetic location of excited O_4 states formed in charge transfer. The dotted lines refer to the states predicted by Seidl and Schaefer (Ref. 4) (3.6 eV) and by Røggen and Wisløff (Ref. 6) (6.18 eV). The branching among the dissociation limits observed for the electronic states A, B, C, and D is shown by lines. Thick lines indicate the dominant dissociation path (see Table I).

rized in Fig. 2 which gives the coincident counts of $O_2 + O_2$ pairs as a function of the kinetic energy release in the center of mass system of O_4. In all cases the fragments observed were $O_2 + O_2$. No contribution from monoatomic oxygen fragments was detected. We conclude that dissociation channels leading to atomic oxygen must be less than $\sim 5\%$ of the total fragment signal.

Electron transfer from NO and O_2

Figure 2 shows that transfer with NO and O_2 leads to qualitatively similar fragment energy spectra with characteristic minima and maxima. The energetics of the transfer process with NO and O_2 are indicated in Fig. 3. The length of the arrows from O_4^- gives the final state energy position for a reaction with zero energy defect. For example, the reaction

$$O_4^- + NO \rightarrow O_4^* + NO^- - (\Delta E \sim 0). \qquad (1)$$
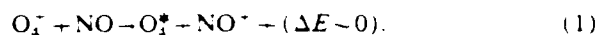
should land at an energy $IP(O_4)[11.65 \text{ eV}] - IP(NO)[9.2 \text{ eV}] = 2.5$ eV above the energy limit of separated ground state oxygen molecules in the case of zero energy defect.

The similar fragment energy spectra from NO and O_2 suggest that similar lower states of O_4 are accessed in the two cases. No theoretical guidance to the possible nature of excited electronic states of O_4 exists other than the prediction by Dunn et al.[5] of the ring structure at approximately 3.6 eV above the lowest dissociation limit. The states involved in our charge transfer experiment must rapidly predissociate as demonstrated by the lack of a measurable O_4 neutral beam emerging from the cell, and by the absence of vibrational structure in the distributions obtained with NO and O_2.

The structured fragment energy spectra obtained with NO and O_2 cannot be assigned to dissociation of a *single* excited electronic state to different dissociation limits. In addition to the ground state limit, the low-lying limits $O_2(X^3\Sigma_g^-) + O_2(a^1\Delta_g)$ at 0.98 eV, $O_2(X^3\Sigma_g^-) + O_2(b^1\Sigma_g^+)$ at 1.64 eV and $O_2(a^1\Delta_g) + O_2(a^1\Delta_g)$ at 1.96 eV are energetically possible dissociation products. We assign the broad peaks of the fragment energy distributions near 0.5 eV, near 0.8 eV, and near 1.3 eV to population of different excited electronic states of O_4 in the transfer process.

The energy release spectra can be modeled by assuming that four dissociative electronic states are initially populated and that they branch among different dissociation limits. The populations and their branching as derived from fitting the experimental fragment energy spectrum with Gaussian functions are given in Table I. For example, a state labeled A that lies 2.4 eV above the lowest dissociation limit is populated initially in charge transfer. Approximately 20% of this state dissociates to $O_2(X) + O_2(a)$ giving rise to fragments at an energy of $(2.40 - 0.98) = 1.42$ eV. Approximately 42% of this state dissociates to $O_2(X) + O_2(b)$ giving rise to fragments at an energy of $(2.40 - 1.64) = 0.76$ eV, and the remainder dissociates to $O_2(a) + O_2(a)$ giving rise to fragments with an energy of $(2.40 - 1.96) = 0.44$ eV. The peaks in Fig. 4(b) represent the location, the width and the fractional population of the excited O_2 states formed initially. Figure 4(a) shows a fit using these parameters and the branching values given in Table I. The energetic position of these O_4^*

TABLE I. Fitting parameters used in the simulation of the energy release spectra observed for $O_2^- - O_2$ and for $O_2^- - NO$.

Label	Energy[a] (eV)	Width (meV)	Relative population	$X + X$ %	$X + a$ %	$X + b$ %	$a + a$ %
A	2.40	160	1.0	$\cdots$	20	42	38
B	2.24	190	1.1	$\cdots$	63	37	$\cdots$
C	1.94	290	1.7	$\cdots$	36	64	$\cdots$
D	0.15[b]	110[b]	0.5[c]	100	$\cdots$	$\cdots$	$\cdots$

[a] Relative to $O_2(X^3\Sigma_g^- v=0) + O_2(X^3\Sigma_g^- v=0)$.
[b] Unreliable due to cutoff of detector efficiency.
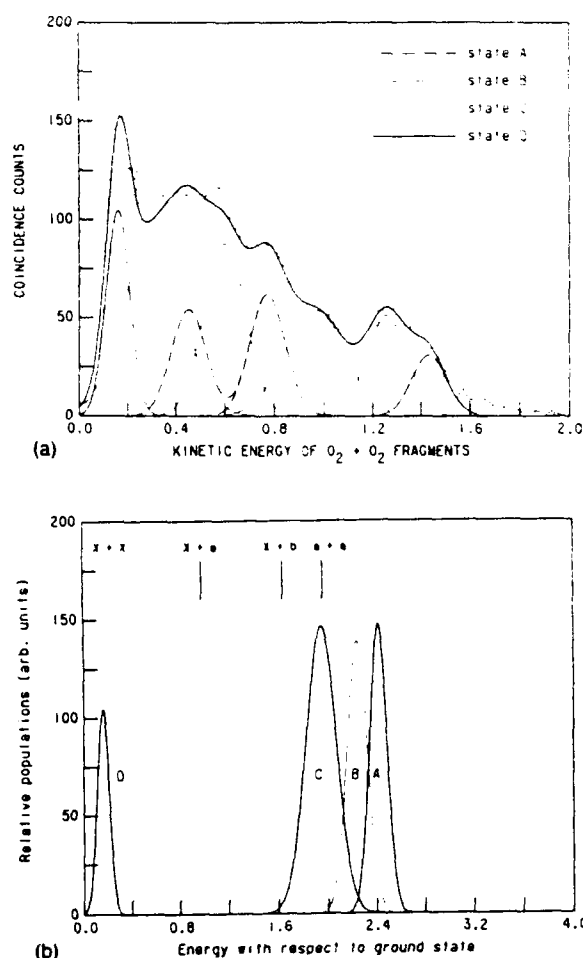[c] Value for $O_4^- + O_2$ only.

(a)

(b)

FIG. 4. (a) A spectral simulation (full line) composed of the individual contributions listed in Table I (shown by the Gaussian distributions) is compared with the observed fragment energy distribution obtained from $O_4^+ + O_2$. (b) The molecular excitations of O_4^+ that are used in the simulation. The energy scale refers to the dissociation limit $O_2(X^3\Sigma_g^+) + O_2(X^3\Sigma_g^+)$. For example, peak C indicates that a dissociative O_4 state at an energy of about 1.94 eV is initially populated in the charge transfer process. The width of this peak (290 meV FWHM) reflects the slope of the dissociative state over which population is produced. The branching values in Table I indicate that this O_4 state dissociates to $O_2X + O_2a$ with a probability of ~1/3 and to $O_2(X) + O_2(b)$ with a probability of ~2/3. Unresolved remains the vibrational degree of excitation in the molecular oxygen products; it is contained in the peak width.

states is shown in the center column of Fig. 3 by the full lines.

The branching and population of these states for the case of $O_4^+ + NO$ is quite similar to that given in Table I for $O_4^+ + O_2$, with the exception of a marked reduction of the lowest energy peak. This likely reflects the energetically much more favorable situation for transfer to the repulsive ground state surface $O_2(X^3\Sigma_g^-) + O_2(X^3\Sigma_g^-)$ when molecular oxygen is the electron donor.

The low energy cutoff in the spectra at 100 meV kinetic energy is due to the apparatus function which limits fragment detection to the range from ~100 meV to ~8 eV. As a consequence the low energy side of the fitting function D (Table I) is certainly not realistic. The energy width of O_4 states shown in Fig. 4(b) inherently contains any vibra-

tional distribution in the O_2 product molecules. As seen in the top spectrum in Fig. 2 for transfer with cesium the apparatus resolution is easily sufficient to resolve vibrational distributions if they are distinct. Due to the absence of vibrational information in the spectra with O_2 and NO, the fitting functions given in Table I cannot be claimed to be unique. Nevertheless the appearance of several excited O_4^+ states in this energy range is not surprising because a multitude of potential energy surfaces arise from the lowest dissociation limits and because the dominant molecular orbital configuration[26] of the neutral ground state, $X^3\Sigma_g^-$, and the neutral excited states $a^1\Delta_g$ and $b^1\Sigma_g^-$ is given by adding a single $(1\pi_g)$ electron to the dominant molecular orbital configuration of O_2^- ($X^2\Pi_g$).

Electron transfer from cesium

The kinetic energy distribution in transfer from cesium is dramatically different. In this case, precisely reproducible vibrational structure appears in the fragment energy distribution. The energetics for this process are again given in Fig. 3. For zero energy defect we expect that transfer in cesium populates a high-lying Rydberg state of O_4, at approximately the ionization potential of Cs (3.9 eV) below the molecular ion energy. Similar behavior has been seen in charge transfer from Cs to a variety of molecular ions.[15-18] This would place the O_4 state at 7.6 eV above the lowest dissociation limit $O_2(X^3\Sigma_g^-) + O_2(X^3\Sigma_g^-)$. While energy resonance is not explicitly required in a charge transfer process at keV energies (as evidenced by the similar states populated with NO and O_2 as electron donors), we nevertheless conclude from the maximum fragment energy observed of only 2.5 eV (see Fig. 2) that the significant excess energy goes primarily into excitation of the neutral O_2 products.

The internal excitation energy can in principle be stored in electronic, vibrational and rotational degrees of freedom. However, we can exclude the possibility of electronic excitation in the fragments, other than the $a^1\Delta_g$ or $b^1\Sigma_g^-$ state. This is because the binding energy of the higher excited electronic states of O_2 is small and their vibrational spacings are smaller than those observed here.

A consistent interpretation of the fragment kinetic energy release spectrum in cesium is the assignment of the molecular fragment products to molecules in high vibrational states of ground state $O_2(X^3\Sigma_g^-)$. This is demonstrated by the rather good agreement of a series of vibrational peaks in the experimental energy distribution with the energies[27] of the vibrational levels $v = 24$ to $v = 32$ of ground state O_2 (see Fig. 5). We note that assignment of the individual peaks in Fig. 5 to the vibrational energies indicated by the tickmarks gives for the sum of the translational energy in both O_2 molecules and vibrational energy in one of them, $E_{trans}(v) + E_v$, a value of 5.05 eV. At this point the energy content in the second O_2 molecule is not yet known. Initial population of a Rydberg state of O_4 at 7.6 eV (corresponding to $n = 2$ with near zero energy defect) would require that the second O_2 molecule carries away ~2.6 eV in internal excitation. No obvious candidate state exists for such a choice but if the second O_2 molecule
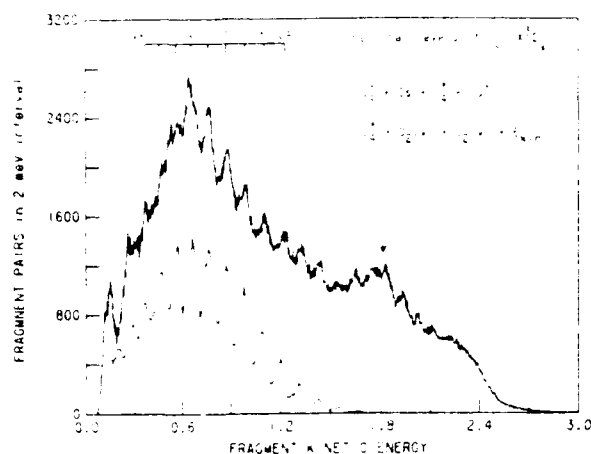
FIG 5 Fragment kinetic energy distribution of $O_2 + O_2$ obtained in charge transfer of O_4^- with cesium. The tickmarks at the top give vibrational spacings of $O_2(X\,^3\Sigma_g^-)$. The thin curve gives a simulation of the energy distribution using the model described in the text [Eq. (2)]. The low energy cutoff at 100 meV is caused by the translational energy spectrometer, however, the high energy cutoff is not an experimental artifact. The arrow indicates the position of the peak intensity of the distributions produced by the O_4^* state at 10.5 eV (at a translational energy of 1.80 eV).

were formed in $v = 16$ of the ground state the total energy would add up to 7.6 eV. Such an assignment would require that the second molecule is *always* in $v = 16$ of $O_2(X\,^3\Sigma_g^+)$, but never in $v = 15$ or $v = 17$ or other vibrational states. This is because the vibrational spacing $v = 15$, 16, 17 (150 meV) is inconsistent with the observed spacings here (100–120 meV). We consider such an outcome of dissociation of O_4^* as highly improbable.

A more plausible assignment is obtained with the assumption that both molecules are formed in similarly high vibrational levels of $O_2(X\,^3\Sigma_g^-)$, with a peak in the population around $v = 29$. For example, a simple population distribution given by

$$P(v,v') = \exp[-(E_v - E_{29})^{**}2/T]$$

$$\times \exp\{-(E_{v'} - E_{29})^{**}2/T\} \qquad (2)$$

produces the simulation shown by the thin line given in Fig. 5 for $T = 0.1$ eV^2. In Eq. (2) E_v, $E_{v'}$ represents the vibrational energy of the two O_2 molecules with respect to the lowest vibrational level of ground state O_2. Obviously improved fits to the spectrum could be obtained with less restricted population distributions in the two neutral oxygen products. The main point to make here is that the energy distributions appear consistent with high vibrational excitation in both products. Such an assignment places the predissociated O_4^* state that is populated initially at an energy of ~ 9.40 eV, rather than the value of 7.6 eV expected in the case of zero energy defect. Considering the ionization limit of O_4 (11.66 eV), the effective quantum number for this state turns out to be $n = 2.45$.

We may then investigate where the next higher Rydberg state would be expected. For a state with $n = 3.45$, the O_4^* energy should be 10.52 eV. If the latter state is also populated in charge transfer with cesium and if it decays in

a similar fashion to the state located at 9.4 eV we anticipate fragment energies with a similar pattern but shifted to higher energies by 1.12 eV. Evidence for this to happen can indeed be found in the observed energy spectrum by comparing the similarity of features near the peak of the distribution at 0.67 and 1.8 eV (see location of arrow in Fig 5). We consider this as further support for the present assignment. The energy location of both states accessed in charge transfer with cesium is also shown in the center column of Fig. 3.

Probably the most surprising feature of the cesium spectrum is the relatively narrow peak structure of the fragment energy distributions. It permits us to make the following conclusions on the excited state of O_4 that is formed in electron transfer from Cs to O_4^-.

The lifetime of the neutral O_4^* state formed in electron transfer with Cs must be long enough to develop the narrow peak widths (typically 40 meV). Since the instrumental peak width of the apparatus for dissociative charge transfer[28] is of the order of 20 meV (at 1 eV energy release) and since the rotational energy width at room temperature is of the order of 30 meV we estimate the natural width of the predissociating O_4^* state to be less than 5 meV. This corresponds to lifetimes exceeding 1×10^{-13} s. The peakwidth allows us to also place an upper limit to the lifetime of the O_4^* state. If this lifetime were larger than a few hundred nanoseconds then dissociation of O_4^* molecules formed in the charge transfer cell would occur along an extended section of beam path between the charge transfer cell and the detector. This would smear out the kinetic energy spectrum, which is not observed experimentally.

A second conclusion refers to the energy partitioning between the dissociation fragments. Assuming that the O_4^* state has a nuclear geometry similar to that of the molecular ion, O_4^-, we expect that vibrational excitation of the neutral O_2 product follows Franck–Condon overlaps determined by the restricted geometry of O–O bonds in the ion and neutral states of O_4. The overlap can be examined qualitatively by comparing the geometry of O_4^- and that of ground state O_2. The differences between the short bond lengths in O_4^- and O_2 are in fact small (see Fig. 1), suggesting that excitation of only a few quanta of vibration is possible in a vertical electron capture process. We note that the initial degree of vibrational excitation of O_4^- is limited to less than 0.4 eV, owing to the low binding energy[8] of $O_2 + O_2^-$, and due to the requirement that the parent ion must be stable on the time scale of tens of microseconds to permit passage from the ion source to the charge transfer region.

In the light of the above arguments based on Franck–Condon overlaps, the high degree of vibrational excitation in the final products is indeed puzzling. To explain the vibrational excitation we postulate that the predissociation process of the Rydberg state is mediated by a state of O_4^* of geometry greatly different from that of ground state O_4^-. Such states can be expected to arise, for example, from the ion pair dissociation limit $O_2^-(X\,^2\Pi_g) + O_2^-(X\,^2\Pi_g)$ which lies energetically 0.44 eV below the molecular ion dissoci-

ation limit[7] (see Fig. 3). Mixing of ion pair and Rydberg character is a well documented phenomenon in many molecular systems.[29] In the dissociation process here the requirement is that the O_4 Rydberg state is mixed with the ion pair state, enabling the molecule to experience vibrational turning points at large internuclear separation, according to the long range ion-pair interaction. Projection of turning points at large internuclear distance (much larger than possible in stable O_4^- or in a Rydberg state of O_4 with ground state O_4^- as ion core) would permit population of O_2 products in high vibrational states of excitation. That large internuclear separations are required is illustrated by the position of the right hand turning points in $O_2(X\,^3\Sigma_g^-)$. For $v=29$, the peak in the experimental vibrational distribution, the turning point lies at 2.4 Å.

A third observation in Cs is that the observed fragment distribution is inconsistent with greatly disparate vibrational excitation of the two O_2 products. Since the energy appears to be partitioned in approximately equal and high vibrational levels in both fragments we require that the long lived O_4^* state is of a symmetric geometry with extended bond lengths. A possible candidate is the hypothetical ion-pair structure

$$\begin{array}{cc} O^+ & -O^- \\ | & | \\ O^- & -O^+ \end{array} \quad (3)$$

In order to explain the vibrational excitation of the fragments the bond lengths of this structure should fall into the range of 2–3 Å. This state is not the tightly bonded ring configuration of Dunn et al.[5] for which approximately equal bond lengths of about 1.44 Å are reported.

As an alternative to the above explanation, consider the possibility that the initial gas phase O_4^+ species is not of the geometry detected in the matrix[9] but rather is closer to the rectangular structure proposed by Peel[10] as shown in Fig. 1(h). The counterintuitive process that capture of an electron leads eventually to fission of O_4^* along the short bond lengths (1.160 Å) would produce two O_2 molecules at internuclear separations of 2.4 Å, just as required to form O_2 in the high vibrational states detected here.

CONCLUSION

We have obtained the first experimental information for neutral states of the tetraoxygen molecule at geometries other than the van der Waals complex. The neutral states of O_4 that are formed in electron transfer are unstable, decaying by dissociation and/or predissociation. Our initial motivation for carrying out this study was the hope to find a signature of the low-lying and presumably long-lived state predicted by Schaefer's group.[4,5] In the light of the recent finding by Jacox[9] that the geometry of ground state O_4^- is represented by C_{2h} symmetry with bond lengths far removed from Schaefer's predicted D_{2d} geometry it is highly unlikely that such states could be formed by charge transfer in our experiments.

Nevertheless, our observation of several low-lying states of O_4 and of Rydberg states of O_4 is interesting by

itself, and we present a tentative assignment of the electronic energies of the dissociative O_4^* states. While this assignment cannot be considered unique, our experimental information can be compared with theoretical predictions of electronically excited states of O_4, once such work is undertaken. We hope that our study will provide an impetus for such a study.

[1] C. A. Long and G. E. Ewing, J. Chem. Phys. **58**, 118 (1973).
[2] F. Canrovale, J. B. Peel, and R. G. Rothwell, Org. Mass Spectrosc. **26**, 201 (1991).
[3] V. Adamantides, D. Neisius, and G. Verhaegen, Chem. Phys. **48**, 215 (1980).
[4] E. T. Seidl and H. F. Schaefer, J. Chem. Phys. **88**, 7043 (1988).
[5] K. M. Dunn, G. E. Scuseria, and H. F. Schaefer, J. Chem. Phys. **92**, 6077 (1990).
[6] I. Røeggen and E. Wisløff-Nilssen, Chem. Phys. Lett. **157**, 409 (1989).
[7] K. P. Huber and G. Herzberg, Molecular Structure and Molecular Spectra, Vol. IV (Van Nostrand, New York, 1979).
[8] K. Hiraoka, J. Chem. Phys. **89**, 3190 (1988).
[9] W. E. Thompson and M. E. Jacox, J. Chem. Phys. **91**, 3826 (1989).
[10] J. B. Peel, J. Chem. Phys. **94**, 5774 (1991).
[11] L. B. Knight, S. T. Cobranchi, and J. Petty, J. Chem. Phys. **91**, 4423 (1989).
[12] D. L. Huestis, G. Black, S. A. Edelstein, and R. A. Blunt, J. Chem. Phys. **60**, 4471 (1974).
[13] V. I. Dianov-Klokov, Opt. Spectrosc. **6**, 290 (1959); **16**, 224 (1964).
[14] W. C. Stwalley, A. Mariotta-Lyyra, and W. T. Zemke, in Proceedings of the High Energy Density Matter Conference, Albuquerque NM, 1991, edited by M. E. Cordonnier (Phillips Laboratory, Edwards Air Force Base, CA), p. 1.
[15] J. R. Peterson and Y. K. Bae, Phys. Rev. A **30**, 2807 (1984).
[16] W. J. van der Zande, W. Koot, J. R. Peterson, and J. Los, Chem. Phys. Lett. **140**, 175 (1987); Chem. Phys. **126**, 169 (1988).
[17] D. P. deBruijn, J. Neuteboom, V. Sidis, and J. Los, Chem. Phys. **85**, 215 (1984).
[18] W. J. van der Zande, W. Koot, C. Kubach, and D. P. deBruijn, Phys. Rev. Lett. **57**, 1219 (1986).
[19] P. C. Cosby and H. Helm, Phys. Rev. Lett. **61**, 298 (1988).
[20] J. R. Peterson, P. Devynck, Ch. Hertzler, and W. G. Graham, J. Chem. Phys. **96**, 8128 (1992).
[21] H. Helm, Phys. Rev. A **38**, 3425 (1988).
[22] H. Helm, D. deBruijn, and J. Los, Phys. Rev. Lett. **53**, 1642 (1984).
[23] For example, electron transfer is readily observed at 3 keV energy for the reaction $H_2^- + Xe \rightarrow H_2(c\,^3\Pi_u) + Xe^+$ which has an energy defect of ~ 8 eV. Also, processes for which electron transfer is accompanied by electronic excitation can be observed as recently shown in the reaction $O_2^- (a\,^4\Pi_u) + Cs \rightarrow O_2^{**} + Cs^+$, where O_2^{**} is a Rydberg state built on a core of $O_2^+ (X\,^2\Pi_g)$ [C. W. Walter (unpublished)].
[24] H. Helm and P. C. Cosby, J. Chem. Phys. **86**, 6813 (1987).
[25] This current is comparable to that obtained in charge transfer of $H_3^+ + Cs$, where the long lived H_3 species is formed (see Ref. 21).
[26] P. H. Krupenie, J. Phys. Chem. Ref. Data **1**, 423 (1972).
[27] T. G. Slanger and P. C. Cosby, J. Phys. Chem. **92**, 267 (1988).
[28] The poor resolution in dissociative charge transfer is primarily related to the length of the charge transfer cell (5 mm from aperture to aperture). This leads to an uncertainty in the distance of the dissociation point to the detector surface.
[29] S. Ross and Ch. Jungen, Phys. Rev. Lett. **59**, 1297 (1987).

Appendix H

DISSOCIATION OF RYDBERG STATES OF O_2 INDUCED BY IMAGE CHARGES IN A METAL SURFACE

SPONTANEOUS DISSOCIATION OF EXCITED OXYGEN MOLECULES IN THE VICINITY OF A METAL SURFACE

P. C. Cosby, I. Hazell,[†] C. W. Walter,[‡] and H. Helm

Molecular Physics Laboratory
SRI International
Menlo Park, CA 94025

ABSTRACT

Dissociation of long-lived, electronically excited O_2 molecules is observed to occur as the molecules pass through a 300 μm wide metal slit. Spatial and temporal analysis of the correlated dissociation fragments is used to identify the dissociating O_2^* states and to determine the branching in dissociation to the $O(^1S) + O(^1D)$, $O(^1D) + O(^1D)$, $O(^1D) + O(^3P)$, and $O(^3P) + O(^3P)$ dissociation limits. Studies of this phenomenon as a function of electric field applied across the slit suggests that the dissociation is induced by Stark mixing of long-lived O_2 molecules that leads to predissociation by the valence continuum states. In the absence of an external electric field the mixing is induced by forces exerted on the molecule as a consequence of the image charges that the Rydberg molecule induces in the metal surface, when the molecule travels close to, but does not physically touch, the metal surface.

[†] Permanent Address: Institute of Physics, University of Aarhus, DK-8000 Aarhus C, Denmark.
[‡] Present Address: Department of Mathematics, Saint Mary's College of California, Moraga, CA 94575.

INTRODUCTION

Several recent papers have explored the influence of an external electric field on dynamic properties of molecular Rydberg states. These studies were concerned with two effects induced by the electric field: For one, the lowering of the ionization threshold leads to electric-field induced ionization. This effect has been studied for the molecules H_2, Li_2, Na_2, and H_3.[1-5] A second influence of the electric field derives from its effect of ℓ-mixing which can lead to selective predissociation of the molecular Rydberg. Such observations have been reported for the molecules H_2[6-8] and H_3[9]. The effect of ℓ-mixing may be interpreted in general terms by considering three electronic states: R_a, R_b, and C. Here R_a is a Rydberg state that is stable against dissociation at zero field and can couple to a Rydberg state of different parity, R_b, through the Stark effect. Predissociation of R_a can be "turned on" by an external electric field, provided a dissociative continuum state, C, is available which has a favorable coupling to R_b. While the intrinsic Stark matrix element merely couples ℓ with $\ell\pm1$, all ℓ values will tend to get mixed by the time that the electric field exceeds the critical value for mixing n-states[10].

In the present paper, we report observations of externally induced predissociation of O_2 Rydberg states when these molecules come close to, but do not touch, a metal surface. We attribute this process to forces exerted on the molecular Rydberg state by the image dipole, that is induced in the metal surface by the Rydberg dipole (core plus electron). We speculate that these forces induce ℓ-changes of an initially stable (long-lived) molecule, thereby opening a channel with good overlap to a dissociative continuum. This behavior is observed for excited states of the oxygen molecule that lie below the lowest ionization threshold, $v^+ = 0$ of $O_2^+(X^2\Pi_g)$, as well as for Rydberg states belonging to vibrationally excited levels that lie energetically in the autoionization continuum (but are stable on the time scale of microseconds before they approach the metal surface).

We investigate the vibrational dependence of the predissociation branching among the available dissociation limits of O_2, and we study the influence of an external electric field on this predissociation phenomenon.

EXPERIMENT

The apparatus used in the present investigation is essentially identical to that used in previous work[11-17] with one minor exception that will be detailed below. In brief, O_2^+ ions are produced by electron impact on O_2 gas and are extracted by a weak repeller field, accelerated, mass selected, and collimated into a beam with a specific kinetic energy E_0. Following a total flight distance of 250 cm from the ion source, the collimated O_2^+ beam passes through a cell containing Cs vapor (see Fig. 1). A small fraction (<<1%) of the O_2^+ beam is neutralized in the Cs vapor to produce O_2 molecules. Charged particles leaving the cell are swept out of the beam by an electric field applied 26 cm downstream from the cell. Neutral particles travel unimpeded from the cell to a slit assembly (50 cm). The slit, fabricated from razor blades with a nominal radius of curvature of order 1 μm, provides an opening of dimension 300 μm x 10 mm. All particles passing through the open area of the slit are collected by a 1.27 mm × 50 mm beam flag positioned 10 cm downstream from the slit. With the exception of the immediate vicinity of the Cs cell, all regions of the apparatus are maintained at a vacuum of 5 ·. 10^{-8} Torr or less. No contribution from collisional dissociation due to background gas is detected.

If a molecule dissociates in the region between the slit and the beam flag and its fragments escape collection by the beam flag, these fragments travel to a position-sensitive detector for correlated fragments. The detector explicitly measures the spatial ($R=R_1+R_2$) and temporal (Δt) separations of the two correlated fragments produced by the dissociation of a single molecule of mass M, energy E_0, and velocity v ($E_0 = Mv_0^2/2$) to define the center of mass translational energy (W) released in the dissociation:[11,18]

$$W = \frac{E_0}{4L^2}(R^2 + v_0^2\Delta t^2).$$ (1)

The combination of the narrow slit and the beam flag geometrically defines a range of distances from the detector, L, for which the two correlated fragments can be both produced and detected. The narrow slit (110.8 cm from the detector) defines the maximum value for L;[19] the beam flag (100.8 cm from the detector) defines the minimum value for L. The effect of an indeterminacy in L, $\Delta L \leq 10$ cm, is to produce a broadening in the correlation of the fragment temporal and spatial separations with W, in case dissociation occurs over this broad range of L values. Differentiating Eqn. (1), this broadening is

$$\Delta W/W = 2\Delta L/L.$$ (2)

Thus ΔW is a constant proportional to the translational energy release. For unimolecular dissociation that occurs with equal probability over the full range of the interaction region ($\Delta L \sim 10$ cm), the resolution is quite poor with $\Delta W/W = 0.18$. On the other hand, prompt dissociation of a single molecular energy level prepared by photoexcitation within a ~2 mm laser beam diameter is found to yield $\Delta W = 0.025$ eV at $W = 1.7$ eV.

The state distribution in the precursor O_2^+ beam was selected by adjusting the ion source pressure and residence time in the source. The actual electronic, vibrational, and rotational populations of the O_2^+ ions at the time of charge-transfer neutralization was explicitly determined by Walter et al.[16] and by van der Zande et al.[20] Their results were confirmed in the present work for the specific experimental conditions employed here. Briefly, production of the O_2^+ beam at high O_2 source pressure and long source residence times produced an ion beam with >95% population in the first several vibrational levels of the $X^2\Pi_g$ state. Production of the beam at low source pressures and short residence times produced comparable populations in the $X^2\Pi_g$ state and the $a^4\Pi_u$ states, with the population of the latter extending to v>14. The $a^4\Pi_u$ state is the

only electronic state of O_2^+ that is sufficiently long-lived to survive the >14 μs flight time between the ion source and the Cs charge transfer cell.

OBSERVATIONS

A weak dissociation signal of O_2 molecules produced by the reaction

$$O_2^+ + Cs \rightarrow O_2^* \qquad (3a)$$

is observed following passage of the molecules through the slit assembly:

$$O_2^* \rightarrow slit \rightarrow O + O + W, \qquad (3b)$$

where W is the released translational energy. The distribution of energy releases observed in this dissociation for a 5 keV beam of O_2^+ is shown in Figure 2. The spectrum in Fig. 2 is a histogram of the number of detected pairs of correlated fragments (fragment intensity) yielding [Eqn. (1)] a given value of energy release W in the range 0.5 eV ≤ W ≤ 8.5 eV. The spectrum has been corrected for the variation of the collection efficiency with energy release.

The ratio of the fragment positions for each correlated dissociation pair relative to the center of the detector is found to be peaked at unity. This is consistent with the dissociation products being of equal mass, as expected for fragmentation from O_2 molecules. In addition, the degree of correlation in the spatial and temporal separations of the dissociation fragments proves that the signal does not arise from grazing collisions of the molecules with the surface of the slit.

It can be seen in Fig. 2 that the energy release peaks fall into four groups, each containing 6 or 7 peaks of significant intensity. The energy release values corresponding to the midpoint of each peak are given in Table I. Within the experimental uncertainty (±10 meV), the spacings of the peaks within each group are identical and these spacings correspond to those[21,22] of the vibrational levels v=0-6 of the O_2^+ $X^2\Pi_g$ state. As discussed in the next section, the observed

107

fragmentation arises from dissociation of near-degenerate (very high n) Rydberg states of O_2 on this core to produce four sets of O + O fragments with differing degrees of electronic excitation. For the purpose of referring to specific features in the spectra, we label each of the peaks within each group by consecutive vibrational numbers with v=0 being assigned to the peak at lowest W within each group. The four groups are labeled from low to high W as $O(^1S) + O(^1D)$, $O(^1D) + O(^1D)$, $O(^1D) + O(^3P)$, and $O(^3P) + O(^3P)$.

The spectrum in Figure 2 was recorded with the same potential (ground) applied to the two razor blades that form the slit assembly. However, dissociation is also observed with an electrostatic potential difference applied between the two razor blades. The effect of the potential difference on the fragment energy release spectrum is shown in Fig. 3 for the 3 keV beam. Each of the spectra in this figure is approximately normalized to the same beam flux and accumulation time to allow comparison. It can be seen in this figure that increasing the applied field affects the widths, relative intensities, and nominal values of the energy releases of the spectrum. In particular:

1. With the exception of the lowest group $[O(^1S) + O(^1D)]$, the intensity of the v=0 peak increases with applied voltage whereas the intensities in v > 0 decrease rapidly. In the $O(^1S) + O(^1D)$ group, all peaks decrease in intensity with applied field with v=0 and v=2 exhibiting the smallest effect.

2. The positions of the peaks within each group, as defined by the apparent W value at their Gaussian centroids, shift slightly to lower values of W with applied field.

3. With the exception of the lowest W group $[O(^1S) + O(^1D)]$, the peaks corresponding to v = 0 appreciably broaden to lower W with applied field. This broadening will also influence the apparent midpoint of the v=0 peaks.

Peaks $v > 0$ and all peaks in the $O(^1S) + O(^1D)$ group show no observable dependence of peak width on applied field.

4. The flux of detected dissociation fragments is found to scale directly with the concentration of O_2^+ $a^4\Pi_u$ in the precursor ion beam. The relative intensities of the vibrational peaks within each group are unaffected by the $a^4\Pi_u$ concentration.[23]
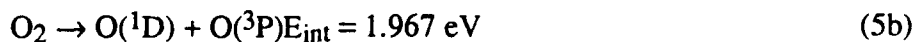
DISCUSSION

NATURE OF THE DISSOCIATING STATES

In molecular dissociation, the potential energy of the dissociating state (E_{tot}) is released as kinetic (translational, W) and potential (internal, E_{int}) energy of its dissociation products at infinite separation

$$E_{tot} = E_{int} + W. \qquad (4)$$

In the present experiment, the translational energy spectrum of the fragments specifically measures only the kinetic energy component, W. However, the possible internal energy states in the product atoms are relatively few and are widely separated in energy. The lowest dissociation limit of the O_2 molecule is to form ground state atoms:

$$O_2 \rightarrow O(^3P) + O(^3P) \qquad E_{int} \equiv 0 \text{ eV}. \qquad (5a)$$

If we choose this as the reference of total energy (E_{tot}), the next higher limits lie at:

$$O_2 \rightarrow O(^1D) + O(^3P) \qquad E_{int} = 1.967 \text{ eV} \qquad (5b)$$

$$O_2 \rightarrow O(^1D) + O(^1D) \qquad E_{int} = 3.935 \text{ eV} \qquad (5c)$$

$$O_2 \rightarrow O(^1S) + O(^3P) \qquad E_{int} = 4.190 \text{ eV} \qquad (5d)$$

$$O_2 \rightarrow O(^1S) + O(^1D) \qquad E_{int} = 6.157 \text{ eV} \qquad (5e)$$

$$O_2 \rightarrow O(^1S) + O(^1S) \qquad E_{int} = 8.380 \text{ eV}, \qquad (5f)$$

where the atomic excitation energies are taken from Moore.[24] With this energy reference, the lowest energy levels of O_2 ($X^3\Sigma_g^-$, v=0,N=1,J=0) and O_2^+ ($X^2\Pi_{1/2}$, v=0) lie at -5.1167 eV and 6.954 eV, respectively, where the dissociation energy (D_0^0 = 5.1167 eV)[25] and the ionization potential (IP = 12.071 eV)[26] of O_2 provide the necessary connections between the neutral and ionic molecular levels and the atomic energy levels.

The separations among the four groups of peaks observed in the translational energy release spectrum of the O_2 molecule (see Fig. 2 and Table I) match the energy separations of the various O_2 dissociation limits, hence a unique assignment of the dissociation products can be made. Each of the groups contains at 6 or 7 discrete peaks spaced by roughly 0.23 eV. This corresponds to the vibrational spacing of the O_2^+ $X^2\Pi_g$ state, $\Delta G_{1/2} = \omega_e - 2\omega_e x_e = 0.2322$ eV. If we consider each of the peaks within a group to have a relative vibrational energy (G_v) equal to that of the $X^2\Pi_g$ state, then all of the observed peaks should be described by

$$E_{level} = W - G_v + E_{int}, \qquad (6)$$

where E_{int} is given by Eqn. (5). Assigning the vibrational numbering of the peaks as given in Table I, i.e. with the lowest member of each group assigned as v=0, and taking $W_{obs} = W$, the values of E_{level} for the four groups of peaks are found to be: 6.951±0.017 eV for $O(^1S) + O(^1D)$, 6.973±0.008 eV for $O(^1D) + O(^1D)$, 6.970±0.012 eV for $O(^1D) + O(^3P)$, and 6.953±0.008 eV for $O(^3P) + O(^3P)$. The four values are reasonably consistent and yield an energy for v=0 of the dissociating state of 6.963 ± 0.004 eV above ground state atoms. For comparison, the lowest level of the O_2^+ $X^2\Pi_g$(v=0) lies at 6.954 ± 0.001 eV.

Two features of the spectrum argue that the dominant contribution to the observed width of the translational energy peaks is due to the internal energy levels of the dissociating Rydberg

110

molecules (rotational and fine-structure states) and to the presence of molecules in a range

values of the principal quantum number n. One feature, obvious in the Gaussian fits, is that the

peak envelopes tail toward higher energy release, such as would be expected for an ensemble of

unresolved rotational levels. Secondly, the width of the peaks in the energy release spectrum are

relatively broad ($\Delta W \sim 0.1$ eV in the narrowest spectra) in comparison with the intrinsic

resolution of the apparatus ($\Delta W \sim 0.025$ eV), and are very nearly constant as a function of

increasing energy release. In contrast, if fragments are produced over a range of distances

spanning from the slit to the flag, as would occur for a unimolecular dissociation with

microsecond lifetime, a broadening that is linearly dependent on energy release would result [as

predicted in Eqn. (2)]. Since such a dependence is not observed here, the primary contribution to

the observed peak widths must arise from the molecular energies of the dissociating O_2 levels or

atomic fine structure levels in the dissociation products.

Since the dissociating levels appear to describe a very high Rydberg state of O_2, an

internal structure very nearly that of the $O_2^+ X^2\Pi_g$ state could be expected, i.e. a spin-orbit

splitting of order 0.025 eV and a rotational manifold described by the rotational constants of the

ion. Using an apparatus function characteristic of the present experimental arrangement, the

experimental spectra were fit presuming the dissociation of 7 vibrational levels in a single

Rydberg state of O_2 with internal energy levels exactly described by the $O_2^+ X^2\Pi_g$ molecular

constants. We further presumed that both spin-orbit components have equal populations and

dissociation rates, that the rotational population distribution in all vibrational levels can be

characterized by a single Boltzmann temperature (T_{rot}), that ^3P_J dissociation products are

produced in a statistical distribution, and that the dissociations occur within a region of length ΔL

centered at the slit.

The resulting vibrational intensities from the fits are given in Table II. As described for

the Gaussian fits, no evidence was found for the production of products in Reaction (5d). Both

the 3 keV and 5 keV spectra were found to be well described by a single rotational temperature

$T_{rot} = 630\pm50K$. This is comparable to the rotational temperature of $675\pm200K$ observed by Walter et al.[16] for the $C^3\Pi_u$ state of O_2 produced by charge transfer of $O_2^+(X^2\Pi_g)$ in Cs. Also, both spectra yielded the same value for the energy of the dissociating state, Eqn. (6), $E_{level} = 6.931 \pm 0.004$ eV, where the error refers only to the standard deviation in the fits. This value lies 31 meV below that estimated from the Gaussian fits. This was to be expected because now the energy refers to the lowest energy level rather than to the peak of a rotational and spin-orbit population distribution. In comparison to the energy of $O_2^+(X^2\Pi_g)$ at 6.954 eV, E_{level} lies 23 meV lower. This too is expected for a Rydberg state converging to this ion core. Of particular significance is that the 3 keV and 5 keV spectra could not be fit using a single value for ΔL, considering the participation of only a single Rydberg state in each case. Rather, values for ΔL of 4.2 ± 0.2 mm and 6.4 ± 0.2 mm had to be assumed for the 3 keV and 5 keV spectra, respectively. These would correspond to effective dissociation lifetimes of 31 ns and 37 ns, respectively.

Thus a single dissociating Rydberg state of O_2 cannot provide the proper description of the observed spectrum. However a consistent representation of the experimental spectrum is obtained if a series of Rydberg states is assumed to be present, that lie within a specific energy range and dissociate. This range is essentially equal to the difference in energy between E_{level} and the ionization energy of O_2, 0.023 eV, corresponding to a series of O_2 Rydberg states with effective quantum numbers in the range $24 \leq n \leq \infty$. This reasoning also implies that the dissociation lifetime is much smaller than 30 ns, that is the dissociation is confined into a narrow range of distances, L, in the vicinity of the slit. In Figure 4 we give an energy diagram that shows the location of the dissociating states relative to the lowest vibrational levels of the molecular ground state ion. The range of energies over which excited states participate in the dissociation process for zero field and for a potential difference of 200 V applied to the slit is indicated as well.

112

FORMATION OF THE DISSOCIATING STATES

The direct variation of dissociation fragment flux with the concentration of O_2^+ $a^4\Pi_u$ in the ion beam suggests that this state is the precursor of the dissociating O_2^* state that is formed by charge transfer in Cs vapor. The $a^4\Pi_u$ state lies 4.03 eV above the O_2^+ $X^2\Pi_g$ state or 4.05 eV above the range of Rydberg states that are observed here to dissociate. Given the 3.8939 eV ionization potential of Cs, the charge transfer reaction

$$O_2^+(a^4\Pi_u, v) + Cs \rightarrow O_2^*(v+\Delta v) + Cs^+ + \Delta E \tag{7}$$
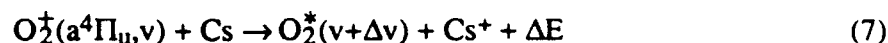
is near resonant ($\Delta E \sim 0$) for $\Delta v \sim 1$ if it is assumed that the O_2^* states are high Rydberg states of the ground state ion core. Thus, the energetics of the reaction strongly favor it.

Given the electron configurations[21] of the $O_2^+(a^4\Pi_u)$, $a^+ = ...(3\sigma_g)^2(1\pi_u)^3(1\pi_g)^2$, and O_2^+ $X^2\Pi_g$, $X^+ = ...(3\sigma_g)^2(1\pi_u)^4(1\pi_g)^1$, electron capture in Reaction (7) to form a $(n\ell)X^+$ Rydberg state must also involve the excitation of a core electron. Such a process is thought to be highly improbable. However, if we compare the observed flux of dissociation fragments in the present experiment with that produced by prompt dissociation at the Cs cell, the relative concentration of the O_2^* observed here to that of the $(3s\sigma_g)X^+$ states formed in Reaction (7) is only $\sim 10^{-6}$! Thus the reduced probability for a two electron process necessary to form $(n\ell)X^+$ states in Reaction (7) is consistent with the observed fragment flux.

DISSOCIATION PRODUCT BRANCHING

Figure 5 gives the relative flux of fragments at each of the four dissociation limits as a function of the vibrational quantum number of the dissociating state. The data shown represent the average between the results obtained at 3 keV and at 5 keV beam energies. It can be seen that the greatest flux of fragments is produced at the $O(^1D) + O(^3P)$ limit. The next higher product channel is the production of two ground state atoms, accounting for roughly 20% of the fragments. Production of $O(^1D) + O(^1D)$ is also found to be highly probable. The highest

113

energy dissociation channel $O(^1S) + O(^1D)$ is a relatively minor channel. No evidence is found in the experimental spectra for production of $O(^1S) + O(^3P)$ fragments. Such contributions would have to be less than 1% in the total product yield to escape detection.

DISSOCIATION MECHANISM

It is clear from our results that the process leading to dissociation of O_2^* must be confined to a narrow region in the vicinity of the slit assembly. We propose that the following mechanisms are primarily responsible for the observed effects:

Let us assume that the charge transfer process leads to production of $(n\ell)X^+$ Rydberg states with a wide range of values of n and ℓ. Rydberg states with low values of ℓ generally have more efficient coupling to the valence continuum states. Hence, these lower ℓ members of the O_2^* ensemble of states will be removed from the beam during the transit period to the slit assembly by predissociation. Rydberg states with low values of n and ℓ can also be removed from the O_2^* ensemble by radiative decay to lower O_2 states.

Thus at the slit, only a small concentration of O_2^* will remain undissociated, and these will consist of high ℓ and high n Rydberg states that are relatively immune to predissociation and to radiative decay. At the slit, the O_2^* beam is subjected to one of several effects that can give rise to a Stark mixing of the nℓ states, thereby admixing to all or some of the high ℓ quantum levels, components of lower ℓ states that are predissociated.

The high n Rydberg states are also subject to field-induced ionization. Here, the field can either lead to direct field ionization of Rydbergs with n greater than a critical value. This process will affect all vibrational levels of the O_2^*. In addition, the Stark mixing from the field can increase the rate of autoionization of Rydberg states with v > 0 (for n > 7 these levels lie in the ionization continuum). Since only neutral fragments are detected in the present experiments, the effect of O_2^* ionization is to remove it from contributing to the dissociation flux. This is evident for the dependence of the flux of dissociating molecules on the magnitude of the electric

114

field applied across the slit as shown in Figure 3. The depletion of the dissociative signal due to field induced ionization and the origin of the dissociation signal due to an electric field related effect is further supported by the observations that the v = 0 peaks broaden to lower energy release with applied field, whereas v > 0 peaks do not perceptibly broaden, but only shift to lower values of energy release.

RELATIONSHIP TO DISSOCIATIVE RECOMBINATION

The variation of the predissociation branching with vibrational level reflects the availability of the different continuum states of O_2 to which the O_2^+ core can couple, as well as the dynamics of the dissociating system as it experiences the molecular continuum. In this sense, the dissociative process investigated here is related to the molecular dynamics involved in dissociative recombination (DR) of O_2^+ with electrons, both in the direct as well as in the indirect DR channel.[27] Therefore, as a corollary to our results, we can answer the important question of which final atomic states are produced when a specific vibrational level of superexcited oxygen molecule predissociates. This process is related to the dynamics of O_2^+ that undergoes dissociative recombination.

Previous investigations of dissociative recombination of O_2^+ were primarily concerned with the rate of formation of $O(^1S)$, the origin for the green atomic oxygen emission in the night sky.[28] Theory[29] predicts a yield of $O(^1S)$ (relative to a yield of 2 for all atoms) of 0.0024 for v=0, 0.051 for v=1, and 0.15 for v=2. This vibrational sensitivity is primarily a consequence of the location of the continuum state that is expected to contribute most strongly to the dissociative recombination reaction. Generally higher yields are deduced from satellite based observations,[30] which also predict an increase in the yield with vibrational quantum number. By comparison our experimental yields for $O(^1S)$ are 0.033, 0.041, 0.045, 0.018, 0.010, 0.015, and 0.007 for v increasing from v=0 to v=6, in marked disagreement with the strong vibrational dependence currently accepted from theoretical and experimental results. On the other hand our experimental yields for $O(^1D)$ are 0.73, 0.79, 0.83, 0.81, 0.78, 0.82, 0.78, for the vibrational

levels v=0 to 6. Previous laboratory and satellite-based observations place this yield near unity.[30]

ACKNOWLEDGMENT

REFERENCES

1. D. Eisel, and W. Demtröder. Chem. Phys. Lett. **88**, 481 (1982).

2. C. Bordas, P. Brevet, M. Broyer, J. Chevalyere, and P. Labastie, Europhys. Lett. **3**, 789 (1987).

3. E. Y. Xu, H. Helm, and R. Kachru, Phys. Rev. Lett. **59**, 1096 (1987)

4. C. R. Mahon, G. R. Janik, and T. F. Gallagher, Phys. Rev. A **41**, 3746 (1990).

5. C. Bordas and H. Helm, Phys. Rev. A **47**, 1209 (1993).

6. F. J. Comes, and U. Wenning, Chem. Phys. Lett. **5**, 195 (1970).

7. W. L. Glab and J. P. Hessler, Phys. Rev. Lett. **62**, 1472 (1988).

8. W. L. Glab and J. P. Hessler, Phys. Rev. A **42**, 5486 (1990).

9. C. Bordas and H. Helm, Phys. Rev A **43**, 3645 (1991).

10. C. Bordas and H. Helm, Phys. Rev A **45**, 387 (1992).

11. H. Helm and P. C. Cosby, J. Chem. Phys. **86**, 6813 (1987).

12. P. C. Cosby and H. Helm, Phys. Rev. Lett. **61**, 298 (1988).

13. P. C. Cosby and H. Helm, J. Chem. Phys. **90**, 1434 (1989).

14. H. Helm and P. C. Cosby, J. Chem. Phys. **90**, 4208 (1989).

15. C. Bordas, P. C. Cosby, and H. Helm, J. Chem. Phys. **93**, 6303 (1990).

16. C. W. Walter, P. C. Cosby, and J. R. Peterson, J. Chem. Phys. **98**, 2860 (1993).

17. P. C. Cosby, J. Chem. Phys. **98**, 7804 (1993).

18. D. P. de Bruijn and J. Los, Rev. Sci. Instrum. **53**, 1020 (1982).

19. This definition of the slit establishing the maximum value for L is only approximate because there is a short region upstream of the slit where both fragments from dissociation of a properly aligned O_2 molecule can both pass through the slit, escape collection by the flag, and arrive at an active area of the PSD-C. This upstream distance is 3.1 cm for production of fragments with a minimum separation at the detector and 0.45 cm for production of fragments with a maximum separation at the detector. In all cases, however, such events constitute only a small fraction of the dissociations produced in a randomly aligned beam and can be neglected for the purposes of the present discussion.

20. W. J. van der Zande, W. Koot, J. R. Peterson, and J. Los, Chem. Phys. **126**, 169 (1989).

21. P. H. Krupenie, J. Phys. Chem. Ref. Data **1**, 423 (1972).

22. R. R. Laher and F. R. Gilmore, J. Phys. Chem. Ref. Data **20**, 685 (1991).

23. The population distribution in the $a^4\Pi_u$ state is observed to be unaffected by quenching.

24. C. E. Moore, Nat. Stand. Ref. Data Ser., Nat. Bur. Stand. (U.S.), **34**, (1970).

25. P. C. Cosby and D. L. Huestis, J. Chem. Phys. **97**, 6108 (1992).

26. K. P. Huber and G. Herzberg, *Molecular Spectra and Molecular Structure IV. Constants of Diatomic Molecules* (Van Nostrand Reinhold Co., N.Y., 1979).

27. J. N. Bardsley, J. Phys. B. **1,** 349 (1968).

28. D. R. Bates, Planet. Space Sci. **38**, 889 (1990).

29. S. L. Guberman and A. Giusti-Suzor, J. Chem. Phys. **95**, 2602 (1991).

30. J.-H. Yee, V. J. Abreu, and W. B. Colwell, "Aeronomical Determinations of the Quantum Yields of $O(^1S)$ from Dissociative Recombination" in *Dissociative Recombination: Theory, Experiment, and Applications*, edited by J. B. A. Mitchell and S. L. Guberman (World Scientific, Singapore, 1989), p.286.

Table I. Observed translational energy releases (W_{obs}) of peaks in the O_2 dissociation spectrum. Peaks are fitted as Gaussians and W refers to the centroid of the Gaussian. The upper and lower entries for each vibrational level refer to data obtained with a 3 keV and 5 keV O_2 beam energy, respectively. The entries G_v are the relative vibrational energies of the O_2^+ $X^2\Pi_g$ state, taken from the constants of Ref. 22. Deviations, $W_{obs}-W_c$, are referenced to a calculated value for the translational energy release W_c that assumes a single dissociating state at the ionization limit (IP = 6.954 eV) with vibrational energies G_v.

v	$O(^1S) + O(^1D)$		$O(^1D) + O(^1D)$		$O(^1D) + O(^3P)$		$O(^3P) + O(^3P)$		G_v
	W_{obs} (eV)	$W_{obs}-W_c$ (meV)	W_{obs} (eV)	$W_{obs}-W_c$ (meV)	W_{obs} (eV)	$W_{obs}-W_c$ (meV)	W_{obs} (eV)	$W_{obs}-W_c$ (meV)	(eV)
0	0.790	-7	3.047	28	5.001	14	6.939	-15	0.
	0.761[a]	(-36)	3.027	8	5.029[a]	(42)	6.944	-11	
1	1.044	15	3.270	18	5.235	16	7.178	-8	0.2322
	1.027	-2	3.281	29	5.258	39	7.189	-3	
2	1.261	3	3.498	18	5.446	-1	7.408	-6	0.4604
	1.243	-14	3.505	25	5.449	2	7.417	3	
3	1.481	0	3.713	9	5.675	49	7.635	-4	0.6845
	1.457	-24	3.725	21	5.680	23	7.646	7	
4	1.727	26	3.931	8	5.901	10	7.861	2	0.9045
	1.700	-11	3.949	25	5.914	34	7.862	3	
5	1.964[a]	(46)	4.161	21	6.124	17	8.088	13	1.1206
	1.925	7	4.193[a]	(53)	6.141		8.043[a]	(-32)	

[a] Weak feature in the spectrum.

119

Table II. Observed intensities of the dissociation fragments for $V_{slit} = -1V$ for the 3000 eV and 5000 eV O_2 beam energies. The intensities at each beam energy are given by I which is normalized to a total intensity of 100. The relative vibrational intensities at each dissociation limit are given by I_v.

Beam Energy (eV)	v	O(^{1}S) + O(^{1}D)		O(^{1}D) + O(^{1}D)		O(^{1}D) + O(^{3}P)		O(^{3}P) + O(^{3}P)		Normalization
		I	I_v	I	I_v	I	I_v	I	I_v	
3000	0	0.18	.06	2.08	.10	1.63	.03	1.32	.06	
	1	0.70	.21	4.49	.22	4.90	.09	2.67	.13	
	2	1.10	.34	5.18	.25	7.74	.14	2.74	.13	
	3	0.69	.21	4.54	.22	15.0	.27	4.94	.24	
	4	0.39	.12	2.07	.10	17.6	.32	5.79	.28	
	5	0.19	.06	1.0	.05	6.70	.12	2.36	.11	
	6	0.03	.01	1.0	.05	2.15	.04	0.82	.04	
	SUM	3.3		20.4		55.7		20.6		= 100.
5000	0	0.07	.05	0.34	.04	1.55	.02	0.64	.03	
	1	0.29	.22	1.20	.14	7.05	.10	2.36	.12	
	2	0.36	.28	1.78	.21	10.5	.15	2.38	.12	
	3	0.28	.22	2.54	.29	21.5	.30	5.26	.27	
	4	0.18	.14	1.19	.14	21.2	.30	6.16	.31	
	5	0.10	.07	0.69	.08	7.20	.10	2.20	.11	
	6	0.02	.02	0.88	.10	1.41	.02	0.61	.03	
	SUM	1.3		8.6		70.5		19.6		= 100.

120

FIGURE CAPTIONS

Figure 1. Schematic of fast beam apparatus to study dissociation of neutral molecules. Excited O_2 molecules, produced by neutralization of O_2^+ ($a^4\Pi_u$) in cesium vapor, are observed to dissociate at the slit assembly, both in the presence and absence of an applied electric field. The correlated neutral dissociation products are monitored on the position and time-sensitive detector.

Figure 2. Measured energy release distribution for O + O atoms formed by dissociation of 5 keV O_2 at the slit in the absence of an applied electric field.

Figure 3. Dependence of the energy release distribution on the magnitude of the potential difference applied across the slit observed for a 3 keV O_2 beam.

Figure 4. Location of the excited states of O_2 that participate in the observed dissociation process, relative to the lowest vibrational levels of the molecular ion.

Figure 5. Measured branching of dissociation products that originate from Rydberg states belonging to the vibrational core states, v+ = 0 to 6, among the available dissociation limits of O_2.
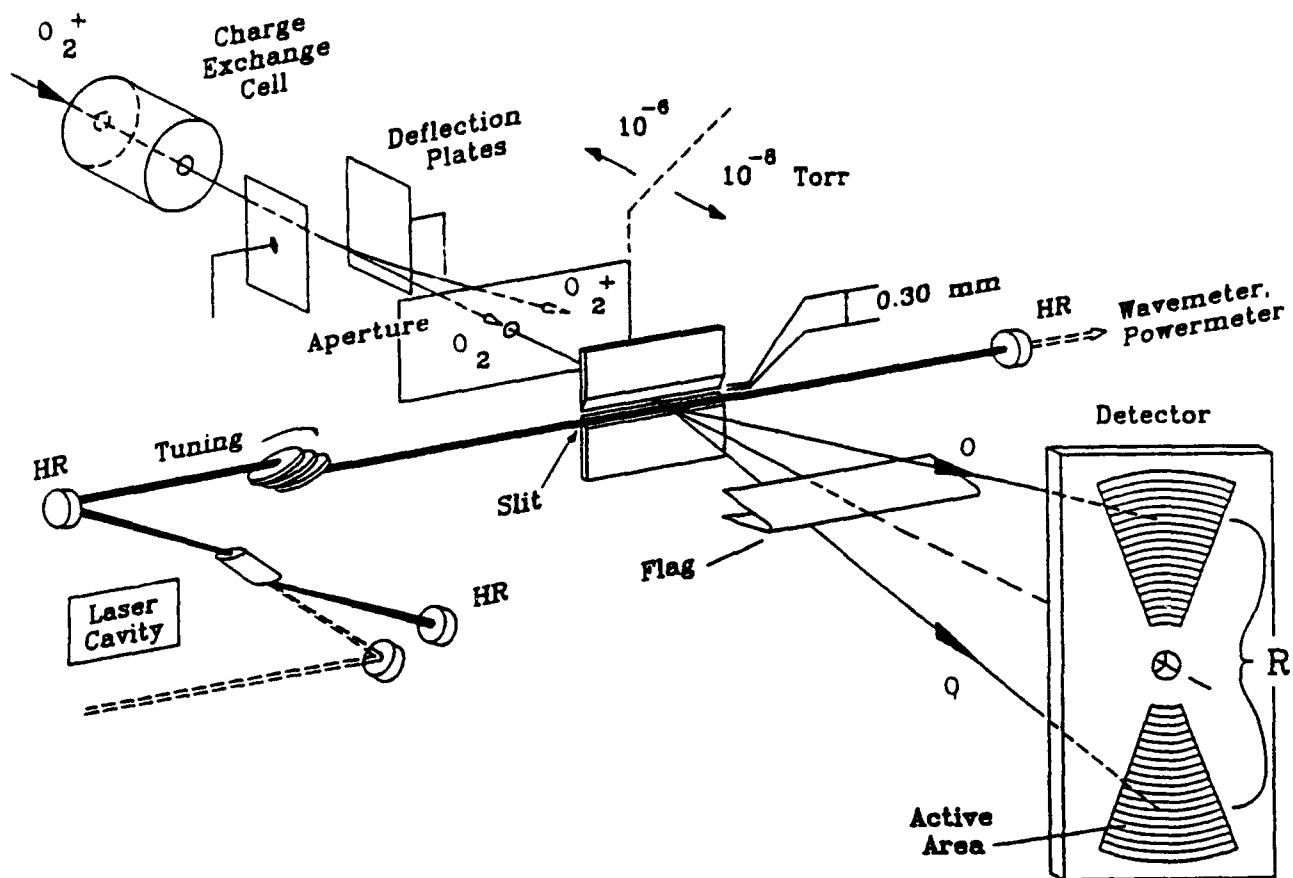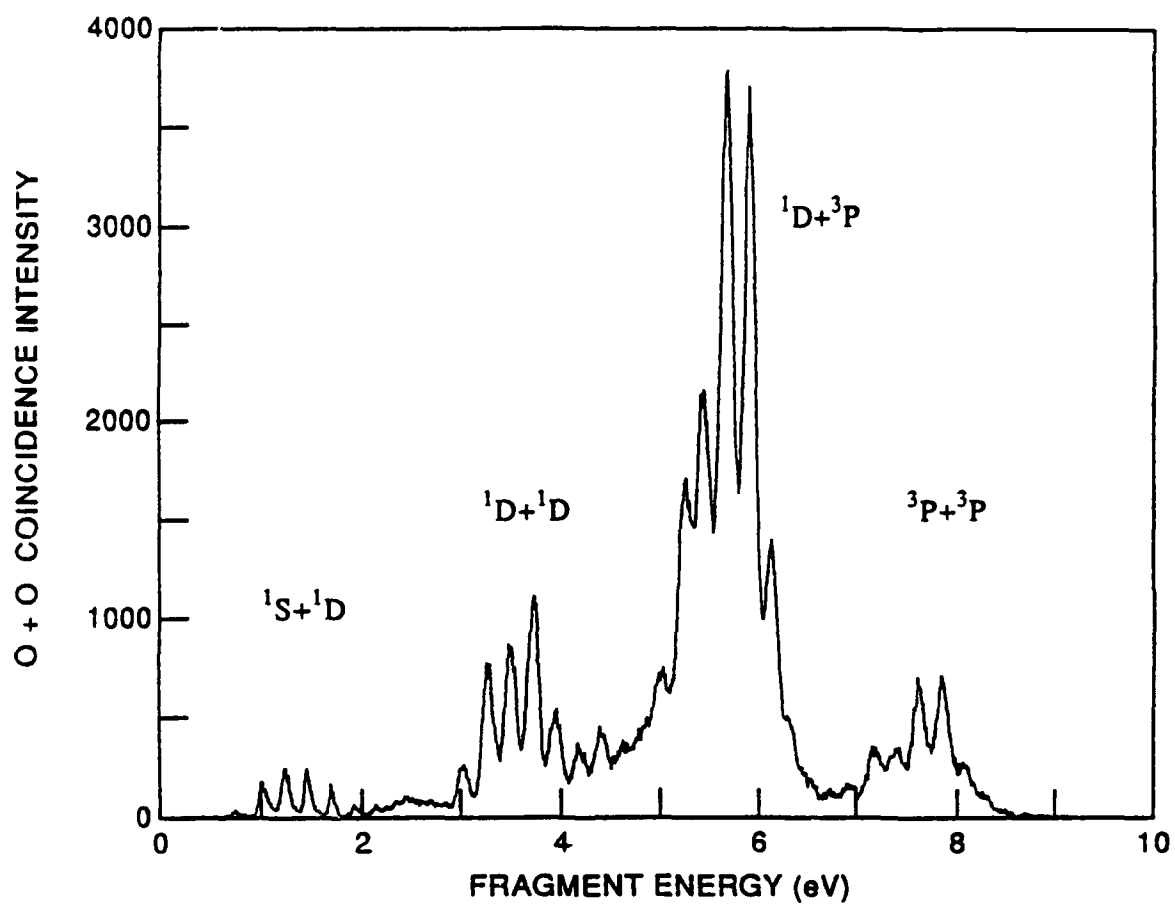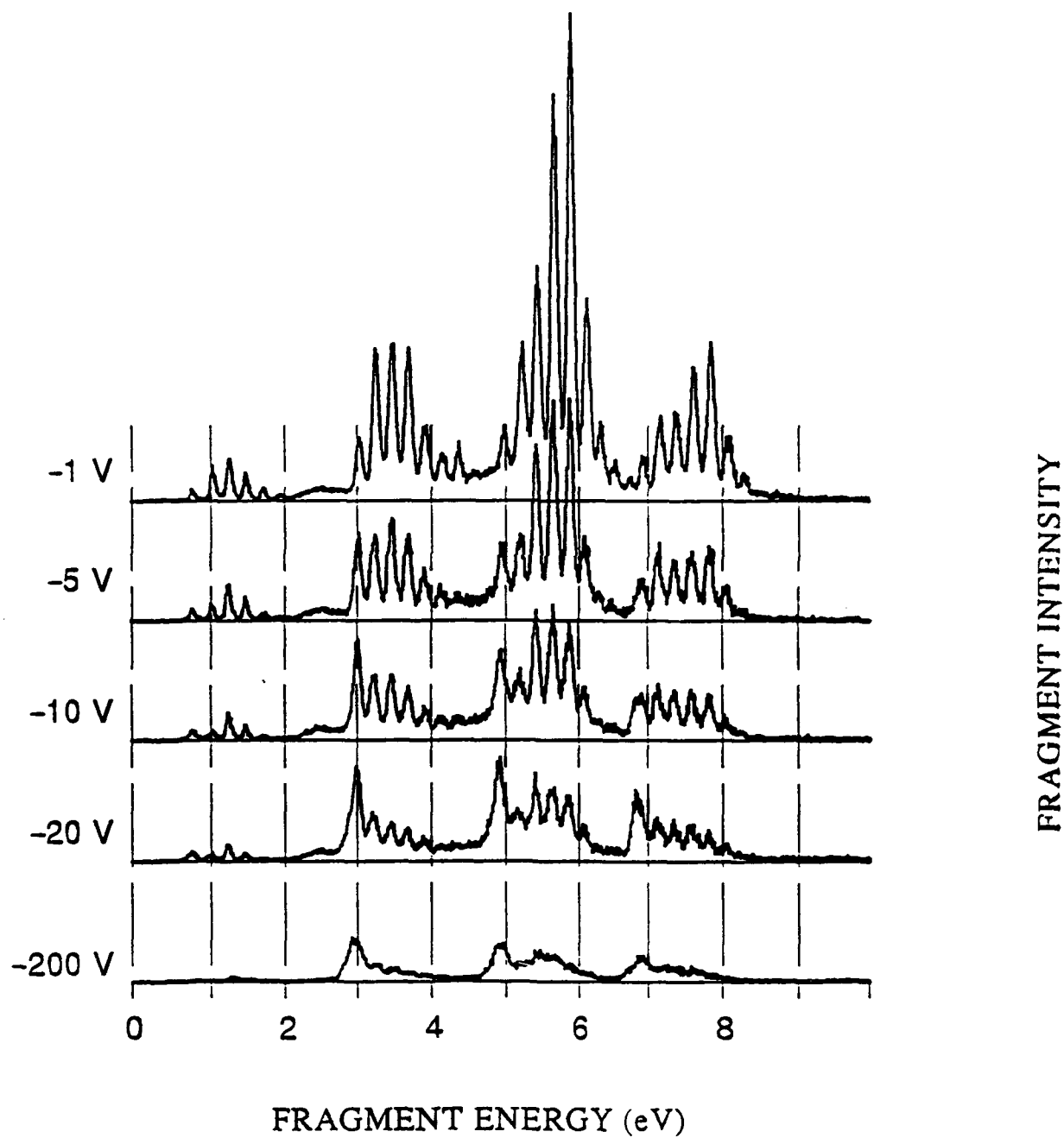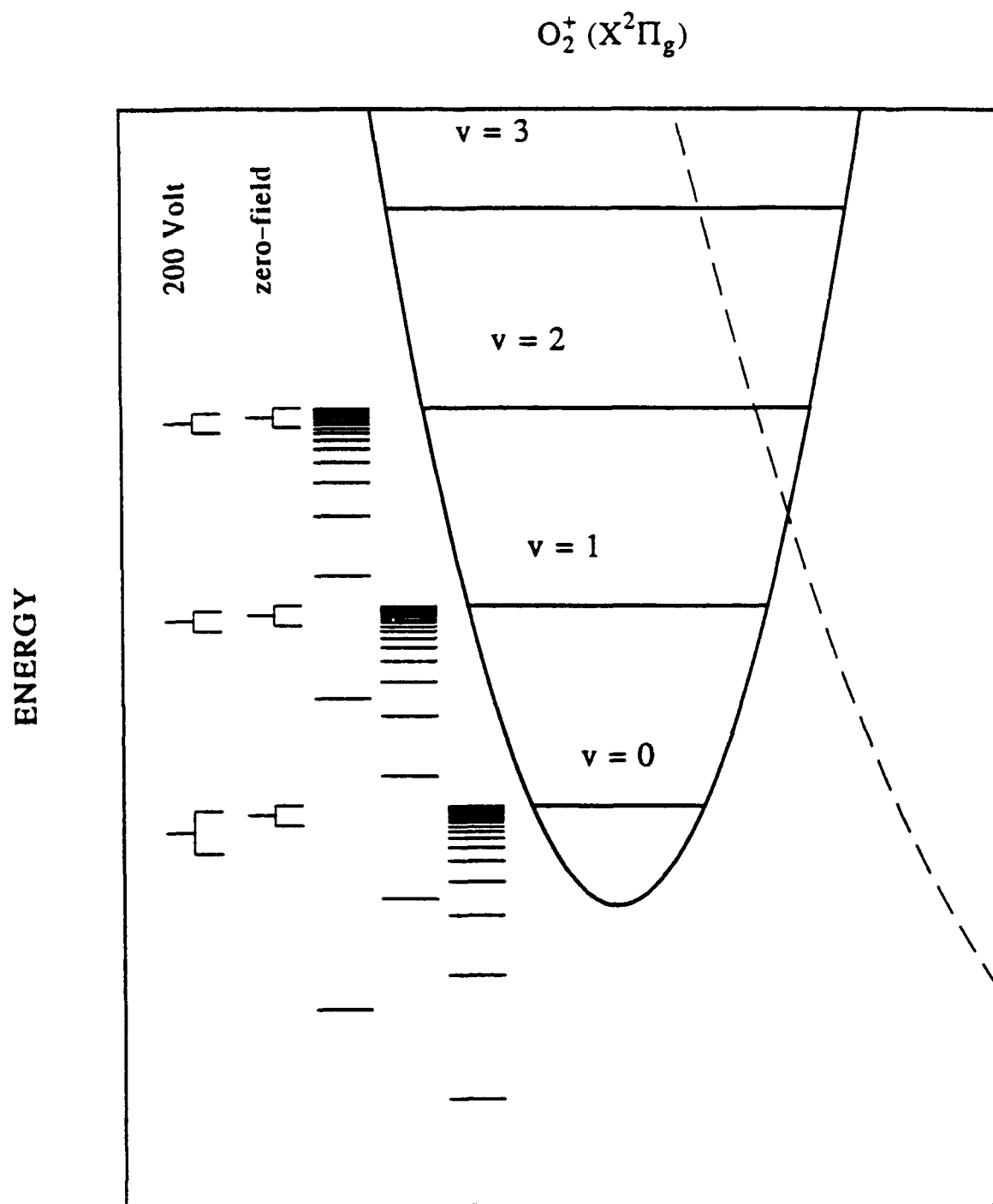
Figure 1

Figure 2

ELECTRIC FIELD DEPENDENCE

Figure 3

$O_2^+ (X^2\Pi_g)$

PREDISSOCIATION OF RYDBERG STATES OF O_2

Figure 4

125

Branching of $O_2^+(v) + e$
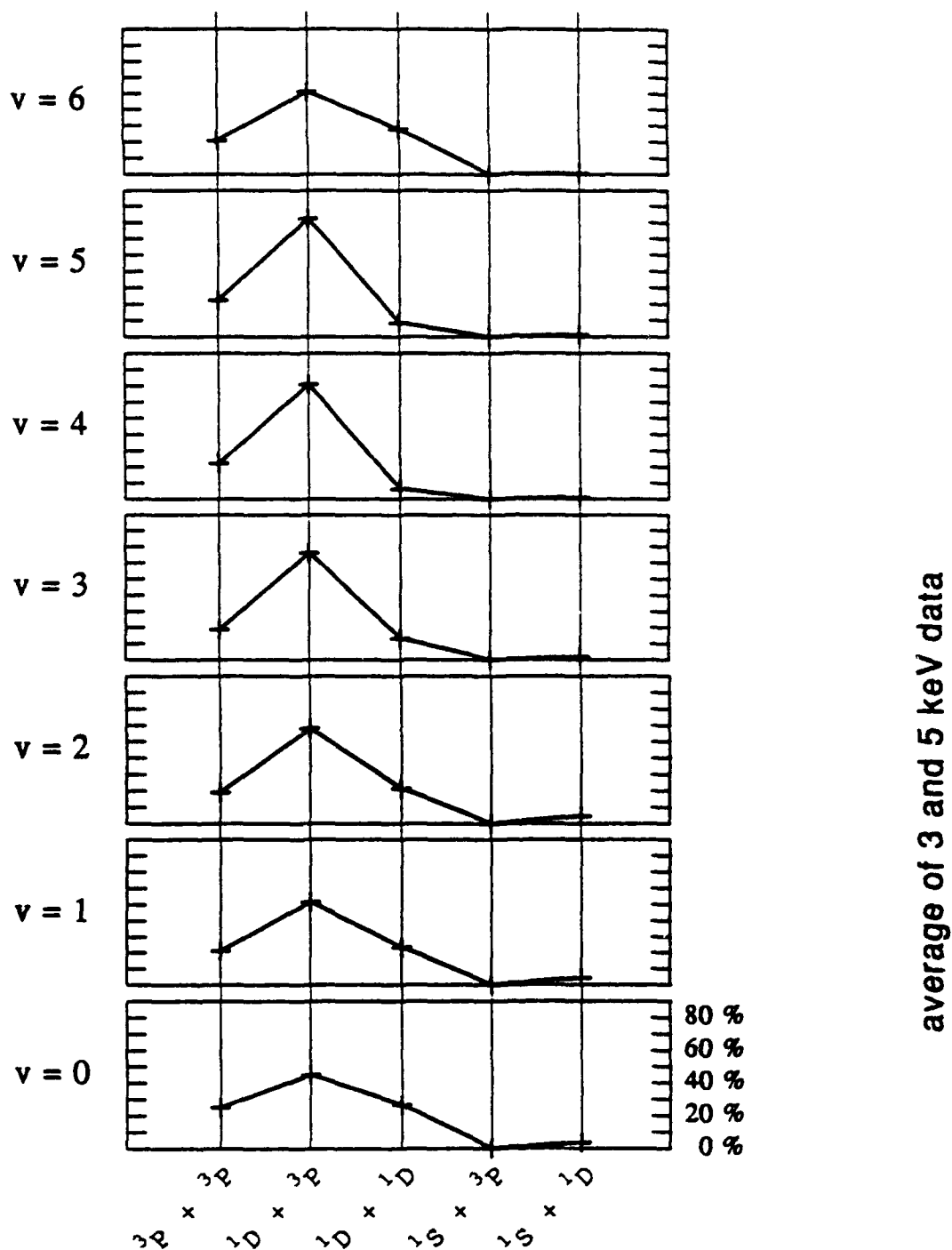

Figure 5